-conjugated organic semiconductor materials for molecular electronics: sustainable synthesis and properties

D.R.R.S.

POLITECNICO DI BARI

Doctor of Philosophy in Risk and Environmental, Territorial and Building Development

09

Coordinator: Prof. Michele Mossa

2023

XXXV CYCLE
Curriculum: CHIM/07

DICATECh
Department of Civil, Environmental, Land, Building Engineering and Chemistry

π-conjugated organic semiconductor materials for molecular electronics: sustainable synthesis and properties

Supervisor:

Prof. Gian Paolo Suranna
DICATECh, Polytechnic University of Bari

Ph.D candidate:
Daniele Conelli

D.R.R.S.

Dottorato di Ricerca in Rischio e Sviluppo ambientale, territoriale ed edilizio

POLITECNICO DI BARI

09

2023

Coordinatore: Prof. Michele Mossa

XXXV CICLO
Curriculum: CHIM/07

DICATECh
Dipartimento di Ingegneria Civile, Ambientale, del Territorio, Edile e di Chimica

Materiali semiconduttori organici π-coniugati per l'elettronica molecolare: sintesi sostenibile e proprietà

Supervisore:

Prof. Gian Paolo Suranna
DICATECh, Politecnico di Bari

Dottorando:
Daniele Conelli

π-conjugated organic semiconductor materials for molecular electronics: sustainable synthesis and properties

Materiali semiconduttori organici π-coniugati per l'elettronica molecolare: sintesi sostenibile e proprietà

EXTENDED ABSTRACT *(eng)*

The need to meet the growing global energy demand has generated an urgent need for more sustainable sources of energy production, storage, and use. In this context, the research is aiming at the generation of new materials based on a simpler and more environmentally friendly chemistry. The study of fundamental chemistry is essential to reach this aim, as it provides the basic knowledge for understanding the chemical processes at the basis of widely used technologies such as photovoltaic cells and light-emitting devices. This PhD Thesis aims to highlight a rational approach to molecular design, eco-sustainable synthesis and characterization of novel conjugated organic materials for different applications in optoelectronics and is divided into three macro sections. The first part provides a focus on the Direct arylation polymerization (DArP) as a facile synthetic tool for the preparation of high-quality conjugated polymers through an atom-economical C–H activation pathway. In this regard, the compatibility of the most advantageous synthetic protocols based on the C-H bond activation in different "green" solvents has been studied in order to explore environmentally sustainable reaction conditions in the context of transition metal catalysed polymerizations for the synthesis of π-conjugated materials.

The second part of the Dissertation describes a rational approach of molecular design, synthesis and characterization of novel and structurally simplified organic molecules conceived for applications such as Hole-Transporting-Materials, low cost and dopant-free for Perovskite Solar Cells (PSCs). The role of a specific match between the perovskite and Hole-Transporting-Materials in order to attain stable Perovskite Solar Cells (PSCs) via effective bonding will be discussed, as well as how these aspects are crucial to preserve the photovoltaic efficiencies for long times under ambient conditions. These results were pursued in collaboration with the research group led by Prof. Paola Vivo (Tampere University, Finland) regarding the photovoltaic characterization and with Prof. Michele Pavone and Prof. Ana Belén Muñoz-García (Federico II University of Naples) for perovskite/HTM interactions.

The third part of the Dissertation describes the development of suitable molecular design strategies, synthesis and characterization of a series of conjugated organic molecules potentially exploitable as luminophores in OLED devices with thermally activated delayed fluorescence (TADF). In addition to synthesis, the thermal, photophysical and electrochemical properties of the synthesized molecules have also been studied and will be presented. The presence of charge transfer states (CT) inherent in the designed molecules, studied in collaboration with the Institute of Nanotechnology of CNR (NANOTEC, Lecce, Dr. Vincenzo Maiorano) confers the new organic materials very interesting optical properties, still the subject of my study, of potential application interest in various areas of organic electronics such as the aforementioned OLED, but also in bioimaging and sensing.

keywords

Conjugated polymers, Direct arylation, sustainable solvents, hole-transporting materials, TADF.

EXTENDED ABSTRACT *(ita)*

La necessità di soddisfare la crescente domanda energetica mondiale ha generato una richiesta impellente di fonti più sostenibili di produzione, stoccaggio e impiego dell'energia. In questo contesto, la ricerca sta puntando alla generazione di nuovi materiali basati su una chimica più semplice e rispettosa per l'ambiente. Lo studio della chimica di base è fondamentale a questo scopo, poiché fornisce le conoscenze per la comprensione dei processi chimici alla base di tecnologie di vasto impiego quali celle fotovoltaiche e dispositivi emettitori di luce. Questa Tesi di Dottorato ha l'obiettivo di evidenziare un approccio razionale di progettazione molecolare, sintesi ecosostenibile e caratterizzazione di nuovi materiali organici π-coniugati per diverse applicazioni in optoelettronica ed è suddivisa in tre macrosezioni. La prima parte fornisce un focus sulla polimerizzazione ad arilazione diretta (DArP) come protocollo sintetico funzionale, in un'ottica di "*atom-economy*", alla preparazione di polimeri coniugati. A tal fine, è stata studiata la compatibilità dei più vantaggiosi protocolli sintetici basati sull'attivazione del legame C-H in differenti solventi "green" al fine di esplorare condizioni di reazione ecosostenibili nell'ambito delle polimerizzazioni catalizzate da metalli di transizione per la sintesi di materiali π-coniugati. La seconda parte della Tesi descrive un approccio razionale di progettazione molecolare, di sintesi e caratterizzazione di nuovi materiali organici strutturalmente semplificati concepiti per applicazioni come *Hole-Transporting-Materials*, a basso costo e *dopant-free* per celle solari perovskitiche (PSC). Verrà discusso il ruolo delle interazioni chimiche specifiche che si instaurano all'interfaccia tra la perovskite e i materiali progettati come HTM al fine di ottenere PSC stabili nel tempo, evidenziando come questi aspetti siano cruciali per preservare a lungo le efficienze fotovoltaiche in condizioni ambientali. Tali risultati sono stati ottenuti in collaborazione con il gruppo di ricerca guidato dalla Prof.ssa Paola Vivo (Tampere University, Finlandia) per quanto riguarda la caratterizzazione fotovoltaica e con il Prof. Michele Pavone e la Prof.ssa

Ana Belén Muñoz-García (Università degli Studi Federico II di Napoli) per le interazioni perovskite/HTM. La terza parte della Tesi descrive lo sviluppo di adeguate strategie di progettazione molecolare, sintesi e caratterizzazione di una serie di molecole organiche coniugate potenzialmente impiegabili come luminofori in dispositivi OLED dotati di fluorescenza ritardata (TADF). Verranno discusse, oltre alla sintesi, le proprietà termiche, fotofisiche ed elettrochimiche delle molecole ottenute. La presenza di stati di trasferimento di carica (CT) insiti nelle molecole progettate, studiate in collaborazione con l'Istituto di Nanotecnologia del CNR (NANOTEC, sede di Lecce, Dott. Vincenzo Maiorano) conferisce ai nuovi materiali organici ottenuti delle interessantissime proprietà ottiche, tuttora oggetto di un mio approfondimento, di potenziale interesse applicativo in diversi ambiti della elettronica organica quali i già citati OLED, ma anche nel *bioimaging* e *sensing*.

Parole chiave

polimeri coniugati, arilazione diretta, solventi sostenibili, materiali trasportatori di lacune, TADF

INDEX

1 CHAPTER 1

History and state-of-the-art on novel eco-friendly approaches in conjugated polymer synthesis using Direct Arylation Polymerization (DArP)

1.1 INTRODUCTION

Preface and motivations

The design of a simplified and "environmentally friendly" chemistry is a fundamental request from a society which appears in a continuous economic transformation. As efforts are made to counter resource scarcity and address the climate emergency, legislative restrictions on the use of materials perceived to be hazardous or highly polluting are increasing. [1] [2]However, waste prevention at the source represents, nowadays, the first aim for developing cleaner processes and products. Chemists and engineers can pursue this aim in several ways, one excellent issue is to minimise the amount of solvent used in a chemical process, or by replacing it with suitable environmentally friendly solvents, first ensuring that this does not, in itself, lead to increased hazards. Toxicity and environmental reasons as much as cost, determine the choice of the solvent for a chemical and there have been a number of recent publications, particularly from certain companies such as GlaxoSmithKline (GSK) and Pfizer, which have listed solvents and prioritised them in terms of "greenness" including such calculations of green chemistry performance. Nowadays, it is also urgent to think of where our future materials will come from and how might we track them, this is particularly important for the development of new and sustainable energy technologies.

Currently, some of the so defined ''critical materials'' are central components of sustainable energy systems because they are the best performing. A few examples include the permanent magnets based on rare earth metals neodymium, praseodymium and dysprosium (Nd, Pr, Dy) used in the major wind turbine, Lithium (Li) and Cobalt (Co) in Li-ion batteries, Platinum (Pt) and Iridium (Ir) in fuel cells and electrolysers, Silicon (Si), but also Aluminium (Al) and Copper

(Cu), in solar cells. These materials are classified as ''critical'' by the European Union and Department of Energy. [3] In the European Union (EU), the advanced materials sector generates more than 2.5 million direct jobs and a Gross Domestic Product (GDP) of over 650 billion euros. At present, the effort we are pursuing as the biggest challenge for the future is how to improve and support such a materials heavy economy without continuing to harm the planet and destroy its ecosystems. Manufacturing and using truly sustainable materials are key goals for our future global economy and for meeting the *Paris Agreement* targets to a transition to net zero emissions by 2050. Materials sustainability is a very multidisciplinary and complex research area to connect with the direct applications, especially when urgent replacements for ''critical materials'' are required, for example in the energy or in constructions sectors. The development of a circular economy value chain is crucial to solve some of the global challenges, starting from the laboratory scale. Not only is it necessary to continue studying and researching new materials to develop innovative solutions against resource scarcity, but it is also essential that these materials can perform across their useful lifetime at a lower cost. Moreover, they should be scalable and manufacturable with minimum energy/water/toxic elements input and be reusable/recyclable at the end of their first useful life. The global economic trend is reflected in an urgent need for economic and environmentally sustainable chemistry in both academia and industry. Along this trend, the field of organic electronics is also rapidly growing, mainly due to a renaissance in the interest on π-conjugated polymers. These materials exhibit semiconducting features, flexibility and solution processability, overcoming the outdated conception that semiconductors are inorganic and rigid, thus giving life to the innovative idea of flexible electronics. For these reasons and for their suitable optical and electrical peculiarities ''π-conjugated polymers-powered'' technologies are largerly applied in the production of organic light emitting diodes including organic solar cells and organic field-effect transistors that are currently undergoing the commercialisation process, bringing lab-scale research into a viable product.[4]

1.2 Sustainable π-conjugated polymers

According to the best research-cell efficiency chart provided by the National Renewable Energy Laboratory (NREL) (Figure 1.1.), the power conversion efficiency (PCE) of organic solar cells (OSCs) has shown a rapid increase in the past few years, with the state-of-the-art OSCs yielding a certified PCE of 18.2%. More in detail, at present the record efficiencies of organic single junction solar cells have now exceeded 19% efficiency under the standard one-sun condition (AM 1.5G), whereas regarding the maximum mobility in organic field-effect transistors are currently up to 20 $cm^2 V^{-1} s^{-1}$ for p-type and approaching 10 $cm^2 V^{-1} s^{-1}$ for n-type conjugated polymers. [3] Although the efficiency of organic photovoltaics is still lagging in comparison to the values above 26% of inorganic photovoltaics, there are important advantages, compared to traditional semiconductors made with silicon and rare earths. For example π-conjugated materials is expected to alleviate or eliminate concerns about pollution connected with the production of silicon and rare earths in the current semiconductor industry.

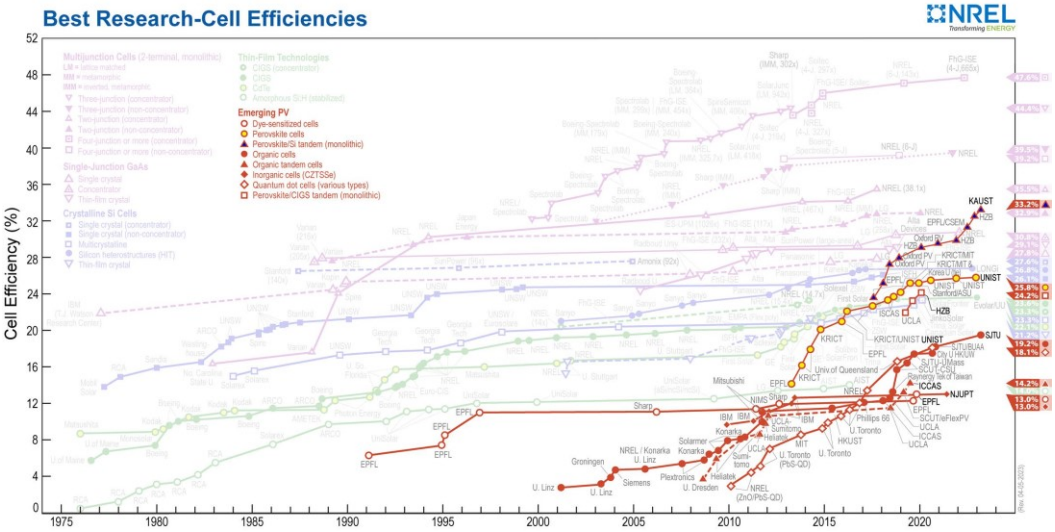

Figure 1.1. *NREL chart of best research-cell efficiencies for emerging PV technologies.* [5]

The plastic solar cells, also known as third-generation solar cells in the emerging PV field, include perovskite solar cells (PSCs), organic solar cells (OSCs), and dye-sensitized solar cells (DSSCs), have gained increasing recognition owing to their

flexibility, low-cost manufacturing or production, ease of synthesis of the materials, and the simplicity of their fabrication processes. Currently, the output of these devices has attained efficiencies for single-junction terrestrial cells of 13%, 16–18.2%, and 25.7% for dye-sensitized solar cells, organic solar cells, and perovskite solar cells, respectively. [6] Specifically, organic solar cells have been receiving increased scientific attention recently, because in addition to the advantages listed above, they can involve the use of π-conjugated polymers whic offer pronounced advantages of excellent mechanical flexibility/stretchability and greatly enhanced device stability as compared to other types of organic solar cells (OSCs). Since the breakthrough discovery of chemical doped polyacetylene possessing electrical conductivity in 1977 by Heeger, MacDiarmid, and Shirakawa, the research has shifted focus towards the area of modeling, fabrication, design and comprehensive investigations of the applications and properties of π-conjugated polymers. With advancement in the field, the focus shifted from insoluble powders like polyacetylene and polyaniline (PANI) to solution processable, high-performance semiconducting polymers such as P3HT can now be used as electrically conducting ink and printed as plastic electronics with roll-to-roll or inkjet printers for large-area and flexible solar panels.[7] However, to meet the requirements of different applications, as reported in the next paragraph, monomers with different π-conjugated structures have been widely studied throughout the years and incorporated into the conjugated backbone to tune the optoelectronic properties of resulting π-conjugated polymers, such as absorption, emission, charge mobility, energy levels. For this purpose are required efficient polymerisation methods compatible with a wide variety of conjugated monomers. Moreover, high-selectivity methods are crucial for the synthesis of defect-free conjugated polymers, essential for optimal performances. [8] In this section of the Dissertation, the most recent advances in the synthesis of π-conjugated polymers is addressed, in the perspective of obtaining them in a greener way with a peculiar emphasis on solvent, reaction conditions and catalyst choice.

1.3 Synthesis of conjugated polymers: an overview

For most of the 20th century, polymers had been considered to be insulators and were utilised as elastic, plastic sacks, paints, channels electrical parts and so on. It was only in 1976, Prof. Alan MacDiarmid together with Prof. Hideki Shirakawa and Prof. Alan Heeger discovered the astonishing conductivity properties of bromine-doped polyacetylene. [9]This has resulted in first pioneering publication on high electrical conductivity of organic polymer, polyacetylene (PA) when doped with halogens (bromine, iodine). [10] In 2000, these three eminent scientists, were awarded with the Nobel Prize in Chemistry for their extraordinary discovery and further development of the new field of electrically conductive organic polymers that revolutionised the way we think about plastics.

In general, a polymer is a macromolecule composes of the repetition of a structural unit, known as monomer. Because most of the polymers are soluble in aqueous or organic solvents, they can be handled easily in solution phase by standard techniques as spin coating, molding or drop casting. In particular, conductive polymers have their backbone built through sp_2 hybridization. In such a configuration π-bonds are responsible for the electronic properties of conjugated polymers since the π-electrons are delocalized throughout the polymer chain over the entire structure which, in turn, allows for fast charge-carrier mobility along the polymer backbone. [11]The π-conjugation concept is illustrated for polyacetylene in Figure 1.2. Examples of the most common conjugated polymers used in organic electronics are illustrated in Figure 1.4.

The conjugated molecular structure leads to one unpaired electron per carbon atom (the π electron).

In the π bonding the carbon orbitals are in the sp_2p_z configuration and the orbitals of successive carbon atoms along the polymer backbone overlap. As represented in Figure 1.2., the overlapping leads to the electron delocalization that permits the charges mobility along the polymer chain. Polymers then can exhibit semiconducting or metallic properties. [12]As a result the electronic structure of

conducting polymers is given by the chain symmetry, that is the number and type of atoms within the repeat unit. [13]

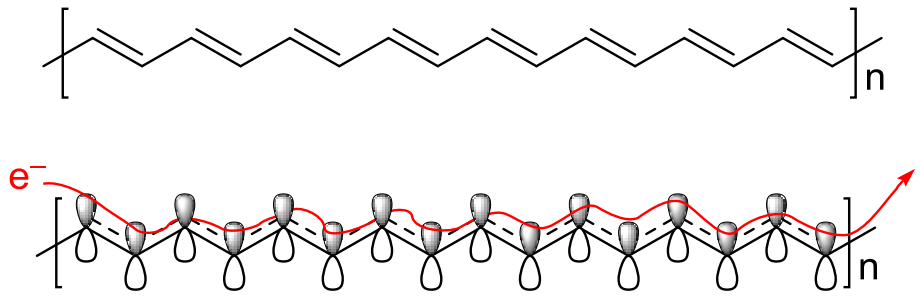

Figure 1.2. *Illustration of how extended p-orbitals in trans-polyacetylene function.*

Polyacetylene (PA) is the archetypal conjugated polymer $(-C_2H_2-)_n$ (Figure 1.2), in which each carbon atom is bonded to two neighboring carbons and one hydrogen atom by a σ bonding, with a π electron on each carbon. The electronic structure of PA, due to an effect called « Peierls instability », derives from the presence of two carbon atoms in the repeat unit, thus, the π band is divided into π and π* bands, each holding two electrons per atom (spin up and down). As a result the π band is complitely filled and the π* is empty. The energy band gap E_g is defined by the energy difference between the highest occupied state in the π band and the lowest unoccupied state in the π* band (Figure 1.3.). The number of the π and π* orbitals is proportional to the number of carbon atoms in the conjugated system.

Consequently, as shown in Figure 1.3., increasing the number of double bonds in the π-conjugated molecule going from butadiene, octatetraene to eventually polyacetylene, the HOMO level increases in energy and the LUMO level decreases in energy. For this reason, the band gap of organic semiconductors, which is typically in the range of 1 to 3 eV, is determined by the structure of the material and decreases for increasing polymer chain length. In analogy to classic inorganic

semiconductors, the filled π-band (HOMO) is often also called valence band and the empty π*-band (LUMO) is referred to as the conduction band.
The alternated structure of polyacetylene characterizes in general conjugated polymers. Because no partially filled bands are present in the electronic structure of conjugated polymers, they typically exhibit semiconducting behavior.

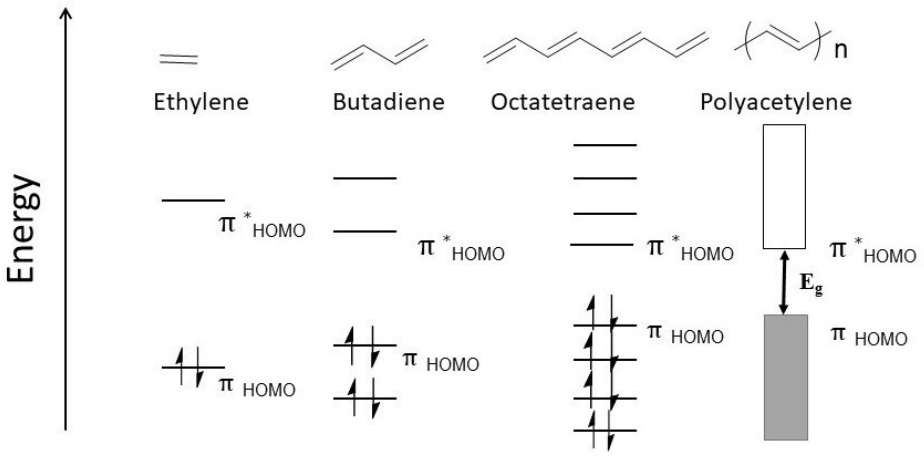

Figure 1.3. *Molecular orbital energy level diagrams for ethylene, butadiene, octatetraene, and polyacetylene.*

1.3.1 Advances towards a focused molecular design

The major breakthrough in the field of organic electronics was the ability to lower the band gap of conjugated polymers. Because E_g depends upon the molecular structure of the repeat unit, synthetic chemists are provided with the opportunity and the challenge to control the energy gap by design at the molecular level. Conjugated systems can be incorporated either in linear or in cyclic structures, they can contain heteroatoms as substituents or even in double bonds involved in the conjugated system.

Simple repeat units, such as polyaniline (PANI), polypyrrole (PPy), poly(paraphenylene) (PPP), and poly(paraphenylenevinylene) (PPV) were state-of-the art during the early stages of the field. This simplicity can be attributed to limited development of structure-function relationships for conjugated polymers where the directive for these materials was primarily to understand their metal-like conductivity achieved by various doping mechanisms. For this purpose it was important that these simple polymers could be easily prepared from simple commercially available starting materials, such as aniline for polyaniline (PANI) or thiophene for polythiophene (PT). However, the main goal was the development of polymeric materials that combined the electrical and optical properties of metals or semiconductors with the processing advantages and mechanical properties of conventional polymers. To meet these requirements, further attempts to achieve much better processability led to the « second generation » of conductive polymers. First experiments showed that the presence of bulky substituents introduced solubility and processability but caused a twisting of the backbone giving poorly conjugated materials. [14]

Generally, advancements within the field of organic electronics have been connected to advancements in organic and polymer synthesis. A breakthrough occurred in the midst of the 80's with the syntheses of highly conjugated and processable poly(3-alkylthiophene)s by a simple one-step oxidation reaction. [15]

Five-membered thiophene rings exhibit a conformation with reduced steric hindrance and processability was ensured by the presence of the solubilizing sidechains.

In this context, the collaborative efforts of Heeger and Wudl paved the way toward further pioneering studies, such as the spectroscopic characterization of poly(alkylthiophene)s (P3AT) and the synthesis of the first narrow bandgap polymer, poly(isothianapthene) (PITN), shown in Figure 1.4. [16] At the time, however, before the discovery of semiconductor applications such as OPV, OLED, or OFET, the conductivity represented the main parameter for evaluating a new polymer. In fact, Heeger et al. reported conductivities of 220 S/cm, 14 S/cm, and 0.4

S/cm for polyacetylene, polythiophene, and PITN. [17] These were performed using oxidized polymer films in the presence of dopants such as AsF_5 (polyacetylene and polythiophene) and bromine (PITN). [18] [19]

A thiophene-based polymer (Figure 1.4.) that continually finds new interest and application from its original disclosure in patent by Bayer A.G. in 1989 is poly(3,4-ethylenedioxythiophene), PEDOT. [20] [21]

The next generation of benchmark materials was introduced in the beginning of 90's by several research groups. The focus shifted from the synthesis of highly conducting polymers to the design of stable semiconducting polymers with tunable electronic and optical properties. This shift was mainly driven by the development of polymeric light emitting diodes and photovoltaic cells.

In particular, of the various applications, a primary focus of conjugated polymer research in the 1990's was in the development of new emitters for OLEDs, which followed the seminal work by Burroughes et al. describing the fabrication of an OLED device incorporating PPV. [22] Following-up this initial report, the research groups of Friend and Holmes provided many additional important advancements within this area.

In summary, the general design criteria for polymers in OLED applications was high luminescence in solution or as films, a useful diagnostic before fabrication of a device, and an amorphous morphology in order to avoid the aggregation induced quenching through interchain interactions.

The use of different aryl units, substituents, and inclusion of heteroatoms allowed for tuning the physical properties, such as solubility and morphology, and also electronic properties, such as the bandgap, influencing the color and intensity of emission. Shortly thereafter, a critical and revolutionary development for the field of conjugated polymers was the report of the polymer MEH-PPV by Wudl and coworkers. [23] This polymer, although structurally similar to its parent-analog, PPV, was a major advancement in that it incorporated branched alkyl substituents, an early example of side-chain engineering, rather than the often encountered linear alkyl substituents. This allowed for increased interchain

polymer distance and an amorphous arrangement of polymer chains. [24] These substituents also allowed for facile solution processing, which is critical for thorough structural characterization and an important attribute for the low-cost manufacture of display devices. MEH-PPV became one of the most studied polymers over the following decade.

Another important class of conjugated polymers studied at the time were polyfluorenes, such as PFO, PFO-CBZ, and F8BT. These polymers incorporated a fused biphenyl with the inclusion of a quaternary carbon, which allowed for the facile inclusion of a variety of solubilizing groups. Additionally, these materials are highly-emissive making them desirable for OLED applications. [25] The fused repeat units of fluorene allow for extended conjugation along the polymer backbone with the inclusion of solubilizing alkyl substituents, which lead to a twisted conformation with the non-fused phenylene based polymers.[26]

Polymers incorporating the fluorene unit also displayed good charge carrier mobilities, allowing them to be incorporated also into OFET devices. The design of polymers for OFET applications follows different guidelines with respect to OLEDs. Specifically, polymers with crystalline properties were desired, such as polythiophenes or polyfluorenes, which allowed for improved charge transport along and between polymer chains. [27] Polythiophenes were also receiving increased attention as well, since the structural tuning of the monomers could be easily accomplished allowing for a broad range of electronic properties.[28]

Additionally, important achievements were made to preserve or improve the regioregularity of this class of polymers through improvements in the synthetic methods, which is further discussed and studied in Chapters 2 and 3 of this Dissertation.

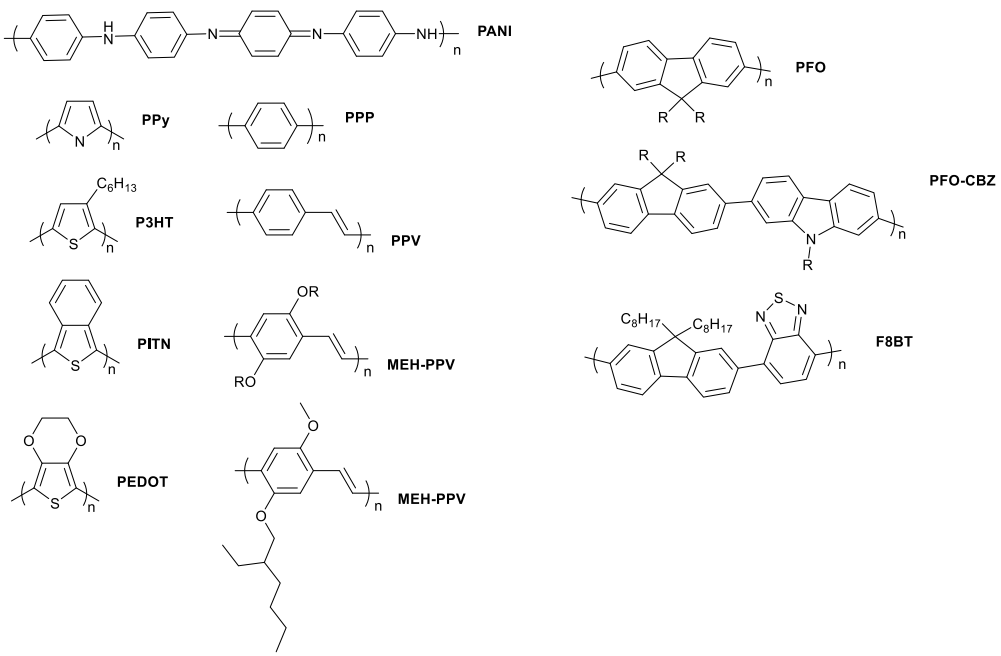

Figure 1.4. *Molecular structures of common π-conjugated polymers in organic electronics.*

Several design strategies to tailor the properties of conjugated polymers for specific applications have been studied. Further progress was dictated by the need of achieving a better control over the bandgap of a conjugated polymer and efficient tuning of energy levels. In this perspective, it has been difficult to reach required conditions in the so called « homopolymer » design concept. Homopolymer consists of a single aromatic/conjugated unit and properties of such polymer are determined by the intrinsic properties of the single aromatic unit. The « third » generation of benchmark materials are marked by the shifting from « homopolymer » to a « donor-acceptor » (D-A) approach. This strategy has been successful in producing polymers with charge-carrier mobilities as high as 14.4 $cm^2\ V^{-1}\ s^{-1}$ in OFETs [(29)] and power conversion efficiencies (PCE) as high as 14% in OSCs. [(30)] In a common design motif of the donor-acceptor approach (D-A), electron rich (D) and electron poor (A) monomers are suitably co-polymerised. The design and synthesis of many new monomers are templated around fused 5- or 6- membered aromatic rings such as thiophene or benzene, and the

stereoelectronic properties of the material can be adjusted or influenced by addition of electron donating or withdrawing atoms (such as nitrogen-containing functional groups). The phenylene vinylene repeat units in polymer showed a good electron donating ability due to the rigid backbone. This also leads the polymer to possess crystallinity with a consequently good hole transporting ability. Thiophene is the most extensively used repeat unit, due to its excellent conjugation, chemical stability and tunability of the property via suitable substitution. Also, polymers based on thiophene building blocks have very good electron donating ability due to high polarizability of sulphur atom in thiophene ring. This makes the charge transport very feasible leading to stable conjugation over the main chain and hence it is ubiquitously used as donor building blocks. Hence, many groups have reported the use of phenylene vinylene as donor repeat unit along with thiophene. Further, several other electron rich donor units have been utilised for the synthesis of polymers such as carbazole, fluorene, benzodithiophene, naphthodithiophene. However, fluorene based polymers have high non-dispersive hole transport mobility and hence, they are used as p-type material for PSC. Because of this property, conjugated polymers based on fluorene have attracted a lot of research attention as hole transport materials (HTMs). [31] Further, the HOMO–LUMO levels of the polymers can be tuned by incorporation of the repeat unit containing heteroatoms. Acceptor units such as benzothiadiazole, thiazolothiazole or diketopyrrolopyrrole have been used so far, which showed a lower band gap due to the better charge transfer (ICT) ability. As shown in Figure 1.5., a large library of organic building blocks is available, regarding both donors and acceptors.

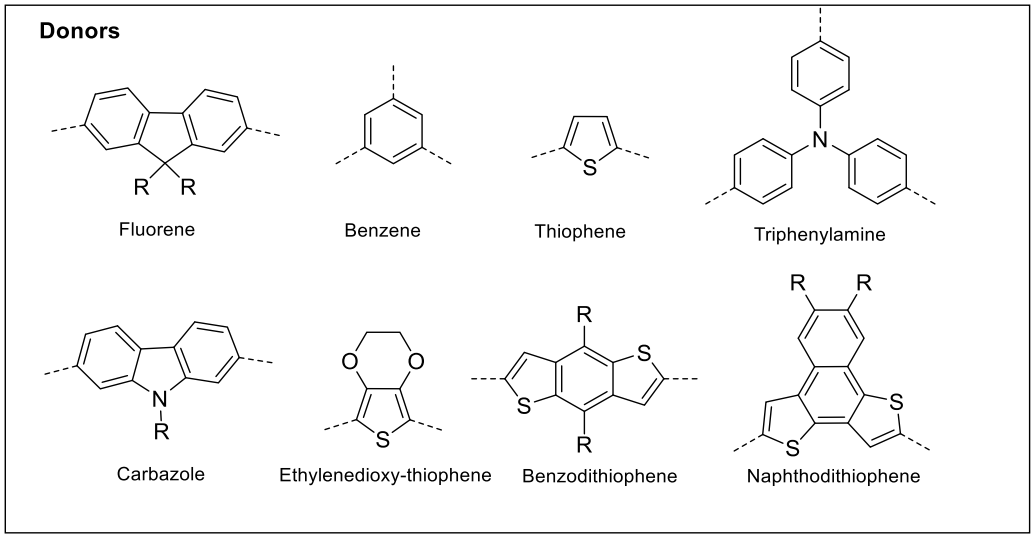

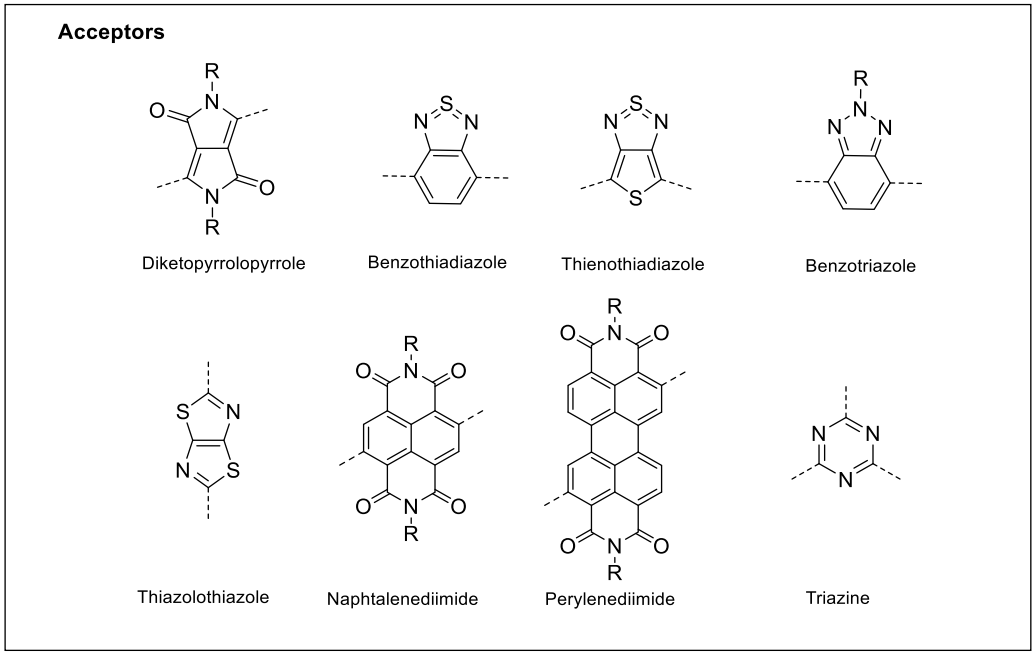

Figure 1.5. *Structures of the main donor and acceptor building blocks commonly used in the synthesis of π-conjugated donor-acceptor (D-A) polymers.*

In conclusion, to design conjugated polymers for different applications several general principles should be kept in mind, including (1) side chains to enhance the solubility and processability, (2) moderate to high molecular weights, (3) tunable band gap and absorption behavior, (4) adjustable HOMO and LUMO energy levels, and (5) suitable morphology. These factors are dependent on each other and must be comprehensively considered for specific applications. For instance, side chains play a significant role for improving the solubility and the obtainable molecular weight of conjugated polymers, but also influence their intermolecular interactions through changes in morphology and thereby the charge carrier mobility. Tuning the energy band gap for obtaining the desired absorptions will usually change the HOMO and LUMO energy levels, and thus change the emitting color in an organic light-emitting diode (OLED) or influence the open-circuit voltage (V_{oc}) in a polymer solar cell (PSC). Therefore it is necessary to fully account for these designing principles and balance the guiding concepts in pursuit of ideal polymers for specific applications.

1.3.2 Synthetic aspects of π-conjugated polymers

As depicted in the previous paragraphs π-conjugated polymers as semiconducting materials have attracted broad academic and industrial interest, especially in the field of organic photovoltaic devices. To encounter the particular needs of such a wide range of applications, tailor-made conjugated polymers must be designed and prepared. A critical aspect of conjugated polymers lies in their preparation as their optical and electronic properties are intrinsically linked to their extended conjugation pathway. Parameters such as molecular weight, molarmass dispersity, and the presence of structural defects are known to affect these properties, which, in turn, impact their performance in organic photovoltaic devices. Robust, reproducible, and reliable polymerization methods are therefore of utmost importance. [32]To obtain high molecular weight polymers with

extended π-conjugation, multiple C−C bond couplings between two sp_2 or sp hybridized carbon atoms are necessary.

Initial examples included the Ziegler−Natta polymerization of acetylene and oxidative polymerization for the synthesis of poly(phenylene)s, poly(thiophene)s, poly(pyrrole)s, and poly(aniline)s. [33]Starting from these early methods, synthesis of poly(hetero-arene)s has increasingly relied on transition metal-catalyzed cross-couplings. [34] In 2010 Richard Heck, Ei-ichi Negishi, and Akira Suzuki were awarded with the Nobel prize in Chemistry for their unquestioned role in both developing and discovering strategies for C-C bond formation. Among thiophene-based homopolymers, polymerizations based on Kumada-Tamao-Corriu, commonly referred to as Kumada, [35] and Negishi couplings[36]are the leading polymerization methods, while Migita-Kosugi-Stille, commonly referred to as Stille, [37] and Suzuki-Miyaura, commonly called Suzuki, [38]couplings are for copolymers based on two or more different repeating units. A general scheme of the cross-coupling reactions is reported in Scheme 1.6.

The next paragraphs will provide a short introduction of the most commonly used cross-coupling reactions for the synthesis of π-conjugated polymers.

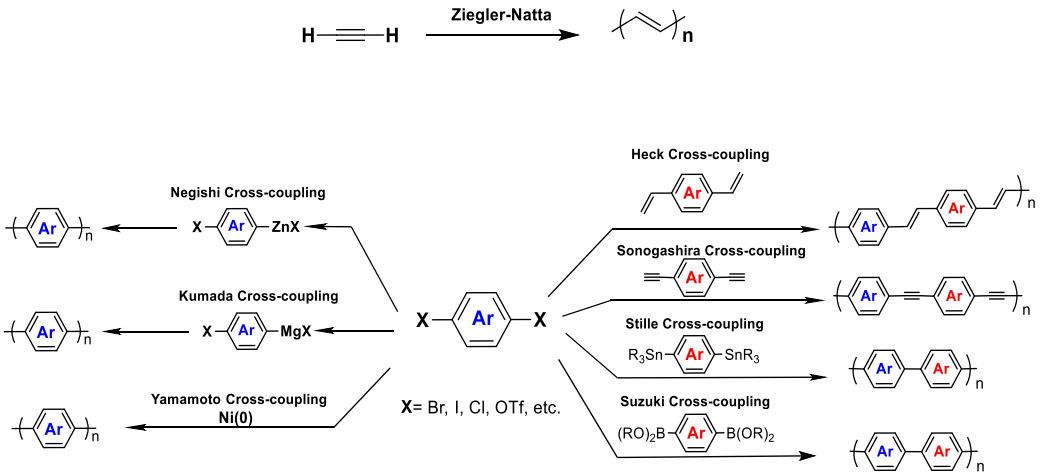

Scheme 1.6. *Overview of traditional C−C coupling techniques for the preparation of π-conjugated polymers.*

Developing an efficient, inexpensive, and green synthetic protocol is important for the large-scale industrial production of conjugated polymers. Recently, transition metal catalysed direct (hetero)arylation polymerization (DArP or DHAP) via C−H bond activation has emerged as a powerful and efficient strategy for the synthesis of organic materials (Scheme 1.7.) [39] reducing organometallic waste and improving step economy. DArP is distinguished as a sustainable and atom-economic approach and will be further discussed in the next chapters of this thesis, as a central topic of the research interests of this Dissertation.

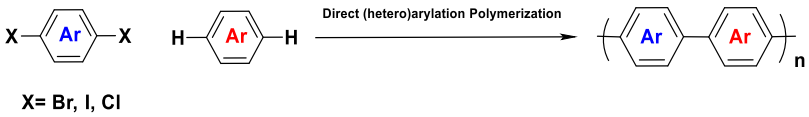

Scheme 1.7. *General scheme of the Direct (hetero)arylation Polimerization approach.*

1.3.3 Cross-coupling polymerizations involving organometallic monomers

In the traditional cross-coupling reactions, organometallic compounds and electrophiles, such as aryl halides, react in the presence of transition metal (mainly Pd- or Ni- catalysts) complexes, forming a new carbon-carbon bond. These transition metal catalysed reactions not only allow the formation of functional polymers from conventional monomers but also the help in the synthesis of new conjugated building blocks by facilitating C(sp_2)-C(sp_2)and C(sp)-C(sp_2) bond formations. [40] It was ascertained that a metal catalysed coupling reaction occurs in three steps as depicted in Scheme 1.8. The reaction begins with 1) oxidative addition of an electrophilic organic halide to a metal catalyst across the C-X bond followed by the 2) transmetallation of the nucleophilic segment of the second reactant placing both the coupling partners across the metal center. Finally, by 3) reductive elimination of the coupled species from the metal complex, following which the catalyst is regenerated, and the coupled product is released.

A detailed description of cross-coupling reactions commonly used for the synthesis of conjugated polymers is given below.

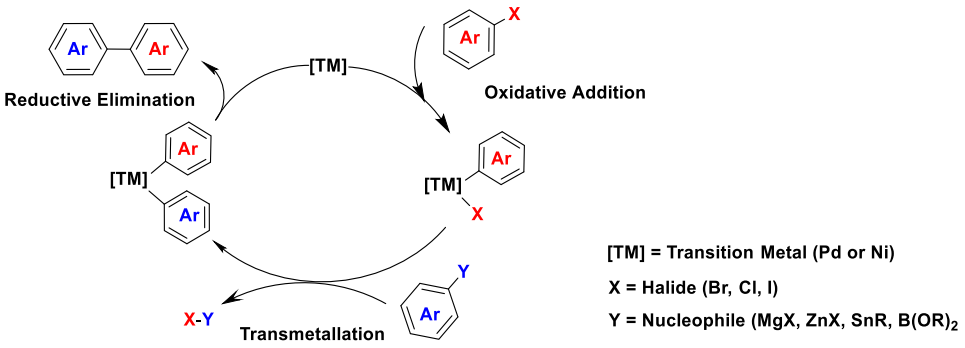

Scheme 1.8. *General mechanism for transition metal catalysed cross-coupling reaction.*

1.3.4 Kumada-Tamao-Corriu cross-coupling

One of the first and most common cross-coupling reactions for C-C bond formation is the Kumada-Tamao-Corriu cross-coupling which allows the rapid stereoselective coupling between alkenyl- and aryl- halides or pseudohalides and aryl-, alkenyl-, and alkyl- Grignard or organolithium reagents, catalysed by a nickel (or palladium) complex. [41]Although it is still not completely understood, a general mechanism of the Kumada-Tamao-Corriu cross-coupling is given in Scheme 1.9. [42]To start the catalytic cycle, the $Ni^{(II)}$ complex first has to be transformed, in situ, to the active $Ni^{(0)}$ complex through the transmetallation step, in which the R group exchanges Mg for Ni, and the reductive elimination step, leading to the active $Ni^{(0)}$. During this activation a small amount of the Grignard reagent is lost and undesired homo-coupling bproducts are formed. The yield of this homo-coupling side product is low (< 1%) because of the low catalyst loading of these reactions.

Next, the active $Ni^{(0)}$ complex is oxidized to the $Ni^{(II)}$ complex by the addition of an organo-halide (R'X), which is called oxidative addition. Then again it is the transmetallation step which is believed to be the rate determining step. The organo-halide subsequently coordinates to the $Ni^{(II)}$ complex, and follows a reductive elimination step to release the homo-coupled product and the active $Ni^{(0)}$ which, in turn, undergoes oxidative addition of the organo-halide, leading to the $Ni^{(II)}$ complex, and completing the catalytic cycle.

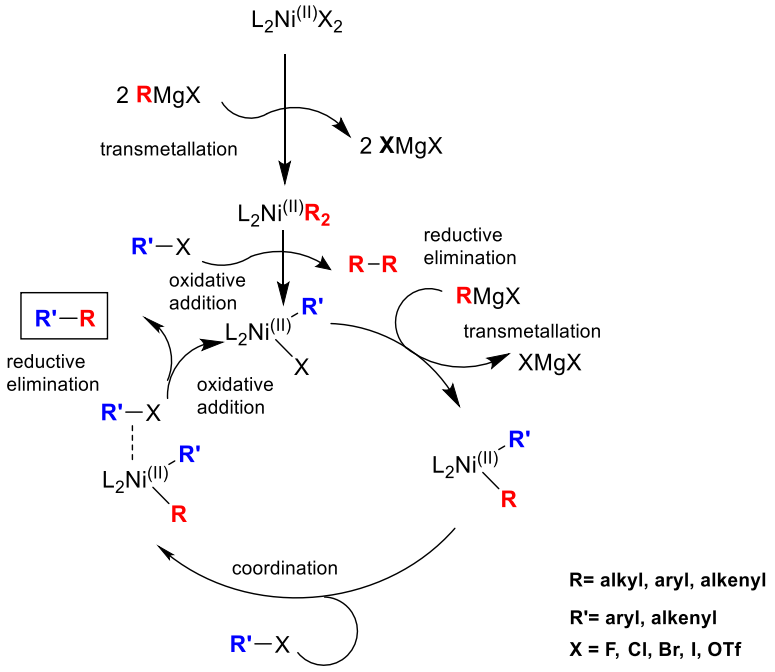

Scheme 1.9. *General catalytic cycle for the Kumada cross-coupling reaction.*

From the catalytic cycle (Scheme 1.9.), the use of the Kumada coupling to synthesize conjugated polymers via the step-growth mechanism is very common, although the reaction can be limited by ineffective magnesium-halogen exchange or ineffective addition of the organic compound to the Grignard regent.

Slow magnesium-halogen exchange occurs in general when the aryl-halide contains more than two aromatic rings, leading to an increase in unwanted side reactions like homo-coupling. [43]Regioselectivity (regioregularity) in the polymerization of 3-alkylthiophenes has profound influence on the conductivity of the formed polymers. Regioregular conjugated polymers, in fact, usually display much higher conductivity than their regiorandom congeners.

Kumada et al. and Corriu et al. reported nickel-catalysed cross-coupling reactions of Grignard reagents with aryl and alkenyl halides back in 1972. Phosphine ligands, able to tune the reactivity of nickel, were introduced by Kumada et al. and their exploration will be the key for synthesizing conjugated polymers with a high degree of regioregularity. It is worth mentioning that McCullough et al. reported that 5-bromo-3-hexyl-2-thienyl magnesium bromide formed in situ could be polymerized using $NiCl_2$(dppp) (dppp = 1,2-bis(diphenylphosphino)propane), producing head-to-tail coupled P3HT. [44] NMR insight showed that the polymers exhibited a 93-98% of the desired regio-chemistry. In 2004, Yokozawa et al. found that Ni(dppp)Cl_2 (dppp = 1,3-bis(diphenyl phos-phino)propane) catalyzed Kumada polymerization of 2-bromo-5-chloromagnesio-3-hexylthiophene followed chain-growth mechanism. [45] Since then, this new polymerization method, named Kumada chain growth polycondensation (KCGP), evolved very fast under the global effort of researchers providing various new polymers with well-defined architectures for understanding the structure-property relationship of conjugated polymers and improving the performance of optoelectronic devices. A major drawback of the Kumada cross-coupling is, however, the low tolerance to reactive functional groups, such as amino-, nitrile-, ester- or carbonyl- groups and the sensitivity of the reaction to water.

1.3.5 Negishi cross-coupling

Negishi cross-coupling may be defined, from a broader point of view, as the palladium- or nickel- catalysed cross-coupling reaction of organometallic building blocks containing metals of intermediate electronegativity (Zn, Al, and Zr) with organic electrophiles such as organic halides and sulfonates. [46] Since its discovery in the middle to late 1970s, Negishi cross-coupling has become a frequently used C–C bond formation method in modern organic synthesis allowing to adopt very mild reaction conditions. [47] Negishi cross-coupling, particularly with the use of organozinc reagents, has enabled cross-coupling of all types of carbon atoms, namely sp, sp_2, and sp_3 carbons, and essentially all possible combinations of various types of organozincs and electrophiles to form carbon–carbon bonds. [48]The generally accepted mechanism for Negishi coupling with organozinc reagents is shown in Scheme 1.10. The reaction involves the oxidative addition of an organic electrophile, typically a halide or a sulfonate ester, to palladium$^{(0)}$, transmetallation with an organozinc reagent, and reductive elimination to release the cross-coupling product and regenerate the catalyst.

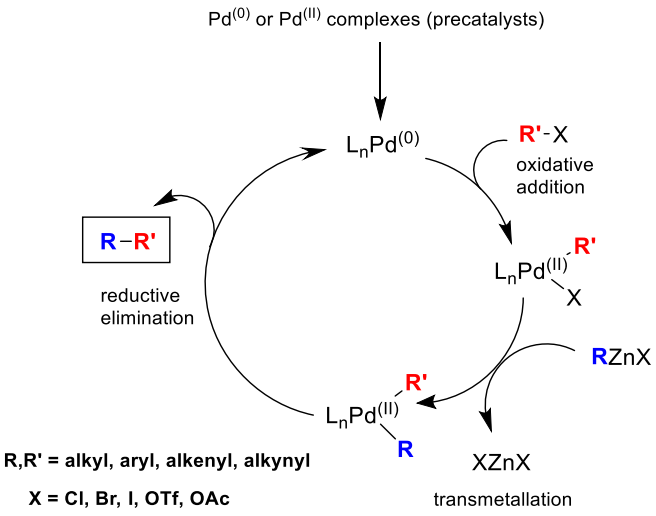

Scheme 1.10. *Mechanism of Negishi cross-coupling reaction with organozinc reagents.*

Negishi coupling becomes the method of choice mainly because of a few beneficial factors to organic synthesis which distinguish it from other cross couplings using tin (Stille coupling), boron (Suzuki coupling), and magnesium (Kumada coupling) organometalics. First, Negishi coupling proceeds with generally high efficiency, namely high yields and high selectivities, which include for example the stereoselectivity in the formation of structurally defined alkenes. Second, Negishi coupling has optimal balance between reactivity and chemoselectivity. Organozinc reagents are more reactive than their Sn and B counterparts, and can tolerate more functional groups than Grignard reagents. Owing to the higher reactivity of organozinc reagents, Negishi coupling can survive the presence of organic tin and boron functionalities, which permits the development of the sequential Negishi–Stille or Negishi–Suzuki coupling methodology and other useful synthetic strategies. Third, Negishi coupling often proceeds under mild conditions. Unlike the Suzuki and Stille couplings, the cross coupling with organozinc reagents typically does not require a base or other additives. Another feature of Negishi coupling is its operational simplicity. The organometals (Al, Zr, and Zn) used in Negishi coupling can be generated in situ and used directly in the subsequent cross couplings. Last but not least, there are multiple convenient and inexpensive accesses to organozinc reagents including transmetalation with organolithiums and Grignard reagents, and particularly, direct zinc insertion in organic halides. [49] Unlike Stille coupling which uses toxic organostannes, Negishi coupling with organozincs is environmentally benign. Negishi cross-coupling has been widely used for the synthesis of π-conjugated polymers such as polythiophenes, polyphenylenes and polyfluorenes. Regioregular, head-to-tail poly(3-alkylthiophenes) (P3AT) can also be prepared with excellent selectivity from the Ni-catalysed cross coupling of the corresponding thiophenylzinc reagents.

The polycondensation of these bifunctional organozinc reagents in the presence of catalyst $NiCl_2$(dppe) (dppe = 1,2-bis(diphenylphosphino)ethane) produced P3AT in greater than 97% head-to-tail regioselectivity.

It has been ascertained that Negishi cross-coupling using for synthesis of conjugated polymers proceeded by step-growth mechanism. [50] However, following the report of Yokozawa in 2004, [45]McCullough and coworkers also reported a similar chain-growth polymerization of 2-bromo-5-chlorozincio-3-hexylthiophene, instead of the Grignard-type monomer, via the Negishi coupling reaction. [51]Later on a universal chain-growth polymerization protocol was developed and demonstrated for the synthesis of both homo-polymers and block-co-polymers. [52] Chain-growth catalyst-transfer Negishi polycondensation has recently been successfully applied for the co-polymerization of electron-rich and electron-deficient monomers. [53] A recent study demonstrates that Negishi polycondensation can offer several critical advantages such as higher reactivity, lower catalyst loading, and higher molecular weight (MW), although π-conjugated polymers are often synthesized by the Stille and Suzuki polycondensations.[54]On the other hand, moisture and oxygen-free conditions seem to be the limitation of Negishi cross-coupling.

1.3.6 Migita-Kosugi-Stille cross-coupling

The Stille cross-coupling reaction between organostannanes and organic halides, triflates or phosphates, to form new carbon-carbon bonds has emerged as a standard approach toward numerous polyaromatic conjugated polymers exhibiting a range of appealing physical properties. The major advantages of the Stille cross-coupling are the growing availability of organostannanes, the high stability towards ambient conditions such as moisture and air, its compatibility with a variety of functional groups and mild reaction conditions. The Stille cross-coupling reaction involves $Pd^{(0)}$-mediated cross-coupling of organohalides, triflates, and phosphates with organostannanes. [55]

The general mechanism of the Stille cross-coupling reaction shown in Scheme 1.11. follows closely that of other $Pd^{(0)}$-mediated reactions, involving an oxidative

addition step, a transmetalation step, and reductive elimination step, which yields the product and regenerates the catalyst.

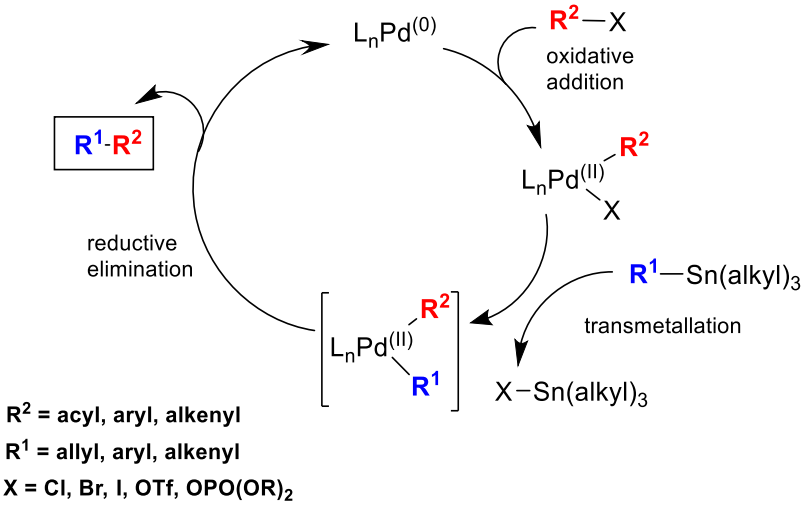

Scheme 1.11. *Mechanism of the Stille cross-coupling reaction.*

The active catalyst is believed to be a 14-electron $Pd^{(0)}$-complex which can be generated in situ. Palladium$^{(0)}$-catalysts such as $Pd(PPh_3)_4$ and $Pd(dba)_2$ with or without an added ligand, are often used. Alternatively, $Pd^{(II)}$-complexes such as $Pd(OAc)_2$, $PdCl_2(MeCN)_2$, $PdCl_2(PPh_3)_2$, $BnPdCl(PPh_3)_2$, etc. are also used as precursors for the catalytically active $Pd^{(0)}$ species, as these compounds are reduced by the organostannane or by an added phosphine ligand prior to the main catalytic process. [56]The first step in the catalytic cycle, oxidative addition, occurs when the organohalide or triflate oxidatively adds to the $Pd^{(0)}$ active catalyst, forming a $Pd^{(II)}$ intermediate $[PdL_nR^2X]$ (L = ligand; R^2 = alkenyl, aryl, acyl; X = Br, I, Cl, OTf or $OPO(OR)_2$).

The second major step in the process, transmetallation, is generally considered to be the rate-determining step. [55] [57] Different groups on the organotin coupling partner transmetallate to the $Pd^{(II)}$ intermediate at different rates and the order of migration is: alkynyl > vinyl > aryl > allyl ~ benzyl ≫ ≫ alkyl. The very slow

migration rate of the alkyl substituents allows the transfer of aryl or vinyl groups when mixed organostannanes containing three methyl or butyl groups are used. Reductive elimination is the final step in the process, which generates the desired product and allows the palladium catalyst to reenter the catalytic cycle. A variety of different organometallic reactions have been utilized in the formation of sp_2-sp_2 carbon-carbon bonds, as typically found in semiconducting polymers, including the Heck, Suzuki-Miyaura, Sonogashira, and Yamamoto reactions. However, the Stille coupling reaction is one of the most versatile. Advantages include the fact that the Stille reaction is stereospecific, regioselective, and typically gives excellent yields. Organotin and organohalide compounds can be conveniently prepared, typically without the requirement for protecting functionalities present in the monomers, and are far less oxygen- and moisture-sensitive than many of their other organometallic counterparts, e.g., Grignard reagents, organo-lithium reagents, and others. With its mild reaction conditions, high monomer solubility, tolerance for a wide range of functional groups, and facile preparation of monomers, the Stille reaction represents one of the most versatile protocols in the arsenal of organometallic chemistry.

While there are many advantages to the Stille methodology for polymerization, one of the main disadvantages is the formation of highly toxic SnR_3X, halogenated tin byproducts, which are known to be harmful to the environment. Additionally, complete removal of tin from the final product is difficult, presenting another key disadvantage. Another potential drawback has been the use of highly expensive and potentially also toxic phosphine ligands as stabilizers for the active catalyst. Additionally, the low reactivity of aryl chlorides under these conditions presents another challenge. In addition, the synthesis of distannane monomers requires use of reactive organometallic compounds, such as organolithium or Grignard reagents, which impose problems in monomer functional group compatibility. The distannane monomers are usually difficult to purify when they are not crystallizable. Palladium catalysts are relatively expensive and $Pd^{(0)}$ (palladium black) formed during polymerization could be detrimental to electrical properties of the

resulting polymers if they are not properly removed. The methodology still yields only low molecular weight polymers, quite often, only oligomers. Side reactions such as homo-coupling of distannane compounds exist in the Stille coupling reaction, which change the stoichiometric balance of monomers and may be one of the reasons for low molecular weight observed in many reports.

1.3.7 Suzuki-Miyaura cross-coupling

Very similar to the Stille cross-coupling is the Suzuki cross-coupling. Suzuki coupling involves the reaction of an organoborane with an organohalide to give the coupled product in a palladium catalysed reaction. Recent development in catalytic conditions has expanded the scope of reactions from aryls to alkyls, alkenyls, and alkynyls. One difference between the Suzuki mechanism and that of the Stille Coupling is that the boronic acid must be activated, for example with base. There are several advantages to this method: 1) mild reaction conditions; 2) commercial availability of many boronic acids; 3) the inorganic by-products are easily removed form the reaction mxiture, making the reaction suitable for industrial processes; 4) boronic acids are enviromentally safer and much less toxic than organostannanes; 5) starting materials tolerate a wide variety of functional groups, and they are unaffected by water; 6) the coupling is generally stereo- and regioselective; and 7) sp_3-hybridized alkyl boranes can also be coupled by the B-alkyl Suzuki-Miyaura cross-coupling. The mechanism of the Suzuki cross-coupling [58] [59]is analogous to the catalytic cycle for the other cross-coupling reactions and has four distinct steps (Scheme 1.12.).

The first step is the oxidative addition of an organic halide to the $Pd^{(0)}$-species to form $Pd^{(II)}$. Next is the exchange of the anion attached to the palladium for the anion of the base (metathesis). The third step is the transmetallation between $Pd^{(II)}$ and the alkylborate complex.

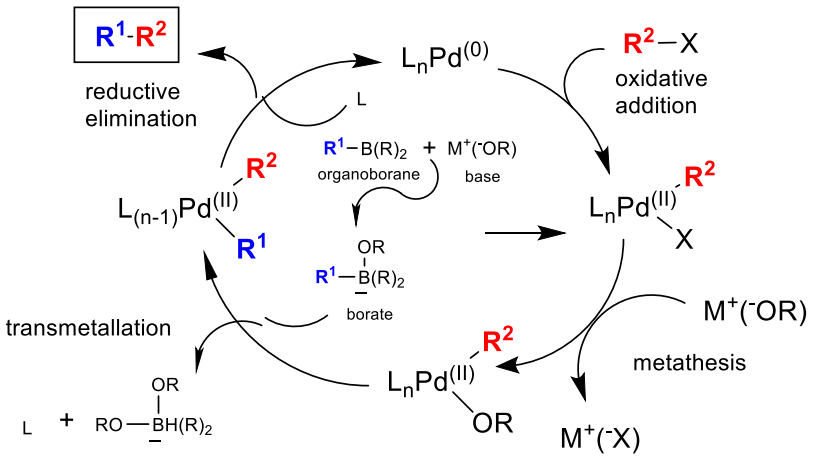

R^1 = alkyl, allyl, alkenyl, alkynyl, aryl

R^2 = alkyl, aryl, alkenyl **X = Cl, Br, I, OTf, $OPO(OR)_2$ (enol phosphate)**

R = alkyl, OH, O-alkyl

Scheme 1.12. *Mechanism of Suzuki- Miyaura cross-coupling reaction.*

Although organoboronic acids do not transmetallate to the $Pd^{(II)}$-complexes, the corresponding ate-complexes readily undergo transmetallation. The quaternization of the boron atom with an anion increases the nucleophilicity of the alkyl group and accelerates its transfer to the palladium in the transmetallation step. Final step is the reductive elimination to form the C-C sigma bond and regeneration of $Pd^{(0)}$. Very bulky and electron-rich ligands (e.g., $P(t\text{-}Bu)_3$) increase the reactivity of otherwise unreactive aryl chlorides by accelerating the rate of the oxidative addition step. Among this variety of cross-couplings, the Suzuki cross-coupling has attracted the greatest attention, as it is compatible with a wider range of functional groups than the Kumada or Negishi cross-couplings, while the organoboronates used have much lower toxicity than the organotins used in the Stille cross-coupling. The organo-boronates also possess high thermal and chemical stability, are relatively inert toward moisture and oxygen, and can generally be prepared efficiently from read-ily available halide precursors under mild conditions. These features of organo-boronates combined with very high efficiency of

Suzuki cross-coupling reaction in terms of C–C bond formation between aryl moieties has turned Suzuki polycondensation (SPC) into one of the most powerful tools for synthesis of conjugated polymers, which have potential applications in emerging technologies such as organic thin-film transistors (OTFTs), organic light-emitting diodes (OLEDs), [60] and organic photovoltaics (organic solar cells, OPVs). [61]Potential side reactions of the Suzuki cross-coupling include oxygen-induced homocoupling of organoboron compounds, B–C bond cleavage, ipso-coupling, and participation of phosphine ligands. In some specific cases, dehalogenation, [62] β-hydride elimination, [63] and cleavage of some functional groups (e.g., amino group) are also possible. [64] In order to reveal the full scope of SPC for the synthesis of high molar mass conjugated polymers, the reaction conditions must be optimized in terms of choice of monomers, catalyst, and solvent, based on careful consideration of the mechanism of the reaction. While much progress has been made, there still remains much scope to further improve these reactions.

The polymers made by SPC often contain significant traces of the Pd catalysts. These have been shown to have adverse effects on the conjugated polymers performance in transistors [65] and in solar cells. [66] The levels can be reduced by appropriate treatment, but total removal may be difficult or impossible without damaging the polymer. This is a problem with all metal-catalysed polymerizations, and so SPC is not disadvantaged compared with other methods, but clearly procedures which minimize the amount of catalyst used or aid in its removal are to be preferred.

1.3.8 Mizoroki-Heck cross-coupling

The Mizoroki–Heck reaction enabling highly efficient synthesis of multisubstituted olefin products. Similar to other Pd-catalysed cross-coupling reactions, aryl halides or pseudohalides are mainly utilized as electrophiles in the Mizoroki–Heck reactions, owing to their superior reactivity and robustness in comparison with those of alkyl analogs. [67]Generally, the reaction undergoes between an

unsaturated halide (or triflate, OTf) with an alkene in the presence of a base and a palladium catalyst to form a substituted alkene (Scheme 1.13.).

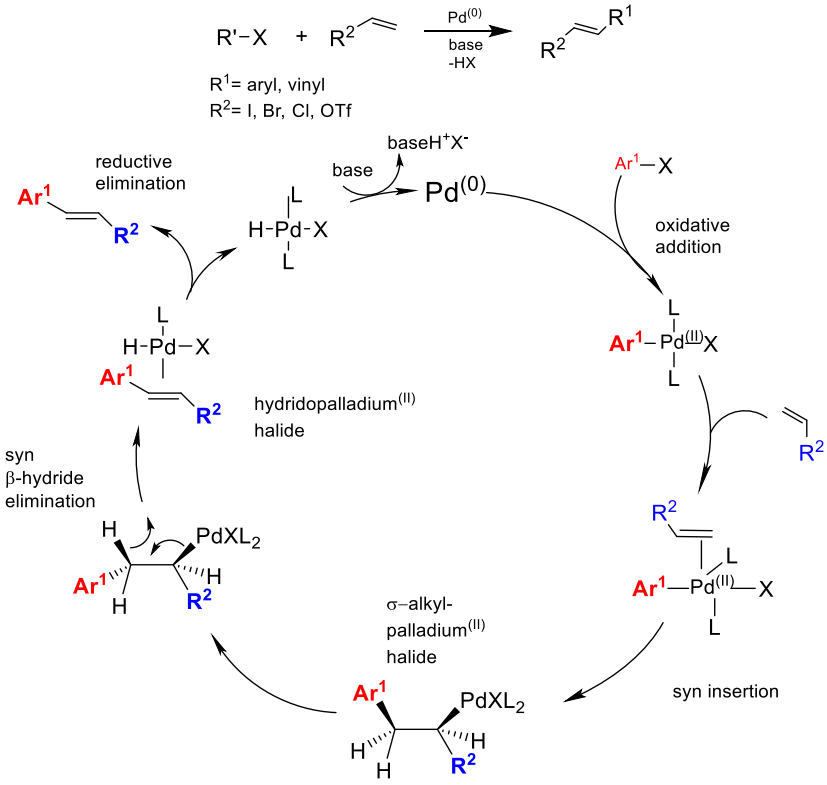

Scheme 1.13. Mechanism of Mizoroki-Heck cross-coupling reaction.

The oxidative addition of the aryl halide to $Pd^{(0)}$ gives a σ-aryl–palladium$^{(II)}$ halide, trans-$ArPdXL_2$, which first coordinates to the alkene after dissociation of one phosphine and then undergoes a *syn* insertion of the alkene, leading to a σ-alkyl–palladium$^{(II)}$ halide. An internal C-C bond rotation in the σ-alkyl–palladium$^{(II)}$ halide brings an sp_3- bonded β-hydrogen in a syn position relative to the palladium atom. A syn β-hydride elimination gives a hydridopalladium$^{(II)}$ halide ligated to the arylated alkene. After dissociation from the arylated alkene, the hydridopalladium$^{(II)}$ halide undergoes a reversible reductive elimination to regenerate the active $Pd^{(0)}$ complex. The base shifts this equilibrium towards the $Pd^{(0)}$ catalyst by

quenching the hydrogen halide. The reactivity order of aryl halides in Mizoroki–Heck reactions is usually: ArI > ArBr >ArCl, suggesting that the oxidative addition is rate determining for the less reactive aryl halides. Besides the usual parameters of all reactions (temperature, solvent, and concentration), other parameters may be varied (Pd precursors, ligands, bases, additives, etc.) to optimize Mizoroki–Heck reactions. An important advantage of this reaction relies the consideration that does not require metalation of monomers, unlike other cross-coupling reactions, and therefore it is easy to prepare monomers. Furthermore, this coupling polymerization has been reassessed as an atom-efficient, greener synthetic method involving direct arylation. Also, the Heck reaction relies on the formal activation of the C-H bonds belonging to the vinyl moiety. In this manner, the polycondensations based on the Heck cross-coupling can build up all-carbon conjugated polymer backbones, thus circumventing the only limitation of DArP (discussed below) consisting in the necessity of using heteroaromatic structures as the monomers. [68]

1.3.9 Tandem Suzuki–Heck polymerization

An interesting evolution of the Heck polymerization is represented by the tandem Suzuki–Heck polymerization, in which the use of the commercially available potassium vinyl-trifluoroborate (PVTB) should avoid an excessive manipulation of the available starting materials (i.e., the dihalo-derivatives) for the preparation of the appropriate monomers. This synthetic procedures has been recently proposed for Poly(arylene vinylene)s (PAVs) preparation in order to reach the goal of an AA/BB chain-growth polycondensation. [69] For this purpose, one of the two co-monomers must exhibit a different reactivity once linked to the growing chain. Grisorio and co-workers [70] conducted Suzuki/Heck copolymerization of dibromofluorene and potassium vinyl trifluoroborate (PVTB) for the synthesis of poly(fluorenylene-vinylene), and they observed that the polymerization proceeded in a chain-growth polymerization fashion until the middle stage, while the formed oligomers were coupled in a step-growth polymerization fashion in

the final stage. Differing from the difunctional ethylene equivalents commonly used for PAV syntheses (e.g., bis-stannyl ethylene or dibromoethylene), the “monofunctional” potassium vinyl trifluoroborate (PVTB), in principle, possesses the requisites to sustain a chain-growth condensation polymerisation. In fact, in the Suzuki–Heck (SuHe) polymerisation with aryl dibromides, PVTB is involved both in Suzuki coupling and, once linked to an aryl derivative, in the Heck coupling. In this Pd-catalysed polycondensation, the Suzuki reaction involving PVTB allows the vinylation of the aryl groups, whereas the Heck cross-coupling between the terminal vinyl and bromo derivatives are the steps leading to the growth of the polymer chain. Using AA to indicate the aryl dibromide, and because of the two fold reactivity of PVTB, it was proposed to denote the reaction course for the SuHe polymerisation as AA/B(C) type, in which B represents the reactivity of the PVTB comonomer towards the Suzuki coupling and C represents the reactivity of the resulting vinyl chain end towards the Heck reaction. The scheme 1.14. depicts the proposed mechanism of the SuHe polycondensation between the fluorenyldibromide and PVTB, which was found to occur by a chain-growth process. The $[Pd^0L_n]$ species resulting from PVTB reduction of the precatalyst catalyses the Suzuki coupling of fluorenyldibromide with PVTB to give fluorenyl-vinyl-bromide derivative. Once formed, this vinylic derivative can react with fluorenyldibromide in a Heck step to give the dimer (containing two externalbromine atoms), which, in turn, is forced to participate in a Suzuki coupling with PVTB by preferential oxidative addition to give the vinyl-dimer derivative. The iteration of alternating Heck reactions with fluorenyldibromide and Suzuki additions of PVTB results in the growing of the chain to eventually produce the polymer. Analizing the catalytic cycle, it is apparent that Pd remains attached to the growing chain throughout the polymer formation.

After the formation of the chain intiatior, the catalytic process begin to give the higher homologues bound to Pd through the terminal vinyl group, which is prone to the addition of a molecule of fluorenyldibromide by a Heck coupling forming a dimer derivative.

The coordination of Pd^0 to the vinyl chain end before the oxidative additions is not surprising in the light of the behaviour exhibited by related d^{10} metal centres such as Ni^0 and Pt^0, which are coordinated by C=C double bonds before undergoing oxidative addition by a Br-C bond. On formation of dimer derivative, the Pd centre (surrounded by the stabilising ligands L_n) reaches the end of the newly elongated polymer through a "ring-walking" process, where it finds the second Br atom formerly belonging to fluorenyldibromide. The preferential oxidative addition of this C-Br moiety gives the dimer bringing the Pd centre at the end of the chain, which, in turn, reacts with PVTB yielding a superior homologue of the dimer that closes the catalytic cycle. The perspective of better physical properties deriving from a narrower molecular weight distribution of the polymers through the development of chain-growth polycondensation methods is recognised as highly desirable in organic electronic devices.

To date, the reassessment in an atom-efficient and greener keys of the synthetic methods involving direct arylation of the monomers is growing in the academic field. In this perspective, the **Chapter 3** of this thesis is focused on the investigation about the compatibility of both the tandem Suzuki–Heck and DArP protocols with two environmentally benign uncommon solvents: anisole and propylene carbonate. In particular, as discussed in the following of this dissertation, implementing these sustainable solvents in the synthesis of poly(9,9-dioctylfluorenylene-vinylene) via tandem SuHe polymerisation, I could be able to obtain satisfactory results concerning both the catalyst performances and the resulting poly(arylene-vinylene) regioregularity. [71]

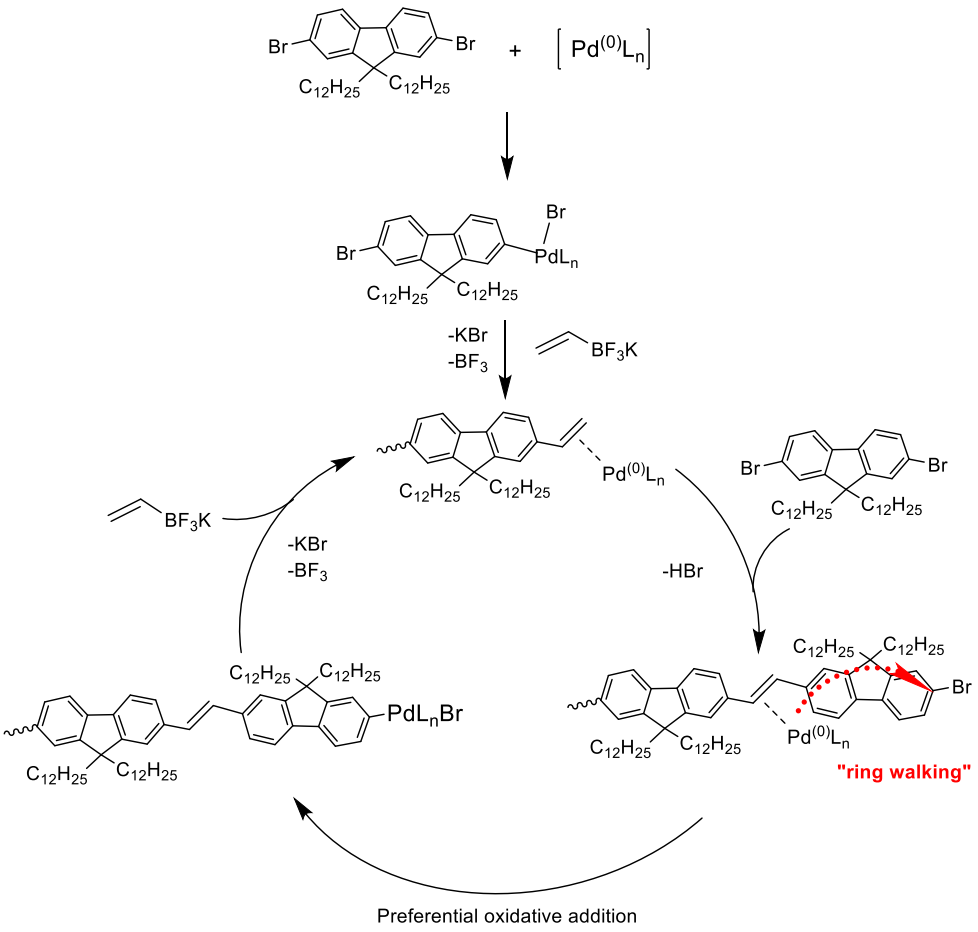

Scheme 1.14. *The proposed catalytic cycle of the "chain-growth" stage of the tandem SuHe*

1.4 Direct Arylation Polymerization (DArP)

Direct arylation through C–H bond activation has the potential to reduce the number of steps and hazards while offering, at the same time, tremendous potential for atom-efficient synthetic methodologies. [72]The main difference from the above reported cross-coupling reactions and direct arylation is that an organometallic monomer is not required in the latter and this enables facile direct coupling of aryl halides with non-substituted heteroaryls without the need of preactivating the sp_2 C-H bonds (scheme 1.15.). [73]

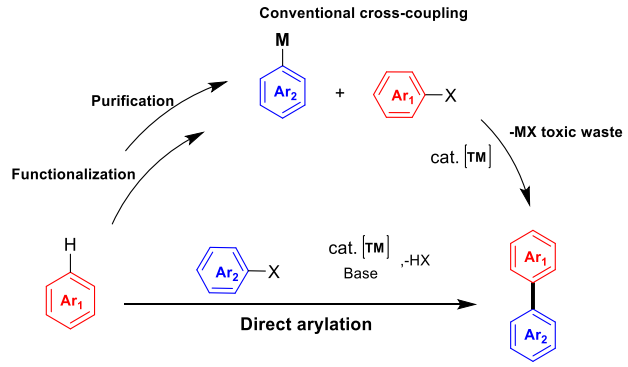

***Scheme 1.15.**: Comparison of traditional cross-coupling reactions with direct arylation.*

As a result, a variety of π-conjugated molecules and polymers could be synthesized via direct C-H arylation in fewer synthetic steps, without involving highly flammable reagents such as butyl lithium and highly toxic agents such as organotin that are often used in Stille coupling. Direct arylation was first reported by Lemaire and coworkers in 1999 [(74)] as an alternative to commonly used routes such as Kumada-Corriu reaction, for synthesis of polythiophenes. 2-Iodo-3-octylthiophene was polymerized under Heck-type reaction conditions using $Pd(OAc)_2$ and tetrabutylammonium bromide as the catalytic system to yield poly(3-octylthiophene) with a molecular weight (M_n) of 3 kDa and a moderate regioregularity of ~90%.

Even though this route circumvented the need for prefunctionalization of thiophene monomers, the oligomeric products obtained made it a poor choice for synthesizing polythiophenes. In 2010, Ozawa's group reported the direct arylation synthesis of poly(3-hexylthiophenes) using Hermann-Beller catalyst instead of $Pd(OAc)_2$ to obtain high molecular weight (M_n = 30.6 kDa) polymers with a regioregularity as high as 98%. [(75)] Several phosphine ligands were tested and tris(2-dimethylaminophenyl)phosphine in combination with cesium carbonate as the base was found to give the best results. The term "catalytic direct arylation" was introduced by Fagnou et al. in 2006 describing those Pd-catalyzed reactions leading to C–C aromatic bond formation from C–H and C–X aromatic bonds

introducing new signature features of the adopted conditions. [76] The first direct arylation protocols were based on palladium catalysts (with palladium diacetate as the most used precatalyst), a carbonate base, a phosphine ligand and a coordinating polar solvent, such as DMA, but with the possibility to conduct the reactions in other aromatic solvents. Such protocols, for instance, were applied for DAr of perfluorobenzenes. Fagnou et al. in 2006 [77]introduced pivalic acid, PivOH, specifically the pivalate anion as a "proton shuttle" from the arene unit to the carbonate base in catalytic direct arylation systems. It was found that the pivalate anion, if combined with a palladium catalyst leads to highly active species efficient for direct arylation of simple arene units. This discovery extended the application of catalytic direct arylation reactions allowing C-H bond activation on many different substrates, not necessarily electron-deficient systems. The advancement deriving by the addition of the carboxylic acid, highlighted the limits in the adopted conditions by Lemaire et al., allowing to obtain polymers with much higher molecular weights. In a 2012 paper, Leclerc and coworkers optimized the direct arylation polymerization of a donor-acceptor polymer synthesized from a C-H active acceptor molecule–thienopyrroledione (TPD) and a brominated bithiophene derivative. Best results were obtained when Pd(OAc)(o-Tol) and tris(o-methoxyphenyl)phosphine were used as the catalyst ligand to give a molecular weight of 56 kDa and polydispersity of 2.6. [78]

C-H activation of TPD demonstrated DArP to be the more efficient choice for synthesis of TPD-based donor acceptor polymers. Other contributions to the development of DArP were made by Kanbara's research group which reported conditions for the C-H activation of 1,2,4,5-tetrafluorobenzene. Polymerization with dibromooctylfluorene using palladium acetate as the catalyst yielded polymers with M_n as high as 31.5 kDa after a reacting for 48 hours. [79]

DArP conditions can be classified into a few different classes which are summarized in Figure 1.16. Class A is derived from the pioneering works of Lemaire et al. [74], Sun et al. [80], Kumar et al. [81], and early DArP conditions employed by Kanbara et al. [82] These conditions are typically run in coordinating polar solvents like

N,N-dimethylformamide (DMF), N,N-dimethylacetamide (DMA), or N-methylpyrrolidone (NMP) with a base (e.g. potassium carbonate (K_2CO_3)) with the optional addition of a phase transfer agent or phosphine ligand but are defined by the absence of a carboxylic acid additive (e.g. pivalic acid (PivOH)) which, as highlighted above are characteristic of Fagnou-derived DArP conditions. Where applicable, the most common phase transfer agent utilized is tetra-n-butylammonium bromide (TBAB). In general, these conditions are compatible with C–H activation of electron-poor and electron-rich moieties but tend to achieve higher molecular weights with C–H activation of electron-poor substrates, which is reasonable considering the theorized concerted metalation deprotonation (CMD) pathway via carbonate or carboxylate additives that direct arylation operates through as discussed below. Class B and Class C are derived from the pioneering work of Fagnou, et al. in 2006. [77] In general, Class B conditions have been broadly applicable across a wide variety of different substrates and polymers and are probably the most attractive for their simplicity. Nonetheless, the utilization of phosphine ligands can sometimes improve the resulting polymer quality.

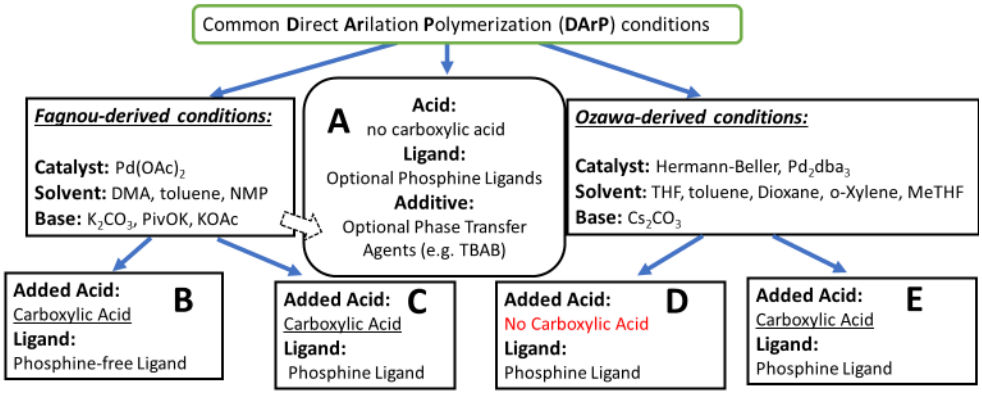

Figure 1.16. *Classification of the developed DArP conditions commonly used.*

1.4.1 Mechanism of Direct Arylation Coupling

The mechanism of direct arylation coupling has been the subject of several experimental and computational reports in the past two decades.

The most studied are concerted metallation-deprotonation (CMD), aromatic electrophilic substitution (S_EAr) and Heck-type arylation. The elucidation of the reaction mechanisms of direct arylation has been undertaken by combining experimental data and theoretical calculations, revealing that CMD is involved in most direct arylation processes through the use of carbonate or carboxylate bases. [83]Scheme 1.17. describes the common mechanism of direct heteroarylation by the CMD pathway for both carboxylate-mediated and carboxylate-free catalytic models. The reaction begins with the oxidative addition of the aryl halide bond (Ar_1-Br) to the $Pd^{(0)}$ complex with bidentate ligands (L) to form an aryl-halo complex. Depending on the catalytic model, a carboxylate or carbonate ion coordinates with the aryl-halo complex to deprotonate Ar_2 while simultaneously forming the Ar_2-Pd bond, hence leading to the formation of the transition state. The concerted-metalation and deprotonation step distinguishes direct C-H arylation from the conventional C-C coupling. It should be noted that while most arenes follow the CMD pathway, the exact mechanism depends on the nature of substrates, ligands and solvents involved. [84] The final product is formed by the reductive elimination of Ar_1-Ar_2 from palladium.

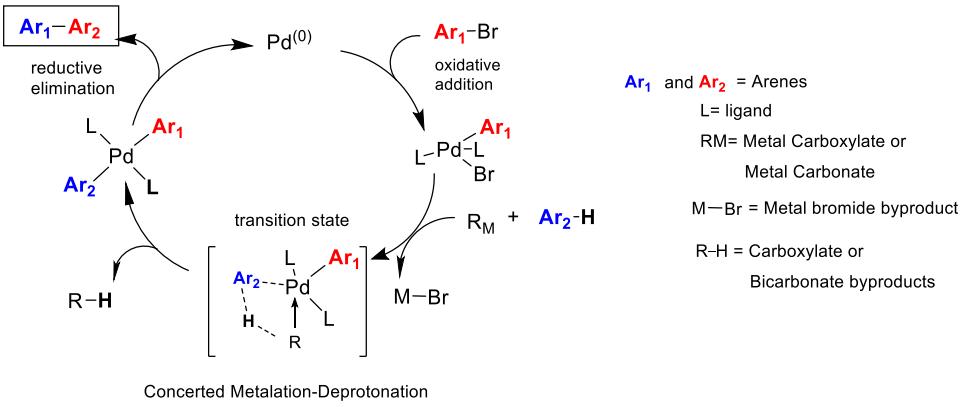

Scheme 1.17. *General mechanism of direct arylation via the concerted metalation-deprotonation (CMD) pathway.*

On the basis of studies performed on small molecules, DArP, which involves the coupling of a (hetero)arene and a (hetero)aryl halide, has been improved remarkably over the last decade and can now be used to prepare some of the most highly performing organic electronic materials reported in the literature. [85] [86] In many studies, DArP represents a competitive alternative to traditional organometallic polycondensation reactions when one considers the reduction of synthetic steps and the absence of stoichiometric quantities of organometallic byproducts.

Many well-defined, nearly defect-free polymeric materials can now be synthesized. [87] For instance, highly regioregular P3HTs have been obtained (over 99% HT-HT coupling) via a DArP protocol. [88] Analysis of side-reactions has helped to identify the reaction conditions best suited to yield families of monomers. In the vast majority of studies, C−H/C−H, C−Br/C−Br homo-couplings and β-defects have been found to be the major source of chain alternation defects. Two distinct approaches have emerged for efficient and selective C−C bond formation by DArP: (1) phosphine-assisted conditions in non-polar solvents (e.g., toluene and THF) [89] and (2) phosphine-assisted or phosphine-free conditions in aprotic and coordinating polar solvents (e.g., DMA and DMF). [90] Non-polar approaches, once optimized, offer both greater selectivity and high molecular weights. [91]Polar systems, on the other hand, use inexpensive reagents and can give rise to higher catalyst activity even at low (ppm) concentrations of palladium. [92] Mixed solvent phosphine-assisted conditions have been recently explored and may be an avenue to balance reactivity, solubility, and selectivity, thereby retaining some of the characteristics of both methods. [93] More recently, oxidative C-H/C-H arylation polymerization, consisting of the coupling of two nonhalogenated (hetero)arenes, has become a viable technique for the synthesis of synthetically meaningful materials. [94] Although direct (hetero)arylation and oxidative C-H/C-H arylation may still be perceived as “immature” polymerization techniques, it is clear that their advantages make it convenient to develop and optimize synthetic

routes that employ these reactions for the production of the next generations of conjugated polymers.

1.4.2 Green synthesis of conjugated polymers

Sustainable thinking in conjugated polymer molecular design is just as important to their economic and environmental sustainability. We need to keep in mind the "12 Principles of Green Chemistry" (Figure 1.18) with the aim of preventing environmental contamination and protecting human health starting from the lab scale onwards. [95] Atom economy and environmental factors are the most commonly used metrics to quantify green chemistry. [96] Atom economy is defined as the percentage of the total product molecular weight over the total reactant molecular weight. It is therefore desirable to increase the atom economy in order to make a reaction greener. Conversely, there is a tendency to establish a low value of the environmental factor (E), since it is defined as the total mass of waste compared to the mass of the product. To date, solvents are the only chemicals that have been ranked in terms of their level of sustainability. Large quantities of organic solvents, relative to reagents, are usually essential for chemical reactions to proceed and to achieve sufficient product purity. Understanding solvent properties is a necessary part of sustainable development, and many solvents have therefore been ranked by their environmental, safety, and health (ESH) characteristics. [97]These rankings are the core principle of solvent selection guides, most of which are published by major pharmaceutical companies such as GSK, AstraZeneca, Pfizer, and Sanofi, and specialty groups such as the ACS Green Chemistry Institute Pharmaceutical Roundtable (GCI-PR) and Innovative Medicines Initiative (IMI)-CHEM21. The aim is to help researchers choose solvents that have low ESH impacts, discouraging the use of toxic, harmful solvents that are of common use in laboratories.

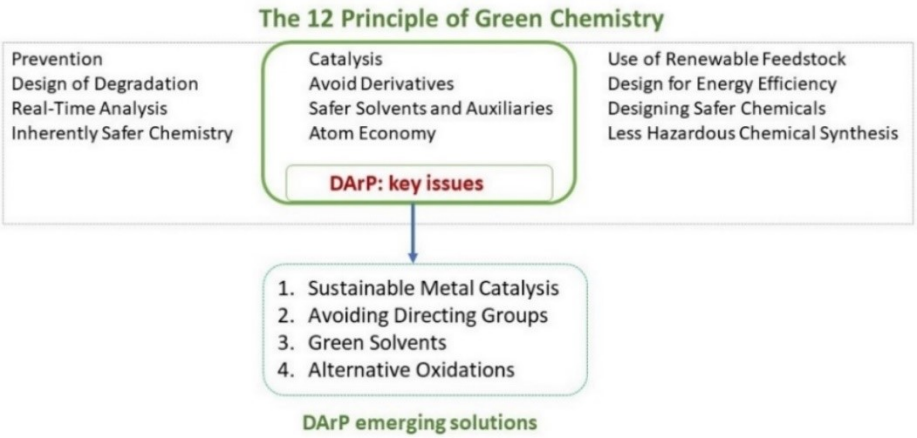

Figure 1.18. *Sustainability trends in DArP approach (from ref (95)).*

1.5 Pd-catalysed DArP in sustainable solvents

Although DArP provides an inherently sustainable pathway for conjugated polymer synthesis by avoiding stoichiometric toxic acute hazards on reagents such as organostannanes, the solvents being employed for DArP are massively used in these reactions and are still hazardous for health and environment. The current synthetic challenge is represented by the replacement of the typical solvents used for DArP without compromising the molecular weights, yields and structural regularity of the resulting conjugated polymers. To date, the research efforts aim at eliminating the dependence from the solvents (xylenes, toluene, tetrahydrofuran, dimethylformamide, and dimethylacetamide) characterized by a high level of toxicity beside to the consideration that many of these (such as THF or toluene) require extensive energy for their synthesis and purification starting from fossil sources. [(98)] Sustainable solvents such as 2-MeTHF and cyclopentyl methyl ether (CPME) have drawn significant attention since high-catalytic efficiencies for small-molecule direct arylation in these solvents were realized. Although Sommer et al. [(99)] and Marks et al. [(100)] reported the synthesis of high M_n conjugated

polymers using 2-MeTHF as the alternative to THF, 2-MeTHF preparation requires a large number of synthetic steps and is more prone to organic peroxide formation compared to THF, despite being capable of derivation from biomass. In an effort to investigate the use of a variety of sustainable solvents for DArP, in 2018, Thompson et al. reported that CPME is the optimal green alternative solvent for the synthesis of selected semiconducting polymers with high M_n (41 kg/mol) and high yields (up to 98%). [101] For comparison, the same polymers synthesized using CPME as a sustainable solvent almost triples the M_n compared to that synthesized using the conventional solvent THF (15 kg/mol). [102]

In this perspective, **Chapter 2** of this Dissertation will be focused on my systematic study performed in order to investigate the best conditions for the obtainment of poly(3-hexylthiophene) (P3HT) in CPME as a sustainable solvent with the aim to optimize the reaction conditions also regarding the catalytic system and the base quantity, which both potentially jeopardize the DArP sustainability. The pursued results, which will be discussed later, demonstrate that the Pd catalytic system displays better performance in the sustainable solvent CPME and these optimized reaction conditions can be adopted for the copolymerization of other differently structured monomer units with satisfactory results in terms of molecular weights of the resulting copolymers. [103]

Very recently, Thompson and coworkers [104] have proposed a natural aromatic compound (p-cymene) as the solvent for selected DArP exhibiting high-solubilizing ability for conjugated polymers, but its use could result in being problematic for safety, health and environment. Along with aliphatic alcohols and esters (incompatible, however, with the conjugated polymers preparation due to solubility issues), anisole can be considered one of the best eco-friendly solvents for DArP with the great advantage to be structurally similar to toluene. [105] [106]

In **Chapter 3**, will be detailed the investigation concerning two paradigmatic polymerization routes to study the potential implementation of anisole as solvents classified as highly sustainable. In this context, we also demonstrated the strong influence of the solvent on the precatalyst performances. Moreover, we found

that the resulting poly(arylene-vinylene) regioregularity resulted to be positively influenced by the polarity of the sustainable medium, introducing propylene carbonate as the cosolvent with anisole. (71)

In **Chapter 4**, we revisited the synthesis of poly(9,9-dioctylfluorene-2,2'-bithiophene) using the DArP conditions and choosing anisole as an eco-friendly solvent under aerobic conditions with the aim to explore the selectivity of DArP also under aerobic conditions.

1.6 References

1. *A Pharmaceutical Industry Perspective on Sustainable Metal Catalysis.* Hayler, J. D., Leahy, D. K. e Simmons, E. M., 2019, Organometallics, Vol. 38, p. 36−46.
2. *Green Chemistry Is Good Process Chemistry.* Laird, T. 2012, Org. Process Res. Dev., Vol. 16, p. 1-2.
3. *The sustainable materials roadmap.* al, Magda Titirici et. 3, 2022, Journal of Physics: Materials, Vol. 5.
4. *Synthesis of Conjugated Polymers for Organic Solar Cell Applications.* Yen-Ju Cheng, Sheng-Hsiung Yang, and Chain-Shu Hsu. 2009, Chemical Reviews, Vol. 109, p. 5868-5923.
5. Chart., NREL Efficiency. http://www.nrel.gov/ncpv/images/efficiency_chart.jpg . [Online] 2023.
6. *Advances in Organic and Perovskite Photovoltaics Enabling a Greener Internet of Things.* Panidi, J., Georgiadou, D. G., Schoetz, T., Prodromakis, T.,. 23, 2022, Adv. Funct. Mater. , Vol. 32, p. 2200694.
7. *Designing π-conjugated polymers for organic electronics.* X. Guo, M. Baumgarten, and K. Müllen. 2013, Progress in Polymer Science, Vol. 38, p. 1832.
8. *Performance Comparisons of Polymer Semiconductors Synthesized by Direct (Hetero)Arylation Polymerization (DHAP) and Conventional Methods for Organic Thin Film Transistors and Organic Photovoltaics.* Hendsbee, A.D. e Li, Y. s.l. : Mario Leclerc, 2018, Molecules, Vol. 23, p. 1255.
9. *New Insight into the "Fortuitous Error" that Led to the 2000 Nobel Prize in Chemistry. .* Rasmussen, S. C. 2021, Substantia,, Vol. 5.
10. *Electrical Conductivity in Doped Polyacetylene.* C. K. Chiang, C. R. Fincher, Jr., Y. W. Park, A. J. Heeger, H. Shirakawa, E. J. Louis, S. C. Gau, and Alan G. MacDiarmid. 17, 1977, PHYSICAL REVIEW LETTERS, Vol. 39, p. 1098-1101.
11. T. N. Sorrell, Sausalito,. *Organic Chemistry, 2nd ed.* California: University Science Books, 2006.
12. *Organic Field-Effect Transistors.* Z. Bao, J. Locklin,. Boca Raton: s.n., 2007., CRC Press.
13. *Organic Field Effect Transistor: Theory, Fabrication and Characterization.* I. Kymissis. New York, USA : s.n., 2009., Springer,.
14. *Semiconducting and Metallic Polymers: The Fourth Generation of Polymeric Material.* Heeger, Alan J. 2001, J. Phys. Chem. B , 105, 36, , Vol. 105, p. 8475–8491.
15. *Discovering new science through making new molecules.* M. Bendikov, N. Martin, D.F. Perepichka, M. Prato, Fred Wudl. 2011, J. Mater. Chem. , Vol. 21, p. 1292–1294.
16. *Spectroscopic studies of soluble poly(3-alkylthienylenes).* S. Hotta, S.D.D.V. Rughooputh, A.J. Heeger, F. Wudl,. 1987, Macromolecules, Vol. 20, p. 212–215.

17. *Synthesis and properties of chemically coupled poly(thiophene).* M. Kobayashi, J. Chen, T.-C. Chung, F. Moraes, A.J. Heeger, F. Wudl,. 1984, Synth. Met., Vol. 9, p. 77–86.
18. *Electrical conductivity in doped polyacetylene.* C.K. Chiang, C.R. Fincher, Y.W. Park, A.J. Heeger, H. Shirakawa, E.J. Louis, S. C.Gau, A.G. MacDiarmid,. 1977, Phys. Rev. Lett., Vol. 39, p. 1098–1101.
19. *Poly(isothianaphthene).* F. Wudl, M. Kobayashi, A.J. Heeger,. 1984, J. Org. Chem, Vol. 49, p. 3382–3384.
20. *PEDOT: principles and applications of an intrinsically conductive polymer.* s.l. ELSCHNER, Andreas, et al.: CRC press, 2010.
21. *Preparation of (alkylenedioxy) thiophene polymers for use as antistatic agents. 3813589: A1.* 1989. DE. JONAS, F., HEYWANG, G. e SCHMIDTBERG, W.
22. *Light-emitting diodes based on conjugated polymers.* J.H. Burroughes, D.D.C. Bradley, A.R. Brown, R.N. Marks, K. Mackay, R. HFriend, P.L. Burns, A.B. Holmes. 1990, Nature, Vol. 347, p. 539–541.
23. *Fibres of poly(methoxy-2-ethyl-hexyloxy) phenylenevinylene prepared from the soluble, fully conjugated polymer.* F. Motamedi, K.J. Ihn, Z. Ni, G. Srdanov, F. Wudl, P. Smith,. 1992, Polymer, Vol. 33 , p. 1102–1104.
24. *Side chain engineering in solution-processable conjugated polymers.* J. Mei, Z. Bao,. 2014, Chem. Mater, Vol. 26, p. 604–615.
25. *Progress with light-emitting polymers.* M.T. Bernius, M. Inbasekaran, J. O'Brien, W. Wu, 2000, Adv. Mater., Vol. 12, p. 1737–1750.
26. *New well-defined poly(2,7-fluorene) Derivatives:photoluminescence and base doping.* M. Ranger, D. Rondeau, M. Leclerc. 1997, Macromolecules, Vol. 30, p. 7686–7691.
27. *Mobility enhancement in conjugated polymer field- effect transistors through chain alignment in a liquid-crystalline phase.* H. Sirringhaus, R.J. Wilson, R.H. Friend, M. Inbasekaran, W. Wu, E.P. Woo, M. Grell, D.D.C. Bradley,. 2000, Appl. Phys. Lett., Vol. 77, p. 406–408.
28. *Conducting poly(3,4-alkylenedioxythiophene) derivatives as fast electrochromics with high-contrast ratios.* A. Kumar, D.M. Welsh, M.C. Morvant, F. Piroux, K.A. Abboud, J.R. Reynolds,. 1998, Chem. Mater, Vol. 10, p. 896–902.
29. *A Thienoisoindigo-Naphthalene Polymer with Ultrahigh Mobility of 14.4 cm2/V·s That Substantially Exceeds Benchmark Values for Amorphous Silicon Semiconductors.* Kim, G., et al. 2014, J. Am. Chem. Soc., Vol. 136, p. 9477-9483.
30. *A Wide Band Gap Polymer with a Deep Highest Occupied Molecular Orbital Level Enables 14.2% Efficiency in Polymer Solar Cells.* Sunsun Li, Long Ye, Wenchao Zhao, Hongping Yan, Bei Yang, Delong Liu, Wanning Li, Harald Ade, and Jianhui Hou. 23, 2018, Journal of the American Chemical Society, Vol. 140, p. 7159-7167.
31. *Chain length dependence of the photovoltaic properties of monodisperse donor–acceptor oligomers as model compounds of poly-disperse low band gap polymers.* C. Zhou, Y. Liang, F. Liu, C. Sun, X. Huang, Z. Xie, F. Huang, J. Roncali, T. P. Russell, and Y. Cao,. 2014, Advanced Functional Material, Vol. 24, p. 7538.
32. *Mechanistic studies of effect of dispersity on the photovoltaic performance of ptb7 polymer solar cells.* L. Lu, T. Zheng, T. Xu, D. Zhao, and L. Yu. 2015, Chemistry of Materials, Vol. 27, p. 537.
33. *Simultaneous polymerization and formation of polyacetylene film on the surface of concentrated soluble ziegler-type catalyst solution,.* T. Ito, H. Shirakawa, and S. Ikeda. 1974, Journal of polymer science: polymer chemistry edition , Vol. 12, p. 11.
34. *Pd-and Ni-catalyzed cross-coupling reactions in the synthesis of organic electronic materials, Science and technology of advanced materials.* S. Xu, E. H. Kim, A. Wei, and E.-i. Negishi. 2014, Vol. 15, p. 044201.
35. *Kumada chain-growth polycondensation as a universal method for synthesis of well-defined conjugated polymers.* Y. Geng, L. Huang, S. Wu, and F. Wang. 2010, Science China Chemistry , Vol. 53, p. 1620.
36. *Negishi coupling in the synthesis of ad-vanced electronic, optical, electrochemical, and magnetic materials.* [41] S. Huo, R. Mroz, and J. Carroll,. 2015, Organic Chemistry Frontiers, Vol. 2, , p. 416.
37. *Stille polycondensation for synthesis of functional materials.* B. Carsten, F. He, H. J. Son, T. Xu, and L. Yu. 2011, Chemical reviews , Vol. 111, p. 1493.
38. *Suzuki polyconden-sation: polyarylenes à la carte.* J. Sakamoto, M. Rehahn, G. Wegner, and A. D. Schlüter. 2009, Macromolecular rapid communications , Vol. 30, p. 653.

39. *C-H activation as a shortcut to conjugated polymer synthesis.* J. T. Blaskovits and M. Leclerc. 2019, Macromolecular rapid communications, Vol. 40, p. 1800512 .
40. *Synthesizing optoelectronic heteroaromatic conjugated polymers by cross-coupling reactions.* Cheng, Y.-J. e Luh, T.-Y. J. 2004, Journal of Organometallic Chemistry, Vol. 689, p. 4137-4148.
41. *Aryl- aryl bond formation one century after the discovery of the ullmann reaction.* J. Hassan, M. Sevignon, C. Gozzi, E. Schulz, and M. Lemaire,. 2002, Chemical Reviews, Vol. 102, p. 1359 .
42. *Kumada–corriu coupling of Grignard reagents, probed with a chiral Grignard reagent.* Hoffmann, B. Hölzer and R. W. 2003, Chemical Communications , Vol. 732.
43. D. Fichou. *Handbook of oligo-and polythiophenes.* s.l. : John Wiley & Sons, 2008.
44. *Enhanced electrical conductivity in regioselectively synthesized poly (3-alkylthiophenes).* Lowe, R. D. McCullough and R. D. 1992, Journal of the Chemical Society, Chemical Communications , Vol. 70 .
45. *Chain-growth polymerization for poly (3-hexylthiophene) with a defined molecular weight and a low polydispersity.* A. Yokoyama, R. Miyakoshi, and T. Yokozawa. 2004, Macromolecules, Vol. 37, p. 1169 .
46. *Handbook of organopalladium chemistry for organic synthesis.* Meijere, E.-I. Negishi and A. De. s.l. : Wiley-Interscience, 2002. Vol. 2.
47. *Novel stereoselective alkenyl–aryl coupling via nickel-catalysed reaction of alkenylanes with aryl halides.* E.-i. Negishi and S. Baba, 1976, Journal of the Chemical Society, Chemical Communications , p. 596b-597b.
48. *A novel stereospecific alkenyl-alkenyl cross-coupling by a palladium-or nickel-catalyzed reaction of alkenylalanes with alkenyl halides,.* S. Baba and E. Negishi. 1976, Journal of the American Chemical Society, Vol. 98, p. 6729 .
49. *Preparation of new classes of aliphatic, allylic, and benzylic zinc and copper reagents by the insertion of zinc dust into organic halides, phosphates, and sulfonates.* Knochel, Carole Jubert and Paul. 20, 1992, The Journal of Organic Chemistry, Vol. 57.
50. G. Odian et al. *Principles of polymerization.* s.l. : John Wiley & Sons, 2004.
51. *Chain growth mechanism for regioregular nickel-initiated cross-coupling polymerizationS.* E. E. Sheina, J. Liu, M. C. Iovu, D. W. Laird, and R. D. McCullough. 2004, Macromolecules, Vol. 37, p. 3526.
52. *Development of a universal chain-growth polymerization protocol of conjugated polymers: Toward a variety of all-conjugated block-copolymers.* Verswyvel, M., Verstappen, P., De Cremer, L., Verbiest, T. and Koeckelberghs, G. 2011, J. Polym. Sci. A Polym. C, Vol. 49, p. 5339 .
53. *One-pot synthesis of all-conjugated block-like bisthiophene–naphthalenediimide/fluorene copolymer.* R. Tkachov, H. Komber, S. Rauch, A. Lederer, U. Oertel, L. Häußler, B. Voit, and A. Kiriy,. 2014, Macromolecules, Vol. 47, p. 4994 .
54. *Palladium-catalyzed chain-growth polycon-densation of ab-type monomers: High catalyst turnover and polymerization rates.* R. Tkachov, V. Senkovskyy, T. Beryozkina, K. Boyko, V. Bakulev, A. Lederer,K. Sahre, B. Voit, and A. Kiriy. 2014, Angewandte Chemie International Edition , Vol. 53, p. 2402.
55. *The palladium-catalyzed cross-coupling reactions of organotin reagents with organic electrophiles [new synthetic methods.* Stille, J. K. 1986, Angewandte Chemie International Edition in English , Vol. 25, p. 508.
56. *The palladium–iminophosphine catalyst for the reactions of organostannanes.* E. Shirakawa and T. Hiyama. 1999, Journal of organometallic chemistry, Vol. 576, p. 169 .
57. *The mechanisms of the Stille reaction.* P. Espinet and A. M. Echavarren. 2004, Angewandte Chemie International Edition , Vol. 43, p. 4704.
58. *Mechanistic studies of the suzuki cross-coupling reaction.* G. B. Smith, G. C. Dezeny, D. L. Hughes, A. O. King, and T. R. Verhoeven. 1994, The Journal of Organic Chemistry , Vol. 59, p. 8151.
59. *Cross-coupling reaction of organoboron compounds via base-assisted transmetalation to palladium (ii) complexes,.* N. Miyaura. 2002, Journal of organometallic chemistry , Vol. 653, p. 54.
60. *Synthesis of light-emitting conjugated polymers for applications in electroluminescent devices.* A. C. Grimsdale, K. Leok Chan, R. E. Martin, P. G. Jokisz, and A. B. Holmes, ,. 2009, Chemical reviews , Vol. 109, p. 897.
61. *Synthesis of conjugated polymers for organic solar cell applications.* Y.-J. Cheng, S.-H. Yang, and C.-S. Hsu,. 2009, Chemical reviews, Vol. 109, p. 5868 .

62. *Axially chiral analogues of 4-(dimethylamino) pyridine: Novel catalysts for nonenzymatic enantioselective acylations.* A. C. Spivey, T. Fekner, and S. E. Spey,. 2000, The Journal of organic chemistry , Vol. 65, p. 3154 .
63. *Novel and convenient method for the stereo- and regiospecific synthesis of conjugated alkadienes and alkenynes via the palladium-catalyzed cross-coupling reaction of 1-alkenylboranes with bromoalkenes and bromoalkynes.* Norio Miyaura, Kinji Yamada, Hiroshi Suginome, and Akira Suzuki. 4, 1985, Journal of the American Chemical Society, Vol. 107 , p. 972-980.
64. *Effect of initiators on the kumada catalyst-transfer polycondensation reaction.* N. Doubina, A. Ho, A. K. Jen, and C. K. Luscombe,. 2009, Macromolecules, Vol. 42, p. 7670.
65. *A study of the effects metal residues in poly(9,9-dioctylfluorene) have on field-effect transistor device characteristics.* Prashant Sonar, Andrew C. Grimsdale, Martin Heeney, Maxim Shkunov, Iain McCulloch, Klaus Müllen,. 21, 2007, Synthetic Metals, Vol. 157, p. 872.
66. *Detection and role of trace impurities in high-performance organic solar cells,* M. P. Nikiforov, B. Lai, W. Chen, S. Chen, R. D. Schaller, J. Strzalka, J. Maser, and S. B. Darling,. 2013, Energy & Environmental Science, Vol. 6, p. 1513 .
67. *Pd-catalyzed formal Mizoroki–Heck coupling of unactivated alkyl chlorides. .* Lee, G.S., Kim, D. & Hong, S.H. 2021, Nat Commun , Vol. 12, p. 991.
68. *Pd-Catalyzed Cross-Couplings: On the Importance of the Catalyst Quantity Descriptors, mol % and ppm.* Fairlamb, Christopher S. Horbaczewskyj and Ian J. S. 8, 2022 , Organic Process Research & Development, Vol. 26, p. 2240-2269.
69. *Diversifying Cross-Coupling Strategies, Catalysts and Monomers for the Controlled Synthesis of Conjugated Polymers.* M. A. Baker, C.-H. Tsai, K. J. T. Noonan,. 2018, Chem. Eur. J. , Vol. 24, p. 13078.
70. *Chain-Growth Versus Step-Growth Mechanisms for the Suzuki–Heck Polymerisation of Fluorenyldibromides with Potassium Vinyl Trifluoroborate. Chemistry.* Grisorio, R., Suranna, G. and Mastrorilli, P. 2010, A European Journal, Vol. 16, p. 8054-8061.
71. *Implementation of Sustainable Solvents in Green Polymerization Approaches.* Daniele Conelli, Nicola Margiotta, Roberto Grisorio, Gian Paolo Suranna. 2, Macromolecular Chemistry and Physics, Vol. 222, p. 2000382.
72. *Semiconducting Polymers Prepared by Direct Arylation Polycondensation. Angew. Chem. Int. Ed., 51: 3520-3523. https://doi.org/10.1002/anie.201200199.* Facchetti, A., Vaccaro, L. e Marrocchi. 15, 2012, Angew. Chem. Int. Ed. Engl. , Vol. 51, p. 3520.
73. *Direct C–H arylation: a "Greener" approach towards facile synthesis of organic semiconducting molecules and polymers.* Bohra, H. e M., Wang. 2017, J. Mater. Chem. A , Vol. 5, p. 11550-11571.
74. *New synthetic method for the polymerization of alkylthiophene.* Marc Se´vignon, Julien Papillon, Emmanuelle Schulz, Marc Lemaire,. 32, 1999, Tetrahedron Letters, Vol. 40, p. 5873-5876.
75. *Palladium-Catalyzed Dehydrohalogenative Polycondensation of 2-Bromo-3-hexylthiophene: An Efficient Approach to Head-to-Tail Poly(3-hexylthiophene).* Qifeng Wang, Ryo Takita, Yuuta Kikuzaki, and Fumiyuki Ozawa. 33, 2010 , Journal of the American Chemical Society , Vol. 132, p. 11420-11421.
76. *Direct arylation polymerization: A guide to optimal conditions for effective conjugated polymers,.* Nemal S. Gobalasingham, Barry C. Thompson,. 2018, Progress in Polymer Science, Vol. 83, p. 135-201.
77. *Palladium-Catalyzed Benzene Arylation: Incorporation of Catalytic Pivalic Acid as a Proton Shuttle and a Key Element in Catalyst Design.* Fagnou, Marc Lafrance and Keith. 51, 2006 , Journal of the American Chemical Society, Vol. 128 , p. 16496-16497.
78. *Synthesis of 5-Alkyl[3,4-c]thienopy201rrole-4,6-dione-Based Polymers by Direct Heteroarylation .* Berrouard, P., Najari, A., Pron, A., Gendron, D., Morin, P.-O., Pouliot, J.-R., Veilleux, J. and Leclerc, M.,. 2012 : s.n., Angew. Chem. Int. Ed., Vol. 51, p. 2068-2071.
79. *Polycondensation of Dibromofluorene Analogues with Tetrafluorobenzene via Direct Arylation.* Wei Lu, Junpei Kuwabara, and Takaki Kanbara. 6, 2011, Macromolecules, Vol. 44, p. 1252-1255.
80. *Synthesis and characterization of regioregular poly(3-hexylthiophene) by Heck reaction.* Zhang, Jie and Li, Jian and Sun, Minghui. 6, Huagong Xuebao/CIESC Journal, Vol. 61, p. 1587 – 1591.

81. *Single step reductive polymerization of functional 3{,}4-propylenedioxythiophenes via direct C–H arylation catalyzed by palladium acetate.* Kumar, Anshu and Kumar, Anil. 3, 2010, Polym. Chem., Vol. 1, p. 286-288.
82. *Polycondensation of dibromofluorene analogues with tetrafluorobenzene via direct arylation.* Lu W, Kuwabara J, Kanbara T. 2011, Macromolecules, Vol. 44:, p. 1252–5.
83. *Carboxylate-Assisted Transition-Metal-Catalyzed C−H Bond Functionalizations: Mechanism and Scope.* Ackermann, Lutz. 2011, Chemical Reviews, Vol. 111, p. 1315–1345.
84. *Room-Temperature Direct β-Arylation of Thiophenes and Benzo[b]thiophenes and Kinetic Evidence for a Heck-type Pathway.* Chiara Colletto, Saidul Islam, Francisco Juliá-Hernández, and Igor Larrosa. 5, 2016, Journal of the American Chemical Society, Vol. 138 , p. 1677-1683.
85. *Direct heteroarylation polymerization: Guidelines for defect-free conjugated polymers,.* T. Bura, S. Beaupré, M.-A. Légaré, J. Quinn, E. Rochette, J. T. Blaskovits, F.-G. Fontaine, A. Pron, Y. Li, and M. Leclerc,. 2017, Chemical science , Vol. 8, p. 3913.
86. *Direct arylation polycondensation as simplified alternative for the synthesis of conjugated (co)polymers,* . S. Kowalski, S. Allard, K. Zilberberg, T. Riedl, and U. Scherf,. 2013, Progress in Polymer Science , Vol. 38, p. 1805.
87. *Defect-free naphthalene diimide bithiophene copolymers with controlled molar mass and high performance via direct arylation polycondensation.* R. Matsidik, H. Komber, A. Luzio, M. Caironi, and M. Sommer,. 2015, Journal of the American Chemical Society , Vol. 137, p. 6705.
88. *Structural analysis of poly (3-hexylthiophene) prepared via direct heteroarylation polymerization, .* J.-R. Pouliot, M. Wakioka, F. Ozawa, Y. Li, and M. Leclerc,. 2016, Macromolecular Chemistry and Physics , Vol. 217, p. 1493.
89. *Alkali-induced disproportionation of palladium (II) tertiary phosphine complexes,[L_2PdCl_2], to L0 and palladium (0). key intermediates in the biphasic carbonylation of arx catalyzed by [$L2PdCl_2$], .* V. V. Grushin and H. Alper. 1993, Organometallics , Vol. 12, p. 1890 .
90. *Optimization of direct arylation polymerization conditions for the synthesis of poly (3-hexylthiophene), .* A. E. Rudenko, C. A. Wiley, J. F. Tannaci, and B. C. Thompson,. 2013, Journal of Polymer Science Part A: Polymer Chemistry , Vol. 51, p. 2660 .
91. *Analysis of diverse direct arylation polymerization (DArP) conditions toward the efficient synthesis of polymers converging with stille polymers in organic solar cells.* Livi, F., Gobalasingham, N.S., Thompson, B.C. and Bundgaard, E. 2016, J. Polym. Sci. Part A: Polym. Chem., , Vol. 54, p. 2907-2918.
92. *Minimization of the auxiliary reagent loading for direct arylation polymerization Minimization of the auxiliary reagent loading for direct arylation polymerization (DArP) of 2-bromo-3-hexylthiophene.* Rudenko, A.E., Latif, A.A. and Thompson, B.C. 2015, J. Polym. Sci. Part A: Polym. Chem., Vol. 53, p. 1492-1499.
93. *Identifying homo-couplings as critical side reactions in direct arylation polycondensation.* F. Lombeck, H. Komber, S. I. Gorelsky, and M. Sommer,. 2014, ACS Macro Letters , Vol. 3, p. 819 .
94. *Oxidative c–h/c–h coupling reactions between two (hetero) arenes, .* Y. Yang, J. Lan, and J. You,. 2017, Chemical reviews , Vol. 117, p. 8787.
95. *C–H Activation: Toward Sustainability and Applications.* Toryn Dalton, Teresa Faber, and Frank Glorius. 2, 2021, ACS Central Science , Vol. 7 , p. 245-261.
96. *Metrics of Green Chemistry and Sustainability: Past, Present, and Future.* Sheldon, R. A. 2018, ACS Sustainable Chem. Eng. , Vol. 6, p. 32−48.
97. *Tools and techniques for solvent selection: green solvent selection guides. .* Byrne, F.P., Jin, S., Paggiola, G. et al. 7 , (2016), Sustain Chem Process , Vol. 4.
98. *Improving the efficiency and sustainability of catalysts for direct arylation polymerization (DArP).* Ye, L., Thompson, B. C. 3, 2022, J. Polym. Sci. , Vol. 60, p. 393.
99. *Effects of PNDIT2 end groups on aggregation, thin film structure alignment and electron transport in field-effect transistors.* Matsidik, Rukiya and Luzio, Alessandro and Hameury, Sophie and Komber, Hartmut and McNeill, Christopher R. and Caironi, Mario and Sommer, Michael,. 43, 2016, Vol. 4, p. 10371-10380.

100. *Tin-Free Direct C–H Arylation Polymerization for High Photovoltaic Efficiency Conjugated Copolymers.* Alexander S. Dudnik, Thomas J. Aldrich, Nicholas D. Eastham, Robert P. H. Chang, Antonio Facchetti, and Tobin J. Marks. 48, 2016 , Journal of the American Chemical Society , Vol. 138, p. 15699-15709.
101. *Investigation of green and sustainable solvents for direct arylation polymerization (DArP).* Pankow, Robert M. and Ye, Liwei and Gobalasingham, Nemal S. and Salami, Neda and Samal, Sanket and Thompson, Barry C. 28, 2018, Polym. Chem., Vol. 9, p. 3885-3892.
102. *Analysis of diverse direct arylation polymerization (DArP) conditions toward the efficient synthesis of polymers converging with stille polymers in organic solar cells.* Livi, F., Gobalasingham, N.S., Thompson, B.C. and Bundgaard, E. 2016, J. Polym. Sci. Polym. Chem, Vol. 54, p. 2907-2918.
103. *Implementation of Sustainable Solvents in Green Polymerization Approaches.* Conelli, D., Margiotta, N., Grisorio, R., Suranna, G. P.,. 2021, Macromol. Chem. Phys. , Vol. 222, p. 2000382.
104. *p-Cymene: A Sustainable Solvent that is Highly Compatible with Direct Arylation Polymerization (DArP),* . Thompson, Liwei Ye and Barry C. 6, 2021 , ACS Macro Letters, Vol. 10 , p. 714-719.
105. *Tools and techniques for solvent selection: green solvent selection guides.* Byrne, F.P., Jin, S., Paggiola, G. et al. 7, 2016, Sustain Chem Process , Vol. 4, p. 7.
106. *Green-Solvent-Processed Amide-Functionalized Conjugated Polymers Prepared via Direct Arylation Polymerization (DArP).* Liwei Ye, Robert M. Pankow, Mami Horikawa, Elizabeth L. Melenbrink, Kangying Liu, and Barry C. Thompson. 23, 2019 , Macromolecules , Vol. 52 , p. 9383-9388.
107. *Chain growth mechanism for regioregular nickel-initiated cross-coupling polymerizations.* E. E. Sheina, J. Liu, M. C. Iovu, D. W. Laird, and R. D. McCullough. 2004, Macromolecules, Vol. 37, p. 3526 .

2 Chapter 2

Sustainable Reaction Conditions for Direct Arylation Polymerizations in CPME

2.1 Motivation

The C–H bond activation is undoubtly one of the most important transition-metal catalysed reactions, that is widely employed in applications ranging from fundamental organic chemistry to industrial manufacturing processes, especially in the field of polymer synthesis. However, as discussed above, the compatibility with environmentally benign, non-hazardous, and low-cost solvents still represents the critical aspect for developing direct arylation polymerization (DArP) as an industrial-scale method for the preparation of conjugated polymers. In this study, we implemented a "green" solvent (i.e., cyclopentyl methyl ether, CPME) for the obtainment of poly(3-hexylthiophene) (P3HT) by DArP reaction, in order to explore the compatibility of sustainable reaction conditions also with the catalytic system and the base quantity, all factors potentially undermining the sustainability of the DArP protocol. Considering the molecular weights as the indicator of precatalyst performance in determined conditions, the work described in this chapter establishes that the cheapest palladium source ($PdCl_2$) combined with two equivalents of $(o\text{-Anisyl})_3P$ can yield the best results in the green ethereal solvent CPME. Another important aspect of the present study concerns the quantity of the expensive base (Cs_2CO_3), that can be reduced with respect to the common DArP protocols without compromising molecular weights and regioregularity of the resulting P3HT polymer. These optimized reaction conditions can be extended to the copolymerization of diketopyrrolopyrrole-based units with satisfactory results in terms of molecular weights. This chapter of the Dissertation contains data that have been published by : **Conelli, D**, Grisorio, R., Suranna, G. P. Macromol. Chem. Phys. 2020, 221, 2000041.

2.2 *Introduction*

In the quest to probe DArP as an environmentally benign protocol for the obtainment of π-conjugated polymers, a further effort should be carried out regarding the search for more sustainable and benign alternatives for solvents able to replace the commonly used ones. In fact, the typical solvents used for DArP (xylenes, toluene, THF, DMF, and DMA) are energy demanding in terms of synthesis and purification, and possess a high level of toxicity. [1]

The choice of a green solvent is largely dependent on the type of reaction considered. In particular, a green organic solvent should ensure feasible separation of produced salts by filtration (during the product washing step) and easy recyclability by distillation, preferably with higher efficiency than water. Promising developments such as bio-based solvents as alternatives to petroleum-based organic solvents paved the way to the replacement of hazardous ethereal solvents like diethyl ether (Et_2O), tetrahydrofuran (THF), 1,4-dioxane, dimethoxyethane, methyl tert-butyl ether (MTBE), and others (which are heavily utilized in laboratories) by less toxic, less hazardous, and recoverable ethers prepared either from renewable resources or through atom-economy processes (Figure 2.1).

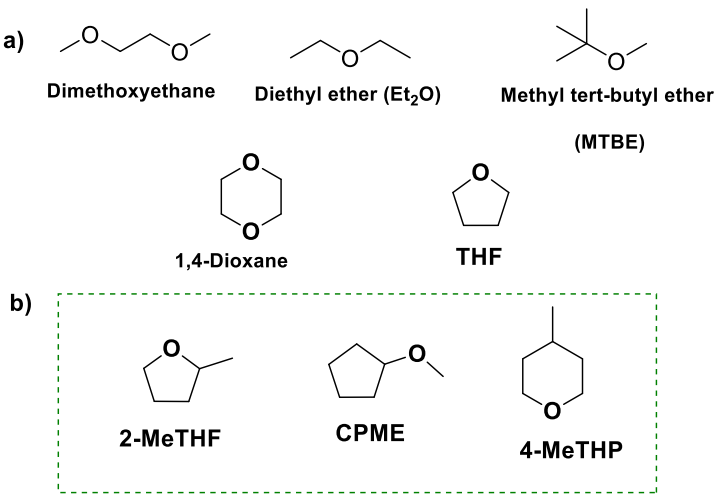

Figure 2.1 *a) Traditional ethereal solvents used in laboratories and b) low environmental impact alternatives.*

In recent years, novel unconventional ethers such as 2-methyltetrahydrofuran (2-MeTHF), cyclopentyl methyl ether (CPME), and 4-methyltetrahydropyran (4-MeTHP) have garnered attention in lab scale usage.

However, there are still some drawbacks such as low solubility, instability under acidic conditions, and low flash point (related to MTBE) or easy peroxides formation (associated to 2-MeTHF). In such a situation, cyclopentyl methyl ether (CPME) has proven to be quite useful as a process solvent for organic synthesis because it is free from those drawbacks that are associated with the classical ethereal solvents. In 2007, a seminal review by Watanabe et al. [2] highlighted the most important physical–chemical properties of cyclopentyl methyl ether (CPME), industrially produced through a 100% atom-economical reaction by Zeon Corporation (Scheme 2.2). This advantageous process is based on an addition reaction which produces no apparent waste. In this context, authors simultaneously reported its successful employment as a solvent in a variety of organic reactions.

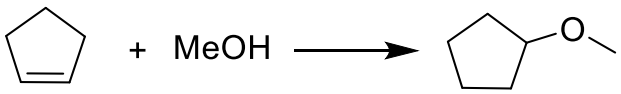

Scheme 2.2. *Zeon's process for the production of CPME.*

CPME possesses many favorable characteristics such as a high boiling point (bp) and a low melting point (mp), high hydrophobicity and a low heat of vaporization (Table 2.3). These prerequisites, as well as relative stability in acidic and basic medium, higher efficiency for azeotropic dehydration, narrow explosion range, confirm its contribution toward sustainable chemistry, promoting the employment as a solvent within a wide range of temperatures, easy recovery, purification and drying after aqueous treatment.

Table 2.3. Physical properties of CPME [2]	
bp [°C]	106
mp [°C]	< -140
density [gml^{-1}, at 20°C]	0.86
solubility in H_2O [g per 100 g. at 23°C]	1.1
solubility of H_2O in CPME [g per 100 g. at 23°C]	0.3
azeotropic bp with H_2O [°C]	83
azeotropic composition [CPME/H_2O, w/w)	83.7:16.3
dielectric constant [at 25°C]	4.76
explosion range [vol %, lower limit-upper limit]	1.84-9.9
latent heat of vaporization [kcal kg^{-1}, at the bp]	69.2
ignition point [°C]	180
flash point [°C]	-1

Furthermore, one of the most important property of CPME relies in a particularly high resistance to peroxides formation, which can be correlated to an unusually high bond dissociation energy (BDE) of the secondary α-C-H bond. In fact, as known, safety concerns for ethereal solvents closely relate to its explosive nature arising from the concomitant peroxides generation. Accordingly, for safety reasons, commercial CPME is available with a minimal amount (50 ppm) of peroxide inhibitor (butylhydroxytoluene, BHT) in comparison to the commercially available THF and 2-MeTHF (250 ppm BHT). Using stabilized CPME, it is possible to run reactions at high temperatures exposed to air without observing the formation of any peroxides. [3] The versatility of Pd-catalysed arylation processes in CPME relies on the capability of the reaction medium to sustain (and not interfere with) the catalytic cycle. [4] CPME can promote the palladium-catalysed direct arylation of heteroaromatics in the presence of lower amount of a palladium catalysts with a beneficial effect in terms of stereocontrol.

The reaction is strictly dependent on the nature of the phosphine ligand and shows an impressive level of functional-group tolerance. [5]

In this study, I selected 2-bromo-3-hexyl-thiophene as paradigmatic monomer for direct arylation polymerization, in order to investigate the best conditions for the obtainment of P3HT in CPME as a sustainable solvent. A first reaction screening allowed the assessment that the optimized conditions required the use of the cheapest palladium source ($PdCl_2$) in the presence of (o-Anisyl)$_3$P as the ligand, pivalic acid as the additive and the minimal amount of the base (Cs_2CO_3). Interestingly, these conditions can also be extended to the copolymerization of diketopyrrolopyrrole-based units, further consolidating the sustainability aspects of DArP protocols as an appealing alternative to commonly employed polymerization methods (Scheme 2.3.). [6]

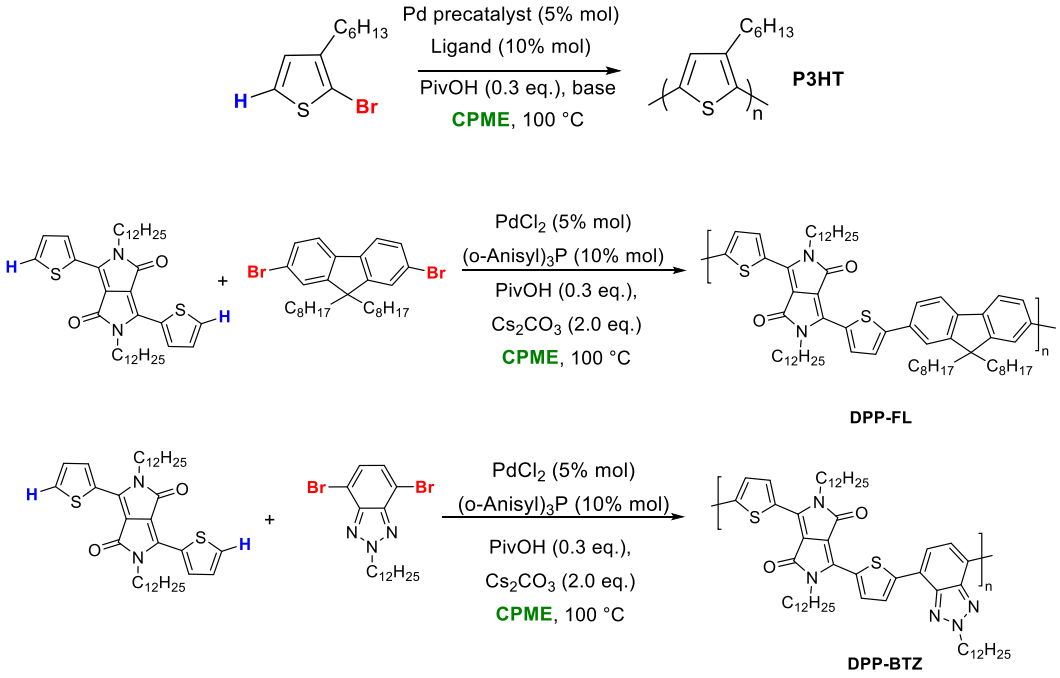

Scheme 2.3. *The optimized DArP protocols in CPME studied in this section of the Dissertation.*

2.3 Results and discussion

The catalytic conditions for DArP of 2-bromo-3-hexyl-thiophene in CPME were optimized on the bases of previous studies, [7] in which $Pd_2(dba)_3$, Cs_2CO_3 and an additive were used as a palladium precursor, a base and a carboxylate source, respectively (entry 1 of Table 2.4.). Thompson and coworkers employed $(o\text{-Anisyl})_3P$ as the ligand, 3.0 equivalents of Cs_2CO_3 with respect to the monomer and 1.0 equivalent of neodecanoic acid as the additive. Consistent with the previous observations which confirmed that linear, secondary, and even some tertiary aliphatic carboxylic acids bulkier than PivOH (neoheptanoic and neoctanoic acid) do not prevent β-defects in P3HT via optimized DArP conditions, for the systematic study, pivalic acid (PivOH, 0.3 equivalents with respect to the monomer) was chosen as the additive and 1.0 equivalent of the base to carry out the initial screening of the precatalyst efficiency. The reaction was carried out for 24h to avoid the formation of insoluble products. In these conditions, I investigated the behaviors of Pd^{II}-precatalysts because their cost is lower than that of typical commercial zero-valent palladium species, although the formation of necessary $Pd^{(0)}$-based species should require the in situ reduction of the Pd^{II}-precatalyst, which can be a favourable process only for specific monomers. [8] The results of this systematic experimental investigation are reported in Table 2.4. Initially, palladium carboxylates were used as precatalysts in the presence of two equivalents of $(o\text{-Anisyl})_3P$, in order to explore the effect of the presence of ancillary ligands (acetate or pivalate) belonging to the palladium source, which can potentially have an active role in the catalytic cycle. [9] [10]As evident from entries 2 and 3 of Table 2.4., no improvement in terms of molecular weights (even by prolonging the reaction time up to 48 hours) was obtained with respect to the results obtained by Thompson and coworkers. [7] This leads to the deduction that ancillary ligands of the Pd-source that could be involved in the formation of palladium-carboxylate species produce an unforeseen adverse effect on the polymerization course via DArP.

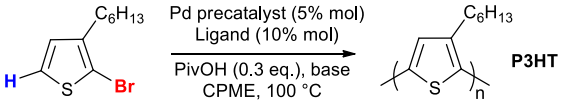

Entry	Precatalyst	Ligand	Base (equiv.)	Time (h)	Yield (%)[a]	M_n (kg/mol)[b]	DP_n[c]	M_w (kg/mol)[b]	Đ[b]
1[d]	$Pd_2(dba)_3$	(*o*-Anisyl)$_3$P	Cs_2CO_3 (3.0)	24	34	12.0	72	15.6	1.30
2	$Pd(AcO)_2$	(*o*-Anisyl)$_3$P	Cs_2CO_3 (1.0)	48	49	9.6	58	14.3	1.48
3	$Pd(PivO)_2$	(*o*-Anisyl)$_3$P	Cs_2CO_3 (1.0)	48	43	8.0	48	11.1	1.39
4	$(CH_3CN)_2PdCl_2$	(*o*-Anisyl)$_3$P	Cs_2CO_3 (1.0)	48	62	9.9	60	16.4	1.64
5	$PdCl_2$	(*o*-Anisyl)$_3$P	Cs_2CO_3 (1.0)	48	49	10.3	62	16.3	1.59
6	$PdCl_2$	(*p*-Anisyl)$_3$P	Cs_2CO_3 (1.0)	48	–	–	–	–	–
7	$PdCl_2$	(*o*-Tolyl)$_3$P	Cs_2CO_3 (1.0)	48	–	–	–	–	–
8	$PdCl_2$	S-Phos	Cs_2CO_3 (1.0)	48	–	–	–	–	–
9	PEPPSI-iPr	–	Cs_2CO_3 (1.0)	48	27	5.1	31	6.1	1.19
10	$PdCl_2$	(*o*-Anisyl)$_3$P	K_2CO_3 (1.0)	48	5	5.5	33	7.7	1.40
11	$PdCl_2$	(*o*-Anisyl)$_3$P	Ag_2CO_3 (1.0)	48	–	–	–	–	–
12	$PdCl_2$	(*o*-Anisyl)$_3$P	Cs_2CO_3 (2.0)	24	77	23.0	139	49.1	2.10
13	$PdCl_2$	(*o*-Anisyl)$_3$P	Cs_2CO_3 (3.0)	24	89	14.6	88	25.7	1.76

Table 2.4.*[a] Measured after polymer purification carried out by multiple precipitations;[b] Number-average molecular weights (M_n), weight-average molecular weights (M_w), and dispersity (Đ) as determined by GPC (PS standards, THF);[c] Calculated dividing the number- average molecular weights of the polymer by the mass of the repeating unit (166.3 g mol^{-1});[d] Data from ref.* [7]

On these bases, the behaviour of $(CH_3CN)_2PdCl_2$ and $PdCl_2$ (entries 4 and 5 of Table 2.4., respectively) was investigated. Although still lower than those reported by Thompson and coworkers, [7] we obtained the first promising results in terms of molecular weights (entry 5) using a palladium source virtually deprived of auxiliary ligands. This confirmed our hypotesis that the presence of coordinating ancillary ligands belonging to the palladium source employed for the polymerizations (i.e., pivalate, acetate or acetonitrile) can influence the DArP catalyst performance. Inspired by the use of $PdCl_2(PPh_3)_2$ as an effective catalyst for DArP methodologies, [11] [12] I also explored the possibility of modulating the reactivity of the catalytic system by combining $PdCl_2$ with phosphine ligands structurally similar to $(o\text{-Anisyl})_3P$. In fact, as described in the literature, the role of the ligand could be crucial in stabilizing the catalyst, [13] especially in the case of reactions carried out in low coordinating solvents such as CPME. However, I also attempted to use $(p\text{-anisyl})_3P$ or $(o\text{-tolyl})_3P$ instead of $(o\text{-anisyl})_3P$ (see entries 6 and 7 of Table 2.4, respectively) confirming the expected detrimental effects, since no solid product was observed by precipitation from methanol after the catalytic run. Moreover, notwithstanding the recent promising results on the performances of Buchwald-type ligand in DArP, [14] also the use of S-Phos resulted unsuccessful under the conditions of our study (entry 8 of Table 2.4.). A further attempt wasmade by changing the nature of the ligand, but, although carbene-based ligands have been widely exploited by Luscombe and co-workers, [15] it was observed that the catalytic activity of PEPPSI-iPr precatalyst is somehow limited in CPME, leading only (entry 9 of Table 2.4.) to low molecular weight products. The ligand role in weakly coordinating solvents can be rationalized by considering the generally accepted catalytic cycle for direct arylation reaction (discussed in Chapter 1), which is initiated by oxidative addition of aryl halides to Pd^0-based species (I in Scheme 2.5.) and is terminated by reductive elimination of cross-coupling products from diarylpalladium intermediate (IV in Scheme 2.5.).

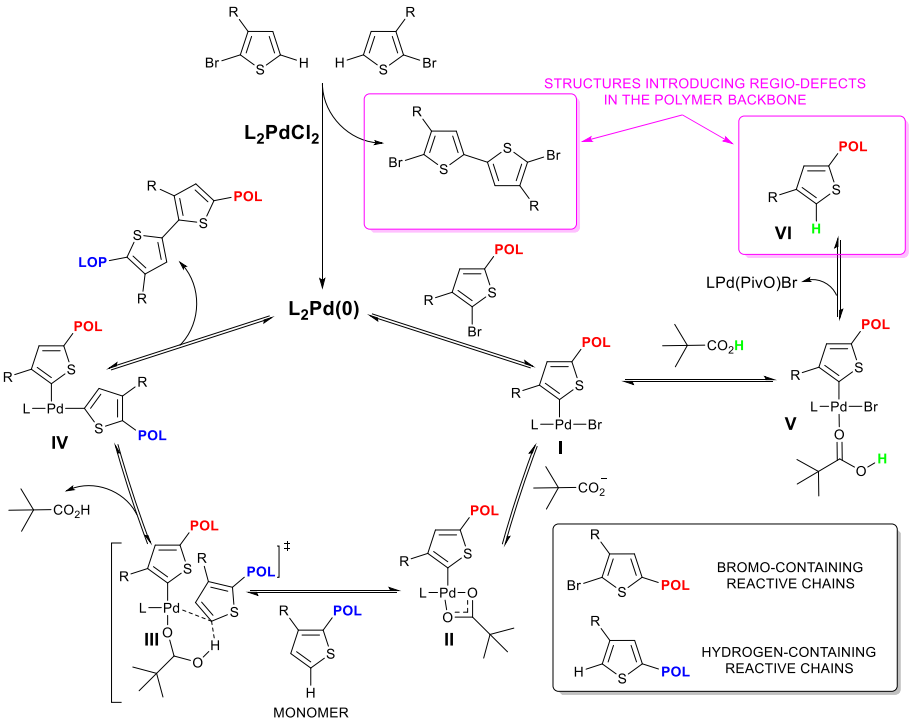

Scheme 2.5. *Plausible catalytic cycles for direct arylation polymerization of 2-bromo-3-hexylthiophene, highlighting the reduction step of $Pd^{(II)}$-precatalyst and the side reaction of Br/H exchange responsible for the polymer regioregularity. L= (o-Anisyl)$_3$*

As reported in Chapter 1, with respect to conventional cross-couplings, the formation of diarylpalladium complex invokes the C–H bond activation of aromatic substrates instead of transmetalation. Infact, this cycle proceeds through the so-called concerted metalation–deprotonation pathway (the transition state III in Scheme 2.5.) involving an arylpalladium carboxylate species (II in Scheme 2.5.). [16] Since carboxylate-based palladium species tend to form inactive multimetallic bridged complexes, especially in weakly-coordinating solvents, [17] the distinctive performances of (o-Anisyl)$_3$P as the ligand are probably related to its ability of generating monomeric species due to the proximity of the coordinating oxygen atoms, thereby favouring the concerted deprotonation pathway. [18],[19]At this stage, it could be rationalized the fact that P3HT endowed with relatively high molecular weights has been obtained by using only 1.0 equivalent of the base

(Cs_2CO_3). This means that also the $CsHCO_3$ byproduct is reactive under these reaction conditions. Additional investigations were carried out to control the observed reactivity by changing the base using K_2CO_3 and Ag_2CO_3 (entries 10 and 11 of Table 2.4., respectively). However, these modifications did not provide satisfactory results in terms of polymer yield after the catalytic run. In detail, the low molecular weights and yields (entry 10 of Table 2.4.) obtained in the case of K_2CO_3 are imputable to the lower solubility of the base in the reaction medium, as observed during the experimental activity. When Ag_2CO_3 was used as base, on the other hand, no polymer product was formed, notwithstanding the known beneficial effect exerted by silver-based species for P3HT synthesis via DArP. [12] It can be supposed that, under the peculiar conditions used in this investigation, the catalytic cycle (Scheme 2.5) is interrupted as a consequence of the $Pd^{(0)} \rightarrow Pd^{(II)}$ oxidation by means of $Ag^{(I)}$ ions, [20] [21], which in turn, prevents the oxidative addition of aryl-halides to the zero-valent metal center, with the result of inhibiting the polymerization course. Subsequently, the role of the base was further investigated by changing its quantity in the reaction mixture. We carried out two reactions under conditions similar to those of entry 5, but progressively increasing the relative amount of Cs_2CO_3 with respect to the monomer (2.0 and 3.0 equivalents: entries 12 and 13 of Table 2.4.). Interestingly, it was found that both yields and molecular weights of the resulting polymers increased with respect to the reaction in the presence of an equimolar amount of the base. However, the investigations reported in this paragraph allowed to ascertain that the best results were obtained when 2.0 equivalents of the base are used (entry 12) with respect to the common conditions which envisage the use of 3.0 equivalents of the base. Furthermore, comparison with entry 1 of table 2.4 allowed to confirm that the results in terms of polymer molecular weights and yields are definitely improved with respect to those by Thompson. The hypotesis that can be put forward is that in this peculiar solvent the strong excess of the base (3.0 equivalents) might inhibit the catalytic performance because of the carbonate coordination to the metal center competing with pivalate.

2.4 Spectroscopic characterization of P3HTs

One very interesting aspect of this study concerns the optical characterization of the obtained materials. The properties of P3HT in diluted chloroform solutions were analyzed by UV–Vis spectroscopy. The observed peaks correspond to the π–π* transition that indicates the conjugation length of the polymer. [22] The obtained values for the absorption maxima for the three polymers from entries 5, 12, and 13 (spectra reported in Figure 2.6.a) are in agreement with the corresponding molecular weights of the polymers, passing from 451 nm (in the case of entry 12) to 441 nm (in the case of entry 5). The regioregularity (RR), defined as the percent degree of regioregular head-to-tail (HT) arrangement, of the synthesized P3HT (entries 5, 12, and 13) was determined using ^{1}H-NMR spectroscopy ($CDCl_3$, 25 °C). Notwithstanding the contribution of chain terminations, [23] RR was quantified using previously described methods based on the values of the different chemical shifts related to the α-methylene groups in dependence on their arrangement (2.80 ppm for HT and 2.58 ppm for HH linkage), by calculating the ratio of the integrals spanning from 2.90–2.65 and 2.90–2.40 ppm (Figure 2.6.b). [24]

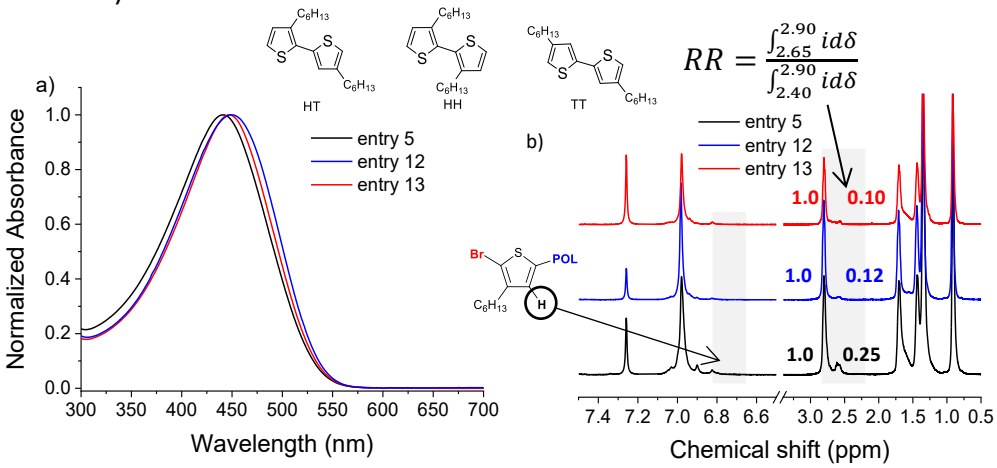

Figure 2.6. *(a) Comparison between the absorption spectra (chloroform solutions) of P3HT obtained under the conditions reported in Table 2.4. (entries 5,12 and 13). (b) ^{1}H-NMR spectra of the aforementioned polymers recorded in $CDCl_3$ for the determination of their regioregularity (RR) and chain-termination. The values of the exact integrals used for the determination of the regioregularity are also reported*

Based on this ratio, the regioregularity was found to be 80%, 89%, and 91% for the three P3HT of entries 5, 12, and 13, respectively, while the presence of β-defects (δ = 2.35 ppm) was not observed. These observation allowed to conclude that the regioregularity of P3HT synthesized in these conditions seems to be influenced by the base amount. Such a correlation is unprecedented in the literature, but the regioregularity of the P3HTs remains lower with respect to those reported by Thompson. [7]On the basis of the catalytic cycle represented in Scheme 2.5., the theoretical limit of the regioregularity for the obtained P3HT in the explored conditions should be 90% (in agreement with the values recorded for entries 12 and 13), due to the homocoupling of the monomer required for the palladium activation. In fact, the dibromo-bithiophene derivative generated for the formation of zero-valent species (Scheme 2.5.) can be incorporated in the polymer backbone, thus explaining the relatively low regioregularity of obtained polymers. However, in the case of the P3HT obtained by entry 5 (synthesized with the lowest quantity of Cs_2CO_3) the observed regioregularity is lower (80%). It can be supposed that the role of the base in determining the regioregularity of P3HT can be rationalized on the basis of the pivalic acid/pivalate equilibrium, which, consequently, depends on the Cs_2CO_3 quantity. A lower base amount leads, in fact, to a higher amount of indissociated pivalic acid in the reaction mixture. It can be hypothesized that the relatively higher quantity of pivalic acid (present in the reaction mixture of entry 5) can compete with thiophene for the metal center (generating the palladium species V in Scheme 2.5.). Moreover, as suggested by Ozawa and co-workers, [25]a proton transfer to the aryl fragment previously incorporated by oxidative addition to the metal center can introduce new aryl species (VI) in the reaction mixture, as the result of a H/Br exchange. These species can subsequently be incorporated in the polymer backbone, altering the regioregularity of the resulting P3HT. In order to support further this hypothesis on the reaction pathway for the polymerization initiation, I carried out an end-group analysis on P3HT samples (entries 5, 12, and 13) via ^{1}H-NMR. In Figure 2.6b, the presence of low-intensity signals at δ = 6.82 ppm is revealed, which are typical of

Br-terminating polythiophene chains, while the signal at δ = 7.16 ppm belonging to H-terminating chains is not observed. [26]This observation is indicative of the fact that most of the polymer chains are terminated with bromine atoms, probably because of the displacement of the initial H/Br ratio belonging to the monomer feed due to the palladium activation (forming the bithiophene derivative in Scheme 2.5.). [27]Although it is possible that more extensive optimization should be conceived for improving regioregularity, the results described in this section of the investigation provide evidence that DArP can be optimized in CPME representing a more sustainable, more benign alternative to commonly employed solvents. [28]

2.5 Copolymerization Reactions

Once investigated the scope of the optimized conditions of this study, I tried to extend it toward other monomeric units in order to explore new sustainable copolymerization approaches. Scheme 2.7. highlights the reaction of one of the archetypal monomers employed in DArP [29]—2,5-didodecyl-3,6-di(thiophen-2-yl)pyrrolo[3,4-c]pyrrole-1,4-(2H,5H)-dione with an equimolar amount of dibromo-aryl derivatives (i.e., 9,9-dioctylfluorene or 2-dodecyl-benzotriazole units).

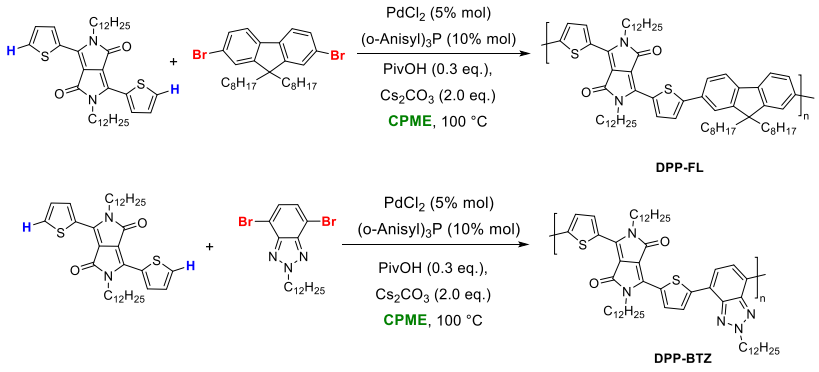

Scheme 2.7. *Synthetic approach for the obtainment of DPP-FL and DPP-BTZ copolymers in CPME.*

Table 2.8. summarizes yields and molecular weights of the obtained copolymers: it was observed that the molecular weights obtained in the case of 2,5-di-n-dodecyl-3,6-di(thiophen-2-yl)pyrrolo[3,4-c]pyrrole-1,4-(2H,5H)-dione(DPP)-4,7-dibromo-2-n-dodecylbenzotriazole (BTZ) are remarkably higher than those recorded for DPP-2,7-dibromo-9,9-di-n-octylfluorene (FL).

Polymer	Yield (%)[a]	M_n (kg/mol)[b]	M_w (kg/mol)[b]	Đ[b]	λ_{max}	DPP/comonomer[c]
DPP-FL	37	12.1	17.3	1.43	556	1.00/1.12
DPP-BTZ	56	20.9	43.7	2.09	702	1.00/1.03

Table 2.8. *All monomer concentrations were 0.2 M. [a]Measured after polymer purification carried out by multiple precipitations. [b]Number-average molecular weights (M_n), weight-average molecular weights (M_w) and dispersity (Đ) as determined by GPC (PS standards, THF); [c]Obtained by the ratio of selected proton integrals (see Figure 2.9.).*

2.6 Spectroscopic characterization of the copolymers

Analyzing the optical properties of the two copolymers (par. 2.5), it was observed that the introduction of the electron-deficient unit (BTZ) induced a remarkable red-shift of the absorption maximum (λ_{max} = 702 nm) in the UV–vis spectrum of the relevant polymer recorded in solution. This observation provides further indication of how the biphenyl repeat unit for this class of polymers influences the orbital overlap of the π-system along the polymer backbone and the π–π interactions between polymer chains. [(30) (31)] In the case of DPP-FL copolymer, the UV–vis absorption profile in solution shows a vibronic shoulder at longer wavelengths, while in the case of DPP-BTZ, features attributable to the formation of aggregates in solution are clearly evident.

The composition of the two copolymers was confirmed by ^{1}H-NMR analysis by comparing the integrals of specific signals ascribable to the two comonomers. These signals (evidenced in Figure 2.9.b) belong to the aliphatic chains introduced to improve the solubility of the resulting polymers (Table 2.8.).

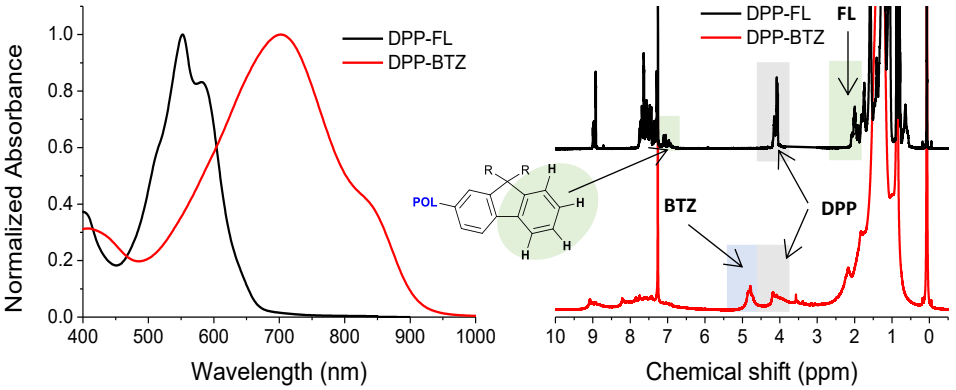

Figure 2.9. *(a) Comparison between the absorption spectra (chloroform solutions) of DPP-FL and DPP-BTZ copolymers synthesized using the conditions reported in Table 2.8. (b) ^{1}H-NMR spectra of the same polymers recorded in $CDCl_3$ for the determination of their composition through the integral comparison between the α-methylene protons of the aliphatic chains.*

In the case of DPP-FL, the aromatic region of the ^{1}H-NMR spectrum shows typical features ascribable to debrominated fluorene units, [32]suggesting that the reasons of the lower molecular weight of this copolymer could be traced down to the dehalogenation process involving the fluorene unit, as proposed by Ozawa and co-workers. [21] While dehalogenation is a favourable process for fluorene units due to their higher propensity, in the course of the mechanism, to undergo protonation when coordinated to palladium, the corresponding debrominated units cannot propagate the polymerization because they are inert toward C-H bond activation. Finally, the significant differences in molecular weights observed between DPP-BTZ and DPP-FL could be rationalised, through the hypothesis that an electron-poor monomer (BTZ), more resistant to the protonation side-reaction described in Scheme 2.5., prevents the interruption of the polymerization course, thereby warranting higher molecular weights.

2.7 Conclusions

In this section of the Dissertation, I have reported the investigation concerning the application of a *green*, ethereal solvent (CPME) for the preparation of P3HT. In particular, I have focused on the exploration of ecofriendly reaction conditions also regarding the catalytic system and the base quantity, which equally undermine the sustainability of DArP protocols. Considering the molecular weights as the indicator of precatalyst performance under specified conditions, it has been established that the cheapest palladium source (i.e., $PdCl_2$) in the presence of two equivalents of $(o\text{-anisyl})_3P$ as ligand provides the best results in the sustainable CPME solvent. Furthermore, with respect the common DArP protocols, the quantity of the expensive base (i.e., Cs_2CO_3) can be reduced in these reaction conditions without affecting molecular weights and regioregularity of the resulting polymer. These optimized reaction conditions can be extended for the copolymerization of other differently structured monomer units with satisfactory results in terms of molecular weights of the resulting copolymers. The results further consolidate the sustainability aspects of DArP protocols as an appealing alternative to commonly employed polymerization methods.

2.8 Experimental section

All reagents and solvents were purchased from standard commercial sources and used as received. The syntheses were carried out under inert nitrogen atmosphere using standard Schlenk techniques. NMR spectra were recorded on a Varian 500 MHz instrument. Gel-permeation chromatography (GPC) analyses were carried out on an Agilent Series 1100 instrument equipped with a Pl-gel 5 µm mixed-C column. The samples were dissolved in THF and were eluted at a 1.0 mL/min flow rate. Detection was performed by a multiple wave UV-Vis detector. Number-average molecular weights (M_n), weight-average molecular weights (M_w) and dispersity (Đ) were calculated against polystyrene standards. The syntheses of 2,7-dibromo-9,9-di-n-octylfluorene(FL), [33] 4,7-dibromo-2-n-dodecylbenzotriazole (BTZ), [34]and 2,5-di-n-dodecyl-3,6-di(thiophen-2-yl)pyrrolo[3,4-

c]pyrrole-1,4-(2H,5H)-dione (DPP) [35] were carried out according to literature procedures.

2.9 General procedure for P3HT synthesis via DArP.

A mixture of 2-bromo-3-hexylthiophene (0.247 g, 1.00 mmol, 1.0 equiv.), Pd precatalyst (0.05 equiv.), $P(o\text{-anisyl})_3$ (0.10 equiv.), pivalic acid (0.30 equiv.), base (1.0-3.0 equiv.) and anhydrous cyclopentyl methyl ether (CPME, 5.0 mL) was stirred at 100 °C for 24 or 48 hours. The reaction mixture was then cooled to room temperature and poured into MeOH (150 mL) under vigorous stirring for the precipitation of the polymer. The precipitate was collected by filtration, dissolved into the minimum amount of chloroform and precipitated in cold methanol. This purification procedure was repeated by using ethanol and acetone as the solvent for the precipitation to obtain a brown solid that was dried in vacuo for 12 hours. ^{1}H NMR (500 MHz, $CDCl_3$): δ 7.02-6.96 (1H), 2.83-2.77 (2H), 1.75-1.67 (2H), 1.47-1.27 (6H), 0.94-0.85 (3H) ppm.

2.10 General procedure for copolymerization reactions

A mixture of 2,5-didodecyl-3,6-di(thiophen-2-yl)pyrrolo[3,4-c]pyrrole-1,4-(2H,5H)-dione (DPP, 0.318 g, 0.50 mmol), the comonomer (FL or BTZ, 0.50 mmol), $PdCl_2$ (8.86 mg, 0.05 mmol), $P(o\text{-Anisyl})_3$ (35.2 mg, 0.10 mmol), pivalic acid (0.030 mg, 0.30 mmol), Cs_2CO_3 (2.0 mmol, 0.652 g, 2.00 mmol) and anhydrous cyclopentyl methyl ether (CPME, 5.0 mL) was stirred at 100 °C for 24 hours. The reaction mixture was then cooled to room temperature and poured into MeOH (150 mL) under vigorous stirring for the precipitation of the polymer. The precipitate was collected by filtration, dissolved into the minimum amount of chloroform and precipitated in cold methanol. The polymer was collected after filtration and dried in vacuo for 12 hours. DPP-FL as a purple solid; ^{1}H NMR (500 MHz, $CDCl_3$): δ 9.02-8.90 (2H), 7.77-7.42 (6H), 7.31-7.26 (2H), 4.22-4.01 (4H), 2.12-1.96 (4H), 1.85-0.97 (60H), 0.91-0.75 (12H), 0.74-0-59 (4H) ppm. DPP-BTZ as a blue solid; ^{1}H NMR (500 MHz, $CDCl_3$): δ 9.17-8.74 (2H), 8.29-7.35 (4H), 4.97-4.56 (4H), 4.29-3.82 (2H), 2.44-1.08 (60 H), 0.96-0.69 (9H) ppm.

2.11 References

1. *Unconventional Ethereal Solvents in Organic Chemistry: A Perspective on Applications of 2-Methyltetrahydrofuran, Cyclopentyl Methyl Ether, and 4-Methyltetrahydropyran.* Rachel Bijoy, Pratibha Agarwala, Lisa Roy, and Bhaskar N. Thorat. 3, 2022 , Organic Process Research & Development , Vol. 26, p. 480-492.

2. *Cyclopentyl Methyl Ether as a New and Alternative Process Solvent.* Kiyoshi Watanabe, Noriyuki Yamagiwa, and Yasuhiro Torisawa. 2, 2007 , Organic Process Research & Development , Vol. 11 , p. 251-258.

3. *Replacement of Less-Preferred Dipolar Aprotic and Ethereal Solvents in Synthetic Organic Chemistry with More Sustainable Alternatives.* Andrew Jordan, Callum G. J. Hall, Lee R. Thorp, and Helen F. Sneddon. 6, Chemical Reviews 2022 , Vol. 122, p. 6749-6794.

4. *Solvent effects in catalysis: rational improvements of catalysts via manipulation of solvent interactions.* Dyson, Paul J. and Jessop, Philip G. 10, 2016, Catal. Sci. Technol., Vol. 6, p. 3302-3316.

5. *Design of bifunctional chiral phenanthroline ligand with Lewis basic site for palladium-catalyzed asymmetric allylic substitution.* Naganawa, Yuki and Abe, Hiroki and Nishiyama, Hisao. 21, 2018, Chem. Commun., Vol. 54, p. 2674-2677.

6. *Optimization of the Reaction Conditions for Direct Arylation Polymerizations in a Sustainable Solvent.* Conelli, D., Grisorio, R., Suranna, G. P.,. 2020, Macromol. Chem. Phys, Vol. 221 , p. 2000041.

7. *Investigation of green and sustainable solvents for direct arylation polymerization (DArP).* Pankow, Robert M. and Ye, Liwei and Gobalasingham, Nemal S. and Salami, Neda and Samal, Sanket and Thompson, Barry C. 28, 2018, Polym. Chem., Vol. 9, p. 3885-3892.

8. *Design and preparation of new palladium precatalysts for C–C and C–N cross-coupling reactions.* Bruno, Nicholas C. and Tudge, Matthew T. and Buchwald, Stephen L. 3, 2013, Vol. 4, p. 916-920.

9. *Equilibrium Study of Pd(dba)2 and P(OPh)3 in the Pd-Catalyzed Allylation of Aniline by Allyl Alcohol.* Sawadjoon S, Orthaber A, Sjöberg PJ, Eriksson L, Samec JS. 1, 2014, Organometallics, Vol. 33, p. 249-253.

10. *The Sonogashira Reaction: A Booming Methodology in Synthetic Organic Chemistry.* Nájera, Rafael Chinchilla and Carmen. 3, 2007 , Chemical Reviews , Vol. 107, p. 874-922.

11. *C–H Arylation in the Synthesis of π-Conjugated Polymers.* Sabin-Lucian Suraru, Jason A. Lee, and Christine K. Luscombe. 6, 2016, ACS Macro Letters , Vol. 5 , p. 724-729.

12. *Synthesis of random poly(hexyl thiophene-3-carboxylate) copolymers via oxidative direct arylation polymerization (oxi-DArP).* Gobalasingham, Nemal S. and Pankow, Robert M. and Thompson, Barry C. 12, 2017, Polym. Chem., Vol. 8, p. 1963-1971.

13. *Impact of Precatalyst Activation on Suzuki-Miyaura Catalyst-Transfer Polymerizations: New Mechanistic Scenarios for Pre-transmetalation Events.* Suranna, Roberto Grisorio and Gian Paolo. 11, 2017 , ACS Macro Letters, Vol. 6 , p. 1251-1256.

14. *Exploring the Utility of Buchwald Ligands for C–H Oxidative Direct Arylation Polymerizations.* Reynolds, Graham S. Collier and John R. 8, 2019 , ACS Macro Letters, Vol. 8 , p. 931-936.

15. *Dual-Catalytic Ag-Pd System for Direct Arylation Polymerization to Synthesize Poly(3-hexylthiophene).* J. A. Lee, C. K. Luscombe. 7, 2018, ACS Macro Lett. , Vol. 7, p. 767-771 .

16. *Carboxylate-Assisted Transition-Metal-Catalyzed C−H Bond Functionalizations: Mechanism and Scope.* Ackermann, Lutz. 3, 2011 , Chemical Reviews , Vol. 111, p. 1315-1345.

17. *Direct Arylation of 2-Methylthiophene with Isolated [PdAr(μ-O2CR)(PPh3)]n Complexes: Kinetics and Mechanism.* Masayuki Wakioka, Yuki Nakamura, Qifeng Wang, and Fumiyuki Ozawa. 13, 2012 , Organometallics, Vol. 31 , p. 4810-4816.

18. Direct Arylation of 2-Methylthiophene with Isolated [PdAr(μ-O_2CR)(PPh_3)]n Complexes: Kinetics and Mechanism. Masayuki Wakioka, Yuki Nakamura, Qifeng Wang, and Fumiyuki Ozawa. 13, 2012 , Organometallics , Vol. 31, p. 4810-4816.

19. *Remarkable Ligand Effect of P(2-MeOC_6H_4)$_3$ on Palladium-Catalyzed Direct Arylation.* Masayuki Wakioka, Yuki Nakamura, Michelle Montgomery, and Fumiyuki Ozawa. 1, 2015 , Organometallics , Vol. 34 , p. 198-205.

20. *Syntheses and Properties of Donor–Acceptor-Type 2,5-Diarylthiophene and 2,5-Diarylthiazole.* Kentaro Masui, Atsunori Mori, Kunihiko Okano, Kenji Takamura, Motoi Kinoshita, and Tomiki Ikeda. 12, 2004 , Organic Letters , Vol. 6 , p. 2011-2014.
21. *Palladium-Catalyzed C–H Homocoupling of Thiophenes: Facile Construction of Bithiophene Structure.* Kentaro Masui, Haruka Ikegami, and Atsunori Mori. 16, 2004, Journal of the American Chemical Society , Vol. 126 , p. 5074-5075.
22. *Investigation of the electropolymerization of terthiophenein boron fluoride-ethyl ether.* Zhang, D., Qin, J. & Xue, G. 1999, Synth. Met. , Vol. 100, p. 285–289 .
23. *On the Role of Single Regiodefects and Polydispersity in Regioregular Poly(3-hexylthiophene): Defect Distribution, Synthesis of Defect-Free Chains, and a Simple Model for the Determination of Crystallinity.* Peter Kohn, Sven Huettner, Hartmut Komber, Volodymyr Senkovskyy, Roman Tkachov, Anton Kiriy, Richard H. Friend, Ullrich Steiner, Wilhelm T. S. Huck, Jens-Uwe Sommer, and Michael Sommer. 10, 2012 , Journal of the American Chemical Society, Vol. 134, p. 4790-4805.
24. *Optimization of direct arylation polymerization (DArP) through the identification and control of defects in polymer structure.* Rudenko, A.E. and Thompson, B.C. 2015, J. Polym. Sci. Part A: Polym. Chem., , Vol. 53, p. 135-147. .
25. *Mixed-Ligand Approach to Palladium-Catalyzed Direct Arylation Polymerization: Effective Prevention of Structural Defects Using Diamines.* Eisuke Iizuka, Masayuki Wakioka, and Fumiyuki Ozawa. 9, 2016 , Macromolecules , Vol. 49, p. 3310-3317.
26. *Effect of the Nature and the Position of Defects on the Chiral Expression in Poly(3-alkylthiophene)s.* Lize Verheyen, Julien De Winter, Pascal Gerbaux, and Guy Koeckelberghs. 22, 2019, Macromolecules , Vol. 52 , p. 8587-8595.
27. *Mechanistic studies and optimisation of a Pd-catalysed direct arylation reaction using phosphine-free systems.* Kuwabara, Junpei and Sakai, Masaru and Zhang, Qiao and Kanbara, Takaki. 5, 2015, Org. Chem. Front., Vol. 2, p. 520-525.
28. *Updating and further expanding GSK's solvent sustainability guide.* Alder, Catherine M. and Hayler, John D. and Henderson, Richard K. and Redman, Anikó M. and Shukla, Lena and Shuster, Leanna E. and Sneddon, Helen F. 13, 2016, Green Chem., Vol. 18, p. 3879-3890.
29. *Suppressing Defect Formation Pathways in the Direct C–H Arylation Polymerization of Photovoltaic Copolymers.* Thomas J. Aldrich, Alexander S. Dudnik, Nicholas D. Eastham, Eric F. Manley, Lin X. Chen, Robert P. H. Chang, Ferdinand S. Melkonyan, Antonio Facchetti, and Tobin J. Marks. 22, 2018 , Macromolecules , Vol. 51, p. 9140-9155.
30. *Monodispersed vs. polydispersed systems for bulk heterojunction solar cells: the case of dithienopyrrole/anthracene based materials.* Grisorio, Roberto and Allegretta, Giovanni and Suranna, Gian Paolo and Mastrorilli, Piero and Loiudice, Anna and Rizzo, Aurora and Mazzeo, Marco and Gigli, Giuseppe. 37, 2012, J. Mater. Chem., Vol. 22, p. 19752-19760.
31. *Influence of Keto Groups on the Optical, Electronic, and Electroluminescent Properties of Random Fluorenone-Containing Poly(fluorenylene-vinylene)s.* Roberto Grisorio, Claudia Piliego, Marinella Striccoli, Pinalysa Cosma, Paola Fini, Giuseppe Gigli, Piero Mastrorilli, Gian Paolo Suranna, and Cosimo Francesco Nobile. 50, 2008, The Journal of Physical Chemistry C , Vol. 112, p. 20076-20087.
32. *A $Pd(AcO)_2$/t-Bu_3P/K_3PO_4 catalytic system for the control of Suzuki cross-coupling polymerisation.* Grisorio, R. and Mastrorilli, P. and Suranna, G. P. 14, 2014, Polym. Chem., Vol. 5, p. 4304-4310.
33. *Catalyst-transfer polymerization of arylamines by the Buchwald–Hartwig cross-coupling.* Grisorio, Roberto and Suranna, Gian Paolo. 15, 2019, Polym. Chem., Vol. 10, p. 1947-1955.
34. *Donor–Acceptor Polymer with Benzotriazole Moiety: Enhancing the Electrochromic Properties of the "Donor Unit".* Abidin Balan, Gorkem Gunbas, Asuman Durmus, and Levent Toppare. 24, 2008 , Chemistry of Materials, Vol. 20, , p. 7510-7513.
35. *A Selenium-Substituted Low-Bandgap Polymer with Versatile Photovoltaic Applications.* Dou, L., Chang, W.-H., Gao, J., Chen, C.-C., You, J. and Yang, Y. 2013, Adv. Mater., Vol. 25, p. 825-831.

3 Chapter 3

Implementation of Sustainable Solvents in Green Polymerization Approaches

3.1 Motivation

The compatibility of the polymerization protocols based on the C–H bond activation with environmentally benign solvents could be considered the "ultimate effort" for effectively projecting the synthesis of conjugated polymers to an actually sustainable industrial scale.

In this Chapter, the focus relies on the study of the effects of the best "green" solvents (i.e., anisole and propylene carbonate) in consolidated polycondensations, such as the tandem Suzuki–Heck and the direct arylation polymerizations (DArP). In the synthesis of poly(9,9-dioctylfluorenylene-vinylene), we assess that the selected green solvents yielded better results with respect to conventional media. Additionally, the modulation of the medium polarity using mixtures of these green solvents and changing the reaction temperature affords a suitable compromise between high molecular weights and regioregularity of the resulting polymers. Concerning the DArP of 2-bromo-3-hexylthiophene yielding poly(3-hexylthiophene) (P3HT), the catalyst performances in anisole strictly depend on the palladium source used. The best conditions are obtained using $PdCl_2(PPh_3)_2$ as the precatalyst, affording a highly regioregular (93%) P3HT in quantitative yields (98%) and high molecular weights (26.7 kg/mol). In view of the huge efforts of the polymer chemistry scientific community devoted to the development of sustainable polymerization protocols, the aim of this research was to offer new ideas and outlooks for the implementation of environmentally benign solvents. This chapter of the Dissertation contains data that have been published by : **Conelli, D.,** Margiotta, N., Grisorio, R., Suranna, G. P., Macromol. Chem. Phys. 2021, 222, 2000382. https://doi.org/10.1002/macp.202000382

3.2 Introduction

Sustainable chemistry, as outlined in this Dissertation, is a rapidly advancing field. The attention toward the output and identification of new sustainable solvents that are applicable in cross-coupling reactions should lead to the discovery of innovative solvents compatible with atom-economical protocols such as DArP. [1] The substitution of a traditional solvent for another requires a suitable rationalization of the reaction conditions including solubility and stability of the catalyst and base, stability at high-temperatures, and propensity to stabilize the intermediates present in transition-metal cross-coupling reactions. [2] For these purposes, the solvent structure must be delicately balanced to promote high reactivity but not inhibit association of the palladium and arene or ligation of palladium. [3] The ranking based on the environmental, safety, and health (ESH) characteristics of the solvents allows to rapidly highlight suggestions for more sustainable solvent alternatives. [4] In particular, the selection guides published by GSK, [5] furnish detailed scoring information (Figure 3.1.) providing a comparison of different solvents for each chemical class. The present and future works with sustainable solvents will require their implementation in a variety of protocols (some of which are discussed below), so as to show good tolerance also for the structural variation of monomers. Identifying additional sustainable solvents that can satisfy this role and a general utility for the synthesis of a variety of conjugated polymers would be a significant advance. There are relatively greener and more sustainable organic solvents that have been proven to be amenable to organometallic reactions. Anisole is a low-cost, non-toxic, biodegradable, and highly recommended organic solvent based on recent solvent selection guides, with the great advantage to be structurally similar to toluene. Propylene carbonate (PC) is also considered as a “green” sustainable alternative solvent exhibiting potential beneficials effects in the field of the Pd-catalysed reactions. It is a polar aprotic, non-toxic, and biodegradable solvent with similar physico-chemical characteristics to standard polar solvents such as acetonitrile and acetone. [6]

Classification	Solvent Name	CAS Number	Composite Colour‡	Boiling Point (°C)	Incineration	Recycling	Biotreatment	VOC Emissions	Aquatic Impact	Air Impact	Health Hazard	Exposure potential	Flammability & Explosion	Reactivity & Stability	Life Cycle Analysis†
Water & Acids	Water	7732-18-5		100	4	2	4	6	10	8	10	9	8	10	10
	Acetic Acid	64-19-7		118	3	5	4	7	8	4	7	5	8	6	8
	*Trifluoroacetic acid**	76-05-1		72	1	5	2	4	4	4	4	3	7	6	
Alcohols	1-Heptanol	111-70-6		178	9	8	10	9	8	4	10	7	9	10	
	Ethylene glycol	107-21-1		197	4	5	5	10	10	8	7	10	10	10	9
	1-Octanol	111-87-5		196	9	7	8	10	5	4	7	10	9	10	
	1-Butanol	71-36-3		118	6	7	5	8	9	8	7	7	8	9	5
	1-Propanol	71-23-8		97	5	3	3	6	10	4	10	7	8	10	7
	Ethanol	64-17-5		78	5	5	3	4	9	5	10	8	6	10	
	2-Propanol	67-63-0		82	5	5	3	5	8	7	10	6	6	8	4
	t-Butanol	75-65-0		82	5	5	3	5	9	7	7	5	6	10	8
	IMS (ethanol, denatured)	64-17-5		78	5	5	3	5	9	5	4	7	6	10	
	Methanol	67-56-1		65	4	7	3	3	10	7	4	6	5	10	9
Esters	Glycerol diacetate	111-55-7		187	5	6	6	10	6	6	10	8	10	10	
	Isobutyl acetate	110-19-0		116	7	9	8	6	9	6	10	6	8	10	
	Isoamyl acetate	123-92-2		142	9	9	8	8	4	6	7	8	8	10	
	Isopropyl acetate	108-21-4		89	6	7	5	5	9	5	10	6	6	10	7
	Ethyl acetate	141-78-6		77	5	6	5	4	9	5	10	7	5	10	6
Carbonates	*Propylene carbonate**	108-32-7		242	4	5	6	10	10	10	10	10	10	10	
	*Diethyl carbonate**	105-58-8		126	7	9	8	7	9	8	4	5	8	10	
	Dimethyl carbonate	616-38-6		91	4	8	5	5	9	7	10	6	6	10	8
Ketones	Cyclopentanone	120-92-3		131	8	9	6	7	10	5	7	6	8	10	6
	Methylisobutyl ketone	108-10-1		117	7	8	5	7	9	3	7	6	7	9	2
	Methylethyl ketone	78-93-3		80	5	5	3	4	8	4	10	6	5	9	3
	Acetone	67-64-1		56	5	6	2	2	10	6	10	6	4	9	7
Aromatics	Anisole	100-66-3		154	8	8	8	8	7	6	7	8	7	9	5
	p-Xylene	106-42-3		138	10	9	6	7	5	2	7	7	5	10	7
	p-Cymene*	99-87-6		177	10	8	7	9	3	2	10	6	6	9	
	Toluene	108-88-3		111	10	7	6	7	7	2	7	6	5	10	7
	Trifluorotoluene	98-08-8		102	4	4	5	6	3	8	10	4	4	10	
	Pyridine	110-86-1		115	3	6	2	7	7	3	4	4	8	9	2
	Benzene	71-43-2		80	9	6	6	4	7	5	1	1	3	10	7
Hydrocarbons	Isooctane	540-84-1		99	10	4	5	6	2	5	10	7	3	10	7
	Heptane	142-82-5		98	10	4	5	6	3	5	10	6	3	10	7
	Cyclohexane	110-82-7		81	10	6	5	4	3	5	10	6	2	10	7
	Hexane	110-54-3		69	10	8	4	3	3	5	7	4	2	10	7
	Petroleum spirits	8032-32-4		55	8	9	4	2	5	5	1	6	2	10	7
Ethers	*Dimethyl isosorbide**	5306-85-4		236	4	4	5	10	9	6	4	9	9	8	
	Cyclopentyl methyl ether	5614-37-9		106	8	4	5	6	4	3	4	4	6	9	4
	*2-Methyltetrahydrofuran**	96-47-9		78	6	5	3	4	7	4	4	3	4	6	4
	t-Butylmethyl ether	1634-04-4		55	7	8	4	2	7	5	7	4	1	9	8
	Diisopropyl ether	108-20-3		68	9	7	6	3	5	4	10	6	4	3	9
	Tetrahydrofuran	109-99-9		65	5	5	2	3	9	3	7	5	4	6	4
	1,4-Dioxane	123-91-1		102	4	1	3	6	8	4	4	3	4	6	6
	Diethyl ether	60-29-7		35	7	7	3	1	5	3	10	4	2	6	6
	1,2-Dimethoxyethane	110-71-4		85	4	4	3	5	8	7	3	4	4	6	7
Dipolar Aprotics	Dimethyl sulphoxide	67-68-5		189	3	4	4	3	8	6	7	5	5	5	6
	Acetonitrile	75-05-8		82	3	5	3	4	10	6	7	5	6	10	4
	N-Methyl pyrrolidone	872-50-4		202	3	4	3	10	10	6	1	9	9	9	4
	N,N-Dimethyl acetamide	127-19-5		165	3	6	3	9	10	6	1	7	9	9	2
	N,N-Dimethyl formamide	68-12-2		153	3	6	3	8	10	4	1	6	9	9	7
Chlorinated	Dichloromethane	75-09-2		40	2	10	4	1	8	6	7	4	4	10	7
	1,2-Dichloroethane	107-06-2		84	2	7	5	5	9	7	1	2	5	10	7
	Chloroform	67-66-3		61	3	9	5	3	7	5	4	1	5	10	6
	Carbon tetrachloride	56-23-5		77	3	7	5	4	4	1	4	1	4	10	7

GSK Solvent Sustainability Guide

gsk

Column Headings Colour Key

- Waste
- Environment
- Human Health
- Safety

Composite Colour Key

- Few Known Issues
- Some Known Issues
- Major Known Issues

**The scoring assessment for this solvent includes 4 or more data gaps, therefore there is a lower level of confidence in the solvent's placement on this guide.*

†A blank value for Life Cycle Analysis (LCA) indicates that this data is currently not available.

‡The composite colour represents an overall categorization of the holistic sustainability of a solvent, taking all category scores into consideration.

Figure 3.1. *GSK Solvent Sustainability Guide (from ref. (5)) providing scoring breakdowns for selected solvents.*

In order to investigate the polymerizations based on C–H bond activations as environmentally benign protocols we focused on the possibility to implement two advantageous synthetic protocols using more sustainable media.

As discussed in Chapter 1, also the Heck reaction relies on the formal activation of the C–H bonds belonging to the vinyl moiety [(7)] allowing to build up all-carbon conjugated polymer backbones without the limitation to use only heteroaromatic structures as the monomers. [(8)] It was previously depicted the tandem Suzuki-Heck polymerization (SuHe) as an evoluted protocol in which the use of the commercially available potassium vinyl-trifluoroborate (PVTB) should avoid an excessive manipulation of the available starting materials (i.e., the dihalo-derivatives) for the preparation of the appropriate monomers. [(9)] [(10)]

In this study, we choose two paradigmatic polymerization routes (Scheme 3.2.) to study the potential implementation of solvents classified as highly sustainable (i.e., anisole and propylene carbonate). [5] In the Suzuki-Heck polymerization of 2,7-dibromo-9,9-dioctylfluorene with potassium vinyltrifluoroborate (PVTB), we found that the catalyst performances were improved by carrying out the reaction in anisole, while the resulting poly(arylene-vinylene) regioregularity resulted to be positively influenced by the polarity of the sustainable medium, introducing propylene carbonate as the cosolvent. On the other hand, concerning the DArP of 2-bromo-3-hexyl-thiophene, we assessed that the molecular weights of the relevant poly(3-hexylthiophene) were strongly influenced by the precatalyst in anisole. [11] The observed effects allowed us to understand the importance of a rational approach in the implementation of alternative green solvents in sustainable polymerization protocols.

a)

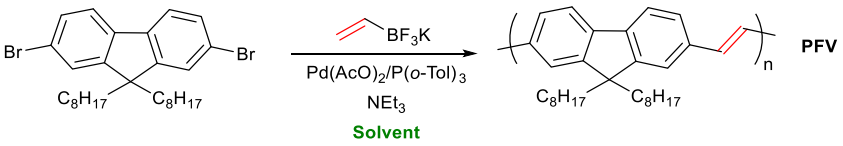

b)

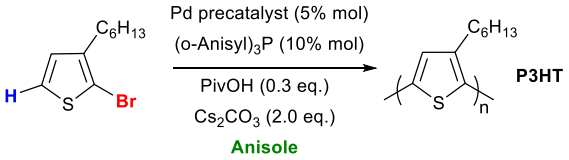

Scheme 3.2. The implemented Polymerization protocols studied in this work: a) tandem Suzuki-Heck polymerization of 2,7-dibromo-9,9-dioctylfluorene with PVTB; b) DArP of 2-bromo-3-hexyl-thiophene.

3.3 Results and discussion

3.3.1 Tandem Suzuki-Heck polymerization

A systematic investigation of the tandem Suzuki-Heck polymerization reaction in the chosen sustainable solvents was firstly conducted. The reaction protocol allowed the obtainment of poly(fluorenylene-vinylene)s (PFVs) by reacting 2,7-dibromo-9,9-dioctylfluorene and PVTB, which build up the π-conjugated backbone through concatenated Suzuki and Heck cross-couplings. These monomers were mixed with $Pd(AcO)_2$ (5% mol/mol with respect to the monomer) as the palladium precursor, $P(o\text{-}Tol)_3$ (5.0 equivalents with respect to palladium) as the ligand and triethylamine (NEt_3, 2.5 equivalents with respect to the monomer) as the base, in the chosen solvent, the amount of which is added until a monomer concentration of 0.1 M is reached. A slight excess of PVTB was introduced (1.1 equivalents with respect to the fluorene monomer) to warrant the pre-reduction of the $Pd^{(II)}$ source necessary for the activation of the catalytic cycle. [12] The reactions were carried out at the desired temperature for 24 h to avoid the formation of insoluble products, deriving from further substitution at the double bonds of the polymer backbone. In these conditions, the conventional solvent of this synthetic protocol (1,4-dioxane) yielded a polymer endowed with 8.0 kg/mol as average molecular weights in good yields (entry 1 of Table 3.3.). At this stage, the solvent effect was investigated by keeping the other reaction parameters unmodified. The molecular weights of the obtained polymers were taken as the main parameter to evaluate the performance of the solvent for the polymerization. The results of the catalytic study are summarized in Table 3.3. (entries 2-5 of Table 3.3.). While ethereal 2-MeTHF and CPME (entries 2 and 3 of Table 3.3.) afforded poorer results in terms of both yield and molecular weights with respect to the conventional solvent (1,4-dioxane), interesting performances were recorded when anisole (95% yield, M_n = 8.5 kg/mol and Đ = 1.53, entry 4) and propylene carbonate (77% yield, M_n = 8.9 kg/mol and Đ = 1.69, entry 5) were used as green polymerization solvents. Interestingly, we found that the molecular

weights of the PFV obtained in propylene carbonate (PC) was the highest observed in the series of experiments, notwithstanding the precipitation of the polymer in the reaction medium, which could have hampered the proper growth of the polymer chains. We think that the scarce affinity of propylene carbonate with the long and apolar aliphatic chains decorating the fluorene units is to be held responsible for the polymer precipitation.

Table 3.3. Reaction conditions adopted for the polymerization of 2,7-dibromo-9,9-dioctylfluorene (PFV synthesis)

Entry	Solvent	Temperature (°C)	Yield (%)[a]	M_n (kg/mol)[b]	M_w (kg/mol)[b]	Đ[b]	RR (%)
1	dioxane	100	80	8.0	21.7	2.71	–
2	2-MeTHF	100	64	6.7	10.0	1.49	–
3	CPME	100	32	5.6	8.1	1.45	–
4	Anisole	100	95	8.5	13.0	1.53	–
5	PC	100	77	8.9	15.1	1.69	–
6	PC	120	insoluble	–	–	–	–
7	Anisole	120	82	17.7	59.3	3.35	88
8	Anisole	140	88	12.1	18.2	1.50	–
9	Anisole/PC (1/1 vol/vol)	120	insoluble	–	–	–	–
10	Anisole/PC (4/1 vol/vol)	120	43	12.4	25.1	2.02	95

[a]Measured after polymer isolation carried out by multiple precipitations. [b]Number-average molecular weights (M_n), weight-average molecular weights (M_w) and dispersity (Đ) as determined by GPC. PC: propylene carbonate. RR: polymer regioregularity estimated by ^{1}H NMR.

The good performances of high-boiling green solvents (i.e., propylene carbonate and anisole) in this kind of polymerization paved the way to the possibility of exploring the temperature effect on the reaction course, a degree of freedom precluded to the reactions carried out in dioxane (b.p. = 101°C).

In the case of propylene carbonate as the solvent, the reaction performed at 120 °C yielded an insoluble material (entry 6 of Table 3.3.) precluding any solution characterization. Therefore, it was not possible to establish if the polymer

insolubility is the result of its exceptionally high molecular weights of the product or is due to backbone reticulation occurring after precipitation in propylene carbonate and promoted by the higher reaction temperature. The same polymerization carried out in anisole afforded excellent results in terms of molecular weights (17.7 kg/mol, entry 7 of Table 3.3.), confirming that the temperature plays a crucial role in determining the catalyst performance in tandem Suzuki-Heck polymerizations. We rationalized these observations considering the balance between the necessity of using a large excess of phosphine ligands with respect to the palladium (to warrant catalyst stability) and of freeing active sites onto the coordination sphere of the metal center (promoted by higher temperatures) in the Heck catalytic cycle. [13] For these reasons, a further increase of the temperature (140 °C, entry 8 of Table 3.3.) resulted detrimental for the molecular weights of the obtained PFV. This result was probably connected to a catalyst deactivation effect induced, at relatively higher temperatures, by more extensive decoordination of the ligands from the metal center. With the aim to improve the regioregularity of the polymer, preserving, at the same time, the process sustainability, we tried to modify the polarity of the reaction medium by using propylene carbonate (PC) as the cosolvent with anisole. However, the reaction carried out with an equivolumetric mixture of anisole and propylene carbonate at the optimized temperature of 120 °C (entry 9 of Table 3.3.) led again to a completely insoluble material. After several experiments, a soluble polymer in the reaction medium was obtained by using an anisole/propylene carbonate volumetric ratio of 4/1 (entry 10 of Table 3.3.) with satisfactory results in terms of molecular weights (12.4 kg/mol). We observed, however, that the reaction led to an insoluble organic fraction also in this case, justifying both the lower yield (43%) and molecular weights recorded for the entry 10 with respect to the reaction carried out in anisole (entry 7).
Our hypothesis is that longer polymer chains are lost as an insoluble products due to the medium polarity.

3.3.2 Spectroscopic characterization of PFVs

We investigated the structure of the polymer obtained from the reaction conditions specified in entry 7 by NMR spectroscopy. In this contest, the ^{1}H-NMR analysis was also used to assess the presence of 1,1-diarylenevinylene defects in the polymers, which can origin after the Heck reaction step (the polymer segments containing these regio-defects are represented in Figure 3.4.A.). The resonances of these defects typically fall in the range δ 5.3-5.5 ppm in the ^{1}H-NMR spectra of the polymers and the relevant signal integrals can be compared with those of the α-methylene protons belonging to the aliphatic chains of the fluorene units. In this way, the amount of such defects was determined as ~12%, in agreement with that of the polymers synthesized in conventional solvents. [14] The stereochemistry of the double bonds present in the polymer backbone obtained from entry 7 was ascertained by inspecting its IR spectrum. A band at 957 cm^{-1} (marked with an arrow in Figure 3.4.B.) was clearly identifiable and we ascribed it to the out-of-plane C–H bending mode of trans-vinylene moieties. The absence of the bands at ~650 cm^{-1} typical of cis-vinylene moieties, [15] allowed us to conclude that the the double bonds in the obtained PFV macromolecular backbone are prevalently in the trans configuration.

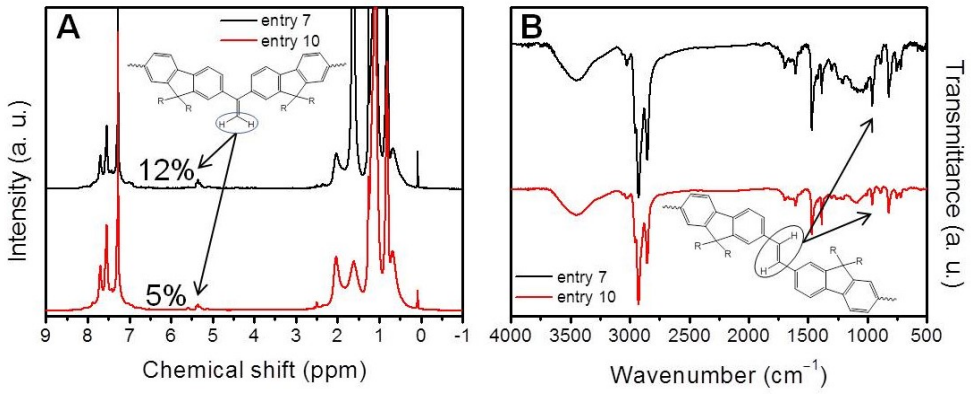

Figure 3.4 (A) ^{1}H-NMR spectra ($CDCl_3$) of the PFVs synthesized in anisole (entry 7) and in a mixture of anisole and propylene carbonate (4/1 vol/vol, entry 10) indicating the resonances ascribable to the 1,1-diarylene-vinylene defects. (B) IR spectra of the same polymers highlighting the bands ascribable to the out-of-plane C–H bending mode of trans-vinylene moieties.

We obtained that PFV arised from entry 10 exhibited a higher regioregularity, as estimated by the quantity of the 1,1-diarylene-vinylene defects by ^{1}H-NMR (~5%, Figure 3.4.A.) which was lower than the one assessed for the polymer synthesized in anisole. This result suggests that the presence of the suitable quantity of the polar propylene carbonate was beneficial for preserving the polymer regioregularity, because the transition state concerning the aryl migration onto the double bond is stabilized by solvents with high dielectric constants. [16] [17] [18] In Heck reactions, in fact, the regioselectivity is dominated by steric effects, disfavoring (although not completely) the formation of 1,1-diaryl alkenes. Also in this case, IR analyses allowed to ascertained the prevalent trans-configuration of the vinylene double bonds present in this polymer by (Figure 3.4.B).

3.3.3 DArP of 2-bromo-3-hexylthiophene

With the aim to further investigate the potentialities of these green solvents, we conducted a systematic study using anisole and propylene carbonate also in the paradigmatic DArP leading to poly(3-hexylthiophene) (P3HT) and employing 2-bromo-3-hexylthiophene as the monomer. The initial attempts were carried out using zero-valent palladium precursors in the presence of $(o\text{-Anisyl})_3P$ [19] as the ligand, pivalic acid as the additive and Cs_2CO_3 as the base. As first results, the reaction carried out in anisole gave a polymer endowed with satisfactory molecular weights (8.4 kg/mol, entry 1 of Table 3.5.), whereas no reaction was observed when a mixture (4/1 vol/vol) of anisole and propylene carbonate was used as the solvent. This observation led us to exclude the use of propylene carbonate as the (co)-solvent in this type of reaction. Next, we studied the effect of changing the $Pd^{(II)}$-based precatalyst on the polymerization course starting our investigations by the palladium precursors containing carboxylate species (acetate or pivalate) as the ancillary ligands, being potentially active in the DArP catalytic cycle. [20] As reported in entries 2 and 3 of Table 3.5., improvements in terms of molecular weights were obtained with respect to the results of zero-valent palladium precursors only in the case of palladium acetate (92% yield, M_n = 13.7 kg/mol and

Đ = 1.37, entry 2). In the case of chloride-based palladium species as the precatalysts, [21] we explored the reactivity of $PdCl_2$ and $PdCl_2(PPh3)_2$ in combination with $(o\text{-Anisyl})_3P$ as the ligand (entries 4 and 5 of Table 2). In both cases, the obtained molecular weights were remarkably higher (M_n = 15.9 kg/mol and 17.2 kg/mol respectively) than those recorded for the reaction carried out using palladium acetate. Regarding the precatalyst performance, a similar trend was also observed for the synthesis of P3HT starting from the same monomer and using CPME as the alternative green solvent, as discussed in Chapter 2, [22] confirming the efficacy of chloride-based palladium precursors in DArP.

In detail, the presence of coordinating ancillary ligands belonging to the palladium source (PPh_3) warranted the best results in the polymerization in terms of molecular weights. We rationalized this interesting result considering that the higher solubility of the $Pd^{(II)}$precatalyst in the initial stages of the polymerization is beneficial to the overall performance of the catalytic system. The attempts related to the effect of the temperature increase (entries 6 and 7) did not lead to any improvement in the case of DArP carried out in anisole.

Table 3.5. *Reaction conditions adopted for the DArP of 2-bromo-3-hexylthiophene (P3HT synthesis) in anisole.*

Entry	Precatalyst	Temperature (°C)	Yield (%)[a]	M_n (kg/mol)[b]	M_w (kg/mol)[b]	Đ[b]	RR (%)
1	$Pd_2(dba)_3$	100	61	8.4	10.7	1.27	–
2	$Pd(AcO)_2$	100	92	10.0	13.7	1.37	–
3	$Pd(PivO)_2$	100	42	5.3	6.3	1.18	–
4	$PdCl_2$	100	98	15.9	24.3	1.53	–
5	$PdCl_2(PPh_3)_2$	100	98	17.2	26.7	1.55	93
6	$PdCl_2(PPh_3)_2$	120	83	12.5	16.0	1.28	–
7	$PdCl_2(PPh_3)_2$	140	86	11.5	16.2	1.41	–

[a]Measured after polymer purification carried out by multiple precipitations. [b]Number-average molecular weights (M_n), weight-average molecular weights (M_w) and dispersity (Đ) as determined by GPC. RR: polymer regioregularity estimated by ^1H NMR.

3.3.4 Spectroscopic characterization of P3HTs

In order to confirm the advancement of the DArP protocol, besides to the further sustainability increase obtained, we also investigated the optoelectronic properties of the obtained material evaluating the UV-vis absorption properties of the best polymer (entry 5) both in solution ($CHCl_3$) and as thin film (Figure 3.6.A.). As we expected, it can be observed that the intermolecular interactions in the solid state promoted a remarkable red-shift of the absorption maximum (λ_{max} = 554 nm) in the UV-vis spectrum of the relevant polymer with respect to that recorded in solution (λ_{max} = 446 nm). This effect is due to the orbital overlap of the π-system along the polymer backbone and to the π–π interactions between polymer chains. [23]The reported absorption λ_{max} values for the polymer are in agreement with previous reports of P3HT synthesized using DArP and Stille reactions. [24]Furthermore, the presence of a vibronic shoulder at longer wavelengths in the solid state evidence a specific molecular aggregation or π-stacking along the lattice alignments of high regioregular P3HT that allowed us to indirectly conclude that β-defects of the synthesized P3HT are undetectable. [25]

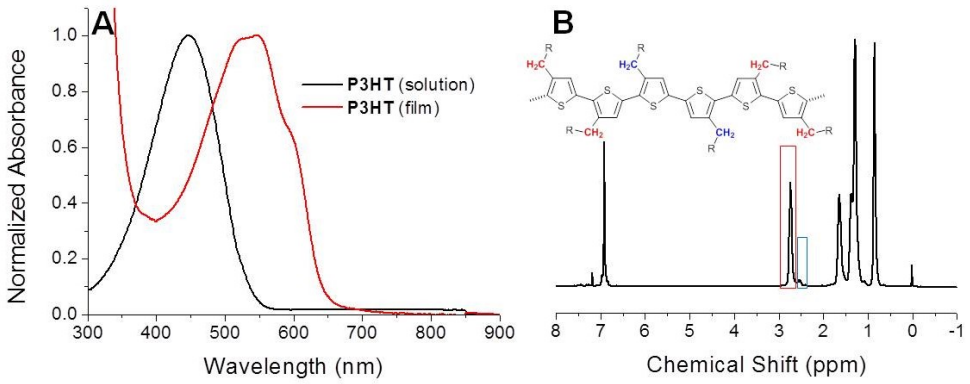

Figure 3.6. *(A) Comparison between the absorption spectra of P3HT (entry 5 of Table 2) in solution ($CHCl_3$) and in the solid state. (B) ^{1}H-NMR spectrum of the same polymer recorded in $CDCl_3$ for the determination of their regioregularity by the comparison of the integrals of the marked resonances.*

To confirm the discussed observation, the regioregularity of the synthesized P3HT obtained from entry 5 was determined using ^{1}H-NMR spectroscopy.

Notwithstanding the contribution of chain terminations, [26] the regioregularity was assessed using previously described methods, by calculating the ratio of the signal integrals spanning from 2.90–2.65 ppm and 2.90–2.40 ppm (Figure 3.6.B). [27] Based on this evaluation, the regioregularity for the P3HT of entry 5 was found to be 93%, while the presence of β-defects (typically showing a signal at δ = 2.35 ppm) was not observed. This result concerning the P3HT regioregularity obtained in anisole is promising and could be explaned considering a suitable pre-reduction of the palladium precatalyst without involving the substrate. [28] [29]

3.4 Conclusions

In this Chapter a further improve regarding the sustainability of metal-catalyzed polymerizations for the obtainment of π-conjugated materials was investigated. With this aim, we explored the compatibility of both the tandem Suzuki-Heck and direct arylation polymerizations with environmentally benign uncommon solvents: anisole and propylene carbonate. These promising sustainable solvents were implemented in the synthesis of poly(9,9-dioctylfluorenylene-vinylene) by using the traditional $Pd(AcO)_2$/$P(o\text{-}Tol)_3$/NEt_3 catalytic system. Considering the molecular weight as indicator of the solvent performance, we concluded that anisole and propylene carbonate constituted the best media for this kind of polymerization, even in comparison with conventional solvents (1,4-dioxane). The pursued results suggested us the possibility of modulating the reaction temperature and the medium polarity, reaching the desired compromise between high molecular weights and regioregularity of the resulting polymers. Conversely, in the case of the direct arylation polymerization of 2-bromo-3-hexylthiophene for the obtainment of poly(3-hexylthiophene), it was proved that the presence of propylene carbonate inhibited the reaction, while the performances in anisole were dependent on the palladium source used. The best conditions are obtained with $PdCl_2(PPh_3)_2$ as the precatalyst, affording a highly regioregular (93%) poly(3-hexylthiophene) in quantitative yields with high (26.7 kg/mol) molecular weights

and low dispersity. The rationalization of these results contributes to growing interest in the potential of green solvents in polymerization protocols.

3.5 Experimental section

All reagents and solvents were purchased from standard commercial sources and used as received. The syntheses were carried out under inert nitrogen atmosphere using conventional Schlenk techniques. ^{1}H-NMR spectra were recorded on a Bruker Avance DPX 300 MHz instrument. ^{1}H chemical shifts were referenced to TMS in $CDCl_3$. Gel-permeation chromatography (GPC) was carried out on an Agilent Series 1100 instrument equipped with a Pl-gel 5 µm mixed-C column. The samples for GPC analyses were dissolved in THF and eluted at a 1.0 mL/min flow rate. Detection was performed by a multiple wave UV-Vis detector. Number-average molecular weights (M_n), weight-average molecular weights (M_w) and dispersity (Đ) were calculated against polystyrene standards. UV–vis absorption spectra were recorded using a Jasco V670 spectrometer operated in transmission mode. FT-IR measurements were recorded on a JASCO 4200 spectrophotometer in attenuated total reflectance (ATR) mode. The synthesis of 2,7-dibromo-9,9-di-n-octylfluorene was carried out according to a literature procedure. [30]

3.6 Synthesis of poly(9,9-dioctylfluorenylene-vinylene) via tandem Suzuki-Heck polymerization

A mixture of 2,7-dibromo-9,9-dioctylfluorene (0.274 g, 0.50 mmol), potassium vinyl trifluoroborate (0.073 g, 0.55 mmol), $Pd(AcO)_2$ (5.5 mg, 0.025 mmol), P(*o*-Tolyl)$_3$ (0.038 g, 0.125 mmol.), triethylamine (0.18 mL, 1.25 mmol) and the rele-vant solvent (5.0 mL) was stirred at 100 °C for 24 hours. The reaction mixture was then cooled to room temperature and poured into methanol (100 mL) kept under vigorous stirring causing the polymer precipitation. The precipitate was filtered, dissolved into the minimum amount of chloroform, and reprecipitated in cold methanol. The whole purification procedure was repeated using ethanol as sol-vent, yielding a green solid that was dried in vacuo for 12 hours.

^{1}H NMR (300 MHz, $CDCl_3$): δ 7.74–7.63 (2H), 7.59–7.47 (4H), 7.27–7.18 (2H), 2.11–1.99 (4H), 1.52–1.40 (2H), 1.22–1.01 (12H), 0.94–0.57 (24H) ppm. IR (ATR): ν 3020, 2975, 2931, 2868, 1598, 1464, 1356, 957 (*trans* HC=CH), 817, 734 cm^{-1}.

3.7 Synthesis of poly(3-hexylthiophene) via DArP

A mixture of 2-bromo-3-hexylthiophene (0.247 g, 1.00 mmol), the suitable palladium precatalyst (0.05 equiv. with respect to the monomer), P(*o*-Anisyl)$_3$ (35.2 mg, 0.10 mol), pivalic acid (30.6 mg, 0.30 mol), Cs_2CO_3 (0.650 g, 2.0 mol) and anisole (5.0 mL) was stirred at 100 °C for 24 hours. After cooling to room temperature, the mixture was poured into 150 mL of methanol kept under vigorous stirring, to obtain the precipitation of the polymer. The precipitate was filtered, dissolved into the minimum amount of chloroform and reprecipitated in cold methanol. The whole purification procedure was carried out using ethanol and acetone for the precipitation, to eventually yield a brownish solid that was dried in vacuo for 12 hours. ^{1}H NMR (300 MHz, $CDCl_3$): δ 7.02–6.96 (1H), 2.83–2.77 (2H), 1.75–1.67 (2H), 1.47–1.27 (6H), 0.94–0.85 (3H) ppm.

3.8 References

1. *Green chemistry for organic solar cells.* Burke, Daniel J. and Lipomi, Darren J. 7, 2013, Energy Environ. Sci., Vol. 6, p. 2053-2066.

2. *Solvent effects in palladium catalysed cross-coupling reactions.* Sherwood, James and Clark, James H. and Fairlamb, Ian J. S. and Slattery, John M. 9, 2019, Green Chem., Vol. 21, p. 2164-2213.

3. *Approaches for improving the sustainability of conjugated polymer synthesis using direct arylation polymerization (DArP).* Pankow, Robert M. and Thompson, Barry C. 3, 2020, Polym. Chem., Vol. 11, p. 630-640.

4. *Tools and techniques for solvent selection: green solvent selection guides.* Byrne, F.P., Jin, S., Paggiola, G. et al. 1, 2016, Sustain Chem Process, Vol. 4, p. 7.

5. *Updating and further expanding GSK{'}s solvent sustainability guide.* Alder, Catherine M. and Hayler, John D. and Henderson, Richard K. and Redman, Anikó M. and Shukla, Lena and Shuster, Leanna E. and Sneddon, Helen F. 13, 2016, Green Chem., Vol. 18, p. 3879-3890.

6. *Carbonates: eco-friendly solvents for palladium-catalysed direct arylation of heteroaromatics.* Dong, Jia Jia and Roger, Julien and Verrier, Cécile and Martin, Thibaut and Le Goff, Ronan and Hoarau, Christophe and Doucet, Henri. 11, 2010, Green Chem., Vol. 12, p. 2053-2063.

7. *The Heck Reaction as a Sharpening Stone of Palladium Catalysis.* Cheprakov, Irina P. Beletskaya and Andrei V. 8, 2000 , Chemical Reviews , Vol. 100 , p. 3009-3066.

8. *Poly (fluorenevinylene) derivatives by Heck coupling: Synthesis, photophysics, and electroluminescence.* Mikroyannidis, J.A., Yu, Y.J., Lee, S.H. and Jin, J.I.,. 15, 2006, Journal of Polymer Science Part A: Polymer Chemistry, Vol. 44, p. 4494-4507.

9. *Random poly(fluorenylene-vinylene)s containing 3,7-Dibenzothiophene-5,5-dioxide units: Synthesis, photophysical, and electroluminescence proerties.* Grisorio, R., Piliego, C., Cosma, P., Fini, P., Mastrorilli, P., Gigli, G., Suranna, G.P. and Nobile, C.F. 2009, J. Polym. Sci. A Polym. Chem., Vol. 47, p. 2093-2104.

10. *A one-pot synthetic strategy via tandem Suzuki–Heck reactions for the construction of luminescent microporous organic polymers.* Sun, Libo and Zou, Yongcun and Liang, Zhiqiang and Yu, Jihong and Xu, Ruren. 2, 2014, Polym. Chem., Vol. 5, p. 471-478.

11. *Implementation of Sustainable Solvents in Green Polymerization Approaches.* Conelli, D., Margiotta, N., Grisorio, R., Suranna, G. P.,. 2021, Macromol. Chem. Phys. , Vol. 222, p. 2000382.

12. *Design and preparation of new palladium precatalysts for C–C and C–N cross-coupling reactions.* Bruno, Nicholas C. and Tudge, Matthew T. and Buchwald, Stephen L. 3, 2013, Chem. Sci., Vol. 4, p. 916-920.

13. *The Heck Reaction as a Sharpening Stone of Palladium Catalysis.* Cheprakov, Irina P. Beletskaya and Andrei V. 8, 2000 , Chemical Reviews , Vol. 100, p. 3009-3066.

14. *RANDOM POLY(2, 7-FLUORENYLENEVINYLENE) COPOLYMERS OBTAINED BY A SUZUKI-HECK REACTION: SYNTHESIS AND PROPERTIES.* R. Grisorio, P. Mastrorilli, C. F. Nobile, G. Romanazzi, G. P. Suranna, G. Gigli, C. Piliego, G. Ciccarella, P. Cosma, D. Acierno, and E. Amendola. 2008, AIP Conference Proceedings , Vol. 1042, p. 297-299 .

15. *Polyacetylenes Bearing Chiral-Substituted Fluorene and Terfluorene Pendant Groups: Synthesis and Properties.* Piero Mastrorilli, Cosimo Francesco Nobile, Roberto Grisorio, Antonino Rizzuti, Gian Paolo Suranna, Domenico Acierno, Eugenio Amendola, and Pio Iannelli. 12, 2004 , Macromolecules , Vol. 37 , p. 4488-4495.

16. *Cyclic Carbonates as Green Alternative Solvents for the Heck Reaction.* Helen L. Parker, James Sherwood, Andrew J. Hunt, and James H. Clark. 7, 2014 , ACS Sustainable Chemistry & Engineering, Vol. 2 , p. 1739-1742.

17. *Highly Regioselective Palladium-Catalyzed Oxidative Coupling of Indolizines and Vinylarenes via C–H Bond Cleavage.* Yuzhu Yang, Kai Cheng, and Yuhong Zhang. 24, 2009, Organic Letters, Vol. 11 , p. 5606-5609.

18. *Electronic Control of the Regiochemistry in the Heck Reaction.* Henrik von Schenck, Björn Åkermark, and Mats Svensson. 12, 2003, Journal of the American Chemical Society, Vol. 125 , p. 3503-3508.

19. *A Highly Efficient Catalytic System for Polycondensation of 2,7-Dibromo-9,9-dioctylfluorene and 1,2,4,5-Tetrafluorobenzene via Direct Arylation.* Masayuki Wakioka, Yutaro Kitano, and Fumiyuki Ozawa. 2, 2013 , Macromolecules , Vol. 46 , p. 370-374.
20. *Remarkable Ligand Effect of P(2-MeOC6H4)3 on Palladium-Catalyzed Direct Arylation.* Masayuki Wakioka, Yuki Nakamura, Michelle Montgomery, and Fumiyuki Ozawa. 1, 2015 , Organometallics , Vol. 34, p. 198-205.
21. *Impact of Precatalyst Activation on Suzuki-Miyaura Catalyst-Transfer Polymerizations: New Mechanistic Scenarios for Pre-transmetalation Events.* Suranna, Roberto Grisorio and Gian Paolo. 11, 2017 , ACS Macro Letters , Vol. 6 , p. 1251-1256.
22. *Optimization of the Reaction Conditions for Direct Arylation Polymerizations in a Sustainable Solvent.* Conelli, D., Grisorio, R., Suranna, G. P.,. 2020, Macromol. Chem. Phys., Vol. 221, p. 2000041.
23. *Monodispersed vs. polydispersed systems for bulk heterojunction solar cells: the case of dithienopyrrole/anthracene based materials.* Grisorio, Roberto and Allegretta, Giovanni and Suranna, Gian Paolo and Mastrorilli, Piero and Loiudice, Anna and Rizzo, Aurora and Mazzeo, Marco and Gigli, Giuseppe. 37, 2012, J. Mater. Chem., Vol. 22, p. 19752-19760.
24. *Evaluating structure–function relationships toward three-component conjugated polymers via direct arylation polymerization (DArP) for Stille-convergent solar cell performance.* Gobalasingham, Nemal S. and Pankow, Robert M. and Ekiz, Seyma and Thompson, Barry C. 27, 2017, J. Mater. Chem. A, Vol. 5, p. 14101-14113.
25. *Third-order nonlinear optical properties of regioregular poly(3-hexylthiophene) thin film on quartz glass modified by HMDS and ODTS.* S. Ochiai, J. Ramajothi, K. Kojima and T. Mizutani,. 2008. p. 255-258.
26. *Effect of the Nature and the Position of Defects on the Chiral Expression in Poly(3-alkylthiophene)s.* Lize Verheyen, Julien De Winter, Pascal Gerbaux, and Guy Koeckelberghs. 22, 2019 , Macromolecules, Vol. 52 , p. 8587-8595.
27. *Optimization of direct arylation polymerization (DArP) through the identification and control of defects in polymer structure.* Rudenko, A.E. and Thompson, B.C. 2015, J. Polym. Sci. Part A: Polym. Chem.,, Vol. 53, p. 135-147.
28. *Advances in applying C–H functionalization and naturally sourced building blocks in organic semiconductor synthesis.* Xing, Liwen and Luscombe, Christine K. 46, 2021, J. Mater. Chem. C, Vol. 9, p. 16391-16409.
29. *Optimization of the Reaction Conditions for Direct Arylation Polymerizations in a Sustainable Solvent.* Conelli, D., Grisorio, R., Suranna, G. P.,. 2020, Macromol. Chem. Phys. , Vol. 221, p. 2000041.
30. *Catalyst-transfer polymerization of arylamines by the Buchwald–Hartwig cross-coupling.* Grisorio, Roberto and Suranna, Gian Paolo. 15, 2019, Polym. Chem., Vol. 10, p. 1947-1955.
31. *Unconventional Ethereal Solvents in Organic Chemistry: A Perspective on Applications of 2-Methyltetrahydrofuran, Cyclopentyl Methyl Ether, and 4-Methyltetrahydropyran.* Rachel Bijoy, Pratibha Agarwala, Lisa Roy, and Bhaskar N. Thorat. 3, 2022 , Organic Process Research & Development , Vol. 26, p. 480-492.
32. *Cyclopentyl Methyl Ether as a New and Alternative Process Solvent.* Kiyoshi Watanabe, Noriyuki Yamagiwa, and Yasuhiro Torisawa. 2, 2007 , Organic Process Research & Development , Vol. 11 , p. 251-258.
33. *Replacement of Less-Preferred Dipolar Aprotic and Ethereal Solvents in Synthetic Organic Chemistry with More Sustainable Alternatives.* Andrew Jordan, Callum G. J. Hall, Lee R. Thorp, and Helen F. Sneddon. 6, Chemical Reviews 2022 , Vol. 122, p. 6749-6794.
34. *Solvent effects in catalysis: rational improvements of catalysts via manipulation of solvent interactions.* Dyson, Paul J. and Jessop, Philip G. 10, 2016, Catal. Sci. Technol., Vol. 6, p. 3302-3316.
35. *Design of bifunctional chiral phenanthroline ligand with Lewis basic site for palladium-catalyzed asymmetric allylic substitution.* Naganawa, Yuki and Abe, Hiroki and Nishiyama, Hisao. 21, 2018, Chem. Commun., Vol. 54, p. 2674-2677.
36. *Optimization of the Reaction Conditions for Direct Arylation Polymerizations in a Sustainable Solvent.* Conelli, D., Grisorio, R., Suranna, G. P.,. 2020, Macromol. Chem. Phys, Vol. 221 , p. 2000041.

37. *Investigation of green and sustainable solvents for direct arylation polymerization (DArP).* Pankow, Robert M. and Ye, Liwei and Gobalasingham, Nemal S. and Salami, Neda and Samal, Sanket and Thompson, Barry C. 28, 2018, Polym. Chem., Vol. 9, p. 3885-3892.
38. *Design and preparation of new palladium precatalysts for C–C and C–N cross-coupling reactions.* Bruno, Nicholas C. and Tudge, Matthew T. and Buchwald, Stephen L. 3, 2013, Vol. 4, p. 916-920.
39. *Equilibrium Study of Pd(dba)2 and P(OPh)3 in the Pd-Catalyzed Allylation of Aniline by Allyl Alcohol.* Sawadjoon S, Orthaber A, Sjöberg PJ, Eriksson L, Samec JS. 1, 2014, Organometallics, Vol. 33, p. 249-253.
40. *The Sonogashira Reaction: A Booming Methodology in Synthetic Organic Chemistry.* Nájera, Rafael Chinchilla and Carmen. 3, 2007 , Chemical Reviews , Vol. 107, p. 874-922.
41. *C–H Arylation in the Synthesis of π-Conjugated Polymers.* Sabin-Lucian Suraru, Jason A. Lee, and Christine K. Luscombe. 6, 2016, ACS Macro Letters , Vol. 5 , p. 724-729.
42. *Synthesis of random poly(hexyl thiophene-3-carboxylate) copolymers via oxidative direct arylation polymerization (oxi-DArP).* Gobalasingham, Nemal S. and Pankow, Robert M. and Thompson, Barry C. 12, 2017, Polym. Chem., Vol. 8, p. 1963-1971.
43. *Impact of Precatalyst Activation on Suzuki-Miyaura Catalyst-Transfer Polymerizations: New Mechanistic Scenarios for Pre-transmetalation Events.* Suranna, Roberto Grisorio and Gian Paolo. 11, 2017 , ACS Macro Letters, Vol. 6 , p. 1251-1256.
44. *Exploring the Utility of Buchwald Ligands for C–H Oxidative Direct Arylation Polymerizations.* Reynolds, Graham S. Collier and John R. 8, 2019 , ACS Macro Letters, Vol. 8 , p. 931-936.
45. *Dual-Catalytic Ag-Pd System for Direct Arylation Polymerization to Synthesize Poly(3-hexylthiophene).* J. A. Lee, C. K. Luscombe. 7, 2018, ACS Macro Lett. , Vol. 7, p. 767-771 .
46. *Carboxylate-Assisted Transition-Metal-Catalyzed C−H Bond Functionalizations: Mechanism and Scope.* Ackermann, Lutz. 3, 2011 , Chemical Reviews , Vol. 111, p. 1315-1345.
47. *Direct Arylation of 2-Methylthiophene with Isolated [PdAr(μ-O2CR)(PPh3)]n Complexes: Kinetics and Mechanism.* Masayuki Wakioka, Yuki Nakamura, Qifeng Wang, and Fumiyuki Ozawa. 13, 2012 , Organometallics, Vol. 31 , p. 4810-4816.
48. —.Masayuki Wakioka, Yuki Nakamura, Qifeng Wang, and Fumiyuki Ozawa. 13, 2012 , Organometallics , Vol. 31, p. 4810-4816.
49. *Remarkable Ligand Effect of P(2-MeOC6H4)3 on Palladium-Catalyzed Direct Arylation.* Masayuki Wakioka, Yuki Nakamura, Michelle Montgomery, and Fumiyuki Ozawa. 1, 2015 , Organometallics , Vol. 34 , p. 198-205.
50. *Syntheses and Properties of Donor–Acceptor-Type 2,5-Diarylthiophene and 2,5-Diarylthiazole.* Kentaro Masui, Atsunori Mori, Kunihiko Okano, Kenji Takamura, Motoi Kinoshita, and Tomiki Ikeda. 12, 2004 , Organic Letters , Vol. 6 , p. 2011-2014.
51. *Palladium-Catalyzed C−H Homocoupling of Thiophenes: Facile Construction of Bithiophene Structure.* Kentaro Masui, Haruka Ikegami, and Atsunori Mori. 16, 2004, Journal of the American Chemical Society , Vol. 126 , p. 5074-5075.
52. *Investigation of the electropolymerization of terthiophenein boron fluoride-ethyl ether.* Zhang, D., Qin, J. & Xue, G. 1999, Synth. Met. , Vol. 100, p. 285–289 .
53. *On the Role of Single Regiodefects and Polydispersity in Regioregular Poly(3-hexylthiophene): Defect Distribution, Synthesis of Defect-Free Chains, and a Simple Model for the Determination of Crystallinity.* Peter Kohn, Sven Huettner, Hartmut Komber, Volodymyr Senkovskyy, Roman Tkachov, Anton Kiriy, Richard H. Friend, Ullrich Steiner, Wilhelm T. S. Huck, Jens-Uwe Sommer, and Michael Sommer. 10, 2012 , Journal of the American Chemical Society, Vol. 134, p. 4790-4805.
54. *Optimization of direct arylation polymerization (DArP) through the identification and control of defects in polymer structure.* Rudenko, A.E. and Thompson, B.C. 2015, J. Polym. Sci. Part A: Polym. Chem., , Vol. 53, p. 135-147. .
55. *Mixed-Ligand Approach to Palladium-Catalyzed Direct Arylation Polymerization: Effective Prevention of Structural Defects Using Diamines.* Eisuke Iizuka, Masayuki Wakioka, and Fumiyuki Ozawa. 9, 2016 , Macromolecules , Vol. 49, p. 3310-3317.

56. *Effect of the Nature and the Position of Defects on the Chiral Expression in Poly(3-alkylthiophene)s.* Lize Verheyen, Julien De Winter, Pascal Gerbaux, and Guy Koeckelberghs. 22, 2019, Macromolecules , Vol. 52 , p. 8587-8595.
57. *Mechanistic studies and optimisation of a Pd-catalysed direct arylation reaction using phosphine-free systems.* Kuwabara, Junpei and Sakai, Masaru and Zhang, Qiao and Kanbara, Takaki. 5, 2015, Org. Chem. Front., Vol. 2, p. 520-525.
58. *Updating and further expanding GSK's solvent sustainability guide.* Alder, Catherine M. and Hayler, John D. and Henderson, Richard K. and Redman, Anikó M. and Shukla, Lena and Shuster, Leanna E. and Sneddon, Helen F. 13, 2016, Green Chem., Vol. 18, p. 3879-3890.
59. *Suppressing Defect Formation Pathways in the Direct C–H Arylation Polymerization of Photovoltaic Copolymers.* Thomas J. Aldrich, Alexander S. Dudnik, Nicholas D. Eastham, Eric F. Manley, Lin X. Chen, Robert P. H. Chang, Ferdinand S. Melkonyan, Antonio Facchetti, and Tobin J. Marks. 22, 2018 , Macromolecules , Vol. 51, p. 9140-9155.
60. *Monodispersed vs. polydispersed systems for bulk heterojunction solar cells: the case of dithienopyrrole/anthracene based materials.* Grisorio, Roberto and Allegretta, Giovanni and Suranna, Gian Paolo and Mastrorilli, Piero and Loiudice, Anna and Rizzo, Aurora and Mazzeo, Marco and Gigli, Giuseppe. 37, 2012, J. Mater. Chem., Vol. 22, p. 19752-19760.
61. *Influence of Keto Groups on the Optical, Electronic, and Electroluminescent Properties of Random Fluorenone-Containing Poly(fluorenylene-vinylene)s.* Roberto Grisorio, Claudia Piliego, Marinella Striccoli, Pinalysa Cosma, Paola Fini, Giuseppe Gigli, Piero Mastrorilli, Gian Paolo Suranna, and Cosimo Francesco Nobile. 50, 2008, The Journal of Physical Chemistry C , Vol. 112, p. 20076-20087.
62. *A $Pd(AcO)_2$/t-Bu_3P/K_3PO_4 catalytic system for the control of Suzuki cross-coupling polymerisation.* Grisorio, R. and Mastrorilli, P. and Suranna, G. P. 14, 2014, Polym. Chem., Vol. 5, p. 4304-4310.
63. *Catalyst-transfer polymerization of arylamines by the Buchwald–Hartwig cross-coupling.* Grisorio, Roberto and Suranna, Gian Paolo. 15, 2019, Polym. Chem., Vol. 10, p. 1947-1955.
64. *Donor–Acceptor Polymer with Benzotriazole Moiety: Enhancing the Electrochromic Properties of the "Donor Unit".* Abidin Balan, Gorkem Gunbas, Asuman Durmus, and Levent Toppare. 24, 2008 , Chemistry of Materials, Vol. 20, , p. 7510-7513.
65. *A Selenium-Substituted Low-Bandgap Polymer with Versatile Photovoltaic Applications.* Dou, L., Chang, W.-H., Gao, J., Chen, C.-C., You, J. and Yang, Y. 2013, Adv. Mater., Vol. 25, p. 825-831.

4 Chapter 4

Direct arylation polymerizations under aerobic conditions in anisole

4.1 Motivation

Environmentally benign, non-hazardous, and low-cost solvents have been proposed for developing direct arylation polymerization (DArP) as an industrial-scale method for the preparation of conjugated polymers. Although the implementation of sustainable solvents from the safety, health and environment viewpoint (2-methyltetrahydrofuran, p-cymene and anisole) has been proposed and highlighted in this Dissertation, their compatibility with aerobic reaction conditions has remained thus far poorly explored.

In this Chapter, we investigated the viability of applying anisole in the preparation of poly(9,9-dioctylfluorene-2,2'-bithiophene) (PF8TT) under undried and aerobic conditions by employing the catalytic system consisting of $(PPh_3)_2PdCl_2$/P(o-Anisyl)$_3$/Cs_2CO_3 in the presence of pivalic acid as the proton transfer agent. The polymerization kinetics indicated in the catalyst rapid deactivation the main reason of the low molecular weights obtained for the resulting polymers. At the same time, we ascertained that our aerobic reaction conditions preclude an uncontrolled polymer growth via radicalic pathways and the incorporation of structural defects. Therefore, the optimization of the work-up protocol enables the obtainment of PF8TT endowed with high molecular weights (M_n = 15900 Da) under completely "green" conditions, thus consolidating the C–H activation route as a sustainable protocol for the construction of conjugated polymers. The same aerobic conditions were adopted for the copolymerization of differently structured units affording molecular weights up to 16500 Da, thus consolidating the C–H activation route as an eco-friendly protocol for the preparation of conjugated polymers. This chapter of the Dissertation contains data that have been published by: Carlucci, C., **Conelli, D.,** Hassan Omar, O., Margiotta, N., Grisorio, R., Suranna, G. Polym. Chem. 2023, 14, 343. http://dx.doi.org/10.1039/D2PY01214F

4.2 Introduction

An important environmental issue pertinent to the solvent regards the fact that, to efficiently perform Pd-catalysed DArP, oxygen- and moisture-free reaction conditions are strictly required to avoid decomposition of the catalytic active species and/or intermediates of the catalytic cycle. To ensure these conditions, the solvent must be dried by distillation prior to use and stored under an inert atmosphere. These energy-demanding steps aggravate the environmental concerns related to the conjugated polymers synthesis. However, the idea of employing commercially available reagent-grade solvents under aerobic conditions for conjugated polymers preparation has been thus far scarcely contemplated. [1] [2] [3]
Alternating copolymers containing bithiophene and fluorene are widely used as high-performance materials when used for manufacturing organic field-effect transistors. [4] [5] In order to bring significant benefits to the synthesis of materials for optoelectronic devices, we investigated innovative solutions to further improve the sustainability of the related synthetic protocol. In this study we selected 2,2'-bithiophene as the comonomer to be coupled with 2,7-dibromo-9,9-dioctylfluorene in DArP to synthesize the paradigmatic poly(9,9-dioctylfluorene-2,2'-bithiophene) (P1) choosing anisole as an eco-friendly solvent under aerobic conditions (Scheme 4.1.). We opted to revisit this polymerization in an ecological key to scrutinize the selectivity of DArP under aerobic conditions by involving the 2,2'-bithiophene unit devoid of orienting groups or steric protection in the polymerization. [6] In the course of our systematic study, we found that the catalytic system comprising $(PPh_3)_2PdCl_2$/P(o-Anisyl)$_3$/Cs_2CO_3 in the presence of pivalic acid (PivOH) as the proton transfer agent [7] was efficiently operative also in the presence of oxygen leading to P1 endowed with molecular weights up to 10200 Da and a regular structure. These first results, inspired us to conceive a broader polymer scope. With this aim, we decided to attempt the polymerization under the same aerobic conditions in anisole extending it to the copolymerization of thiophene-based units and the formulation of fluorene-based terpolymers,

thereby further consolidating the sustainability aspects of DArP protocols as an appealing alternative to commonly employed polymerization methods.

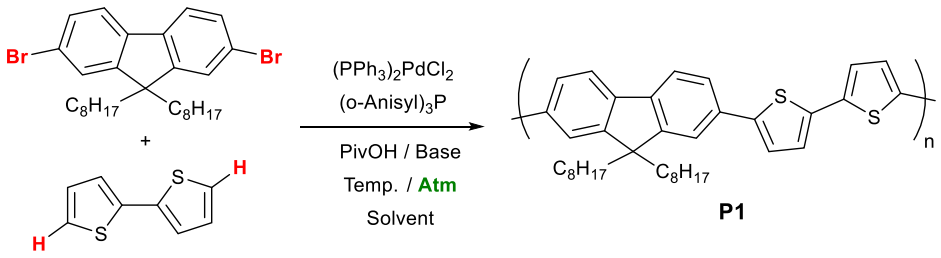

Scheme 4.1. Synthetic procedure adopted in this study for the obtainment of P1 by DArP.

4.3 Results and discussion

4.3.1 DArP conditions for the obtainment of P1

We performed a first experiment in order to evaluate the effects on the polymerization course when a commercially available reagent-grade solvent (toluene) was used without further purification. On the basis of the previous study discussed in Chapter 3, we selected the $(PPh_3)_2PdCl_2$/P(o-Anisyl)$_3$/Cs_2CO_3 catalytic system in the presence of PivOH as the proton transfer agent. [8] The mixture containing all the reagents was deaerated by three vacuum/pump cycles with nitrogen before reaching the chosen reaction temperature (110 °C) and the results of this reaction (Table 4.3., entry 2) were compared with those obtained by using conventional conditions (i.e., distilled solvent under the nitrogen protection) reported in Table 4.3. (entry 1, M_n = 11000 Da). We observed slightly lower molecular weights (M_n = 10700 Da) for the obtained P1, indicating that the presence of water and impurities traces in the solvent does not compromise the catalyst activity under the proposed conditions. This result is supported in the literature, in fact, aqueous palladium-catalysed direct arylation polymerization (DArP) has been previously reported. [9] [10] [11] Surprisingly, also the reaction carried out without deaerating the mixture (Table 4.3., entry 3) afforded very similar results

of entry 2 in terms of molecular weights (M_n = 10400 Da) and yields. Considering its oxidant nature, oxygen can in fact interfere with the normal $Pd^{(0)}/Pd^{(II)}$ catalytic cycle, promoting the oxidation of zero-valent palladium species or of their phosphorous-based ligands, thus reducing their overall catalytic activity. [12] We supposed that the comparability of the molecular weights observed under aerobic conditions (entry 2 vs entry 3) is due to the preserved catalyst performances, probably because the external oxygen to the reaction mixture is impeded to penetrate the solvent due to the higher relative vapor density of toluene (3.1 ×) with respect to air. These experiments allowed us to comprove that the gain in safety by implementing aerobic conditions without distilling the solvent for the polymerization of P1 can be achieved at the acceptable expense of the minimal loss in molecular weights and yields. To simultaneously preserve the health of the operators, we performed the reaction for the obtainment of P1 by adopting the same catalytic system in commercially available reagent-grade anisole used without further purification. First, the reaction was carried out under nitrogen protection (Table 4.3., entry 4), attesting slightly lower molecular weights (M_n = 9500 Da) with respect to those recorded in toluene under inert conditions. On the other hand, interesting results were obtained in anisole under air (Table 4.3., entry 5) being the corresponding P1 endowed with higher molecular weights (M_n = 10200 Da) and relatively narrow polydispersity (Đ = 1.3). Also in this case, the preservation of the polymerization course under aerobic conditions be explained by the high vapour tension of the solvent (3.7 × with respect to air), which keeps away the oxygen from the reaction medium. At the same time, the residual oxygen in the solvent can generate new and probably more performing catalytic species (because of the partial oxidation of the ligands, Figure 4.2.) in a weakly coordinating solvent (anisole). [13] To support this hypotesis, we performed a ^{31}P NMR analysis of P(o-Anisyl)$_3$ dispersed in anisole before and after a thermal treatment at 110 °C for 24 h in air in order to simulate the reaction conditions. The comparison clearly evidences the formation of a new species (the phosphine-oxide) immediately after the phosphine dissolution in

anisole under aerobic conditions. We supposed that the protection exerted by the anisole vapours against the oxygen dissolution in the solvent during the thermal treatment avoids the complete oxidation of the pristine ligand. This interpretation rationalizes the slightly higher molecular weights obtained under aerobic conditions in entry 5.

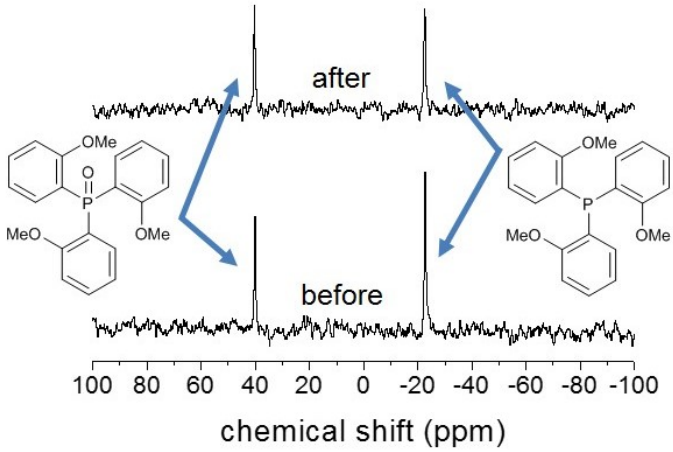

Figure 4.2. *^{31}P NMR spectra (recorded in $CDCl_3$) of P(o-Anisyl)$_3$ dispersed in anisole before and after a thermal treatment at 110 °C for 24 h in air.*

Table 4.3. *Reaction conditions adopted for the obtainment of P1 with the relevant molecular weights and yields*

Entry	Solvent	Base	Atm.	Temp. (°C)	M_n (Da)[a]	M_w (Da)[a]	Đ[a]	Yield (%)[b]
1[c]	Toluene	Cs_2CO_3	N_2	110	11000	15100	1.4	70
2	Toluene	Cs_2CO_3	N_2	110	10700	15200	1.4	68
3	Toluene	Cs_2CO_3	air	110	10400	16100	1.5	65
4	Anisole	Cs_2CO_3	N_2	110	9500	12800	1.4	61
5	Anisole	Cs_2CO_3	air	110	10200	13400	1.3	61
6	Anisole	Cs_2CO_3	air	130	5500	8100	1.5	44
7	Anisole	Na_2CO_3	air	110	–	–	–	–
8	Anisole	K_2CO_3	air	110	6000	8200	1.4	41
9	Anisole	K_3PO_4	air	110	6700	8900	1.3	51
10[d]	Anisole	Cs_2CO_3	air	110	5800	9700	1.7	30

Monomer concentrations = 0.2 M. Reaction time: 24 h. Undried solvents. [a]Number-average molecular weights (M_n), weight-average molecular weights (M_w) and dispersity (Đ = M_w/M_n) as determined by GPC (PS standards, THF). [b]Measured after the following isolation and purification stages: precipitation in methanol, Soxhlet washing with methanol, acetone and hexane, Soxhlet collection with chloroform and reprecipitation in methanol. [c]Carried out in distilled and dried solvent. [d]2,7-Diiodo-9,9-dioctylfluorene as the comonomer.

The formation of cross-linked materials via radical pathways potentially activable due to the presence of oxygen for the reactions carried out in air was excluded ascertaining the absence of an insoluble organic portion in the filter after the Soxhlet extraction with chloroform. [(14)] To achieve P1 under aerobic conditions in anisole, we also explored different palladium precursors (Table 4.4.) without recording an improvement of the relevant molecular weights.

Table 4.4. *Molecular weights and yield of P1 synthesized by using different palladium precatalysts.*

Entry	Palladium source	Yield (%)[a]	M_n (Da)[b]	M_w (Da)[b]	Đ[b]
1	Pd_2dba_3	42	4500	6800	1.5
2	$Pd(AcO)_2$	58	5100	7000	1.4
3	$Pd(PivO)_2$	53	5000	7900	1.6

[a]Measured after polymer precipitation in methanol, Soxhlet washing with methanol, acetone and hexane, Soxhlet extraction with chloroform, and reprecipitation in methanol. [b]Number-average molecular weights (M_n), weight-average molecular weights (M_w) and dispersity (Đ) as determined by GPC (PS standards, THF).

Based on these considerations, we attempted to improve the polymerization course by carrying out the reaction at 130 °C (Table 4.3., entry 6). However, at this temperature, other side reactions, such as debromination, are feasible, thus drastically reducing the molecular weights (M_n = 5500 Da) of the corresponding polymer. In parallel, we proceeded with refining the polymerization conditions by varying the base, which has an influence in regulating the PivOH/$PivO^-$ equilibria indispensable for the catalytic cycle. The chosen bases (i.e., Na_2CO_3, K_2CO_3 and K_3PO_4) did not improve the polymerization course (Table 4.3., entries 7-9) with the best results in terms of molecular weights (M_n = 6700 Da) obtained in the case of K_3PO_4 as the base. Aiming at accelerating the oxidative addition step of the catalytic cycle, we proceeded with the introduction of iodide leaving groups onto the fluorene-based monomer. In this case (Table 4.3., entry 10), however, both the yield and the molecular weights were remarkably lower compared to those recorded in entry 5, suggesting the instability of the aryl comonomer under aerobic conditions. To gain insight into the polymerization behavior, the kinetics of entry 5 were evaluated by monitoring the temporal evolution of the molecular weights of the forming macromolecules (Fig. 4.5.). By sampling small aliquots of the reactions at regular intervals of time, we observed that the molecular weights of the product precipitated in methanol increased over a period of ~210 minutes and subsequently remained unvaried until the end of the reaction (after 24 h).

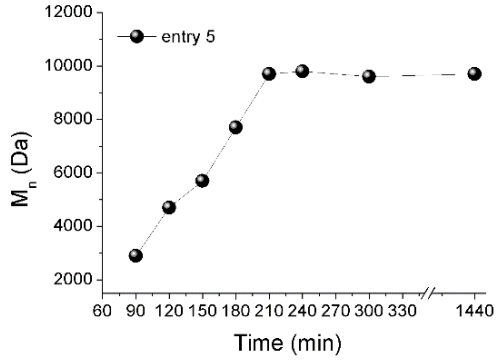

Figure 4.5. *Evolution of the molecular weights of the forming polymer P1 in entry 5.*

Also the yield (63%) of the reaction stopped after 210 minutes resulted to be comparable to that recorded after 24 h. Differently from what observed by Leclerc and coworkers, [15] this outcome suggests that the catalyst remained active only over a short period of time. Furthermore, no further increase of the molecular weights or cross-linked side products were observed during the reaction, likely due to the relatively low reaction temperatures (110 °C) insufficient to trigger a radical pathway. Another interpretation of the kinetics reported in Fig. 4.5. can be proposed taking into account the solubility of the forming polymer during its growth in a relatively polar ethereal solvent (anisole).

4.3.2 Spectroscopic characterization of P1

We investigated the compatibility of anisole with this challenging polymerization under aerobic conditions by NMR spectroscopy. The ^{1}H-NMR spectrum of entry 5 in $C_2D_2Cl_4$ at 70 °C (Fig. 4.6. and Fig. 4.17.) highlights a regular comonomer alternation for P1 synthesized under our aerobic conditions, [16] [17] as found from the integrals ratio between the β-protons signal of the 2,2′-bithiophene unit (7.50÷7.30 ppm) and the α-protons signal of the fluorene octyl chains (2.20÷2.00 ppm). Moreover, we excluded the incorporation of β-defects embedded in the

polymer structure, as also supported by the absence of insoluble materials as mentioned above.

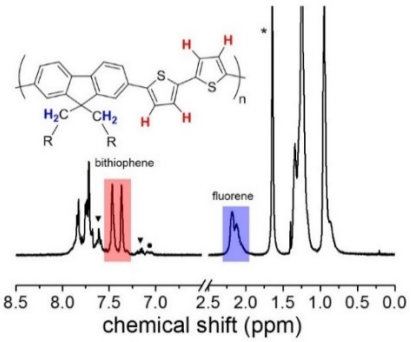

Figure 4.6. *^{1}H NMR spectrum of P1 (entry 5) recorded in $C_2D_2Cl_4$ at 70 °C. (*) Water traces. Signal attributable to the bromo-fluorene (▼) and bithiophene (●) terminating chain.*

Moreover, the ^{1}H-NMR spectrum evidenced also the presence of signals (properly marked in Figure 4.6.) ascribable to the bromo-terminating fluorene units. [18] [19] [20] This peculiar chain termination suggests that the polymer growth is not interrupted by side reactions typical of the catalytic cycle (i.e., reductive dehalogenation or hydroxylation), [10] thus corroborating the feasibility of the proposed reaction conditions. Conversely, it is reasonable to suppose that the catalyst deactivation (due to the aerobic conditions) and/or the scarce solubility of the forming P1 in anisole concurred in limiting the resulting molecular weights, which can be considered respectable but below the state of the art for this class of polymer. Although it is reasonable to predict that further efforts could improve the molecular weights of P1, the current results provide a significant piece of evidence that anisole can represent an eco-friendly solvent for DArP under aerobic and undried conditions. [21]

4.3.3 DArP conditions for the obtainment of the terpolymers

With the aim to broaden the monomers scope, we introduced appropriate di-bromo-aryl comonomers for the formulation of terpolymers structurally analogous to P1 in the same reaction conditions adopted in entry 5 of Table 4.3. As reported in Scheme 4.8., we reduced the fluorene-based units at the 25% of the

monomer feed ratio, while an equimolar amount of phenothiazine-, dioctyloxybenzene- or benzotriazole-based structures was introduced to achieve the right balance with the 2,2′-bithiophene comonomer for the obtainment of the terpolymers P2-P4, respectively. As shown in Table 4.9., these terpolymers were obtained with relatively low molecular weights (M_n = 3700÷5600 Da) despite their unexpected higher yields (63÷88%) with respect to those recorded in entry 5 of Table 4.3. We suspect that this consequence can mainly be attributed to the scarce solubility of the resulting terpolymers (due to the lower portion of the orthogonal octyl chains of the fluorene-based comonomer), which hampered the removal of the short segments during the Soxhlet washing with acetone and hexane.

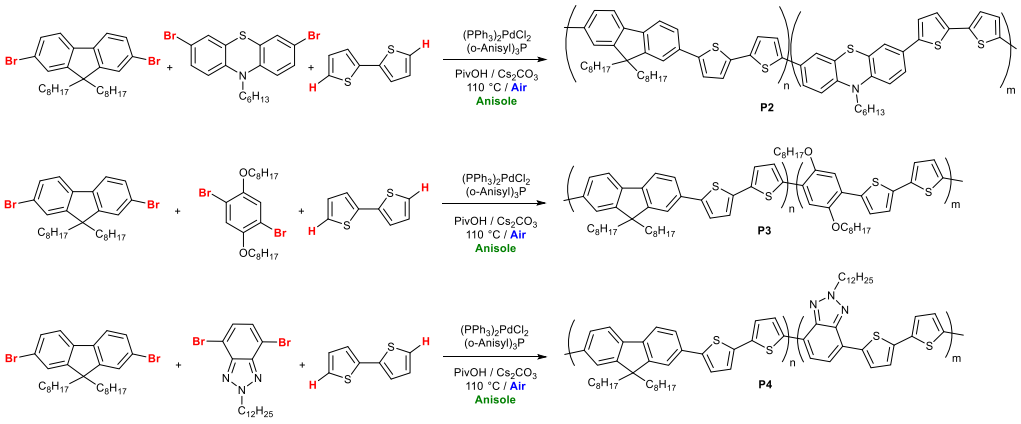

Scheme 4.8. *Synthetic sequence for the obtainment of the terpolymers P2-P4 (n = m).*

Table 4.9. *Molecular weights and yields of P2-P4.*

Polymer	M_n (Da)[a]	M_w (Da)[a]	Đ[a]	Yield (%)[b]
P2	5600	7300	1.3	88
P3	4500	7000	1.5	72
P4	3700	4700	1.3	63

Monomer concentrations = 0.2 M. Reaction time: 24 h. [a]Number-average molecular weights (M_n), weight-average molecular weights (M_w) and dispersity (Đ) as determined by GPC (PS standards, THF). [b]Measured after polymer precipitation in methanol, Soxhlet washing with methanol, acetone and hexane, Soxhlet extraction with chloroform, and reprecipitation in methanol.

4.3.4 Spectroscopic characterization of terpolymers (P2-P4)

The introduction of the chosen aryl units into the polymer backbone was confirmed by ^{1}H-NMR investigations evidencing the diagnostic $–C_\alpha H_2–$ signals of the corresponding alkyl chains (Figure 4.10. and Figure 4.19.-4.21.). Being their integrals as expected in comparison with the fluorene-based units, we can deduce that the reactivity of the three comonomers under the proposed reaction conditions is independent of their electron-donating (phenothiazine) or –withdrawing (benzotriazole) character as well as of the steric hindrance caused by the ortho-groups (dioctyloxybenzene).

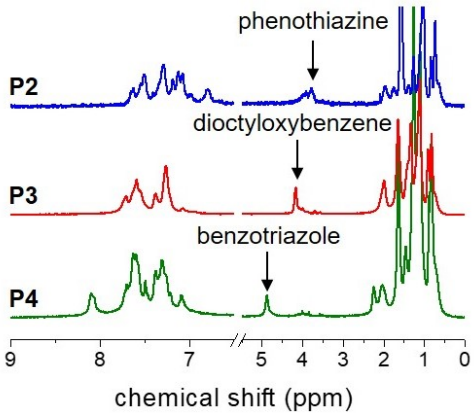

Figure 4.10. *^{1}H NMR spectra of **P2-P4** recorded in $C_2D_2Cl_4$ at room temperature evidencing the diagnostic $–C_\alpha H_2–$ signals of the alkyl chains belonging to the third comonomer.*

We found also that the composition of the terpolymers had a strong influence on their absorption properties, as shown in Figure 4.11. The UV-vis spectrum of P1 exhibited an absorption maximum peaked at 441 nm in chloroform, the profile of which was very similar to that of P2 (λ_{max} = 442 nm), being the phenothiazine units structurally similar to the fluorene ones. Conversely, the introduction of the dioctyloxybenzene units induced a remarkable red-shift of the absorption maximum in P3 (λ_{max} = 456 nm), notwithstanding the plausible backbone distortion caused by the ortho-groups. More evident was the red-shift observed for P4 (λ_{max} = 481 nm) with respect to P1, owing to the donor-acceptor character of this polymer backbone. Importantly, all the polymers exhibited good film forming capability, notwithstanding their relatively low molecular weights. The optical characterization of P1 was completed by recording its emission spectrum in chloroform (Figure 4.18), evidencing the typical vibronic replica of defect-free polymer backbones.

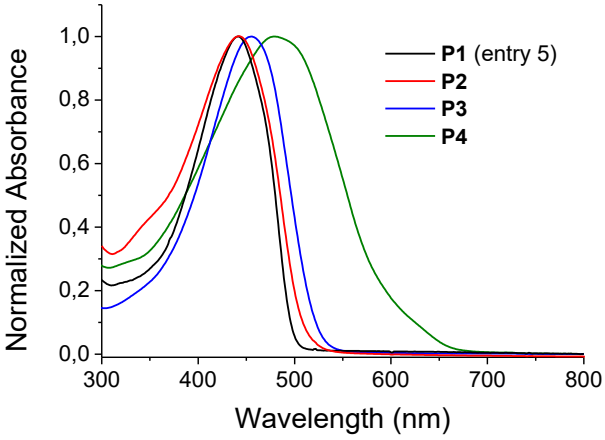

Figure 4.11. *UV-vis spectra of P1-P4 recorded in chloroform.*

4.3.5 DArP conditions for the obtainment of copolymers

To exploit the actual potential of the proposed synthetic protocols, we designed copolymers with a prospected higher solubility in the reaction medium by introducing thiophene or 3-methyl-thiophene as the comonomers for the C–H activation pathway, to achieve the copolymers P5 and P6, respectively (Scheme 4.12.). Analogously to 2,2'-bithiophene, also these comonomers can be considered challenging to be implemented in DArP due to the absence of directing functional groups onto the aryl systems. As a matter of fact, we obtained higher polymerization degrees for these two reactions, leading to molecular weights up to 16500 Da in the case of P6 (Table 4.13.). Probably, the lower molecular weights recorded for P5 (M_n = 10100 Da) were caused by the relatively lower boiling point of thiophene with respect to 3-methyl-thiophene, that can lead to a nonperfect equimolar monomers concentration during the polymerization course carried out at 110 °C. Remarkably, this behaviour was ascertained despite the presence of the methyl group in the α-position of the thiophene ring, which reduced its reactivity due to steric hindrance (Figures 4.22-4.23.). [22]

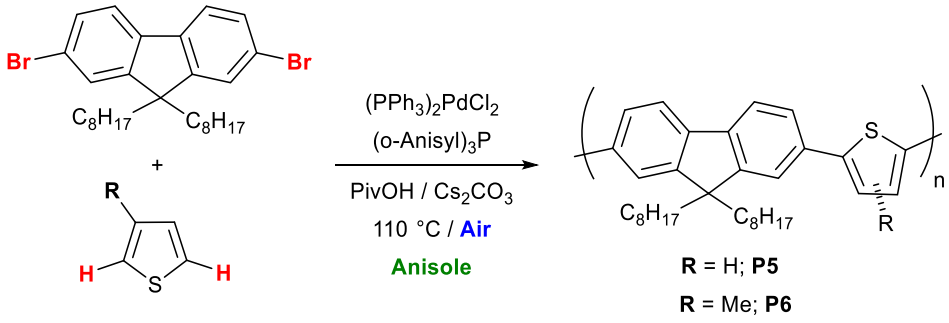

Scheme 4.12. *Synthetic procedure for the obtainment of P5 and P6.*

Table 4.13. *Molecular weights and yields of P5-P8.*

Polymer	M_n (Da)[a]	M_w (Da)[a]	Đ[a]	Yield (%)[b]
P5	10100	13800	1.4	68
P6	16500	26500	1.6	65
P7	–	–	–	84
P8[c]	11200	14100	1.3	76

Monomer concentrations = 0.2 M. Reaction time: 24 h. [a]Number-average molecular weights (M_n), weight-average molecular weights (M_w) and dispersity (Đ) as determined by GPC (PS standards, THF). [b]Measured after polymer precipitation in methanol, Soxhlet was washing with methanol, acetone and hexane, Soxhlet collection with chloroform, and reprecipitation in methanol. [c]Washed with hot methanol, ethanol, acetone, and hexane.

In a further set of experiments we utilized the 4,7-di(thiophen-2-yl)benzothiadiazole comonomer for the preparation of the corresponding copolymer P7 under the same reaction conditions (Scheme 4.14.). This design strategy aiming at producing conjugated polymers with potential applications in solar cells. However, although a red material (the colour is indicative of the effectively occurring polymerization) was obtained in high yields (84%, Table 4.13.), after the reaction, the polymer resulted to be insoluble even in boiling chloroform, precluding its complete characterization. Probably, the high polymerization degree and absence of solubilizing alkyl chains in the benzothiadiazole-based comonomer led to insoluble macromolecules. To overcome this inconvenience, we opted for polymerizing the 5,6-bis(octyloxy)-4,7-di(thiophen-2-yl)benzothiadiazole unit endowed with long alkyl chains for warranting the solubility to the corresponding macromolecule. As shown in Table 4.13., the copolymer P8 was obtained in good yields (76%) with relatively high molecular weights (M_n = 11200 Da).

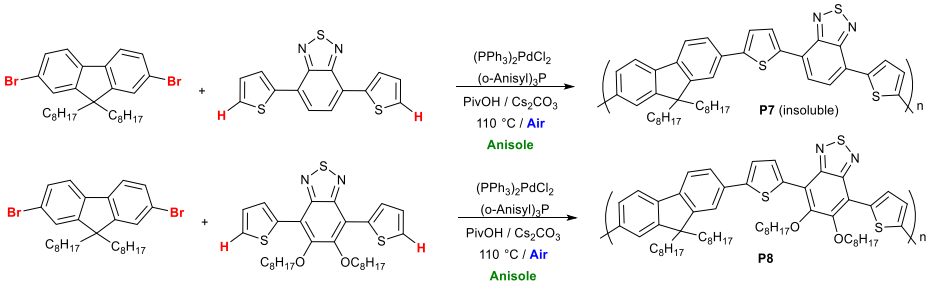

Scheme 4.14. *Synthetic sequence for the obtainment of the terpolymers P7 and P8.*

4.3.6 Spectroscopic characterization of copolymers (P5-P8)

As next step, we gained insight into the optical properties of the two thiophene-based copolymers (P5 and P6) comparing them with those of P1 (Figure 4.15.). It can be observed that the introduction of the thiophene units within the polymer backbones induced a remarkable blue-shift of their absorption maxima that are peaked at 421 nm and 388 nm for P5 and P6, respectively. This result provided an indication that the orbital overlap of the π-systems along the polymer backbone influenced the optical properties of the corresponding macromolecules. The presence of the methyl group onto the α-position of thiophene ring caused a distortion of the polymer backbone for steric reasons, which induced a further blue-shift of the absorption maximum in P6.

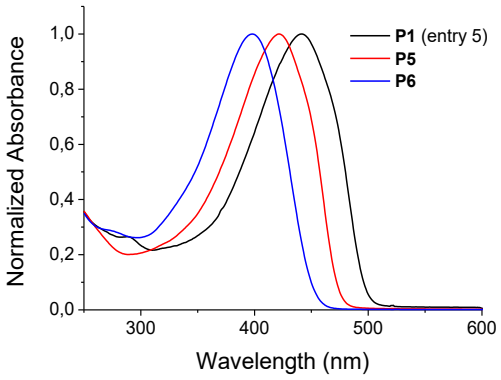

Figure 4.15. *UV-vis spectra of P5 and P6 recorded in chloroform in comparison with P1 (entry 5).*

In the case of P8, the introduction of the donor-acceptor unit was confirmed by ^{1}H-NMR investigations with the presence of the diagnostic signal at 4.20 ppm typical of the $–C_{\alpha}H_2–$ alkoxy chains (Figure 4.16.A. and Figure 4.24.). Also, the optical properties of P8 (λ_{max} = 495 nm, Fig. 4.14.B.) confirmed the generation of a regular polymer backbone, thus corroborating the compatibility of the proposed monomers with the reaction conditions of this synthetic protocol.

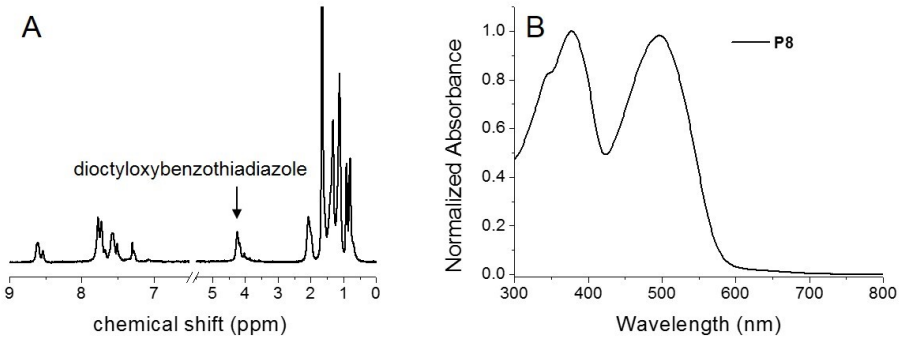

***Figure 4.16**. (A) ^{1}H-NMR spectrum of P8 recorded in $C_2D_2Cl_4$ evidencing the diagnostic –$C_\alpha H_2$– signals of the alkyl chains belonging to the comonomer. (B) UV-vis spectrum of the same polymer in chloroform.*

4.4 Conclusions

In this Chapter was investigated a further improve regarding the application of a non toxic ethereal solvent (anisole) for the preparation of poly(9,9-dioctylfluorene-2,2'-bithiophene) (P1) under undried and aerobic conditions by employing the catalytic system composed of $(PPh_3)_2PdCl_2$/P(o-Anisyl)$_3$/Cs_2CO_3 in the presence of pivalic acid as the proton transfer agent. By analysing the polymerization kinetics, we explained the relatively low molecular weights of the resulting polymers (M_n = 10200 Da) with the rapid quenching of the chain growth, probably due to the incompatibility of the polymer composition with the reaction medium. At the same time, we excluded the activation of radical pathways leading to an uncontrolled growth of the macromolecules under aerobic conditions, even by prolonging the reaction time. The same aerobic conditions can be adopted for the copolymerization of differently structured units with satisfactory results in terms of molecular weights (up to 16500 Da) of the resulting materials, especially in the case of intrinsically more soluble polymers. Therefore, this study further consolidates our observations about the sustainability aspects of DArP as an appealing alternative to commonly employed polymerization methods.

4.5 Experimental section

All reagents and solvents were purchased from standard commercial sources and used as received. The syntheses were carried out under inert nitrogen atmosphere using standard Schlenk techniques. ^{1}H-NMR spectra were recorded on an Agilent 500/54 Premium Shielded spectrometer and a Varian Mercury 300 spectrometer. ^{1}H chemical shifts were referenced using the internal residual peak of the solvent ($C_2D_2Cl_4$: 5.92 ppm; $CDCl_3$: 7.27 ppm). ^{31}P NMR spectra were recorded on a Bruker Avance DPX 300 MHz instrument. ^{31}P chemical shifts were referenced to external H_3PO_4 (85% w/w; 0 ppm). Gel Permeation Chromatography (GPC) analyses were performed with an Agilent Series 1100 instrument equipped with a Pl-gel 5 µm mixed-C column. The samples were dissolved in chloroform, eluted in THF at a 1.0 mL/min flow rate, and analysed using a multiple wave UV-Vis detector. Number average molecular weights (M_n), weight-average molecular weights (M_w) and polydispersity indexes (Đ) were calculated against polystyrene standards. UV–vis absorption spectra were collected using a Jasco V670 spectrometer operating in transmission mode. Steady-state photoluminescence (PL) spectra were acquired on a Varian Cary Eclipse instrument.

4.6 Synthesis of P1

A mixture of 2,7-dibromo-9,9-dioctylfluorene (0.220 g, 0.40 mmol), 2,2'-bithiophene (0.066 g, 0.40 mmol), $(PPh_3)_2PdCl_2$ (11.2 mg, 1.6×10^{-2} mmol), P(o-Anisyl)$_3$ (11.3 mg, 3.2×10^{-2} mmol), pivalic acid (0.040 g, 0.40 mmol), base (1.28 mmol), and anisole (2.0 mL) was charged in a 25 mL Schlenk tube capped with a rubber septum and stirred at 110 °C for 24 hours. The reaction mixture was then cooled to room temperature and poured into MeOH (150 mL) under vigorous stirring for the precipitation of the polymer. The precipitate was collected by filtration and washed in a Soxhlet apparatus with methanol and with chloroform. The chloroform fraction was reduced to 2 mL and precipitated in methanol. ^{1}H-NMR (500

MHz, $C_2D_4Cl_2$, 70 °C): δ 7.90-7.78 (m, 2H), 7.70-7.67 (m, 4H), 7.41-7.31 (m, 4H), 2.13 (s, 4H, br), 1.30-0.90 (m, 20H), 0.80-0.60 (m, 10H) ppm.

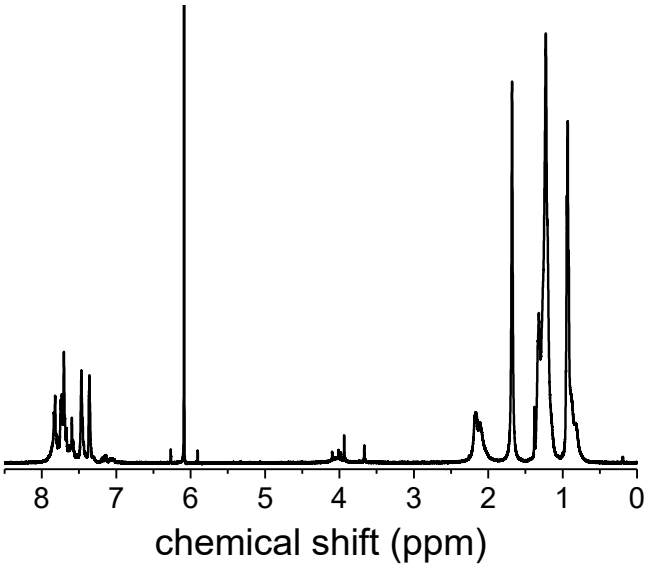

Figure 4.17. *^{1}H NMR spectrum of P1 (entry 5) recorded in $C_2D_2Cl_4$.*

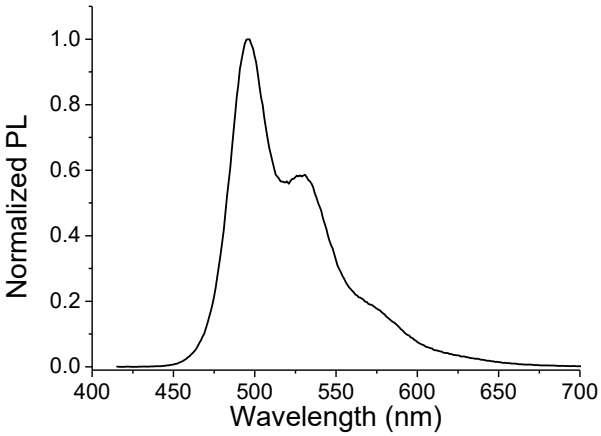

Figure 4.18. *PL spectrum of P1 recorded in chloroform.*

4.7 Synthesis of P2-P4

A mixture of 2,7-dibromo-9,9-dioctylfluorene (0.110 g, 0.20 mmol), 2,2′-bithiophene (0.066 g, 0.40 mmol), 3,7-dibromo-10-hexyl-10H-phenothiazine (0.088 g, 0.20 mmol for **P2**), 1,4-dibromo-2,5-bis(octyloxy)benzene (0.098 g, 0.20 mmol for **P3**) or 4,7-dibromo-2-dodecyl-2H-benzo[d][1,2,3]triazole (0.089 g, 0.20 mmol for **P4**), $(PPh_3)_2PdCl_2$ (11.2 mg, 1.6×10^{-2} mmol), P(o-Anisyl)$_3$ (11.3 mg, 3.2×10^{-2} mmol), pivalic acid (0.040 g, 0.40 mmol), Cs_2CO_3 (0.416 g, 1.28 mmol), and anisole (2.0 mL) was charged in a 25 mL Schlenk tube capped with a rubber septum and stirred at 110 °C for 24 hours. The reaction mixture was then cooled to room temperature and poured into MeOH (150 mL) under vigorous stirring for the precipitation of the polymer. The precipitate was collected by filtration and washed in a Soxhlet apparatus with methanol, acetone, hexane and then with chloroform. The chloroform fraction was reduced to 2 mL and precipitated in methanol. **P2** as a red solid; ^{1}H-NMR (300 MHz, $C_2D_4Cl_2$): δ 7.68-7.43 (m, 6H), 7.41-7.23 (m, 6H), 7.18-6.94 (m, 6H), 6.86-6.73 (m, 2H), 3.77 (br, 2H), 1.97 (br, 2H), 1.31-1.21 (m, 4H), 1.15-0.91 (m, 20H), 0.83-0.73 (m, 9H) ppm.

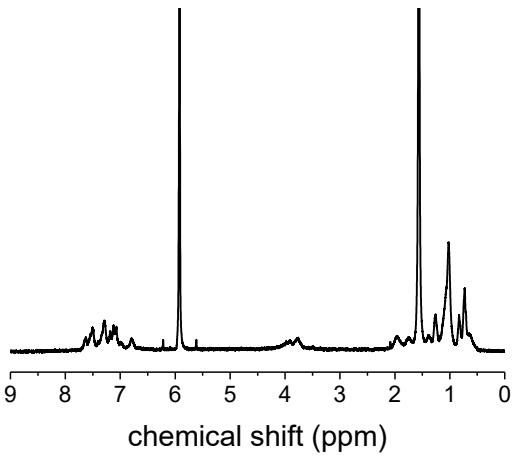

Figure 4.19. *^{1}H NMR spectrum of P2 recorded in $C_2D_2Cl_4$.*

P3 as a red solid; ^{1}H-NMR (300 MHz, $C_2D_4Cl_2$): δ 7.76-7.48 (m, 8H), 7.41-7.19 (m, 8H), 4.16 (br, 4H), 2.20-1.88 (m, 8H), 1.75-1.52 (m, 20H), 1.20-1.00 (m, 20H), 0.93-0.63 (m, 16H) ppm.

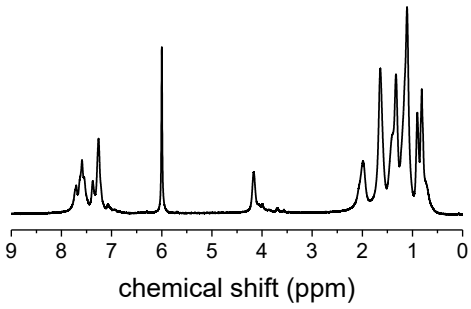

Figure 4.20. *^{1}H NMR spectrum of P3 recorded in $C_2D_2Cl_4$.*

P4 as a purple solid; ^{1}H-NMR (300 MHz, $C_2D_4Cl_2$): δ 8.13-8.05 (m, 2H), 7.80-7.45 (m, 8H), 7.41-7.00 (m, 6H), 4.88 (br, 2H), 2.14-1.90 (m, 10H), 1.78-1.52 (m, 20H), 0.91-0.76 (m, 27H) ppm.

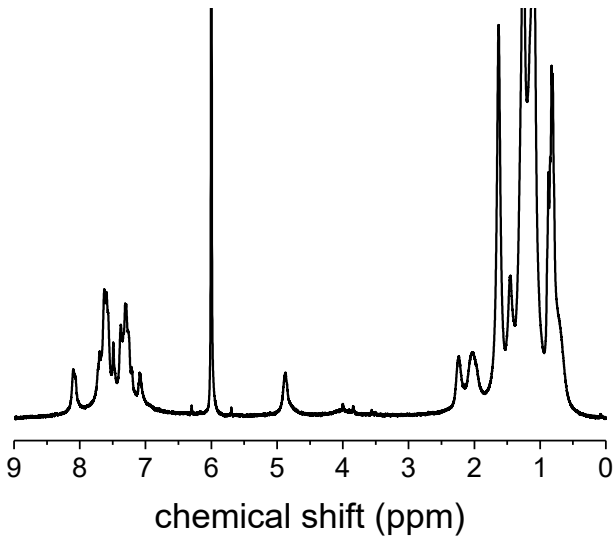

Figure 4.21. *^{1}H NMR spectrum of P4 recorded in $C_2D_2Cl_4$.*

4.8 Synthesis of P5-P6

A mixture of 2,7-dibromo-9,9-dioctylfluorene (0.40 mmol), thiophene or 3-methylthiophene (0.40 mmol), $(PPh_3)_2PdCl_2$ (0.016 mmol), P(o-Anisyl)$_3$ (0.032 mmol), pivalic acid (0.40 mmol), Cs_2CO_3 (0.416 g, 1.28 mmol), and anisole (2.0 mL) was charged in a 25 mL Schlenk tube capped with a rubber septum and stirred at 110 °C for 24 hours. The reaction mixture was then cooled to room temperature and poured into MeOH (150 mL) under vigorous stirring for the precipitation of the polymer. The precipitate was collected by filtration and washed in a Soxhlet apparatus with methanol, acetone, hexane and then with chloroform. The chloroform fraction was reduced to 2 mL and precipitated in methanol.

P5 as a light-yellow solid; ^{1}H-NMR (500 MHz, $CDCl_3$): δ 7.80-7.55 (m, 6H), 7.41 (s, 1H), 7.34 (s, 1H), 2.07 (s, 4H, br), 1.30-0.90 (m, 20H), 0.80-0.60 (m, 10H) ppm.

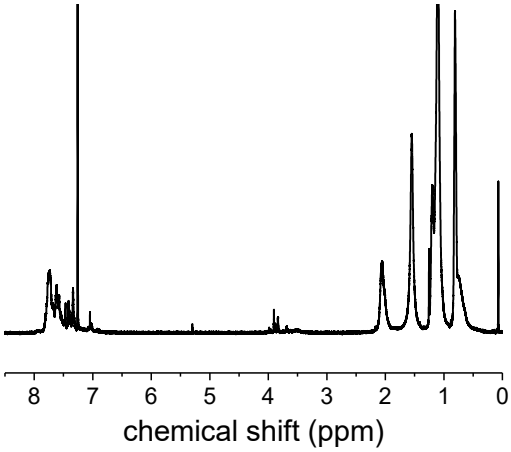

Figure 4.22. *^{1}H NMR spectrum of P5 recorded in $CDCl_3$.*

P6 as a light-yellow solid; ^{1}H-NMR (500 MHz, $CDCl_3$): δ 7.85-7.30 (m, 7H), 2.44-2.41 (m, 3H), 2.08 (s, 4H, br), 1.30-0.90 (m, 20H), 0.80-0.60 (m, 10H) ppm.

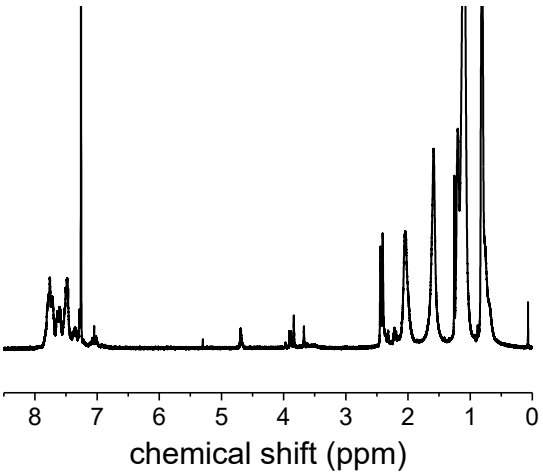

Figure 4.23. *^{1}H NMR spectrum of P6 recorded in $CDCl_3$.*

4.9 Synthesis of P8

A mixture of 2,7-dibromo-9,9-dioctylfluorene (0.105 g, 0.20 mmol), 5,6-bis(octyloxy)-4,7-di(thiophen-2-yl)benzo[c][1,2,5]thiadiazole (0.111 g, 0.20 mmol), $(PPh_3)_2PdCl_2$ (5.6 mg, 8.0×10^{-3} mmol), P(o-Anisyl)$_3$ (5.6 mg, 1.6×10^{-2} mmol), pivalic acid (0.020 g, 0.20 mmol), Cs_2CO_3 (0.208 g, 0.64 mmol), and anisole (1.0 mL) was charged in a 25 mL Schlenk tube capped with a rubber septum and stirred at 110 °C for 24 hours. The reaction mixture was then cooled to room temperature and poured into MeOH (150 mL) under vigorous stirring for the precipitation of the polymer. The precipitate was collected by centrifugation and washed with warm methanol, ethanol, acetone, and hexane to remove impurities, and then dissolved in chloroform before precipitation in methanol, to achieve a purple solid; ^{1}H-NMR (300 MHz, $C_2D_4Cl_2$): δ 8.60-8.53 (m, 2H), 7.77-7.67 (m, 4H), 7.57-7.27 (m, 4H), 4.24-4.14 (m, 4H), 2.06 (s, 8H, br), 1.32-1.12 (m, 40H), 0.91-0.80 (m, 16H) ppm.

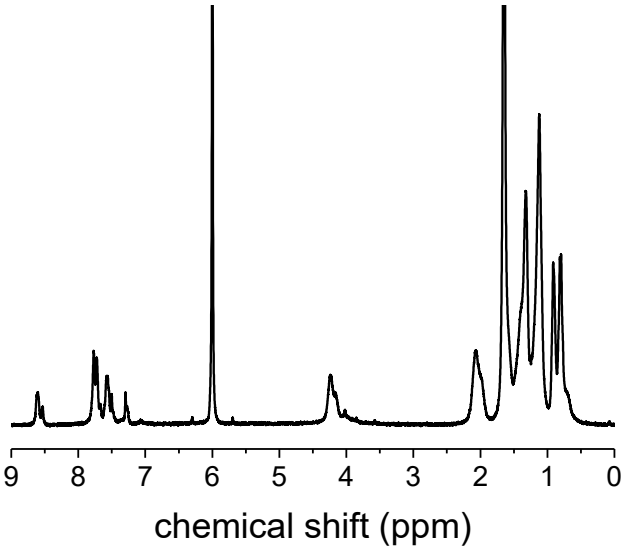

Figure 4.24. ^{1}H NMR spectrum of P8 recorded in $C_2D_2Cl_4$.

4.10 References

1. *Advances in applying C–H functionalization and naturally sourced building blocks in organic semiconductor synthesis.* Xing, Liwen and Luscombe, Christine K. 46, 2021, J. Mater. Chem. C, Vol. 9, p. 16391-16409.

2. *A General and Air-tolerant Strategy to Conjugated Polymers within Seconds under Palladium(I) Dimer Catalysis.* Magnin G, Clifton J, Schoenebeck F. 30, 2019, Angew Chem Int Ed Engl, Vol. 58, p. 10179-10183.

3. *Air-tolerant poly(3-hexylthiophene) synthesis via catalyst-transfer polymerization.* Kubo, T, Young, MS, Souther, KD, Hannigan, MD, McNeil, AJ. 2021, J Polym Sci. , Vol. 59 , p. 268– 273.

4. *High-Resolution Inkjet Printing of All-Polymer Transistor Circuits. .* Sirringhaus, H., Kawase, T., Friend, R.H., Shimoda, T., Inbasekaran, M., Wu, W. and Woo, E.P. 2000, Science, Vol. 290, p. 2123-2126.

5. *Self-aligned, vertical-channel, polymer field-effect transistors.* Stutzmann N, Friend RH, Sirringhaus H. 5614, 2003 , Science, Vol. 299, p. 1881-1884.

6. *Synthesis of Thiophene- and Bithiophene-Based Alternating Copolymers via Pd-Catalyzed Direct C–H Arylation.* Yohei Fujinami, Junpei Kuwabara, Wei Lu, Hideki Hayashi, and Takaki Kanbara. 1, 2012 , ACS Macro Letters , Vol. 1, p. 67-70.

7. *A Highly Efficient Catalytic System for Polycondensation of 2,7-Dibromo-9,9-dioctylfluorene and 1,2,4,5-Tetrafluorobenzene via Direct Arylation.* Masayuki Wakioka, Yutaro Kitano, and Fumiyuki Ozawa. 2, 2013, Macromolecules , Vol. 46, , p. 370-374.

8. *Implementation of Sustainable Solvents in Green Polymerization Approaches.* Conelli, D., Margiotta, N., Grisorio, R., Suranna, G. P.,. 2021, Macromol. Chem. Phys., Vol. 222, p. 2000382.

9. *In-water" direct arylation polymerization (DArP) under aerobic emulsion conditions.* Ye, Liwei and Hooshmand, Tanin and Thompson, Barry C. 46, 2021, Polym. Chem., Vol. 12, p. 6688-6693.

10. *Synthesis of Conjugated Polymers by Sustainable Suzuki Polycondensation in Water and under Aerobic Conditions.* Alessandro Sanzone, Adiel Calascibetta, Mauro Monti, Sara Mattiello, Mauro Sassi, Francesca Corsini, Gianmarco Griffini, Michael Sommer, and Luca Beverina. 8, 2020 , ACS Macro Letters , Vol. 9 , p. 1167-1171.

11. *Aqueous Palladium-Catalyzed Direct Arylation Polymerization of 2-Bromothiophene Derivatives.* Lin YJ, Sun HS, Yang HR, Lai YY, Hou KY, Liu YH. 9, 2020, Macromol Rapid Commun, Vol. 41, p. e2000021.

12. *Are Phosphines Viable Ligands for Pd-Catalyzed Aerobic Oxidation Reactions? Contrasting Insights from a Survey of Six Reactions.* Stephen J. Tereniak, Clark R. Landis, and Shannon S. Stahl. 4, 2018 , ACS Catalysis , Vol. 8 , p. 3708-3714.

13. *Mixed Phosphine−Phosphine Oxide Ligands.* Grushin, Vladimir V. 3, 2004 , Chemical Reviews, Vol. 104, p. 1629-1662.

14. *Enhancement of Photostability through Side Chain Tuning in Dioxythiophene-Based Conjugated Polymers.* D. Eric Shen, Augustus W. Lang, Graham S. Collier, Anna M. Österholm, Evan M. Smith, Aimée L. Tomlinson, and John R. Reynolds. 3, 2022, Chemistry of Materials , Vol. 34 , p. 1041-1051.

15. *Conjugated Polymers à la Carte from Time-Controlled Direct (Hetero)Arylation Polymerization.* Pierre-Olivier Morin, Thomas Bura, Bin Sun, Serge I. Gorelsky, Yuning Li, and Mario Leclerc. 1, 2015 , ACS Macro Letters, Vol. 4 , p. 21-24.

16. *Homocoupling defects in diketopyrrolopyrrole-based copolymers and their effect on photovoltaic performance. .* Hendriks KH, Li W, Heintges GH, van Pruissen GW, Wienk MM, Janssen RA. 31, 2014, J Am Chem Soc. , Vol. 136, p. 11128-11133.

17. *Identifying Homocouplings as Critical Side Reactions in Direct Arylation Polycondensation.* Florian Lombeck, Hartmut Komber, Serge I. Gorelsky, and Michael Sommer. 8, 2014, ACS Macro Letters , Vol. 3, p. 819-823.

18. *Grignard Metathesis Chain-Growth Polymerization for Polyfluorenes.* Li Huang, Shupeng Wu, Yao Qu, Yanhou Geng, and Fosong Wang. 22, 2008 , Macromolecules , Vol. 41 , p. 8944-8947.

19. *Impact of Precatalyst Activation on Suzuki-Miyaura Catalyst-Transfer Polymerizations: New Mechanistic Scenarios for Pre-transmetalation Events.* Suranna, Roberto Grisorio and Gian Paolo. 11, 2017, ACS Macro Letters , Vol. 6 , p. 1251-1256.

20. *Catalyst-transfer polymerization of arylamines by the Buchwald–Hartwig cross-coupling.* Grisorio, Roberto and Suranna, Gian Paolo. 15, 2019, Polym. Chem., Vol. 10, p. 1947-1955.
21. *Updating and further expanding GSK{'}s solvent sustainability guide.* Alder, Catherine M. and Hayler, John D. and Henderson, Richard K. and Redman, Anikó M. and Shukla, Lena and Shuster, Leanna E. and Sneddon, Helen F. 13, 2016, Green Chem., Vol. 18, p. 3879-3890.
22. *All-Conjugated, All-Crystalline Donor–Acceptor Block Copolymers P3HT-b-PNDIT2 via Direct Arylation Polycondensation.* Fritz Nübling, Hartmut Komber, and Michael Sommer. 5, 2017 , Macromolecules, Vol. 50 , p. 1909-1918.
23. *Unconventional Ethereal Solvents in Organic Chemistry: A Perspective on Applications of 2-Methyltetrahydrofuran, Cyclopentyl Methyl Ether, and 4-Methyltetrahydropyran.* Rachel Bijoy, Pratibha Agarwala, Lisa Roy, and Bhaskar N. Thorat. 3, 2022 , Organic Process Research & Development , Vol. 26, p. 480-492.
24. *Cyclopentyl Methyl Ether as a New and Alternative Process Solvent.* Kiyoshi Watanabe, Noriyuki Yamagiwa, and Yasuhiro Torisawa. 2, 2007 , Organic Process Research & Development , Vol. 11 , p. 251-258.
25. *Replacement of Less-Preferred Dipolar Aprotic and Ethereal Solvents in Synthetic Organic Chemistry with More Sustainable Alternatives.* Andrew Jordan, Callum G. J. Hall, Lee R. Thorp, and Helen F. Sneddon. 6, Chemical Reviews 2022 , Vol. 122, p. 6749-6794.
26. *Solvent effects in catalysis: rational improvements of catalysts via manipulation of solvent interactions.* Dyson, Paul J. and Jessop, Philip G. 10, 2016, Catal. Sci. Technol., Vol. 6, p. 3302-3316.
27. *Design of bifunctional chiral phenanthroline ligand with Lewis basic site for palladium-catalyzed asymmetric allylic substitution.* Naganawa, Yuki and Abe, Hiroki and Nishiyama, Hisao. 21, 2018, Chem. Commun., Vol. 54, p. 2674-2677.
28. *Optimization of the Reaction Conditions for Direct Arylation Polymerizations in a Sustainable Solvent.* Conelli, D., Grisorio, R., Suranna, G. P.,. 2020, Macromol. Chem. Phys, Vol. 221 , p. 2000041.
29. *Investigation of green and sustainable solvents for direct arylation polymerization (DArP).* Pankow, Robert M. and Ye, Liwei and Gobalasingham, Nemal S. and Salami, Neda and Samal, Sanket and Thompson, Barry C. 28, 2018, Polym. Chem., Vol. 9, p. 3885-3892.
30. *Design and preparation of new palladium precatalysts for C–C and C–N cross-coupling reactions.* Bruno, Nicholas C. and Tudge, Matthew T. and Buchwald, Stephen L. 3, 2013, Vol. 4, p. 916-920.
31. *Photophysical and Electroluminescence Characteristics of Polyfluorene Derivatives with Triphenylamine. Zhang, Q.; Wang, P.-I.; Ong, G.L.; Tan, S.H.; Tan, Z.W.; Hii, Y.H.; Wong, Y.L.; Cheah, K.S.; Yap, S.L.; Ong, T.S.; Tou, T.Y.; Nee, C.H.; Liaw, D.J.; Yap, S.S.* Polymers *2019,* 11*, 840. https://doi.org/10.3390/polym11050840*
32. *The Sonogashira Reaction: A Booming Methodology in Synthetic Organic Chemistry.* Nájera, Rafael Chinchilla and Carmen. 3, 2007 , Chemical Reviews , Vol. 107, p. 874-922.
33. *C–H Arylation in the Synthesis of π-Conjugated Polymers.* Sabin-Lucian Suraru, Jason A. Lee, and Christine K. Luscombe. 6, 2016, ACS Macro Letters , Vol. 5 , p. 724-729.
34. *Synthesis of random poly(hexyl thiophene-3-carboxylate) copolymers via oxidative direct arylation polymerization (oxi-DArP).* Gobalasingham, Nemal S. and Pankow, Robert M. and Thompson, Barry C. 12, 2017, Polym. Chem., Vol. 8, p. 1963-1971.
35. *Impact of Precatalyst Activation on Suzuki-Miyaura Catalyst-Transfer Polymerizations: New Mechanistic Scenarios for Pre-transmetalation Events.* Suranna, Roberto Grisorio and Gian Paolo. 11, 2017 , ACS Macro Letters, Vol. 6 , p. 1251-1256.
36. *Exploring the Utility of Buchwald Ligands for C–H Oxidative Direct Arylation Polymerizations.* Reynolds, Graham S. Collier and John R. 8, 2019 , ACS Macro Letters, Vol. 8 , p. 931-936.
37. *Dual-Catalytic Ag-Pd System for Direct Arylation Polymerization to Synthesize Poly(3-hexylthiophene).* J. A. Lee, C. K. Luscombe. 7, 2018, ACS Macro Lett. , Vol. 7, p. 767-771 .
38. *Carboxylate-Assisted Transition-Metal-Catalyzed C−H Bond Functionalizations: Mechanism and Scope.* Ackermann, Lutz. 3, 2011 , Chemical Reviews , Vol. 111, p. 1315-1345.

39. *Direct Arylation of 2-Methylthiophene with Isolated [PdAr(μ-O2CR)(PPh3)]n Complexes: Kinetics and Mechanism.* Masayuki Wakioka, Yuki Nakamura, Qifeng Wang, and Fumiyuki Ozawa. 13, 2012 , Organometallics, Vol. 31 , p. 4810-4816.
40. —.Masayuki Wakioka, Yuki Nakamura, Qifeng Wang, and Fumiyuki Ozawa. 13, 2012 , Organometallics , Vol. 31, p. 4810-4816.
41. *Remarkable Ligand Effect of P(2-MeOC$_6$H$_4$)$_3$ on Palladium-Catalyzed Direct Arylation.* Masayuki Wakioka, Yuki Nakamura, Michelle Montgomery, and Fumiyuki Ozawa. 1, 2015 , Organometallics , Vol. 34 , p. 198-205.
42. *Syntheses and Properties of Donor–Acceptor-Type 2,5-Diarylthiophene and 2,5-Diarylthiazole.* Kentaro Masui, Atsunori Mori, Kunihiko Okano, Kenji Takamura, Motoi Kinoshita, and Tomiki Ikeda. 12, 2004 , Organic Letters , Vol. 6 , p. 2011-2014.
43. *Palladium-Catalyzed C–H Homocoupling of Thiophenes: Facile Construction of Bithiophene Structure.* Kentaro Masui, Haruka Ikegami, and Atsunori Mori. 16, 2004, Journal of the American Chemical Society , Vol. 126 , p. 5074-5075.
44. *Investigation of the electropolymerization of terthiophenein boron fluoride-ethyl ether.* Zhang, D., Qin, J. & Xue, G. 1999, Synth. Met. , Vol. 100, p. 285–289 .
45. *On the Role of Single Regiodefects and Polydispersity in Regioregular Poly(3-hexylthiophene): Defect Distribution, Synthesis of Defect-Free Chains, and a Simple Model for the Determination of Crystallinity.* Peter Kohn, Sven Huettner, Hartmut Komber, Volodymyr Senkovskyy, Roman Tkachov, Anton Kiriy, Richard H. Friend, Ullrich Steiner, Wilhelm T. S. Huck, Jens-Uwe Sommer, and Michael Sommer. 10, 2012 , Journal of the American Chemical Society, Vol. 134, p. 4790-4805.
46. *Optimization of direct arylation polymerization (DArP) through the identification and control of defects in polymer structure.* Rudenko, A.E. and Thompson, B.C. 2015, J. Polym. Sci. Part A: Polym. Chem., , Vol. 53, p. 135-147. .
47. *Mixed-Ligand Approach to Palladium-Catalyzed Direct Arylation Polymerization: Effective Prevention of Structural Defects Using Diamines.* Eisuke Iizuka, Masayuki Wakioka, and Fumiyuki Ozawa. 9, 2016 , Macromolecules , Vol. 49, p. 3310-3317.
48. *Effect of the Nature and the Position of Defects on the Chiral Expression in Poly(3-alkylthiophene)s.* Lize Verheyen, Julien De Winter, Pascal Gerbaux, and Guy Koeckelberghs. 22, 2019, Macromolecules , Vol. 52 , p. 8587-8595.
49. *Mechanistic studies and optimisation of a Pd-catalysed direct arylation reaction using phosphine-free systems.* Kuwabara, Junpei and Sakai, Masaru and Zhang, Qiao and Kanbara, Takaki. 5, 2015, Org. Chem. Front., Vol. 2, p. 520-525.
50. *Updating and further expanding GSK's solvent sustainability guide.* Alder, Catherine M. and Hayler, John D. and Henderson, Richard K. and Redman, Anikó M. and Shukla, Lena and Shuster, Leanna E. and Sneddon, Helen F. 13, 2016, Green Chem., Vol. 18, p. 3879-3890.
51. *Suppressing Defect Formation Pathways in the Direct C–H Arylation Polymerization of Photovoltaic Copolymers.* Thomas J. Aldrich, Alexander S. Dudnik, Nicholas D. Eastham, Eric F. Manley, Lin X. Chen, Robert P. H. Chang, Ferdinand S. Melkonyan, Antonio Facchetti, and Tobin J. Marks. 22, 2018 , Macromolecules , Vol. 51, p. 9140-9155.
52. *Monodispersed vs. polydispersed systems for bulk heterojunction solar cells: the case of dithienopyrrole/anthracene based materials.* Grisorio, Roberto and Allegretta, Giovanni and Suranna, Gian Paolo and Mastrorilli, Piero and Loiudice, Anna and Rizzo, Aurora and Mazzeo, Marco and Gigli, Giuseppe. 37, 2012, J. Mater. Chem., Vol. 22, p. 19752-19760.
53. *Influence of Keto Groups on the Optical, Electronic, and Electroluminescent Properties of Random Fluorenone-Containing Poly(fluorenylene-vinylene)s.* Roberto Grisorio, Claudia Piliego, Marinella Striccoli, Pinalysa Cosma, Paola Fini, Giuseppe Gigli, Piero Mastrorilli, Gian Paolo Suranna, and Cosimo Francesco Nobile. 50, 2008, The Journal of Physical Chemistry C , Vol. 112, p. 20076-20087.
54. *A Pd(AcO)$_2$/t-Bu$_3$P/K$_3$PO$_4$ catalytic system for the control of Suzuki cross-coupling polymerisation.* Grisorio, R. and Mastrorilli, P. and Suranna, G. P. 14, 2014, Polym. Chem., Vol. 5, p. 4304-4310.

55. *Catalyst-transfer polymerization of arylamines by the Buchwald–Hartwig cross-coupling.* Grisorio, Roberto and Suranna, Gian Paolo. 15, 2019, Polym. Chem., Vol. 10, p. 1947-1955.
56. *Donor–Acceptor Polymer with Benzotriazole Moiety: Enhancing the Electrochromic Properties of the "Donor Unit".* Abidin Balan, Gorkem Gunbas, Asuman Durmus, and Levent Toppare. 24, 2008 , Chemistry of Materials, Vol. 20, , p. 7510-7513.
57. *A Selenium-Substituted Low-Bandgap Polymer with Versatile Photovoltaic Applications.* Dou, L., Chang, W.-H., Gao, J., Chen, C.-C., You, J. and Yang, Y. 2013, Adv. Mater., Vol. 25, p. 825-831.
58. *Green chemistry for organic solar cells.* Burke, Daniel J. and Lipomi, Darren J. 7, 2013, Energy Environ. Sci., Vol. 6, p. 2053-2066.
59. *Solvent effects in palladium catalysed cross-coupling reactions.* Sherwood, James and Clark, James H. and Fairlamb, Ian J. S. and Slattery, John M. 9, 2019, Green Chem., Vol. 21, p. 2164-2213.
60. *Approaches for improving the sustainability of conjugated polymer synthesis using direct arylation polymerization (DArP).* Pankow, Robert M. and Thompson, Barry C. 3, 2020, Polym. Chem., Vol. 11, p. 630-640.
61. *Tools and techniques for solvent selection: green solvent selection guides.* Byrne, F.P., Jin, S., Paggiola, G. et al. 1, 2016, Sustain Chem Process, Vol. 4, p. 7.
62. *Carbonates: eco-friendly solvents for palladium-catalysed direct arylation of heteroaromatics.* Dong, Jia Jia and Roger, Julien and Verrier, Cécile and Martin, Thibaut and Le Goff, Ronan and Hoarau, Christophe and Doucet, Henri. 11, 2010, Green Chem., Vol. 12, p. 2053-2063.
63. *The Heck Reaction as a Sharpening Stone of Palladium Catalysis.* Cheprakov, Irina P. Beletskaya and Andrei V. 8, 2000 , Chemical Reviews , Vol. 100 , p. 3009-3066.
64. *Poly (fluorenevinylene) derivatives by Heck coupling: Synthesis, photophysics, and electroluminescence.* Mikroyannidis, J.A., Yu, Y.J., Lee, S.H. and Jin, J.I.,. 15, 2006, Journal of Polymer Science Part A: Polymer Chemistry, Vol. 44, p. 4494-4507.
65. *Random poly(fluorenylene-vinylene)s containing 3,7-Dibenzothiophene-5,5-dioxide units: Synthesis, photophysical, and electroluminescence proerties.* Grisorio, R., Piliego, C., Cosma, P., Fini, P., Mastrorilli, P., Gigli, G., Suranna, G.P. and Nobile, C.F. 2009, J. Polym. Sci. A Polym. Chem., Vol. 47, p. 2093-2104.
66. *A one-pot synthetic strategy via tandem Suzuki–Heck reactions for the construction of luminescent microporous organic polymers.* Sun, Libo and Zou, Yongcun and Liang, Zhiqiang and Yu, Jihong and Xu, Ruren. 2, 2014, Polym. Chem., Vol. 5, p. 471-478.
67. *Implementation of Sustainable Solvents in Green Polymerization Approaches.* Conelli, D., Margiotta, N., Grisorio, R., Suranna, G. P.,. 2021, Macromol. Chem. Phys. , Vol. 222, p. 2000382.
68. *Design and preparation of new palladium precatalysts for C–C and C–N cross-coupling reactions.* Bruno, Nicholas C. and Tudge, Matthew T. and Buchwald, Stephen L. 3, 2013, Chem. Sci., Vol. 4, p. 916-920.
69. *The Heck Reaction as a Sharpening Stone of Palladium Catalysis.* Cheprakov, Irina P. Beletskaya and Andrei V. 8, 2000 , Chemical Reviews , Vol. 100, p. 3009-3066.
70. *RANDOM POLY(2, 7-FLUORENYLENEVINYLENE) COPOLYMERS OBTAINED BY A SUZUKI-HECK REACTION: SYNTHESIS AND PROPERTIES.* R. Grisorio, P. Mastrorilli, C. F. Nobile, G. Romanazzi, G. P. Suranna, G. Gigli, C. Piliego, G. Ciccarella, P. Cosma, D. Acierno, and E. Amendola. 2008, AIP Conference Proceedings , Vol. 1042, p. 297-299 .
71. *Polyacetylenes Bearing Chiral-Substituted Fluorene and Terfluorene Pendant Groups: Synthesis and Properties.* Piero Mastrorilli, Cosimo Francesco Nobile, Roberto Grisorio, Antonino Rizzuti, Gian Paolo Suranna, Domenico Acierno, Eugenio Amendola, and Pio Iannelli. 12, 2004 , Macromolecules , Vol. 37 , p. 4488-4495.
72. *Cyclic Carbonates as Green Alternative Solvents for the Heck Reaction.* Helen L. Parker, James Sherwood, Andrew J. Hunt, and James H. Clark. 7, 2014 , ACS Sustainable Chemistry & Engineering, Vol. 2 , p. 1739-1742.
73. *Highly Regioselective Palladium-Catalyzed Oxidative Coupling of Indolizines and Vinylarenes via C–H Bond Cleavage.* Yuzhu Yang, Kai Cheng, and Yuhong Zhang. 24, 2009, Organic Letters, Vol. 11 , p. 5606-5609.

74. *Electronic Control of the Regiochemistry in the Heck Reaction.* Henrik von Schenck, Björn Åkermark, and Mats Svensson. 12, 2003, Journal of the American Chemical Society, Vol. 125 , p. 3503-3508.
75. *A Highly Efficient Catalytic System for Polycondensation of 2,7-Dibromo-9,9-dioctylfluorene and 1,2,4,5-Tetrafluorobenzene via Direct Arylation.* Masayuki Wakioka, Yutaro Kitano, and Fumiyuki Ozawa. 2, 2013 , Macromolecules , Vol. 46 , p. 370-374.
76. *Remarkable Ligand Effect of P(2-MeOC6H4)3 on Palladium-Catalyzed Direct Arylation.* Masayuki Wakioka, Yuki Nakamura, Michelle Montgomery, and Fumiyuki Ozawa. 1, 2015 , Organometallics , Vol. 34, p. 198-205.
77. *Impact of Precatalyst Activation on Suzuki-Miyaura Catalyst-Transfer Polymerizations: New Mechanistic Scenarios for Pre-transmetalation Events.* Suranna, Roberto Grisorio and Gian Paolo. 11, 2017 , ACS Macro Letters , Vol. 6 , p. 1251-1256.
78. *Optimization of the Reaction Conditions for Direct Arylation Polymerizations in a Sustainable Solvent.* Conelli, D., Grisorio, R., Suranna, G. P.,. 2020, Macromol. Chem. Phys., Vol. 221, p. 2000041.
79. *Monodispersed vs. polydispersed systems for bulk heterojunction solar cells: the case of dithienopyrrole/anthracene based materials.* Grisorio, Roberto and Allegretta, Giovanni and Suranna, Gian Paolo and Mastrorilli, Piero and Loiudice, Anna and Rizzo, Aurora and Mazzeo, Marco and Gigli, Giuseppe. 37, 2012, J. Mater. Chem., Vol. 22, p. 19752-19760.
80. *Evaluating structure–function relationships toward three-component conjugated polymers via direct arylation polymerization (DArP) for Stille-convergent solar cell performance.* Gobalasingham, Nemal S. and Pankow, Robert M. and Ekiz, Seyma and Thompson, Barry C. 27, 2017, J. Mater. Chem. A, Vol. 5, p. 14101-14113.
81. *Third-order nonlinear optical properties of regioregular poly(3-hexylthiophene) thin film on quartz glass modified by HMDS and ODTS.* S. Ochiai, J. Ramajothi, K. Kojima and T. Mizutani,. 2008. p. 255-258.
82. *Effect of the Nature and the Position of Defects on the Chiral Expression in Poly(3-alkylthiophene)s.* Lize Verheyen, Julien De Winter, Pascal Gerbaux, and Guy Koeckelberghs. 22, 2019 , Macromolecules, Vol. 52 , p. 8587-8595.
83. *Optimization of direct arylation polymerization (DArP) through the identification and control of defects in polymer structure.* Rudenko, A.E. and Thompson, B.C. 2015, J. Polym. Sci. Part A: Polym. Chem.,, Vol. 53, p. 135-147.
84. *Advances in applying C–H functionalization and naturally sourced building blocks in organic semiconductor synthesis.* Xing, Liwen and Luscombe, Christine K. 46, 2021, J. Mater. Chem. C, Vol. 9, p. 16391-16409.
85. *Optimization of the Reaction Conditions for Direct Arylation Polymerizations in a Sustainable Solvent.* Conelli, D., Grisorio, R., Suranna, G. P.,. 2020, Macromol. Chem. Phys. , Vol. 221, p. 2000041.
86. *Catalyst-transfer polymerization of arylamines by the Buchwald–Hartwig cross-coupling.* Grisorio, Roberto and Suranna, Gian Paolo. 15, 2019, Polym. Chem., Vol. 10, p. 1947-1955.

5 Chapter 5
Simplified molecular design and synthesis of novel hole-transporting materials (HTMs) for stable Perovskite Solar Cells

5.1 GENERAL INTRODUCTION

5.1.1 Preface and motivations

In the recent years, the global clean energy transition is accelerating, driven by a combination of policy, technological and economics changes. Moreover, the actual concerns about supply of conventional fuels such as oil and gas, seem to provide further impetus to the need and policy support for clean energy technologies. As reported in the 2022 IEA outlook, renewable generation capacity increased by 257 GW (+9.1%) in 2021 with solar and wind energy continuing to dominate renewable capacity expansion accounting for 88% of the increase in renewable energy production. Notably, solar energy continued to lead capacity expansion, adding 133 GW. In the same report, the IEA stated that " global solar PV capacity is set to almost triple over the 2022-2027 period, surpassing coal and becoming the largest source of power capacity in the world. Installations of residential and commercial rooftops solar panels are also expected to accelerate, helping consumers reduce energy bills." [(1)]Our planet is capable of absorbing around 3 850 000 EJ of solar energy each year in total, implying that it is estimated that solar irradiation for just one hour can potentially provide enough energy to meet the worldwide annual demand. [(2)]Among all the different technological means capable of capturing and distributing solar energy, one of the most interesting strategies is solar photovoltaics (PV), which can convert solar energy directly into electricity. The solar PV industry experienced a significant growth in recent years (see Figure 5.1.) and is becoming increasingly efficient and cost-competitive with respect to conventional fossil fuels. However, the solar era began as early as 1950, with the so-called 1st generation solar cells, developed after Bell Laboratory scientists created the first practical solar cell in history with a 6% power conversion efficiency (PCE).[(3)] Then, the 2nd generation solar cells, known as thin-film solar cells, have developed very fast, e.g., cadmium telluride (CdTe) [(4)]

and copper indium gallium selenide (CIGS). [5] Both the 1st and 2nd generation solar cells are inorganic-based solar cells, who have achieved promising photovoltaic performance and have already been commercialized for a long time. However, the toxicity and scarcity of several used elements (e.g., Cd, Te and In) as well as high manufacturing costs limit the potential of these type of photovoltaics for large-scale applications. With the increasing demand for solar power, improving the efficiency and driving down the costs of PVs are extremely crucial. Thus, the generation of novel organic-based PVs, i.e., 3rd generation solar cells, has attracted extensive attention during the recent years. Differing from other types, this generation of emerging photovoltaics use organic materials or nanomaterials, as well as inorganic substances. The resulting devices can be divided into organic/polymer solar cells (i.e., organic photovoltaic cells, OPVs), [6] quantum dot solar cells (QDSCs), [7] dye sensitized solar cells (DSSCs), [8] perovskite solar cells (PSCs) [9] and other more specific classes. [10] The research effort along the way of the discovery of low-cost, high-efficiency solar cells, such as fast-growing photovoltaics, PSCs have attracted much attention in recent decades due to their promising PCE and great potential in commercial applications.

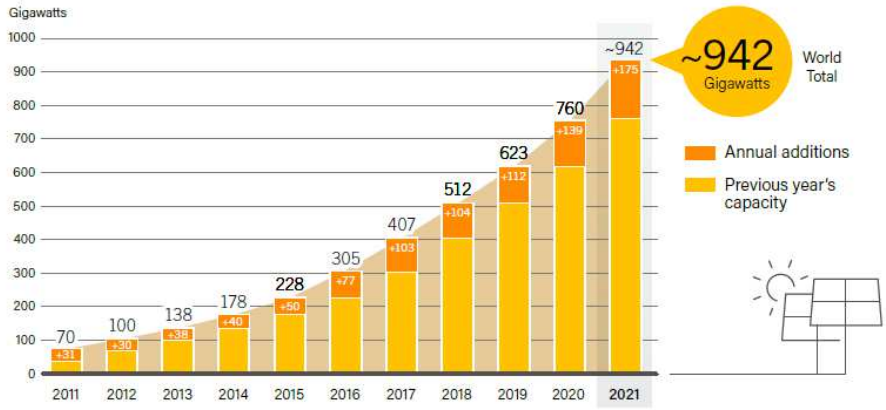

Figure 5.1. Solar PV Global Capacity and Annual Additions, 2011-2021. (Source from REN21 Renewables 2022: Global Status Report.)

5.1.2 Perovskite solar cells

As an efficient light absorbing layer in PSCs, one of the most attractive key components is the hybrid organic-inorganic perovskite material. In the strictest sense of the word, perovskite - bearing the name of Russian mineralogist L. A. Perovski - is simply the calcium titanium oxide mineral ($CaTiO_3$), discovered by Gustav Rose in 1839. [11] However, the term is commonly referred to the group of compounds sharing the same crystal structure of calcium titanate, known as the perovskite structure with the general chemical formula of AMX_3, where A is a monovalent cation (methylammonium $CH_3NH_3^+$ (MA^+), formamidinium $CH_2(NH_2)_2^+$ (FA^+), Cs^+, Rb^+), M is a metallic cation ($Pb^{(II)}$, $Sn^{(II)}$) and X are anions (Cl^-, Br^-, I^-). [12] In the ideal crystal structure, the metallic cation M and halide anions X form MX_6^{4-} octahedra, and A cations occupy the cavities of the 12-fold cuboctahedral coordination complex. [13] The crystal structure of one of the most studied perovskite materials, $MAPbI_3$, is given in Figure 5.2. a) In the field of PSCs, however it is also possible to employ mixed perovskites mixing various proportions of cations and anions, as described in the experimental part of this chapter. While the synthetic approaches which aim to obtain the control of the shape and stability of the perovskite nanocrystals have been the topic of research for some time, [14] [15] [16] PSCs are a very recent discovery. Perovskite semiconductors were used in solar cells by Miyasaka and co-workers in 2006 for the first time using $MAPbBr_3$ as a sensitizer on mesoporous titanium dioxide (titania, TiO_2) in a dye-sensitized solar cell structure (DSSC), obtaining a PCE of 2.19 %. [17] In 2009, they also tested $MAPbI_3$, reaching a PCE of 3.81 %, although the solar cells decayed under illumination and air exposure. [18] Two years later, Park and co-workers improved the PCE of $CH_3NH_3PbI_3$ PSCs to 6.54% with advanced technology, but the PSC devices were still unstable because the perovskite materials could easily be dissolved in liquid electrolytes. [19] After that, a breakthrough happened in 2012 when Park et al. [20] and Snaith et al. [21] reported all-solid-state mesoscopic PSCs with PCEs of 9.7% and 10.9%, respectively. In their studies, liquid electrolytes were replaced by the solid-state hole conductor 2,2',7,7'-tetrakis(N,N'-di-p-methoxyphenylamine)-

9,9'-spirobifluorene (Spiro-OMeTAD) which remarkably improved the device stability. Inspired by these pioneering reports, perovskite solar cells has become promising candidates for the 3rd generation photovoltaic technology during the past years with their PCE which has currently led to a certified power conversion efficiency (PCE) of 25.7% (see NREL chart in Figure 1.1 of Chapter 1), because of the advantages of the perovskite materials, such as a high light absorption coefficient, high intrinsic carrier mobility, long charge carrier diffusion length, and strong absorption over most of the visible part of the solar spectrum (as shown in Figure 5.2 b)). However, due to the intrinsic instability of perovskite materials, they are sensitive to light, oxygen, humidity, and high temperature. Thus, long-term stability issues need to be address to speed-up industrialization. Towards this end, research related to PSCs involves topics such as the study of the interfaces between the perovskite layer and the neighboring charge transport materials, which act as protective layers and play as well a significant role in the longevity of PSCs. (22) (23)

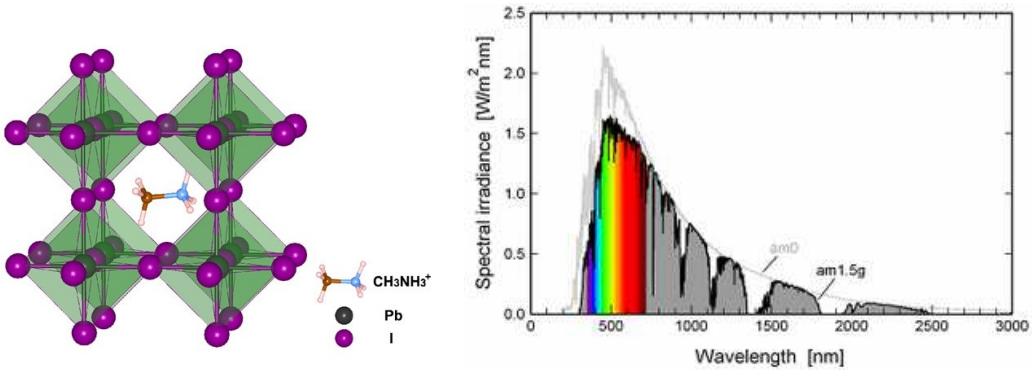

Figure 5.2.a) Crystal structure of $CH_3NH_3PbI_3$ ($MAPbI_3$). The methylammonium cation (CH_3NH^+) occupies the central A site surrounded by 12 nearest-neighbor iodide ions (I^-) in corner-sharing PbI_6 octahedra. b) Solar irradiance spectrum at sea level (AM 1.5G) and a representative illustration of the illumination conditions on a tilted PV flat of a PSC.

Hybrid lead halide perovskites exhibit ambipolar charge transport properties, i.e. they can cumulate the function of light absorption with n- and p-type conduction. This behavior allows versatile device architectures for PSCs.

Commonly, a device consists of five layers: a transparent electrode constituted of a glass coated with conductive fluorine-doped tin oxide (FTO), a n-type semiconductor of electron-transport material (ETM), a photoactive ambipolar semiconductor perovskite, a p-type semiconducting hole-transport material (HTM) and a high workfunction metal as counter electrode. Depending on the arrangement of the ETM and HTM, the solar cells can be classified as n-i-p and p-i-n type structures, *i.e.*, conventional and inverted structures, respectively. Besides considering the structure of the n-type ETM layer, PSCs can also be divided into mesoporous or planar heterojunction structures. In the mesoporous PSCs the perovskite layer is partially blended with a mesoporous scaffolding of TiO_2 that covers the electron transporting layer (ETL) whit the aim to receive the diffusing electrons before they recombine, with the larger contact area also improving charge transfer. Basically, these different types of PSCs (as shown in Figure 5.3.) have their own advantages, for example, the inverted PSCs usually have higher stability with hysteresis-free current-voltage (*J-V*) behavior, while the conventional devices generally exhibit higher PCE, mainly due to the matched energetics and better charge extraction property of the transport layer.

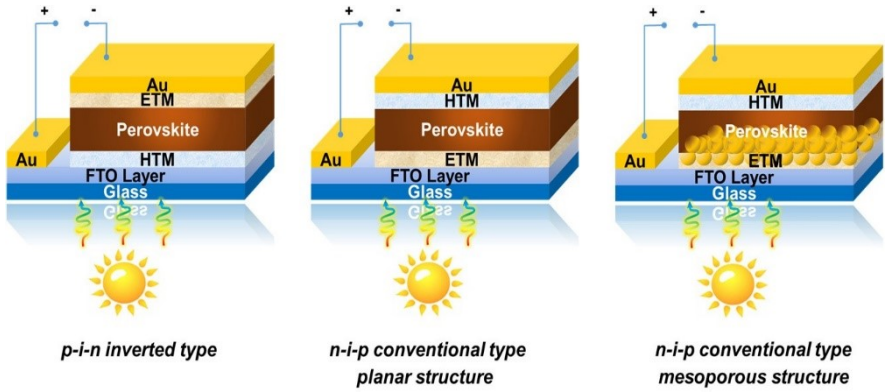

Figure 5.3. Schemes of the three most common architectures used in PSC technology: a) planar inverted (p–i–n), b) conventional planar (n–i–p) and c) conventional mesoporous (n–i–p).

In this section of the Dissertation, conventional n-i-p type perovskite solar cell devices (see Figure 5.3. b)) will be mainly discussed. As depicted in Figure 5.4., generally the light absorber perovskite layer absorbs the photons upon sunlight irradiation, and then the electrons are excited from the valence band (VB) to the conduction band (CB) formed from the limited energy levels of individual atoms packed closely together in the semiconductor layer. These bands are analogous with molecular orbitals HOMO and LUMO in organic molecules respectively. In order for current to flow through the semiconductor, electrons need to be separated from the crystal lattice leaving the electron vacancies (*i.e.*, holes). The photogenerated electrons in the excited state are injected into the CB (LUMO) of the ETMs (2) and then collected by the transparent conductive oxide (FTO layer) (3). Meanwhile, the photogenerated holes transport through the HTM layer (1) and are then collected by the Au (or Ag) counter electrode (4). Finally, the photocurrent is generated in the external circuit of the PSC device by connecting the FTO layer with the counter electrode.

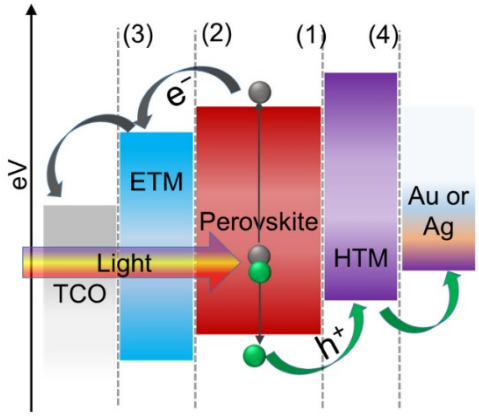

Figure 5.4. Working principles of a conventional n-i-p type perovskite solar cells.

5.1.3 Organic hole-transporting materials

The purpose of an organic hole transporting material in a solar cell is to extract holes from the photo-excited perovskite and promote the transport to the anode of the solar cell as well as restraining charge recombination at the interfaces between the perovskite layer and HTM layer. Moreover, in conventional n-i-p type PSCs, HTMs improve the stability and device performance of the PSCs by acting as a protection layer to prevent moisture in air from contacting, penetrating and degrading the perovskite directly. [24] To achieve effective charge transfer and high efficiency in PSCs, the molecular design of suitable HTMs must be based on the following requirements: [25]

(1) The energy levels of HTMs should match those of the perovskite: the highest occupied molecular orbital (HOMO) energy level should higher positive than the VB of the perovskite layer to inject the holes effectively and the lowest unoccupied molecular orbital (LUMO) energy level needs to be higher in energy than the CB of the perovskite to suppress electron transfer from the perovskite layer to the counter electrode.

(2) The material must have good film-forming ability to facilitate device fabrication, and good solubility in less strong polar and protic solvents is required to avoid dissolution of the perovskite layer.

(3) The desirable HTMs in conventional n-i-p type PSCs also need to display high thermal stability, photochemical stability and hydrophobicity to work as a protection layer to prevent, e.g., water/oxygen penetration and light induced degradation.

(4) High charge carrier mobility and high conductivity are required for HTMs to reduce losses during the hole-transport process.

(5) To realize the great potential low-cost perovskite solar cell application, an ideal designed HTM also needs to be low-cost, transparent and easily affordable

by simple synthetic procedures minimizing the number of steps and with easy workup and purifcation steps for cost-effective upscaling.

To date, the integration of all these favorable properties in a single HTM molecule is highly challenging from the molecular design point of view, and it often requires an evaluation of the different material purposes. In the field of the π-conjugated organic materials, as central topic of this Thesis, the understanding of the correlation between molecular structure and their properties is essential for wisely designing efficient and effective HTMs for PSCs.

5.1.4 Chemically doped organic hole transporting materials

To date, a widely used high-performance hole transporting material for perovskite solar cells is the 2,2',7,7'-tetrakis(N,N'-di-p-methoxyphenylamine)-9,9'-spirobifluorene, commonly known as Spiro-OMeTAD, depicted in Figure 5.5. As mentioned above, it was first used in conjunction with perovskite in 2012 by Park et al. to replace the liquid electrolyte previously used, yielding a PCE of 9.7 % along with increased device stability. [20] Although Spiro-OMeTAD has been used to great effect, it presents several issues as well. As a state-of-the-art HTM, spiro-OMeTAD has well-aligned energy levels with a HOMO energy level around –5.1 eV and a wide bandgap of 2.98 eV, good solubility in organic solvents, such as toluene and chlorobenzene, adequate film-forming ability to perform a transparent thin film through solution-based deposition methods. In addition to spiro-OMeTAD, the polymeric HTM poly[bis(4-phenyl)(2,4,6-trimethylphenyl)amine] (PTAA), which has shown great compatibility for both n–i–p- and p–i–n-structured devices, also achieved excellent device performances with a certified PCE over 23%. [26] [27]

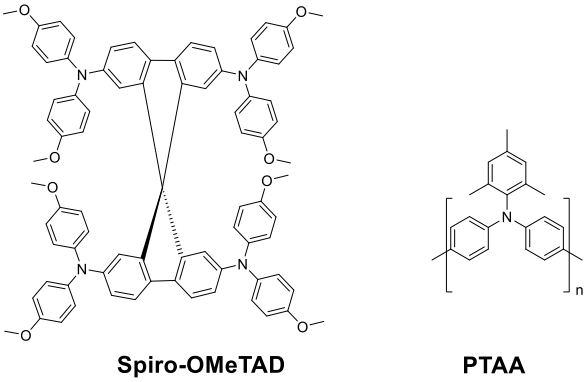

Figure 5.5. Chemical structures of spiro-OMeTAD and PTAA.

However, both spiro-OMeTAD and PTAA have obvious drawbacks, such as their high cost, complex synthetic and purification procedures, low charge carrier mobility and conductivity of the pristine materials, and the requirement of hygroscopic dopants that may accelerate degradation of the perovskite layer. [28] As an example, the commonly adopted complex synthetic routes of spiro-OMeTAD are reported in Scheme 5.6. As shown, the synthetic process of spiro-OMeTAD, including four steps with a total yield of less than 50%. The core structure of 9,9'-spirobi[fluorene] (SBF) can be synthesized after the previous preparation of Grignard reagent of 2-bromobiphenyl in harsh conditions and then the reaction with 9-fluorenone allows to get SBF structure. Electrophilic substitution of SBF with bromide can be performed by means of ferric chloride as catalyst. Finally, spiro-OMeTAD can be obtained at reflux circumstance by Buchwald–Hartwig reaction of brominated SBF core with 4,4-dimethoxydiphenylamine in basic condition with NaOtBu and Pd_2dba_3 catalyst with $(t\text{-}Bu)_3P$ ligand. Clearly, high-purity spiro-OMeTAD is very expensive owing to its tedious synthesis, with the added costly sublimation, toxic and corrosive reagents, which greatly limits its future scalable application. [29] Currently, for one of the chemical suppliers (Sigma-Aldrich) the price for spiro-OMeTAD is € 420 per gram (data accessed in January, 2023).

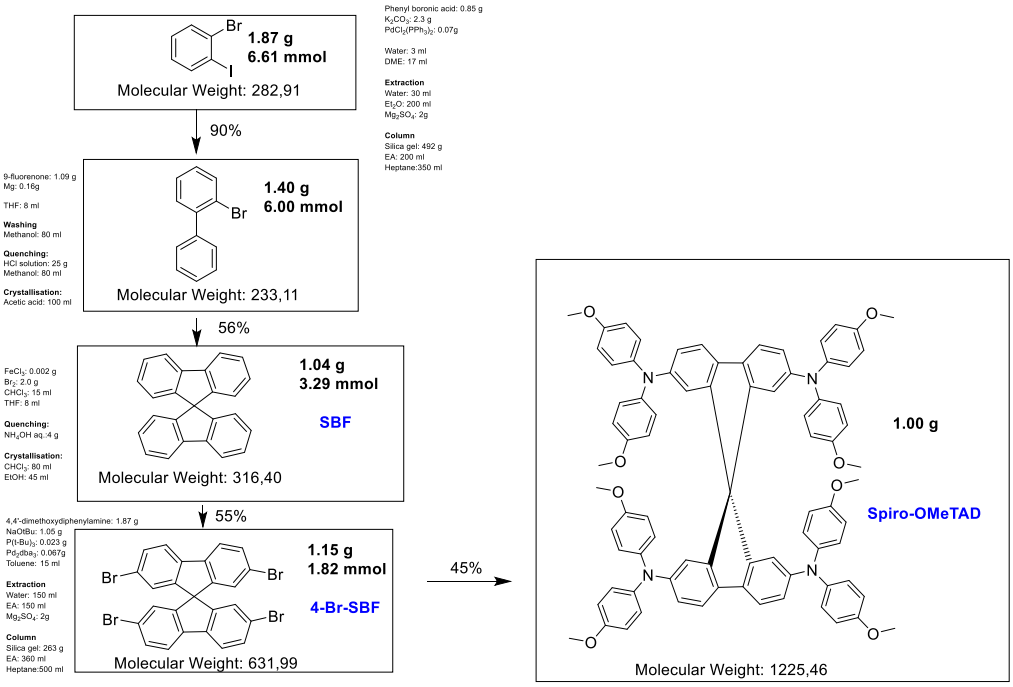

Scheme 5.6. Flowchart describing the synthesis of 1 g of spiro-OMeTAD.

Therefore, developing low-cost and high-conductivity substitutes to replace spiro-OMeTAD is urgently necessary for future application as well as deriving a fundamental understanding of the influence of the molecular structure on the HTM properties. For example, the spirobifluorene central core has been replaced by several other spiro-type cores (Figure 5.7). Sun et al. and Hagfeldt et al. reported two spiro-type HTMs, X59 and X60, based on the spiro[fluorene-9,9'- xanthene] (SFX) core unit, recording PCEs of 19.8% and 19.84% in PSCs, respectively. [30] [31]Both HTMs could be synthesized by a two-step approach using cheap starting materials 2,7-dibromo-9-fluorenone and phenol/4-bromophenol. Due to the easy synthetic route, high yield (>90%) and low cost, this SFX core has attracted significant attention and shown great potential in large-scale applications. Nazeeruddin et al. reported a promising low-cost HTM fluorene-dithiophene (FDT) with

a simple symmetric, easily modified fluorene-dithiophene core, which achieved a device performance of 20.2%. [32] In the same work, an additional thiophene-iodine interaction was ascertained by crystallographic analysis, which may accelerate the hole transfer process at the HTM/perovskite interface. Recently, a fluorene-terminated HTM, termed DM, was presented by Seo et al., [33] with a certified efficiency of 22.6% for small-area solar cells. However, due to the low conductivity of DM itself, the solar cell performance of the device was very poor without addivitives or with only small amounts of additives.

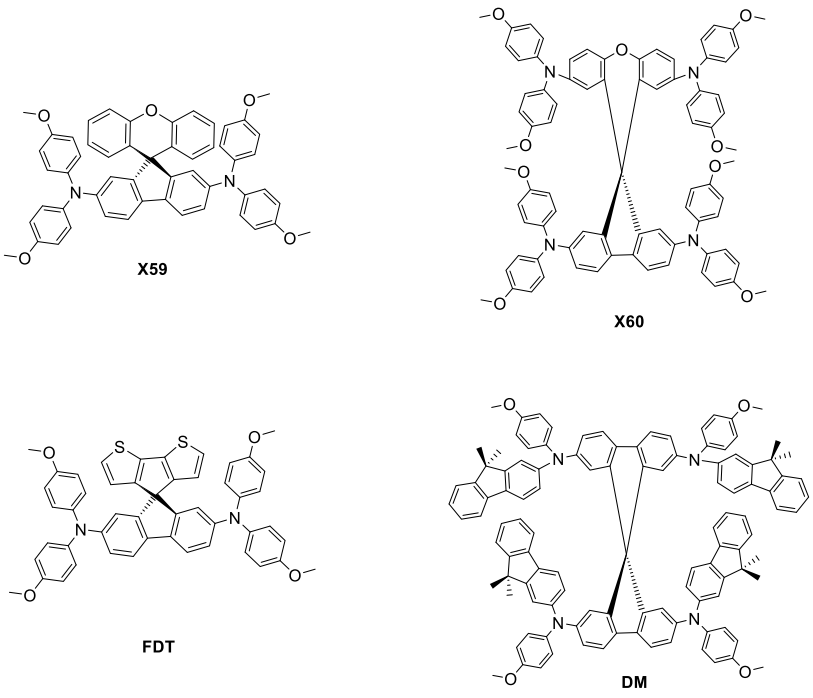

Figure 5.7. Chemical structures of doped organic HTMs with spiro-type core units

In addition to these core units, several other types of molecular moieties have also been extensively investigated, such as carbazole, triazatruxene, pyrene, phenothiazine, phenoxazine, and thiophene, of which only a few examples are shown in Figure 5.8. [34]

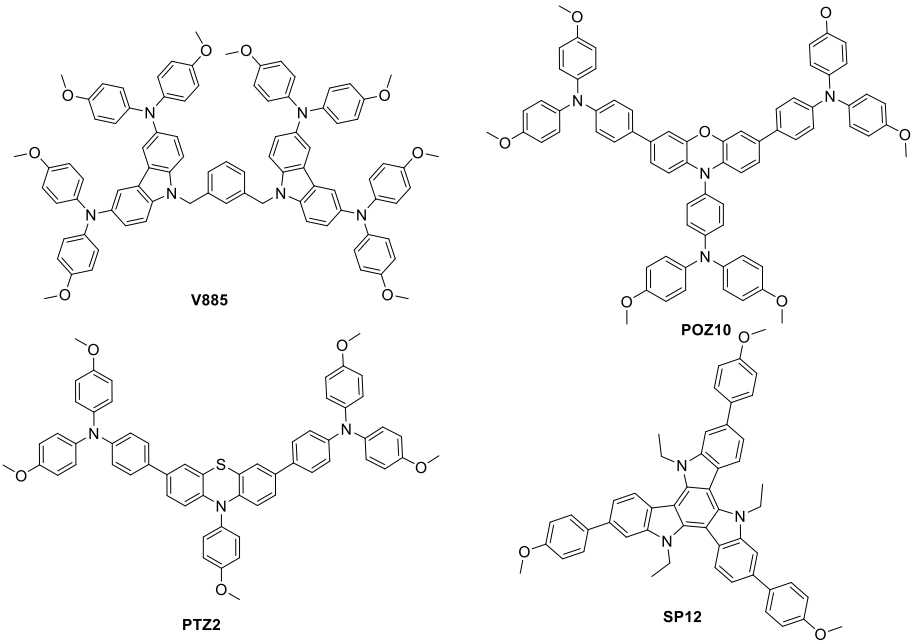

Figure 5.8. Chemical structures of some doped organic HTMs with different core units.

5.1.5 Dopant-free organic hole-transport materials

The intrinsic low hole mobility and the limited conductivity of the pristine organic materials, also found for the champion HTM spiro-OMeTAD, require the chemical doping of most of the developed HTMs. This treatment enhances device performance by improving charge transport capacity and conductivity, as well as reducing ohmic losses in the charge transport layers. [35] The basic principle of p-doping in organic semiconductors, is based on the addition of a mobile charge carriers which are generated employing electron acceptors enable to remove electrons from the HOMO to generate holes of an intrinsic HTM. An efficient doping

process can be pursued when the dopant has an high electron affinity with respect to the energy levels of the organic semiconductor.

The most commonly used p-type dopants have been developed and are still widely used as additives for organic semiconductors applied in PSCs, some of which are shown in Figure 5.9. For example, p-type dopants include 2,3,5,6-tetrafluoro-7,7,8,8- tetracyanoquinodimethane (F4TCNQ), [36] cobalt$^{(III)}$-based coordination complexes, [37] bis(trifluoromethane)sulfonamide (TFSI) salts, [38]and organic small molecules (1,1,2,2-tetrachloroethane, TeCA). [39] In addition, tert-butylpyridine (t-BP) has been demonstrated to be controlling the morphology by reducing the pinholes to further improve the film-forming ability of the HTMs. [40] [41]To date, the co-doping strategy combining bis(trifluoromethane)sulfonamide lithium salt (LiTFSI) [42] and tris[2-(1H- pyrazol-1-yl)-4-tert-butylpyridine]cobalt(III)-tris[bis(trifluoromethylsulfonyl)-imide] (FK209) [43] together with t-BP provides high conductivity of HTMs and leads to an improved device performance.

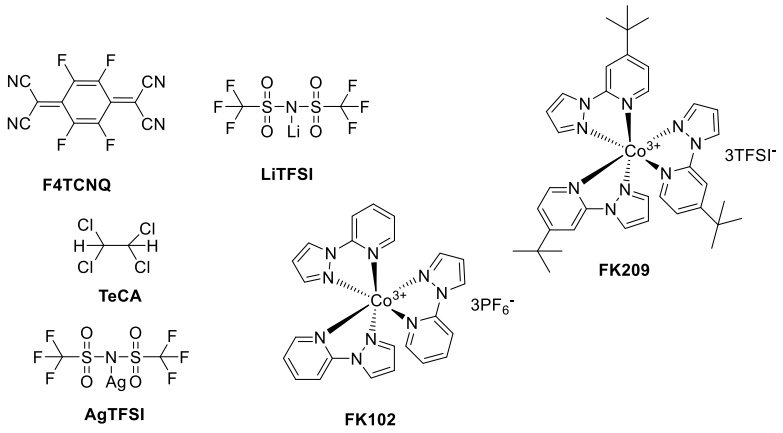

Figure 5.9. Chemical structures of different p-type dopants commonly employed in PSCs.

However, an important disadvantage of the p-dopants, such as LiTFSI and t-BP relies on their deliquescence (due to hygroscopicity), which may accelerate degradation of the perovskite layer, and thus resulting in a poor long-term stability of the solar cells. [44] [45]Also the strong color of some p-type dopants represents

a limit because may compete with the light absorbing layer in the visible region. Based on these and other disadvantages caused by the use of dopants, plenty of novel small molecular and polymeric HTMs with intrinsic high hole mobility and conductivity have been designed and synthesized, which are the so-called dopant-free HTMs. [46] [47] To reach the long-term stability of PSCs the dopant-free approach has already been demonstrated to be very effective. In 2014, Han et al. reported a tetrathiafulvalene derivative, TTF-1 (chemical structure shown in Figure 5.10.), as an efficient pristine HTM which performed with a comparable efficiency as p-doped systems of 11.03% and good stability. [48] The efficient hole conductivity observed in TTF derivatives is due to the inherent π-π stacking and strong S–S interactions. To solve the problem of the poor solubility of these highly rigid conjugated units, they anchored long alkyl chains which could also induce intermolecular stacking. Recently, Zhu et al. designed a couple of dopant-free HTMs based on the tetrathienylethene (TTE) core unit, in one of which (termed TTE-2 as shown in Figure 5.10) the cis thiophene rings can be semi-locked to increase the molecular planarity gradually. [49]In this design strategy, the researchers replace the orthogonal spiro core with the orthogonal-planar configuration to achieve a higher hole mobility, deeper HOMO level, extra thin film morphology, and promising PCE of over 20%. Very recently, Berlinguette et al. designed a low-cost, spiro-type small molecule DFH (chemical structure shown in Figure 5.10) by linking a dioxolane onto the sp^3 carbon atom of fluorene core unit. [50] From the single crystal structure of DFH, strong intermolecular interactions could be confirmed, corroborating the high hole mobility observed. A high PCE of 20.6% was obtained in an inverted PSC without the need of dopants. Moreover, other varieties of small organic molecules with different core units, e.g., diphenylamine (DPA) and triphenylamine units, [51]triazatruxene, [52] and dithieno[3,2-b:2',3'-d]pyrrole (DTP) [53] have also been extensively investigated.

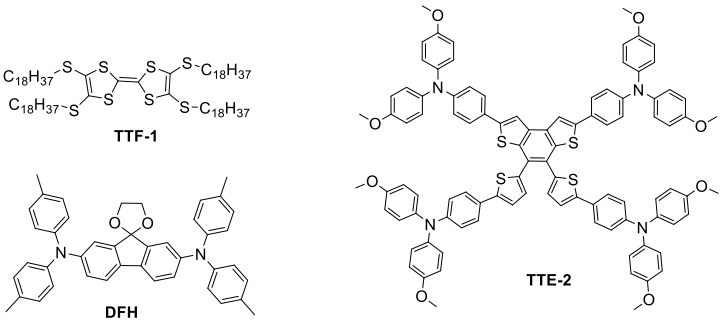

Figure 5.10. Chemical structures of some of the most efficient dopant-free HTMs applied in PSCs.

Compared with the organic small molecules HTMs, polymers have attracted more attention as HTMs in recent years, since they can offer excellent thermal stability, good film-forming ability, mechanical flexibility and tunable functionality. [54] Generally, for the design of polymeric dopant-free HTMs, donor-acceptor (D-A) conjugated systems [55] and non-π-conjugated systems [56] are the two most popular approaches. D-A type dopant-free HTMs show promising performance in solar cell devices according to their tunable electrical and optical properties as well as improved charge-transport properties. [57] [58]For example, Park et al. combined two polymers P-OR and P-R (both with a coplanar donor and a strong electron acceptor, as shown in Figure 5.11) obtaining a random copolymer RCP as a dopant-free HTM which resulted in a PSCs with a PCE of 17.3%. [59] Enhanced π-π stacking and designed functional moieties help to accomplish a high charge mobility and a suitable HOMO energy level in the copolymer RCP. On the other hand, several problems may limit further applications of this kind of material, including the requirement of expensive raw materials and noble-metal catalyst, complex synthetic routes and purification procedures, strong intrinsic light absorption, as well as solubility problems. Non-π-conjugated polymers are typically obtained through free-radical polymerization of suitably placed double bonds [60] and can be subdivided into linear or crosslinked polymers. For the linear polymeric HTMs, several varieties of side-chains have been developed. [61] Huang et al. used hole-transport methoxydiphenylamine-substituted carbazole as side chains

combined with the flexible non-conjugated polyvinyl main chain to build up a non-conjugated polymeric HTM PVCz-OmeDAD (chemical structure shown in Figure 5.11), which achieved an efficiency of 16.09% in PSC devices using ultra-thin layers (≈ 30 nm). [62] In comparison, the three-dimensional (3D) crosslinked polymers exhibit improved charge transporting ability, good solvent resistance, thermal stability and mechanical durability. [63] [64]Shao et al. employed four diphenylamine derivatives with a fluorene core as HTMs in inverted p-i-n planar PSCs. These HTMs were obtained via an in-situ thermally driven polymerization and the resulting devices exhibited a PCE of 18.7% (the monomer termed VB-MeO-FDPA is shown in Figure 5.11). [65] However, the development of 3D crosslinked polymers as dopant-free HTMs for n-i-p type PSCs have been less studied.

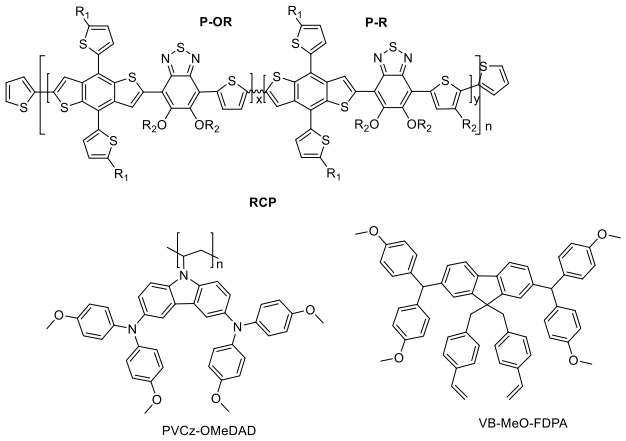

Figure 5.11. Chemical structures of dopant-free polymeric HTMs.

5.2 A straightforward Buchwald–Hartwig amination protocol enables the synthesis of new polymeric HTMs for PSCs

5.2.1 Target

A common trend in the synthetic approaches toward both small-molecule and polymeric HTMs used in PSCs relies on the introduction of the triarylamine moiety as an electron-rich group that may lead to materials with suitable properties such as high hole conductivities. Polymeric HTMs have been reported in literature with either the triarylamine incorporated into the main polymer backbone [66] [67] or as a pendant group. [68]However, these polymers typically require multistep syntheses with laborious purification steps for the prepared monomers, resulting in materials that will ultimately have high cost and low yield.

In this section of Thesis, the inspiration of the discussed work mainly arises from the previous studies related to the polymers developed for organic field effect transistors, [69]considering also the structure-properties relationship exhisting in small-molecular HTMs used in n-i-p PSCs. [70] The aim was the synthesis of two novel copolymers employing a straightforward synthetic protocol for the controlled polymerization of two selected arylamines by the Buchwald–Hartwig cross-coupling, yielding the copolymers FlAnO and FlAnM (Figure 5.12) starting from appropriate AB-type monomers. [71] The satisfactory yielding reactions between 2,7-dibromo-9,9-dioctyl-9H-fluorene with selected primary aromatic amines 4-methoxyaniline or p-toluidine feature a facile workup, thus reducing time-intensive purification steps. The ability to alter the energetic position of the HOMO in these polymers by varying the 4-position of the primary amine demonstrates an ability to customize HTMs to different perovskite compositions. Moreover, this investigation demonstrate how the aryl amine moiety impacts relevant properties for incorporation into PSCs, including morphological and thermal stability, hydrophobicity, also comparing the hole mobility of the two materials to the hole mobility of undoped Spiro-OMeTAD. As promising HTMs, the polymers FlAnO and FlAnM produce n-i-p devices that can still be improved, illustrating the potential of these materials in perovskite photovoltaics. In addition, the reaction shows

promise for scaling up. Finally, the effects of polymer molecular weight and polydispersity on device functionality were explored.

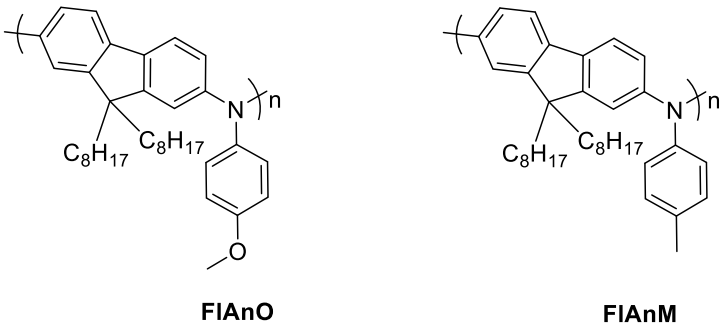

Figure 5.12. Chemical structures of the target copolymers FlAnO and FlAnM.

5.2.2 Results and discussion

Polymer synthesis and characterization

Buchwald−Hartwig amination coupling enables the formation of a carbon−nitrogen linkage between an aryl halide and a primary or secondary amine in the presence of a palladium catalyst and a strong base. In order to prepare the targeted polymers, dibrominated monomer 2,7-dibromo-9,9-dioctyl-9H-fluorene was coupled providing a carbon−nitrogen bond formation with the appropriate primary amine in the presence of palladium acetate, dppf as bidentate ligand and sodium tert-butoxide which acts as a strong base (Scheme 5.13). The adopted conditions (see Experimental section 5.3.) allowed to obtain FlAnO and FlAnM in a single step and with a chain growth control. [(71)] The polymerization reactions progresses were observed by the gradual clouding of the reaction mixture, owing to the precipitation of the sodium bromide byproduct in the toluene solvent system. To minimize the workup steps, the termination of the polymers was carried out in situ after 24 h of reaction. The choice of using p-toluidine (AnM) and p-anisidine (AnO) as aromatic amines was dicted by the idea of evaluating the different electron donating effect in the 4 position on the functionality and characteristics of the final polymers. However, the functional groups were also selected in order to avoid the dimerization of HTM molecules caused by the generation of

a radical placed in position 4 of a pendant group on the amine. [72] The reaction mixtures were cooled to room temperature and poured into MeOH. After extraction and precipitation processes, the resulting polymers were purified from the residual catalyst and low molecular weight impurities by subsequent Soxhlet extraction with methanol and dichloromethane, yielding polymers FlAnO and FlAnM in good yields. Both polymers showed good solubility in common organic solvents, such as dichloromethane (DCM), chlorobenzene, chloroform, tetrahydrofuran (THF) or toluene. Extensive characterization of the physical and electronic properties of the polymers was performed to better understand how different functional groups (-OMe and -CH_3) impact the Buchwald−Hartwig coupling and the potential application of these materials in PSCs. The results of these experiments are presented in Table 5.14.

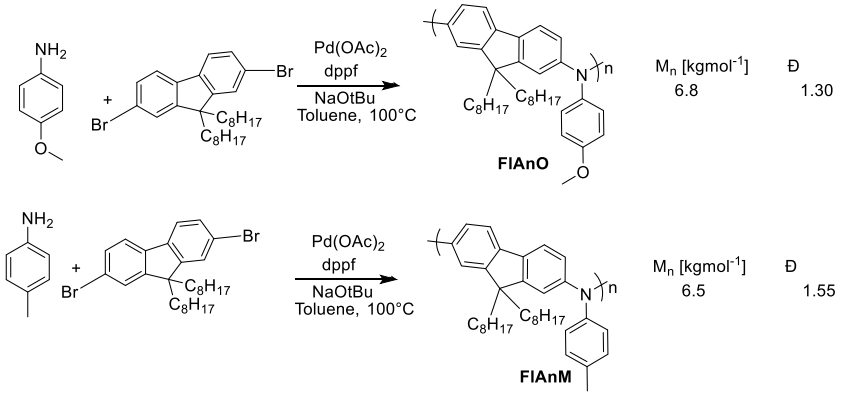

Figure 5.13. Synthetic sequence for the obtainment of P1 and P2 with the related number average molecular weight (M_n) and dispersity (Đ).

The size of the polymers was estimated by size exclusion chromatography (SEC) in THF with polystyrene standards for calibration and the data are found in Table 5.14. The number-average molecular weights M_n of FlAnO and FlAnM were 6.8 and 6.5 Kg mol^{-1}, leading to degrees of polymerization (X_n) of 13 and 12, respectively. The corresponding weight-average molecular weights (M_w) were 7.0 Kg mol^{-1} (FlAnO) and 6.6 Kg mol^{-1} (FlAnM), and both polymers showed very small polydispersities (PDI = M_w/M_n) of 1.30 and 1.55 for FlAnO and FlAnM,

respectively. These low molecular weights can be attributed to electron-donating effects of the primary amine used in the Buchwald−Hartwig coupling leading to faster dissociation during the reductive elimination step of the reaction. Furthermore, the bulky nature of the 9,9-dioctyl group of the fluorene monomer relative to the phenyl rings of p-anisidine (AnO) and p-toluidine (AnM) may lead to steric hindrance, causing these polymers to have the lowest overall M_w. However, as reported in the literature, molecular weights show a minor impact on the PSC performance for these types of HTMs. (73)

Table 5.14. Physical, Thermal, Optical and Electrochemical Properties of the HTM Polymers

HTM	M_n(KDa)[a]	Đ[a]	T_g/T_c (°C)[b]	T_d (°C)[b]	$\lambda_{max,abs}$ (nm)[c]	E_g (eV)[d]	exp. HOMO (eV)[e]	exp. LUMO (eV)[e]
Fl-AnO	6.8	1.30	62.0/213.0	375	397	2.82	–5.04	–2. 22
Fl-AnM	6.5	1.55	68.0/157.0	386	395	2.78	–5.14	–2.36

[a]Number-average molecular weights (M_n), and dispersity (Đ) as determined by GPC (PS standards, THF).

[b]Glass transition and cold crystallization temperatures (2nd heating scan) obtained by DSC under N_2.

[b]Decomposition temperature (5% weight loss) obtained by TGA under N_2. [c]UV VIS absorptions maxima measured in CH_2Cl_2 solution (10^{-5} M) at room temperature. [d]$E_g = 1240/\lambda_{onset}$ (eV).

[e]Determined by cyclic voltammetry: exp. HOMO = – [E_{ox} – $E_{(Fc/Fc^+)}$ + 5.10] (eV); exp. LUMO= E_{HOMO} + Eg (eV).

Investigation of thermal properties

Thermogravimetric analysis (TGA) carried out at a heating rate of 10 °C min^{-1} under nitrogen atmosphere indicated the high thermal stability of copolymers FlAnO and FlAnM (Figure 5.15 b), showing decomposition temperatures (T_d) (5% weight loss) of 375 °C and 386 °C (Table 5.14), which was well above operational conditions of PSCs. Differential scanning calorimetry (DSC) measurements of the investigated polymers revealed their amorphous nature; the second heating scans (Figure 5.15 a)), revealed very weak glass transitions at 62°C and 68 °C and broad cold crystallizations of the amorphous materials at 213°C and 157°C for FlAnO and FlAnM respectively. This last behavior could be due to the formation of different and more stable crystalline phases ascribed to the rearrangement of the alkyl chains on the fluorene units following the thermal history erasure of the as prepared samples. These two relevant thermal events at 213°C for FlAnO and 157°C for FlAnM, respectively, are favorable than those of spiro-OMeTAD, which generally exhibited a glass transition at 104 °C and a cold crystallization at 158 °C [(74)], thus indicating a stabilized amorphous state particularly relevant for photovoltaic applications of the new polymers.

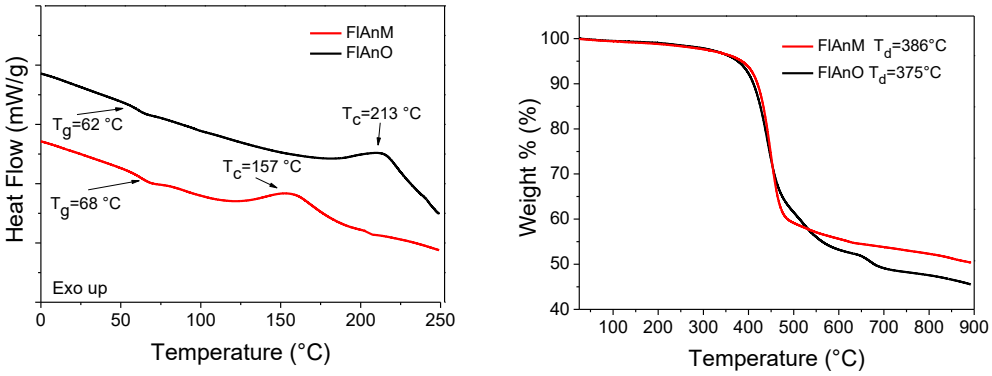

Figure 5.15. a) DSC traces of FlAnO (black) and FlAnM (red) (second heating scans) identifying the glass transitions (T_g) and cold crystallization (T_c) events. b) TGA curves of a) FlAnO (black) and FlAnM (red).

Optical and electrochemical properties

The normalized UV–vis absorption spectra of HTMs were recorded in CH_2Cl_2 (10^{-5} M) and depicted in Figure 5.16, while the corresponding absorption properties in solutions are listed in Table 5.14. Absorption peaks of FlAnO and FlAnM were located in the UV region and there was no significant absorption in the visible region, which is necessary for not competing with the perovskite in the absorption of light. Polymer FlAnO presented a maximum absorption wavelength ($\lambda_{max,abs}$) at 397 nm, which was similar to FlAnM (395 nm). From the onset of the absorption (λ_{onset}) edge in the longer wavelength region, the optical band gap (E_g) was estimated, and the values are 2.82 eV for FlAnO and 2.78 eV for FlAnM.

Cyclic voltammetry (CV, Figure 5.17) was employed to determine the electronic energy levels of the HTMs (these data are reported in Table 5.14). The investigations were performed in dichloromethane (HTM concentration: ~10^{-4} M) containing a 0.1 M solution of tetrabutylammonium tetrafluoroborate (0.10 M) as the supporting electrolyte under N_2 atmosphere. Comparing the electrochemical data listed in Table 5.14, it can be observed that FlAnO was more easily oxidized than FlAnM. The E_{HOMO} values of FlAnO and FlAnM calculated from CV are -5.04 and -5.14 eV, respectively.

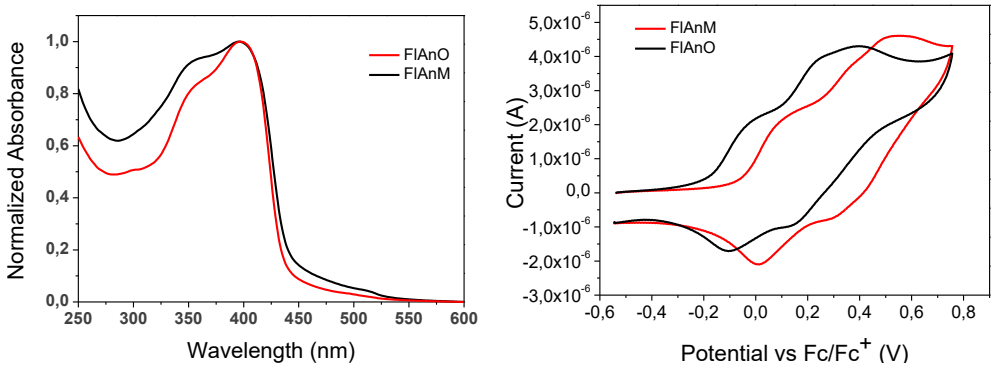

Figure 5.16 a) UV-VIS absorption spectra in dichloromethane (10^{-5} M) and b) cyclic voltammograms of FlAnO (red) and FlAnM (black).

Both polymers revealed suitable energetics to warrant efficient hole transfer from the perovskite to the HTMs. Moreover, the LUMO energy levels (E_{LUMO}) were estimated from the difference between E_{HOMO} and E_g of the polymers as -2.22 and -2.36 eV for FlAnO and FlAnM, respectively. The voltammograms showed two reversible oxidations waves for both materials. The stronger electron-donor properties of the additional -OCH_3 substituents in polymer FlAnO compared to polymer FlAnM are reflected at the remarkably low 1st oxidation potential.

Perovskite Solar Cells Employing Polymers FlAnO and FlAnM

To demonstrate the practical application of the novel polymers as dopant-free HTMs, polymers FlAnO and FlAnM were incorporated as HTMs in PSCs. This study was carried out in collaboration with the Hybrid Solar Cells team of the Chemistry and Advanced Materials group at Tampere University under the supervision of Professor Paola Vivo. The device architecture used for this investigation was the mesoporous regular structure FTO|cTiO2|mTiO2|Perovskite|HTM|Au. The materials and techniques used in this fabrication process are briefly discussed in the Experimental section 5.2.4., while figure 5.17 reports a simplified presentation of the solar cell structure.

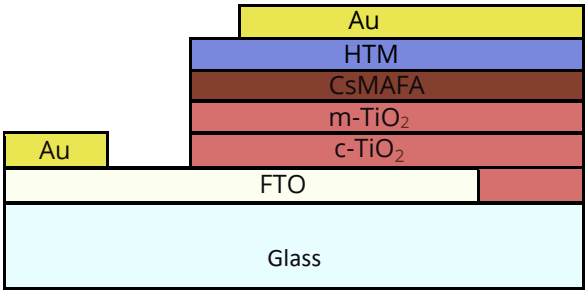

Figure 5.17 A simplified cross-section of the manufactured solar cells with doped Spiro-OMeTAD and new polymeric HTMs.

The perovskite layer was covered with a thin layer of the synthesised polymeric HTMs starting from chlorobenzene solutions at different concentrations in the range 1-20 mg ml^{-1}. Then, the compounds were spin-coated from chlorobenzene solutions and were used without any doping additives. Finally, the cell stacks were topped with a gold counter electrode deposited by thermal evaporation. The best HTM films, in terms of quality, were obtained using a concentration of 1 mg ml^{-1} of the starting solutions for both polymers. Figure 5.18 shows the current density-voltage (J-V) curves for the best perovskite solar cell devices measured under the standard AM 1.5G illumination at 1 sun (100 W cm^{-2}) using the novel polymers FlAnO.

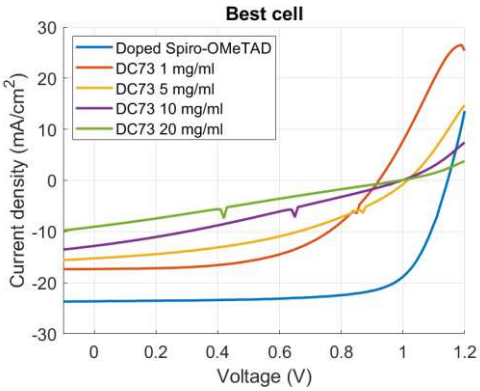

Figure 5.18. J-V curves of PSCs using polymers FlAnO (DC73 in the legend) and doped Spiro-OMeTAD as HTMs.

The highest efficiency corresponded to reference devices, with an average PCE of 8.8% was recorded for 1 mg ml^{-1} thin films of FlAnO and it can be clearly observed that increasing from 1 mg ml^{-1} to 20 mg ml^{-1} reduces device performance. The photovoltaic parameters extracted from J-V curves are summarized in Table 5.19. The low conductivity and hole mobility may explain why higher concentrations resulted in decreased performance, as they affect the fill factor of the cell.

Table 5.19. Average photovoltaic parameters determined form J-V measurements using polymers FlAnO and Spiro-OMeTAD as HTMs. The photovoltaic parameter PCE of the best working cell is shown in brackets.

sample	PCE (%)	FF (%)	Isc (mA/cm^2)	Voc (V)	area (mm^2)
Spiro-doped (Reference)	19.4	72.8	23.5	1.1	20.0
FlAnO 1 mg/ml	7.6 (8.8)	50.3	16.5	0.9	20.0
FlAnO 5 mg/ml	6.1	40.0	15.2	1.0	20.0
FlAnO 10 mg/ml	4.1	37.8	11.3	1.0	20.0
FlAnO 20 mg/ml	2.8	34.7	8.4	1.0	20.0

A similar trend was observed in FlAnM-based devices (J-V curve in Figure 5.20) with the highest efficiency having an average PCE of 7.66% which was recorded for 1 mg ml^{-1} thin films of the polymer as reported in Table 5.21.

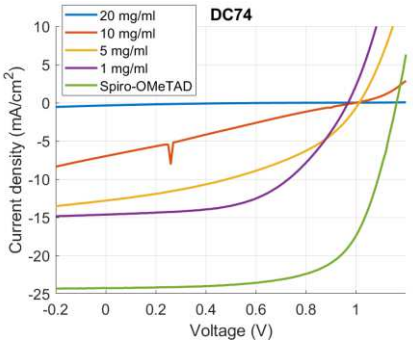

Figure 5.20. J-V curves of PSCs using polymers FlAnM (DC74 in the legend) and doped Spiro-OMeTAD as HTMs.

The low conductivity and hole mobility observed may explain why higher concentrations resulted in decreased performance, as they affect the fill factor of the cell.

However, the hole mobility of these HTMs was somehow low, and thus further study should be directed to doping them may be warranted.

Table 5.21. Average photovoltaic parameters determined form J-V measurements using polymers FlAnM and Spiro-OMeTAD as HTMs.

	PCE (%)	FF (%)	Isc (mA/cm^2)	Voc (V)	Area (mm^2)
Spiro-doped (Reference)	18,30	66,47	23,73	1,16	20,00
FlAnM 1 mg/ml	6,02	50,97	12,93	0,91	20,00
FlAnM 5 mg/ml	5,21	39,82	12,99	1,01	20,00
FlAnM 10 mg/ml	1,58	25,31	6,17	1,00	20,00
FlAnM 20 mg/ml	0,07	15,14	0,47	0,97	20,00
Best cell FlAnM 1 mg/ml	7,66	54,49	14,64	0,96	20,00

In summary, in their n-i-p configuration, devices based on FlAnO and FlAnM significantly underperform compared to the Spiro-OMeTAD. In particular, the J–V behavior appears like a strain line with respect to the diode-like curve shown by the Spiro-OMeTAD device, suggesting that the charge collection is strongly limited by series resistance. It can be concluded that the FlAnO and FlAnM HTM layers in this configuration are significantly less conductive than the Spiro-OMeTAD one. It can be supposed that, in the case of the n-i-p devices, where a thicker layer is required, a certain limitation to the transport properties of the HTM film takes place, leading to a disequilibrium between generated/extracted/transported charges at the perovskite/HTM interface. The effect of alkyl chains decorating the HTM scaffold on the PSC performances in n-i-p configurations was scrutinized by Nazeeruddin [(75)] as well as by Hagfeldt and co-workers: [(76)] indicating that the charge extraction and hole mobility are negatively affected by peripherally positioning the alkyl chains. This behavior may be overcome in a p-i-n device construction, where the contact between the organic layer of FlAnO or FlAnM and the polar solvent dissolving the perovskite precursors, followed by the thermal treatment required for the perovskite layer generation, can reasonably promote the formation of a favorable molecular arrangement at the perovskite/HTM interface, ensuring more efficient device performances in spite of the intrinsic charge transport properties of the employed HTMs.

Conclusions

Two novel polymer HTMs were synthesized utilizing a Buchwald–Hartwig-type polycondensation of aniline derivatives and a poly-alkylated dibromofluorene-based monomer in high yielding, low-cost, and simple workup reactions. The novel HTMs exhibited excellent thermal and optoelectronic properties and they presented suitable HOMO levels, which were perfectly aligned with that of the perovskite material. Co-polymerizations of groups that perform well will also be investigated in order to customize favorable polymer properties. Further investigations are needed to explore the possible advantages that these polymers could give, since devices were not optimized and also investigations regarding stability are required. However, this study clearly demonstrates that investigation of new possible structures as charge carriers is fundamental in order to achieve stable and efficient PSCs. The possibility of working without doping additives is undoubtedly an important step towards this goal and in that way, to open up a space for PSCs in the market. Moreover, I think that understanding the HTM role in differently configured PSCs could open new frontiers for the rational design and manipulation of the perovskite/HTM interface aiming at improving performances beyond the state-of-the-art.

5.2.3 Experimental section

All reagents and solvents were purchased from standard commercial sources and used as received. The syntheses were carried out under inert nitrogen atmosphere using standard Schlenk techniques. ^{1}H-NMR spectra were recorded on a Bruker Avance DPX 300 MHz instrument. ^{1}H chemical shifts were referenced to TMS in $CDCl_3$. Gel-permeation chromatography (GPC) analyses were carried out on an Agilent Series 1100 instrument equipped with a Pl-gel 5 µm mixed-C column. The samples were dissolved in THF and were eluted at a 1.0 mL/min flow rate. Detection was performed by a multiple wave UV-Vis detector. Number-average molecular weights (M_n), weight-average molecular weights (M_w) and

dispersity (Đ) were calculated against polystyrene standards. The synthesis of monomer 2,7-dibromo-9,9-dioctylfluorene (Fl) was performed according to a literature procedure. [71]

Synthesis of the polymer FlAnO

A mixture of 2,7-dibromo-9,9-dioctylfluorene (0.274 g, 0.50 mmol), 4-methoxyaniline (0.062 g, 0.50 mmol), $Pd(OAc)_2$ (11.2 mg, 5.0×10^{-2} mmol), dppf (55.4 mg, 0.10 mmol), sodium tert-butoxide (0.144 g, 1.50 mmol), and toluene (7.5 mL) was charged in a 25 mL Schlenk tube, was then subjected to three vacuum/nitrogen refilling steps and stirred at 110 °C for 24 hours. The reaction mixture was then cooled to room temperature and poured into MeOH (150 mL) under vigorous stirring for the precipitation of the polymer. The precipitate was collected by filtration and washed in a Soxhlet apparatus with methanol and then extracted with dichloromethane. The dichloromethane fraction was reduced to 2 mL and reprecipitated in cold methanol yielding a green solid (0.218 g, yield 81%) that was dried in vacuo for 12 hours. ^{1}H NMR (300 MHz, $CDCl_3$): δ 7.74–7.63 (2H), 7.59–7.47 (4H), 7.29–7.21 (6H), 3.81–3.57 (3H), 1.52–1.40 (2H), 1.22–1.01 (12H), 0.94–0.57 (24H) ppm.

Synthesis of the polymer FlAnM

A mixture of 2,7-dibromo-9,9-dioctylfluorene (0.274 g, 0.50 mmol), p-toluidine (0.054 g, 0.50 mmol), $Pd(OAc)_2$ (11.2 mg, 5.0×10^{-2} mmol), dppf (55.4 mg, 0.10 mmol), sodium tert-butoxide (0.144 g, 1.50 mmol), and toluene (7.5 mL) was charged in a 25 mL Schlenk tube, was then subjected to three vacuum/nitrogen refilling steps and stirred at 110 °C for 24 hours. The reaction mixture was then cooled to room temperature and poured into MeOH (150 mL) under vigorous stirring for the precipitation of the polymer. The precipitate was collected by filtration and washed in a Soxhlet apparatus with methanol and then extracted with dichloromethane. The dichloromethane fraction was reduced to 2 mL and reprecipitated in cold methanol yielding a yellowish-green solid (0.223 g, yield

85%) that was dried in vacuo for 12 hours. ^{1}H NMR (300 MHz, $CDCl_3$): δ 7.74–7.63 (2H), 7.59–7.47 (4H), 7.29–7.21 (6H), 2.61–2.37 (3H), 1.52–1.40 (2H), 1.22–1.01 (12H), 0.94–0.57 (24H) ppm.

Solar cells fabrication

The experimental part described in this subsection was developed at the Hybrid Solar Cells team of the Chemistry and Advanced Materials group at Tampere University under the supervision of Professor Paola Vivo. All reagents and solvents were purchased from standard commercial sources and used as received. Unless specified otherwise, processes were performed in air. The solar cells were fabricated on fluorine-doped tin oxide (FTO) glass substrates (TEC 15, Greatcell Solar) with dimensions 20×20×2.2 mm, which were wet chemically etched on one edge with 2.4 M HCl solution and zinc powder. Etched substrates were cleaned with 2 % Mucasol solution in deionized water and sonicated in DI water, acetone, and 2-propanol for 15 minutes each, followed by swiftly drying under a N_2 stream. A compact TiO_2 layer (c-TiO_2) was deposited on the substrates via spray pyrolysis at 450 °C using N_2 as the carrier gas. The precursor solution was prepared by diluting a titanium diisopropoxide bis(acetylacetonate) stock solution (75 % in 2-propanol, Sigma-Aldrich) further to 17.3 vol%. 12 layers of the precursor solution (< 8 ml) were sprayed on the substrates with 20 seconds between each cycle, followed by sintering at 450 °C in air for a minimum of 45 minutes. A mesoporous TiO_2 (m- TiO_2) scaffold layer was deposited by spin coating an ethanolic suspension of 30 NRD TiO_2 nanoparticle paste (Greatcell Solar), with 150 mg of paste in 1 ml ethanol. 80 µl of suspension was spin coated at 4000 rpm for 10 s, followed by a few minutes of annealing at 100 °C prior to calcination at 450 °C for 30 minutes (heat ramp duration: ~45 minutes). The substrates were then cooled down to 150 °C and transferred to a nitrogen-filled glovebox for perovskite and HTM deposition.

The CsFAMA perovskite precursor was prepared 24–48 hours prior, comprising FAI (0.95 M, Greatcell Solar Materials), MABr (0.19 M, Greatcell Solar Materials),

$PbBr_2$ (1.1 M, TCI), PbI_2 (0.20 M, TCI), and CsI (0.06 M, abcr) in a mixed solvent of DMSO:DMF (1:4 volume ratio). The solution was kept in stirring until use. 50 µl of the solution was spin coated onto the as-prepared FTO/c-TiO_2/m-TiO_2 substrates at 1000 rpm for 10 s, followed by 6000 rpm for 20 s. Antisolvent treatment was done by dropping 100 µl of chlorobenzene onto the substrate 5 seconds prior to the end of the program. The perovskite films were immediately transferred to a hot plate for annealing at 110 °C for 1 hour. After annealing and cooling down, the polymeric HTMs and reference doped Spiro-OMeTAD were dynamically spin coated on top of the perovskite film at 1800 rpm for 40 s. FlAnO and FlAnM HTMs were tested in four concentrations (1, 5, 10, 20 mg/ml in chlorobenzene), with 1 mg/ml yielding highest performance. The doped Spiro-OMeTAD solution was prepared by dissolving Spiro-OMeTAD (Lumtec) in chlorobenzene in a 29.5 mM concentration and stirring at 60 °C for a few minutes. After cooling down dopants were added: 4-tert-butylpyridine (Sigma-Aldrich), Li-TFSI (Sigma-Aldrich, pre-dissolved in acetonitrile 520 mg/ml), and FK209 (Dyenamo, pre-dissolved in acetonitrile 300 mg/ml). Their molar equivalents to Spiro-OMeTAD were 3.2, 0.53, and 0.1, respectively. After HTM deposition, the samples were removed from the glovebox, and kept in a dry cabinet overnight. Finally, 100 nm thick gold electrodes were evaporated on top of the HTM layer using an Edwards Auto 306 vacuum deposition unit in a vacuum of approximately 10^{-5} mbar.

Device and film characterization

The unencapsulated perovskite solar cells, with an active area of 20 mm^2 were characterized in air. The current density (J)-voltage(V) curves were recorded at a scan rate of 50 mV s^{-1} with a Keithley 2450 SMU (controlled by a measurement program written in MATLAB) and a SS150-AAA solar simulator (Sciencetech, Canada) under air mass 1.5 simulated sunlight (100 mW cm^{-2}), calibrated with a KG5 reference cell and meter (Newport, USA).

5.3 Simplified and cost-effective fluorene-based hole-transporting materials for stable perovskite solar cells

5.3.1 Target

Despite the rapid and astonishing development of perovskite halide (PSC) solar cells, which has currently led to a certified power conversion efficiency (PCE) of 25.7%, i.e. comparable to that of silicon photovoltaics, [77] the modest stability of PSCs under environmental conditions, still limits their widespread adoption. The organic hole transporting material (HTM) plays an extremely important role not only in facilitating hole-extraction and electron-blocking but also in improving the device stability, mainly acting as protective layer for perovskite. [78] However, recent research efforts are focused on the specific chemical interactions between the perovskite and the HTM, exploiting novel molecular designs enable to simultaneously improve the HTM function with the formation of compact and ordered interfaces with the perovskite and significantly boosting the PSC stability. [79]

In this perspective, the present section of the Thesis describes the development of a suitable molecular design approach towards new small molecular HTMs, as simplified and cost-competitive alternatives to the traditional Spiro-OMeTAD HTM. These novel molecules have been conceived by eliminating the orthogonal portion of Spiro-OMeTAD scaffold aiming to reduce the molecular distortion required for the surface interaction between the HTM and the perovskite. A straightforward synthetic protocol has been developed to simplify and reduce material consumption allowed us to obtain two potential HTMs, namely SCF1 and SCF2 with high yields (93-95%). Independently of the peripheral functional groups (–OCH_3 or –CH_3 for SCF1 and SCF2, respectively), they exhibited suitable energy levels for charge extraction from the perovskite layer, good thermal and morphological stability, hydrophobicity, as well as comparable hole mobility to undoped Spiro-OMeTAD, yet at a fraction of its synthetic sequence. The collaborative interactions with the Hybrid Solar Cells team of the Chemistry and Advanced Materials group at Tampere University directed by the Professor Paola Vivo and with the Department of Chemical Sciences of the University of Naples

Federico II allowed us to rationalize how the molecular interactions influence the adhesion between the HTM and the perovskite surface promoting the long-term PSC stability by comparing the behavior of traditional Spiro-OMeTAD with simplified structures derived from it (named SCF1 and SCF2, see Figure 5.22.). When SCF-HTMs were employed as thin layers (more than 3 times thinner than traditional HTMs) in n-i-p structure PSCs with triple-cation halide perovskite $Cs_{0.05}(FA_{0.83}\ MA_{0.17})_{0.95}Pb(I_{0.83}Br_{0.17})_3$ (CsFAMA), the champion SCF1-based displayed an impressive shelf-stability with a T_{80} lifetime of 431 days. This collaborative work highlights the importance of the molecular design in the development of novel HTMs enable to establish ordered and stable interfaces with the perovskite. Furthermore, the significance of long-term device stability studies (e.g., > 1 year) when assessing a new HTM is emphasized, as for any practical application the performance over time is more meaningful than that of as-fabricated devices.

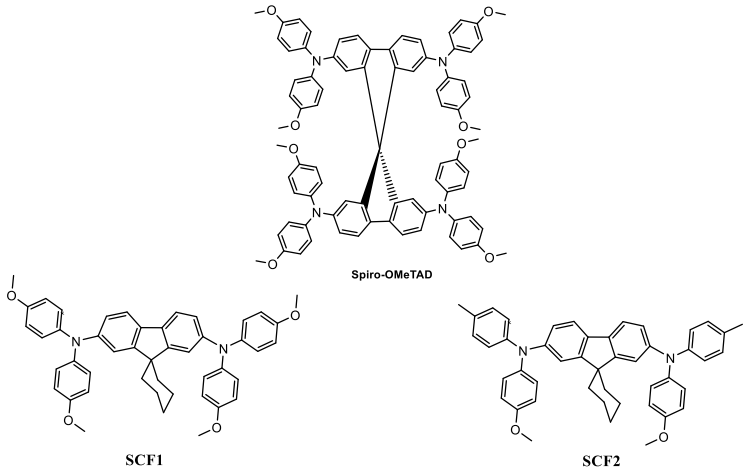

Figure 5.22. Chemical structures of the target HTMs SCF1 and SCF2 in comparison with that of Spiro-OMeTAD.

5.3.2 Results and discussion

Synthesis and characterization

The novel designed HTMs were synthesized adopting a convergent approach which requires sequential Buchwald-Hartwig aminations (Scheme 5.23). The synthetic route for the obtainment of the SCF-scaffold, 2',7'-dibromospiro[cyclohexane-1,9'-fluorene](1) relied on well-established and convenient literature procedure [80] detailed in the Experimental section 5.3.4. The secondary diarylamines bis(4-methoxyphenyl)amine (2) and 4-methoxy-N-(p-tolyl)aniline (3) were synthesized in high yields via catalyzed C–N Buchwald-Hartwig cross coupling reactions between 1-bromo-4-methoxybenzene and 4-methoxyaniline or p-toluidine, respectively. In this last coupling reactions, we selected the suitable catalytic system based on $Pd(OAc)_2$/dppf and sodium tert-butoxide as base. Further Buchwald-Hartwig aminations, in similar conditions, lead to the target molecules SCF1 (95% yields), and SCF2 (93% yields) adopting the catalytic couple Pd_2dba_3/XPhos. [81]

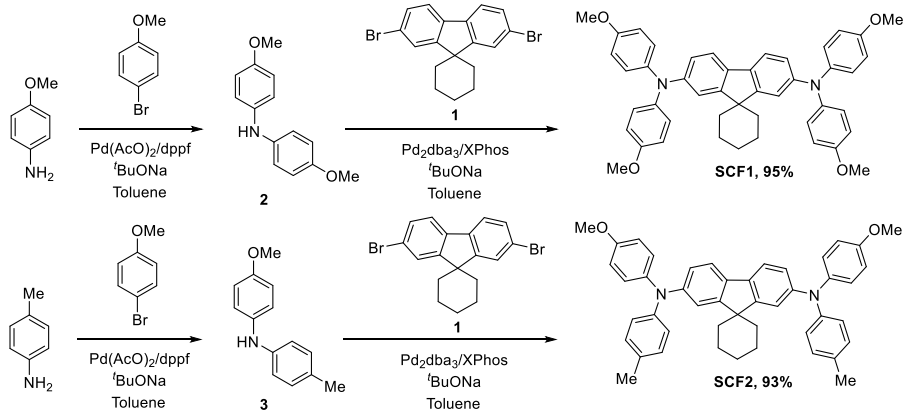

Scheme 5.23. Synthetic sequence for the obtainment of SCF1 and SCF2 and relatives yields %.

Such a synthetic path is much simpler than the synthetic routes for spiro-OMe-TAD as mentioned in section 5.1.4 and proceeded with higher yields. It is worth

mentioning that 2Br-SCF (1) could be obtained from very cheap raw materials with good yield (> 64%), which was highly beneficial to reduce the overall cost of HTMs and PSCs. With the aim to emphasize this important aspect, we estimated the cost of the final products according to the adopted synthetic routes and details are depicted in Tables 5.24. The final costs of 29.40 €/g and 32.78 €/g for SCF1 and SCF2, respectively, resulted significantly lower than what has been estimated for Spiro-OMeTAD (raw material cost is 86 €/g).

Tables 5.24. Cost evaluation of SCF1 and SCF2.

Reagent	Amount (g)	Amount (mL)	Price (€/g or €/mL)	Total price (€)
2,7-dibromofluorene	3.882		7.880	30.590
n-Bu_4NBr	1.328		0.899	1.194
NaOH (50% w/v)		26.00	0.086	1.118
1,5-dibromopentane	2.755		0.467	1.287
Toluene		26.00	0.051	1.326
Silica gel	100		0.037	3.700
Petroleum ether 40-60 °C		450	0.006	2.700
Total cost	41.915 €			
Amount intermediate **1**	2.990 g			
COST for intermediate **1**	14.018 €/g			
Reagent	**Amount (g)**	**Amount (mL)**	**Price (€/g or €/mL)**	**Total price (€)**
4-bromoanisole	2.990		0.399	1.193
I-anisidine	1.970		0.379	0.747
$Pd(AcO)_2$	0.072		91.020	6.553
dppf	0.360		23.520	8.467
^tBuONa	2.310		0.441	1.019
Toluene		20.00	0.051	1.020
Silica gel	100.00		0.037	3.700
Petroleum ether 40-60 °C		300.00	0.006	1.800
Methylene chloride		250.00	0.008	2.000
Total cost	26.499 €			
Amount intermediate **2**	3.118 g			
COST for intermediate **2**	8.499 €/g			

Reagent	Amount (g)	Amount (mL)	Price (€/g or €/mL)	Total price (€)
4-bromoanisole	2.990		0.399	1.193
p-toluidine	1.714		0.052	0.089
$Pd(AcO)_2$	0.072		91.020	6.553
dppf	0.360		23.520	8.467
^{t}BuONa	2.310		0.441	1.019
Toluene		20.00	0.051	1.020
Silica gel	100.00		0.037	3.700
Petroleum ether 40-60 °C		300.00	0.006	1.800
Methylene chloride		250.00	0.008	2.000
Total cost	25.841 €			
Amount intermediate **3**	3.241 g			
COST for intermediate **3**	7.973 €/g			

Reagent	Amount (g)	Amount (mL)	Price (€/g or €/mL)	Total price (€)
1	0.500		14.018	7.009
2	0.640		8.499	5.439
$Pd_2(dba)_3$	0.033		40.200	1.327
XPhos	0.030		42.800	1.284
^{t}BuONa	0.403		0.441	0.178
Toluene		20.00	0.051	1.020
Silica gel	100.00		0.037	3.700
Petroleum ether 40-60 °C		200.00	0.006	1.200
Methylene chloride		350.00	0.008	2.800
Total cost	23.957 €			
Amount **SCF1**	0.815 g			
COST for **SCF1**	29.395 €/g			

Reagent	Amount (g)	Amount (mL)	Price (€/g or €/mL)	Total price (€)
1	0.500		14.018	7.009
3	0.597		7.973	4.760
$Pd_2(dba)_3$	0.033		40.20	1.327
XPhos	0.030		42.80	1.284
^{t}BuONa	0.403		0.350	0.141
Toluene		20.00	0.051	1.020
Silica gel	100.00		0.037	3.700
Petroleum ether 40-60 °C		200.00	0.006	1.200
Methylene chloride		350.00	0.008	2.800
Total cost	23.241 €			
Amount **SCF2**	0.709 g			
COST for **SCF2**	32.780 €/g			

Both SCF-based HTMs showed good solubility in organic solvents, e.g., dichloromethane and chlorobenzene. The molecular structures were characterized and confirmed by ^{1}H and ^{13}C NMR spectroscopy (see Experimental section 5.3.4) and electrospray ionization-mass spectrometry (ESI)-MS study.

Investigation of thermal properties

The thermal stability of newly developed HTMs was investigated by thermal gravimetric analysis (TGA) and differential scanning calorimetry (DSC) techniques performed under nitrogen atmosphere (Figure 5.25). TGA carried out at a heating rate of 10 °C min^{-1} results manifest the excellent thermal stability with decomposition temperatures (T_d) (5% weight loss) of 389 and 370 °C for SCF1 and SCF2 respectively, well above operational conditions of PSCs. Differential scanning calorimetry (DSC) measurements of the investigated HTMs revealed their amorphous nature. According to the second heating scans (Figure 5.25 b)), as expected, similar behavior was observed for both molecules with glass transitions at 80°C and 84 °C for SCF1 and SCF2 respectively, thus indicating a good tendency of SCF1 and SCF2 to resist the change of molecular arrangement in working conditions, showing good potential to sustain thermal stability in PSCs devices.

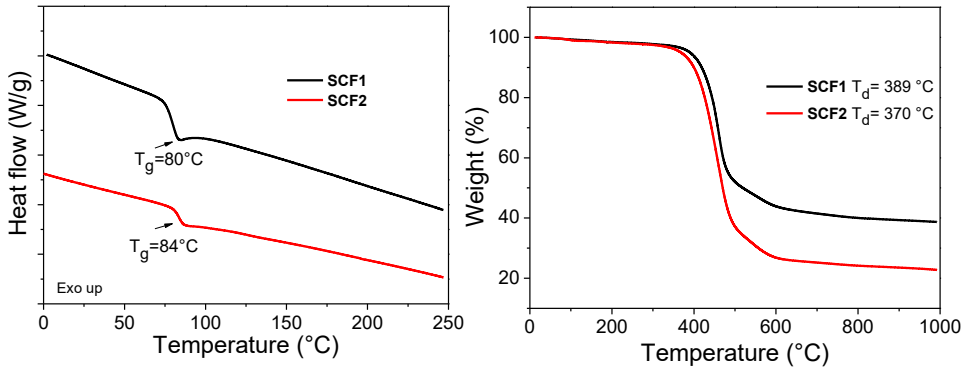

Figure 5.25. a) DSC traces of SCF1 (black) and SCF2 (red) (second heating scans) identifying the glass transitions (T_g) events. b) TGA curves of SCF1 (black) and SCF2 (red).

Optical and electrochemical properties

The normalized UV–vis absorption spectra of HTMs were recorded in CH_2Cl_2 (10^{-5} M) and depicted in Figure 5.26 a), while the corresponding absorption values in solutions are listed in Table 5.27. The absorption bands at the high-energy region at 300–450 nm originated from the localized aromatic π–π* transitions of the SCF-scaffold, thus both SCF1 and SCF2, being nearly transparent in the visible region, are suitable for implementation in p–i–n devices because they do not compete with the perovskite active materials for light harvesting. Cyclic voltammetry (CV, Figure 5.26 b)) was employed to determine the electronic energy levels of the HTMs (the data are reported in Table 5.27). The voltammograms showed two well resolved and reversible oxidation events for both materials, plausibly owing to electronic coupling between the two redox centers present onto the molecules. In fact, electrons from bis(4-methoxyphenyl)amine groups are removed at lower 1st oxidation potential confirming the stronger electron-donor properties of the additional -OCH_3 substituents in SCF1. However, the HOMO levels of SCF1 and SCF2 are well aligned with the valence band (VB) maximum of CsFAMA [82] perovskite and are similar to the highest occupied molecular orbital (HOMO) of Spiro-OMeTAD (–5.02 eV) measured in the same electrochemical conditions.

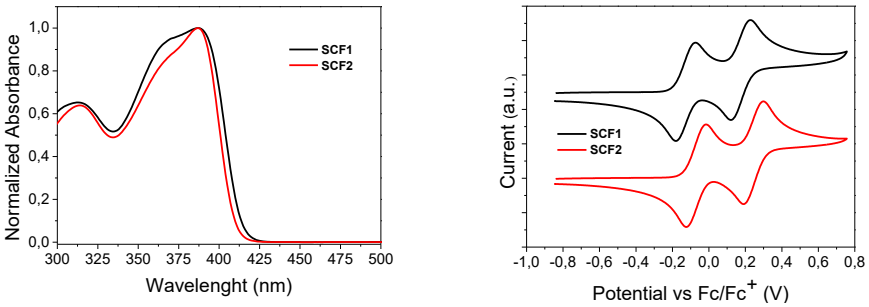

Figure 5.26 a) UV-VIS absorption spectra in dichloromethane (10^{-5} M) and b) cyclic voltammograms of SCF1 (black) and SCF2 (red).

Table 5.27. Thermal, Optical and Electrochemical Properties of the synthesized HTM.

HTM	T_d[a] (°C)	T_g[a] (°C)	λ_{max}[b] (nm)	E_g[c] (eV)	HOMO[d] DFT (eV)	LUMO[d] DFT (eV)	HOMO[e] Exp. (eV)	LUMO[f] Exp. (eV)	μ_h[g] ($cm^2V^{-1}s^{-1}$)	σ[h] ($S\ cm^{-1}$)
SCF1	389	80	388	2.99	–4.69	–1.14	–4.97	–1.98	5.7×10^{-5}	1.5×10^{-6}
SCF2	370	84	387	3.02	–4.79	–1.20	–5.03	–2.01	3.6×10^{-5}	5.7×10^{-7}

[a] Decomposition (T_d, 5% weight loss) and glass transition (T_g) temperatures recorded by TGA and DSC measurements, respectively (10 °C/min, N_2 atmosphere). [b] Absorption maxima measured in CH_2Cl_2 solution (10^{-5} M). [c]Optical bandgap $E_g = 1240/\lambda_{onset}$ (eV). [d] Calculated at the B3LYP/6-311G(d,p)/CPCM(CH_2Cl_2) level of theory. [e] Determined by cyclic voltammetry with the equation: exp. HOMO = – [E_{ox} – E(Fc/Fc$^+$) + 5.10] (eV). [f]exp LUMO = exp. HOMO + E_g (eV). [g] Average hole mobility (μ_h) determined via SCLC method from glass|ITO|PEDOT:PSS|HTM|MoO_3|Au devices. [h] Average HTM-film conductivity (σ) obtained via four-point measurement.

The LUMO energy levels (E_{LUMO}) were calculated from the difference between E_{HOMO} and the optical energy gap E_g. The comparable values of -1.98 eV and -2.01 eV for SCF1 and SCF2, respectively allowed us to predict an efficient electron blocking effect from the conduction band of perovskite active layer. Density functional theory (DFT) calculations resulted fundamental to support and confirm the trend of the experimental data. The analyses of the ground-state geometries were studied using the Gaussian 09 (83) software package. It is worth noting that for both molecules the lowest-unoccupied molecular orbitals (LUMOs) are mainly localized on the SCF core, whereas the electron density of the HOMOs localized on the bis-arylamine groups (Figure 5.28).

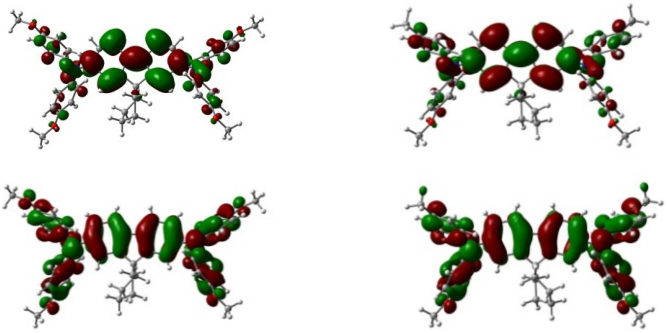

Figure 5.28. Electronic density distribution (isovalue = 0.02 e/Å^3) of the frontier molecular orbitals (HOMO and LUMO) for SCF1 and SCF2.

Perovskite Solar Cells Employing SCF1 and SCF2

A complete photovoltaic characterization of the new SCF-based HTMs was carried out by the Hybrid Solar Cells team of the Chemistry and Advanced Materials group of the Tampere University under the supervision of Professor Paola Vivo. This study was further supported through an extensive theoretical study of the CsFAMA|HTM interfaces thanks to collaboration with the Department of Chemical Sciences, University of Naples Federico II.

Preliminarly, the hole mobility (μ_h) of SCF-HTMs, was determined by space-charge-limited current (SCLC) method, and their conductivity (σ), assessed by four-point probe measurements are listed in Table 5.27, more details of these investigations are described in the Experimental section 5.3.4. Briefly, it was observed that SCF1 displayed higher hole mobility and conductivity than those of SCF2 and the charge transport capabilities of both molecules were compared to that of Spiro-OMeTAD HTM, both doped with and without tBP, Li-TFSI, and FK209 additives (as in traditional PSCs), under identical conditions. SCF1 and SCF2 have a higher potential for effective charge transport than undoped Spiro-OMeTAD.

Hole extraction kinetics

Photoluminescence studies were performed with the aim to reveal and confirm the hole extraction capability of novel SCF-HTMs. As depicted in Figure 5.29 a), an effective analysis consists on the comparison between the steady-state photoluminescence spectra of glass|CsFAMA and glass|CsFAMA|HTMs samples, including the doped Spiro-OMeTAD as the reference, both excited at 600 nm. The result was a clear PL quenching for both the HTMs. By comparing the PL amplitudes of pure perovskite and perovskite|HTM samples, the quenching efficiencies, i.e., hole extraction efficiency, were estimated as 99.6%, 99.7%, and 99.1% for reference Spiro-OMeTAD, SCF1, and SCF2, respectively. This promising behavior was further assessed studying the hole extraction dynamics by measuring the time-resolved PL (TRPL) decays for those same samples, as shown in Figure 5.29 b). A gradual decay acceleration was observed for glass|CsFAMA|SCF-HTMs

when moving from SCF2 to SCF1, revealing that the hole extraction process becomes faster, which is also in agreement with the PL quenching data.

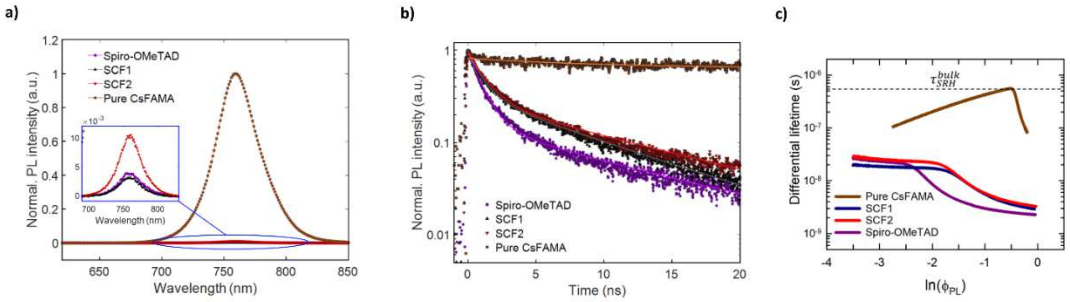

Figure 5.29. a) Normalized photoluminescence (PL) spectra (excited at 600 nm) and b) time-resolved PL (TRPL) decays (excited at 405 nm with a time resolution of 60 ps and monitored at 755 nm) of glass/CsFAMA and glass/CsFAMA/HTM films with SCF-HTMs and doped Spiro-OMeTAD as the reference. Solid lines show the fitting results with a rate law function. c) Differential lifetime as a function of the logarithm of the PL intensity ($ln\,\Phi_{PL}$).

Performance of SCF-HTM-based Solar Cells

The device architecture used for this study was the mesoporous conventional n-i-p structure (glass|FTO|compact TiO_2|mesoporousTiO_2|CsFAMA|HTM|Au). The perovskite contains three different organic cations namely Cs^+, MA^+ and FA^+ and the HTMs were employed without dopants. Figures 5.30 a) shown the energy levels of the PSC constituents and the device architecture, respectively. Details on the fabrication and characterization of PSCs are provided in the Experimental section 5.3.4. After various attempts with different concentrations of SCF-HTMs (as reported in Table 5.55 in Experimental section 5.3.4), the optimized thickness of SCF-HTMs in PSCs (~90 nm) were obtained from a concentration of 10 mg mL^{-1} SCF-HTM in chlorobenzene. A cross-sectional SEM images of the fabricated solar cells was reported in Figure 5.30 c) and Figure 5.54. Further reducing the thickness of SCF-layers led to decreased performance, due to inadequate coverage of the perovskite layer.

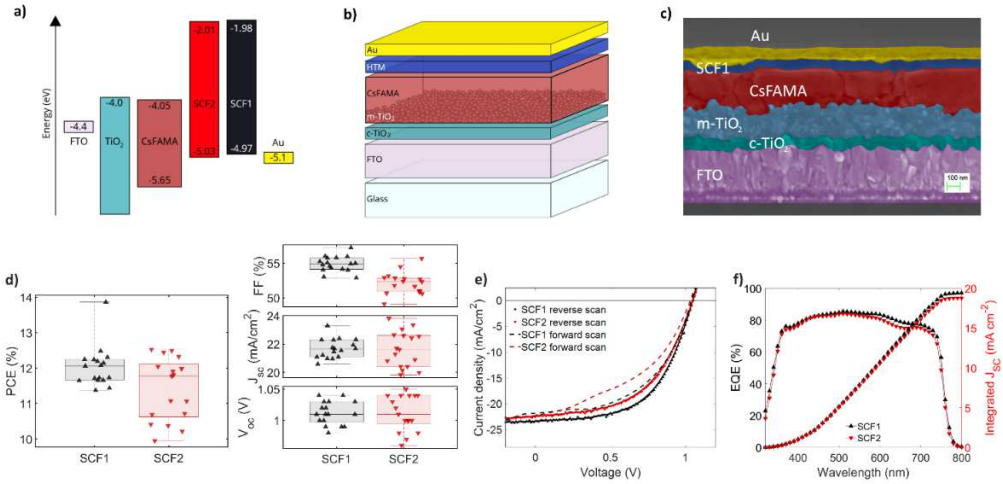

Figure 5.30 a) Energy level diagram for SCF-HTMs and other layers of the fabricated CsFAMA-PSCs. Aside from SCF-HTMs, the values have been taken from the literature. [84] [85] *b) The structure of the fabricated mesoporous n-i-p solar cells. c) Cross-sectional SEM image of a fabricated solar cell employing* ***SCF1*** *as the HTM. d) Statistical representation of the photovoltaic parameters derived from the reverse scans of 17 PSCs for each SCF-HTM. Measurements were taken approximately 1 week after fabrication, under 1-Sun illumination (with a scan rate of 50 mV* s^{-1}*). e) Current density (J) –voltage (V) curves of champion PSCs employing* ***SCF1*** *and* ***SCF2****. f) EQE spectra and integrated* J_{SC} *values of typical SCF-HTMs-based PSCs.*

The performance of the solar cells was evaluated by recording *J–V* characteristics both in dark and under 1-Sun illumination (AM 1.5G, 100 mW cm^{-2}). The PCE of SCF-HTM-based devices improved significantly after fabrication, with the most noticeable effect occurring within one week. The averaged photovoltaic parameters from 17 devices are reported in Table 5.31. and their statistics are illustrated in Figure 5.30 d). In addition to the devices based on the SCF-HTMs, the performance of reference devices using doped Spiro-OMeTAD as HTM (with otherwise identical structures) is also reported in Table 5.31. for comparison. Additionally, Figure 5.30 e) compares the *J–V* curves of the champion devices. The improved performance of SCF1 over SCF2 could be attributed to its greater hole mobility and hole extraction capability.

Table 5.31. Averaged photovoltaic parameters, hysteresis index, and resistance values of 17 solar cells of each HTM characterized after approximately 1 week.

HTM	PCE (%)	FF (%)	Jsc (mA cm^{-2})	Voc (V)	H-index [a]	R_S [b] (Ω cm^2)	R_{SH} [c] (kΩ cm^2)
Spiro-OMeTAD	17.8±1.0 (20.0) [d]	69.3±1.9 (72.2)	22.5±0.7 (23.5)	1.14±0.03 (1.18)	1.05±0.03 (1.06)	6.1±0.8 (4.9)	1.82±0.50 (1.89)
SCF1	12.0±0.6 (13.9)	54.9±1.1 (57.2)	21.7±0.7 (23.3)	1.01±0.02 (1.04)	1.10±0.07 (1.16)	10.8±0.6 (9.3)	0.55±0.18 (0.61)
SCF2	11.4±0.9 (12.7)	52.1±1.5 (53.2)	21.6±1.2 (22.5)	1.01±0.03 (1.06)	1.08±0.10 (1.25)	13.4±1.3 (11.2)	0.45±0.07 (0.44)

[a] Hysteresis index is calculated as PCE_{rev}/PCE_{for}, where 'rev' and 'for' stand for reverse and forward scans, respectively. [b] Series resistance [c] Shunt resistance [d] The photovoltaic figures of merit of the champion devices are reported in brackets.

Compared to the champion SCF2 device (PCE 12.7%), the best SCF1-based PSC showed a higher PCE of 13.9%, with a significantly enhanced J_{SC} of 23.3 mA cm^{-2}, and an improved FF of 57.2%. The high J_{SC} is consistent with the efficient hole extraction from the VB of perovskite to the HOMO level of SCF1, previously demonstrated by the PL quenching data and TRPL decay lifetimes.

Stability study

To assess the effect of SCF-HTMs on PSC stability, a long-term shelf lifetime evaluation was conducted together with a doped Spiro-OMeTAD reference cell. We remark the fact that we are comparing HTM layers (dopant-free SCF-HTMs and doped Spiro-OMeTAD) endowed with very similar glass transition temperatures, thus ruling out the role of the film thermal stability in interpreting the data on the long-term device performances. The stability experiments were carried out in air (40–50% relative humidity) on unencapsulated devices, which were stored in dry air (20–25 % relative humidity) in darkness between the periodic measurements. The normalized PCEs of these samples over a period of 447 days are presented in Figures 5.32 a). It becomes immediately apparent that the performance of SCF-HTM-based devices significantly improves for up to ≈60 days following their fabrication. This behavior was observed with all samples, and the effect was most noticeable over the course of 1 week after fabrication. The improvement

indicates the possibility of an increase in the hole mobility of the SCF-HTMs. [86] It is hypothesized to be a form self-doping, possibly due to reacting with oxygen, in a manner similar to Spiro-OMeTAD, although the period of improvement was much longer. [87] Doped Spiro-OMeTAD-based devices on the other simply degraded over time. As seen in Figure 5.32 a), the reference cell (with Spiro-OMeTAD HTM) and the SCF2-based device degraded to 80 % of their initial PCE after approximately 168 and 208 days of shelf storage, respectively, while the device employing SCF1 has a T_{80} lifetime [88] of over 431 days, which is among the longest shelf-lifetimes ever reported for all the types of PSCs. Compared to a previous study utilizing undoped Spiro-OMeTAD with a similar device structure [86], the best case projected T_{80} lifetime was 366 days, significantly less than our SCF1-device. In the literature, unencapsulated devices utilizing dopant-free HTMs degrade at different rates in air with the PCE degradation typically reported over a period shorter than 100 days. [89] Conversely, the devices based on our SCF-HTMs in the same time span (100 days) do not degrade but their PCE is even still higher than the initial value. After 300 days, the PCEs of Spiro-OMeTAD- and SCF1-based PSCs became nearly identical, despite the big initial discrepancy between them (PCE of Spiro-OMeTAD cell in day 1 is more than double that of SCF1 cell). In other words, the excellent stability of SCF-HTMs, and especially of SCF1, compensates their inability of leading to top-efficiency PSCs because of the modest intrinsic properties (i.e., hole mobility and conductivity). This highlights the importance of looking at the efficiency and stability as a whole [90] when evaluating a device, in this case for the selection of an HTM, especially if other important advantages are gained, like the facile synthesis of the material. The significant shelf-stability of SCF-HTMs suggests that they can effectively cover the perovskite. The study of the water contact angle (CA) confirms a clear difference in hydrophobicity between SCF-HTMs and (doped and undoped) Spiro-OMeTAD, as shown in Experimental section 5.3.4.

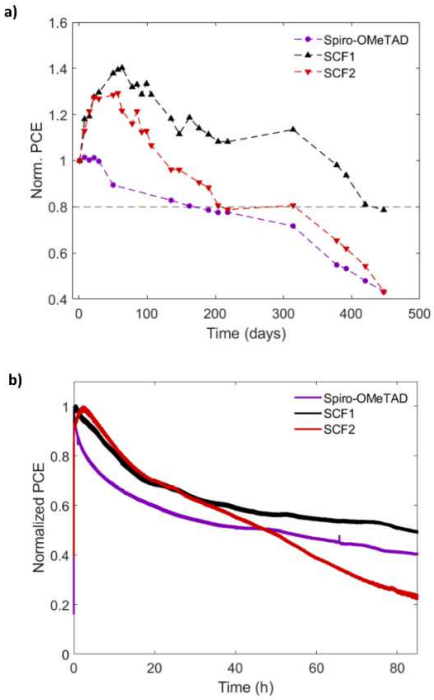

Figure 5.32 a) Normalized power conversion efficiencies (PCEs) of unencapsulated devices employing doped Spiro-OMeTAD and pristine SCF-HTMs observed over a period of 447 days. The T_{80} lifetimes of the various devices are indicated in the Figure. The solar cells were stored in dry air (T≈20 °C, RH=20–25 %) under darkness. b) Maximum power point tracking curves of unencapsulated devices with Spiro-OMeTAD, SCF1, and SCF2 under continuous 1 sun illumination.

Based on these results, the SCF-films can be considered quite hydrophobic, which is one factor explaining the longer shelf-lifetime of devices employing them, as perovskites are vulnerable to moisture. Therefore, the differences in the long-term stability expressed by SCF-HTM devices can be rationalized by the slower perovskite degradation promoted by water in comparison with doped Spiro-OMeTAD behaviour and the improved interface between the perovskite and SCF-HTMs highlighted by the simulation study. Additionally, the stability of unencapsulated devices employing Spiro-OMeTAD, SCF1, and SCF2 was also monitored under 1 Sun constant illumination for 85 hours in maximum power point (MPP) conditions. The MPP tracking curves of the three samples are reported in Figure 5.32 b). The SCF1-based device exhibits the highest stability compared to either

SCF2-based or reference doped Spiro-OMeTAD devices, further confirming the advantages of this HTM. The main reason of the stable performance of SCF1 lies most likely in its capability of effectively passivating the CsFAMA/SCF1 interface [91] [92], as supported by the findings of our computational study.

Theoretical insight of the perovskite|HTM interface

The computational study was performed considering all possible surface terminations of the triple cation perovskite active layer for modeling the HTM/perovskite interactions. The optimized structures of the corresponding interfaces between CsFAMA perovskite and SCF1, SCF2, and Spiro-OMeTAD HTM are shown in Figure 5.33 a). SCF1 forms the most stable interface with the perovskite for all terminations and surface compositions, with binding energies stronger up to 0.4 eV with respect to SCF2 and Spiro-OMeTAD (Figure 5.33 b)). Even if the latter two HTMs present similar binding energies, those of SCF2 are slightly favorable over Spiro-OMeTAD. The enhanced interface realized with SCF1 may promote the stability of the corresponding solar cells, [93]as demonstrated in stability studies.

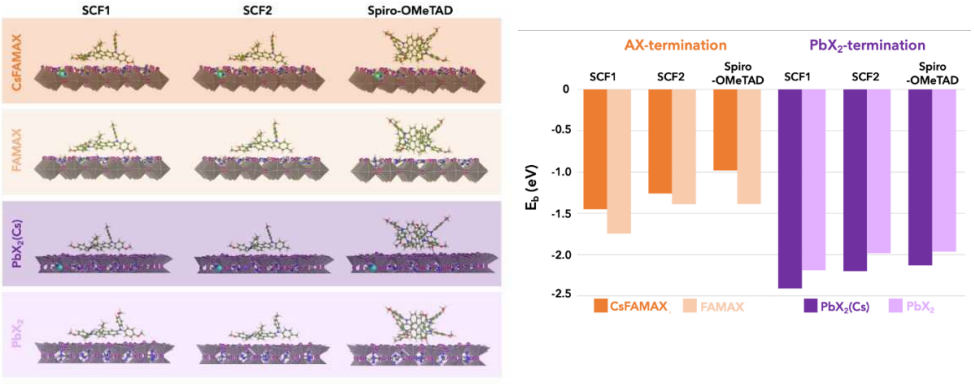

Figure 5.33. a) Lateral views of minimum-energy structures HTM/$Cs_{0.05}(FA_{0.83}MA_{0.17})_{0.95}Pb(I_{0.83}Br_{0.17})_3$ interfaces (HTM= SCF1, SCF2, and Spiro-OMeTAD) considering AX or PbX_2 terminations of the perovskite (010) surface with different compositions. AX terminated surfaces with/without Cs are labelled as CsFAMAX/FAMAX, while PbX_2 terminated surfaces with/without subsurface Cs are labelled as PbX_2(Cs)/ PbX_2. Color code: Pb (grey), I (violet), Cs (cyan), Br (pink), C (green), N (blue), O (red) and H (white). b). Computed binding energies of SCF1, SCF2 and Spiro-OMeTAD HTMs on $Cs_{0.05}(FA_{0.83}MA_{0.17})_{0.95}Pb(I_{0.83}Br_{0.17})_3$ (010) surface for CsFAMAX (dark orange), FAMAX (light orange), PbX_2(Cs) (dark purple), and PbX_2 (purple) terminated surfaces.

Surface termination, i.e., whether the HTMs are adsorbed on AX or PbX_2-type surface, has a more pronounced effect on binding energies than the different composition within a given termination. Binding energies drop ~ 1eV (from -1.45 to -2.41 eV in SCF1, from -1.26 to -2.20 eV in SCF2 and from -0.98 to -2.13 eV in Spiro-OMeTAD) when turning from the CsFAMAX termination to PbX_2 (Cs) one. Different surface compositions have only a mild impact on binding energies (within the 0.17–0.4 eV range), with Cs stabilizing HTM/PbX_2 interfaces but de-stabilizing HTM/AX ones. Additionally, the SCF-HTMs presents a more significant stabilization due to van der Waals forces than Spiro-OMETAD. Detailed informations are reported in the Experimental section 5.3.4. However, the key for the overall stabilization of SCF1 and SCF2 over Spiro-OMeTAD resides in the different molecular distortion patterns (E_{dM}). Spiro-OMeTAD presents a remarkably higher E_{dM} than SCF1 and SCF2 (up to ~0.25 eV), which tips the scales towards the final Energy binding (E_b) trend: E_b(SCF1)< E_b(SCF2)< E_b(Spiro-OMeTAD). This behavior could be ascribed to the presence of the orthogonal fragment in Spiro-OMETAD that enforces a molecular distortion in the surface anchoring, which is not achieved for the SCF-HTMs. The molecule-surface distances show the functional groups -OCH_3 define the main interactions between all HTMs and surface termination. In general, the distances are overall lowest for the SCF1. This result is confirmed by the CD plots, that shows a further interaction between fluorene-ring and MA/FA cation in the SCF1-FAMAX interface. In conclusion, the most stable favorite binding energies of the SCF1 with respect to SCF2 could be ascribed to the major number of -OCH_3 terminal-functional groups (adding further dispersion forces for anchoring to the perovskite surface) and a more favorable conformation that increases the SCF-HTMs perovskite interaction through the main fluorene moiety. The electronic properties of the investigated HTM/perovskite interfaces have also been analyzed in terms of their projected Density of States (pDOS). pDOS allow to evaluate the energy difference of the HTM HOMO and the VB of perovskite, which represents the thermodynamic driving force for hole extraction from the perovskite to the HTM. Defined this way, the HOMO of the

HTM should be higher in energy than the perovskite's VB for an effective hole extraction. SCF1, SCF2 and Spiro-OMeTAD present a very similar electronic behavior for all terminations and compositions explored, with their HOMO well above the perovskite VB, in particular for the PbX_2 termination. Thus, SCF1 and SCF2 are not only predicted to form stable interfaces with $Cs_{0.05}(FA_{0.83}MA_{0.17})_{0.95}Pb(I_{0.83}Br_{0.17})_3$, but also to possess the required features for hole extraction.

Experimental analysis of perovskite|HTM interaction

The interaction between CsFAMA perovskite and HTMs was analyzed by X-ray photoelectron spectroscopy (XPS) using samples spin coated with low concentration (0.25 mg ml^{-1} in chlorobenzene) of HTMs. Except for Cs, all the perovskite elements showed strong XPS signals before and after with the deposition of the HTMs. The surface concentration of Cs was close to the detection limit and Cs-to-Pb atomic ratio at the surface was 0.003 (c.f., nominal bulk ratio of 0.050) indicating strong surface depletion of Cs. Treatments with HTMs induced only little changes to the CsFAMA perovskite species but resulted in a clear and similar increase (from 0.4 at.% to 1.6–1.8 at.%) in O 1s signal at 532.7 eV. This binding energy corresponds to C–O bonds at the surface and supports the modelled HTM interaction with CsFAMA via methoxy (-OCH_3) functional groups.

5.3.3 Conclusions

In summary, this study demonstrated that designing simplified structures for HTMs to employ in perovskite solar cells is the key to preserve the photovoltaic efficiencies for long times under ambient conditions. A collaborative and interdisciplinary investigation allowed us to establish the molecular level of interaction of the designed and synthesized dopant-free fluorene-based hole transport materials (SCF1 and SCF2) derived from the well-known Spiro-OMeTAD. It was ascertained that SCF-based HTMs can form stable interfaces with the triple-cation CsFAMA perovskite. The simulations show that a key factor in the enhanced

binding energies of SCF2 and especially SCF1 is their reduced molecular distortion over the more complex Spiro-OMeTAD. The enhanced perovskite|SCF1 interface is reflected in excellent hole extraction, low hole trap density and an impressive shelf-lifetime (T_{80} = 431 days) of the corresponding unencapsulated devices, which is over twice as long as that of Spiro-OMeTAD and SCF2 devices and one of the longest lifetimes ever reported for PSCs. This work highlights the need to specifically match the perovskite and organic HTMs in order to attain stable PSCs via effective chemical bonding. As an added value, both SCF-HTMs were synthesized through a convergent and high-yield synthetic procedure, featuring significantly lower material and manufacturing costs. The data presented in this section of the Dissertation have been recently published by: P. Mäkinen, F. Fasulo, M. Liu, G. K. Grandhi, D. Conelli, B. Al-Anesi, H. Ali-Löytty, K. Lahtonen, S. Toikkonen, G. P. Suranna, A. B. Muñoz-García, M. Pavone, R. Grisorio, and P. Vivo. Chem. Mater. 2023, 35 (7), 2975-2987. DOI: 10.1021/acs.chemmater.3c00145

Experimental section

Synthesis of the hole-transporting materials

Reagents and solvents were purchased from standard commercial sources (Aldrich® and Honeywell Riedel-de-Haën™, respectively), while chemical manipulations were carried out under an inert nitrogen atmosphere using standard Schlenk techniques. The reaction courses were monitored by thin-layer chromatography (TLC) on Merck® silica gel 60 F254 aluminum sheets. For the cost evaluation of the final HTMs and their intermediates, the prices applied in December 2022 were used. In order to standardize the calculation for auxiliary material consumption, the following restrictions were applied: volumes of each kind of work-up extraction solvent were set to 50 mL and the cost of drying agent was considered negligible. The total volume of solvents used for flash-chromatography purifications was approximated to 500 ml. NMR spectra were recorded on a Bruker Avance DPX 300 MHz instrument.

Synthesis of 2',7'-dibromospiro[cyclohexane-1,9'-fluorene] (1). [80]
A mixture of 2,7-dibromofluorene (3.882 g, 11.98 mmol) and tetrabutylammonium bromide (1.328 g, 4.12 mmol) in a 50% NaOH aqueous solution (26 mL) was stirred for 15 min at 60°C. To the red suspension a solution of 1,5-dibromopentane (2.755 g, 11.98 mmol) in toluene (26 mL) was added and the mixture was kept under overnight stirring. After cooling the solution, the products were extracted with petroleum ether 40-60°C and the organic layer dried over Na_2SO_4. After removing the solvent in vacuo, the crude was purified by flash chromatography (SiO_2, petroleum ether 40-60°C) to afford 1 (2.990 g, 64%) as a white solid.

Synthesis of bis(4-methoxyphenyl)amine (2). [94] A mixture containing p-anisidine (1.970 g, 16.00 mmol), 4-bromoanisole (2.990 g, 16.00 mmol), palladium acetate (0.070 g, 0.32 mmol), dppf (0.360 g, 0.64 mmol) and sodium tert-butoxide (2.310 g, 24.00 mmol) in toluene (20 mL) was stirred at 110 °C overnight. After cooling down the reaction to room temperature, toluene was removed under reduced pressure and dichloromethane (50 mL) was added. The obtained mixture was washed with water (3 × 50 mL), the organic layer was collected and dried over Na_2SO_4. Upon removal of the solvent, the crude product was purified by column chromatography (SiO_2, petroleum ether 40-60 °C/CH_2Cl_2 = 3/2 vol/vol) to obtain 2 (3.118 g, yields: 85%) as a white solid.

Synthesis of N-(4-methylphenyl)-4-methoxyaniline (3). [95] A mixture containing p-toluidine (1.714 g, 16.00 mmol), 4-bromoanisole (2.990 g, 16.00 mmol), palladium acetate (0.072 g, 0.32 mmol), dppf (0.360 g, 0.64 mmol) and sodium tert-butoxide (2.310 g, 24.00 mmol) in toluene (20 mL) was stirred at 110 °C overnight. After cooling down the reaction to room temperature, toluene was removed under reduced pressure and dichloromethane (50 mL) was added. The obtained mixture was washed with water (3×50 mL), the organic layer was collected and dried over Na_2SO_4. Upon removal of the solvent, the crude product was purified

by column chromatography (SiO_2, petroleum ether 40-60 °C/CH_2Cl_2 = 3/2 vol/vol) to obtain 3 (3.241 g, yields: 95%) as a white solid.

2-N',7-N'-tetrakis(4-methoxyphenyl)-spiro[cyclohexane-1,9'-fluorene]-2',7'-diamine (SCF1). A mixture 1 (0.500 g, 1.27 mmol), 2 (0.640 g, 2.80 mmol), Pd_2dba_3 (33.1 mg, 3.20×10^{-2} mmol), XPhos (30.3 mg, 6.40×10^{-2} mmol) and sodium tert-butoxide (0.403 g, 4.20 mmol) in toluene (20 mL) was stirred at 110 °C for 24 h. After cooling down the reaction to room temperature, the reaction mixture was diluted with dichloromethane (50 mL) and the obtained organic layer was washed with water (3 × 70 mL). The organic phase was separated, dried over Na2SO4, and filtered. Upon removing the solvent, the crude product was purified by column chromatography (SiO2, petroleum ether 40-60 °C/CH_2Cl_2 = 2/3 vol/vol) to obtain SCF1 (0.815 g, 93 %) as a white solid. ^{1}H NMR (300 MHz, acetone-d_6) δ 7.50 (d, J = 8.2 Hz, 2H), 7.24 (d, J = 1.5 Hz, 2H), 7.04 (d, J = 8.9 Hz, 8H), 6.90 (d, J = 8.9 Hz, 8H), 6.83 (dd, J = 8.2, 1.5 Hz, 2H), 3.79 (s, 12H), 1.69-1.46 (m, 10H) ppm. ^{13}C NMR (75 MHz, acetone-d_6): δ 158.61, 156.40, 150.15, 144.22, 135.51, 128.73, 122.48, 121.75, 119.97, 117.61, 55.78, 50.76, 36.50, 25.88, 20.81 ppm.

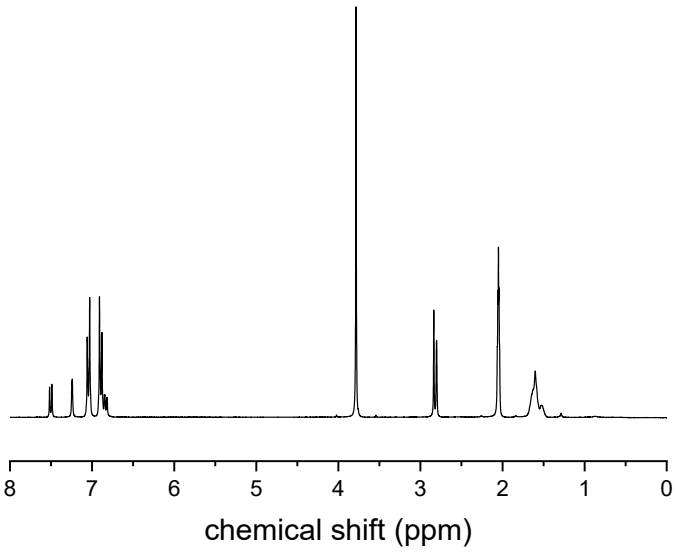

Figure 5.34. ^{1}H NMR spectrum of SCF1 recorded in acetone-d_6.

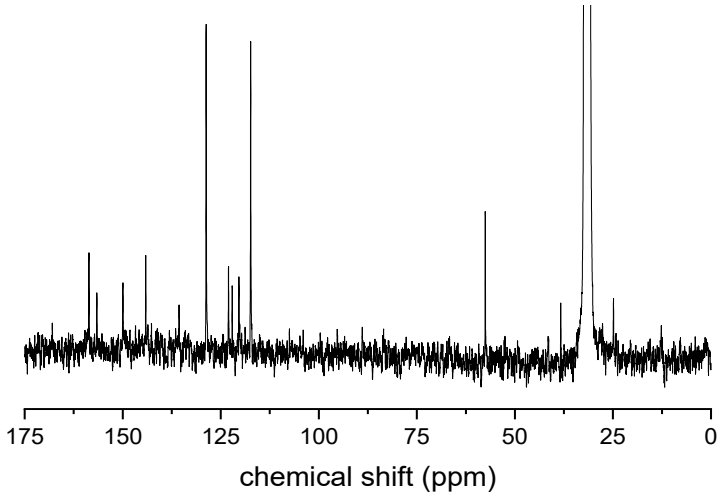

Figure 5.35.[13]C NMR spectrum of SCF1 recorded in acetone-d_6.

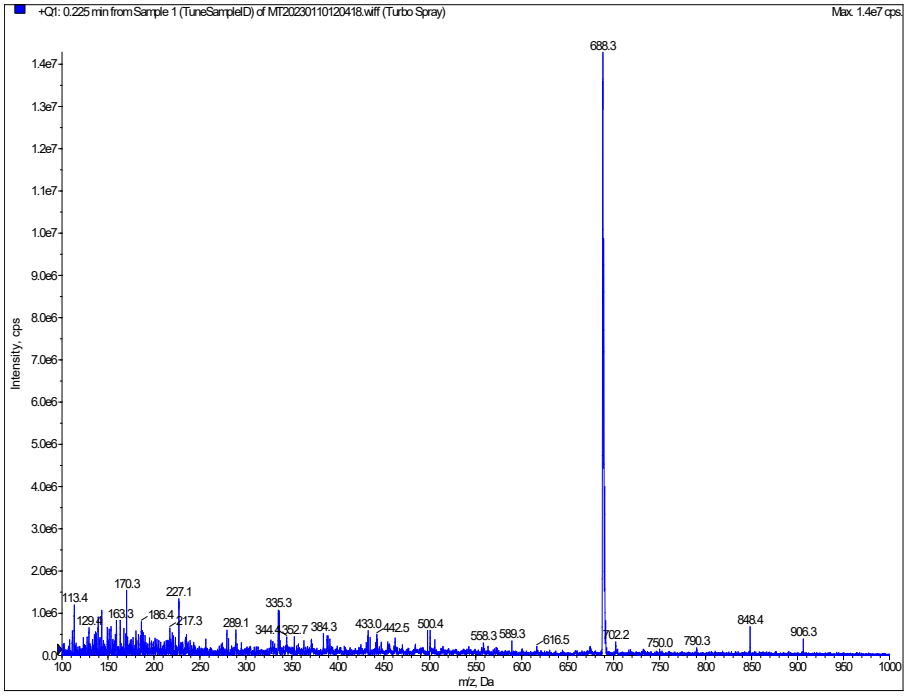

Figure 5.36. ESI-MS spectrum of SCF1 recorded in acetone-d_6.

2-N',7-N'-bis(4-methoxyphenyl)-2-N',7-N'-bis(4-methylphenyl)-spiro[cyclohexane-1,9'-fluorene]-2',7'-diamine (SCF2). A mixture of 1 (0.500 g, 1.27 mmol), 3 (0.597 g, 2.80 mmol), Pd_2dba_3 (33.1 mg, 0.03 mmol), XPhos (30.3 mg, 0.06 mmol) and sodium tert-butoxide (0.404 g, 4.20 mmol) in toluene (20 mL) was stirred at 110 °C for 24 h. After cooling down the reaction to room temperature, the reaction mixture was diluted with dichloromethane (50 mL) and the obtained organic layer was washed with water (3 × 70 mL). The organic phase was separated, dried over Na_2SO_4, and filtered. Upon removing the solvent, the crude product was purified by column chromatography (SiO2, petroleum ether 40-60 °C/CH_2Cl_2 = 2/3 vol/vol) to obtain SCF2 (0.709 g, 85 %) as a white solid. ^{1}H NMR (300 MHz, acetone-d_6) δ 7.53 (d, J = 8.2 Hz, 2H), 7.31 (br, 2H), 7.07 (dd, J = 8.2, 5.6 Hz, 8H), 6.96 – 6.87 (m, 10H), 3.79 (s, 6H), 2.27 (s, 6H), 1.69-1.46 (m, 10H) ppm.
^{13}C NMR (75 MHz, acetone-d_6) δ 157.10, 154.91, 147.76, 146.91, 141.98, 134.38, 132.30, 130.63, 127.59, 124.07, 122.40, 120.47, 119.68, 115.63, 55.74, 50.78, 36.45, 25.85, 23.07, 20.76 ppm.

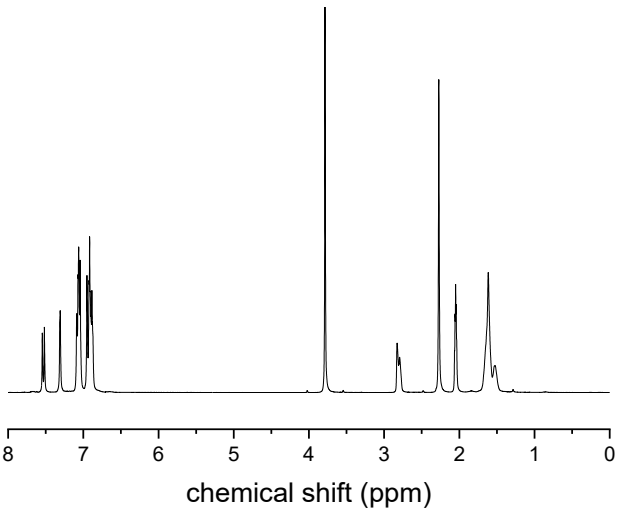

Figure 5.37. ^{1}H NMR spectrum of SCF2 recorded in acetone-d_6.

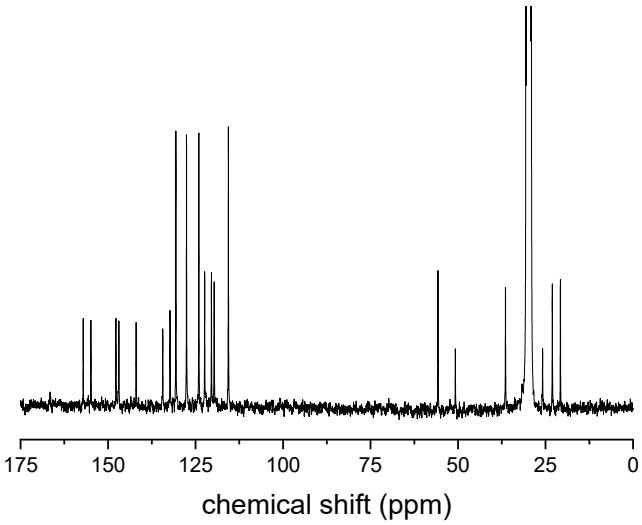

Figure 5.38. ^{13}C NMR spectrum of SCF2 recorded in acetone-d_6.

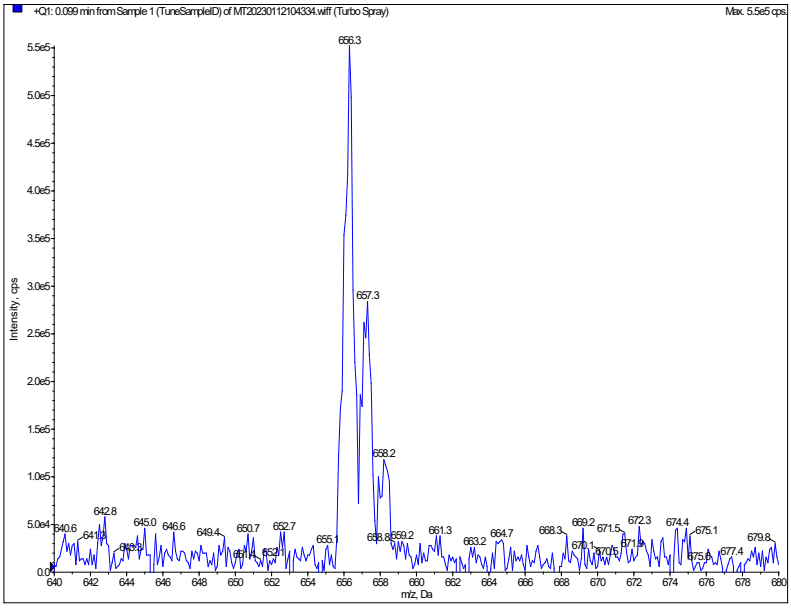

Figure 5.39. ESI-MS spectrum of SCF2 recorded in acetone-d_6.

Spectroscopic characterization

UV-Vis spectra were recorded in o-dichlorobenzene solutions (~10^{-5} M) on a Jasco V-670 instrument.

Thermal characterization

Thermogravimetric analysis (TGA) was carried out on a Perkin-Elmer Pyris 6 TGA instrument under a nitrogen flow (40 mL/min) at a heating rate of 10 °C/min. Differential scanning calorimetry (DSC) was recorded on a Q2000 TA instrument under a nitrogen flow (50 mL/min) at a temperature scan of 10 °C/min.

Electrochemical characterization

The cyclic voltammetry experiments were carried out on a Metrohm Autolab PGSTAT 302-N potentiostat in dichloromethane (HTM concentration: ~10^{-4} M) containing tetrabutylammonium tetrafluoroborate (0.10 M) as the supporting electrolyte at a 100 mV/s scan rate. The potentials were measured with respect to Ag/Ag^+ quasi-reference electrode, that was calibrated against ferrocene (Fc) after each experiment. The evaluation of the HOMO energy level of the HTMs was carried out by measuring the onset of the half-wave potential of the anodic event. The HOMO and LUMO energy levels were calculated according to the following equations:

$$E_{HOMO} = -\left[E_{OX} - E_{(Fc/Fc+)} + 5.10\right] (eV) \qquad \textit{Equation 5.40.}$$

$$E_{LUMO} = E_{HOMO} + E_g\,(eV) \qquad \textit{Equation 5.41}$$

where $E_{(Fc/Fc+)}$ represents the half-wave potential of the Fc/Fc^+ couple, E_{ox} represents the half-wave potential of the HTM/HTM^+ couple and E_g corresponds to the optical band gap calculated by $E_g = 1240/\lambda_{onset}$ (eV) (where λ_{onset} represents the onset of the HTM absorption curve recorded in solution).

Computational study

The analyses of the ground-state geometries were carried out by density functional theory (DFT) calculations using the B3LYP function in conjunction with the 6-31G(d,p) basis set on isolated molecules. Calculated energies of the relevant molecules along with their optimized geometries were carried out with the 6-311G(d,p) basis set including solvent effects (conductor-like polarizable continuum model method, CH_2Cl_2). These theoretical calculations have been carried out using the Gaussian09 [83] program package.

Charge transport characterization

The hole mobility of HTM films was measured by employing the space-charge-limited current (SCLC) method. For this purpose, typical hole-only devices were fabricated in a structure of 'glass/ITO/PEDOT:PSS/HTM/MoO_3/Au'. The devices were characterized by acquiring the dark current density (J)–voltage (V^2) curves under forward bias and the hole mobility was extracted using the Mott-Gurney law, presented in Equation 5.42.:

$$J_D = \frac{9}{8}\epsilon_r\epsilon_0\mu_h\frac{V^2}{d^3} \qquad Equation\ 5.42$$

where J_D is the dark current density, ϵ_r is the relative permittivity of the material, which is ≈3 for organic materials, ϵ_0 is vacuum permittivity $8.854\cdot10^{-12}$ C V^{-1} m^{-1}, μ_h is hole mobility, V is the applied bias, and d is the thickness of the HTM layer. The measurement was conducted with a Keithley 2450 Source Measure Unit (SMU) between 0-2 V at scan rate 0.1 V s^{-1} and a linear fit was applied to data points below 50 mA cm^{-2} (see Figure 5.43 a)).

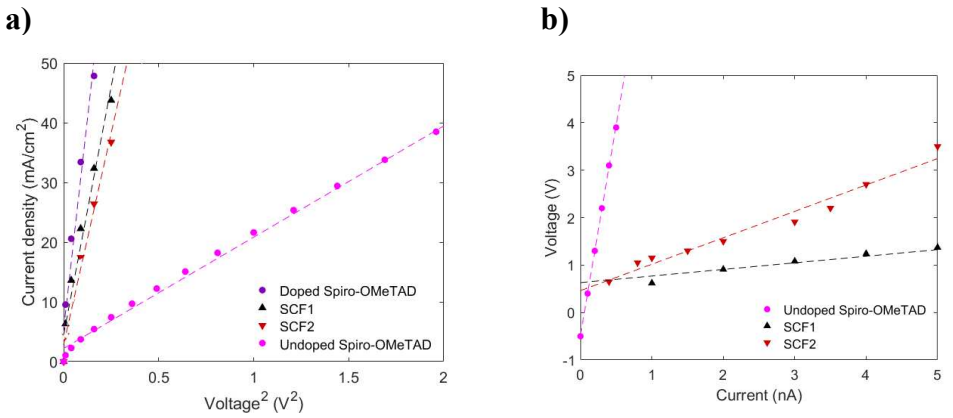

Figure 5.43. *a) Current density (J) –voltage (V^2) curves of hole-only devices measured in dark for both SCF-HTMs as well as both doped and undoped Spiro-OMeTAD as reference. The dashed line represents a linear fit in accordance with the Mott-Gurney law. b) Voltage (V) –current (I) curves of SCF-HTM and undoped Spiro-OMeTAD films coated with Au electrodes obtained via four-point probe measurement. The dashed line represents the linear fit used to calculate film resistance.*

Conductivity was assessed by measuring the resistance of 100 nm HTM-films on glass with four equally spaced 100 nm thick Au lines evaporated on top as electrodes. Current was sourced through the outer electrodes with the Keithley 2450 SMU and the voltage drop between the inner electrodes was measured to calculate resistance R from a linear fit on a Voltage (*V*) –current (*I*) curve (Figure 5.43 b)). Conductivity was then calculated using Equation 5.44.:

$$\sigma = \frac{d}{RA} \qquad Equation\ 5.44$$

where σ is conductivity of the film, d is the distance between electrodes, and A is the cross-section area through which the current is transmitted.

Structural models and computational details

The computational cell of the perovskite $Cs_{0.05}(FA_{0.83}MA_{0.17})_{0.95}Pb(I_{0.83}Br_{0.17})_3$ used in this work consists of 100 $APbX_3$ units (Figure 5.45.). In this way, the resulting $Cs_5FA_{79}MA_{16}Pb_{100}I_{249}Br_{51}$ supercell delivers the exact stoichiometry of the experimental perovskite. This supercell was built by scaling back the $Cs_8FA_{88}MA_{12}Pb_{103}Cd_5I_{269}Br_{55}$ model (108 f.u.) reported by Saidaminov [96], where FA/Cs/MA and I/Br are distributed randomly, and the orientation of the organic cations is determined after NVT molecular dynamics simulations. The lattice constants of our optimized bulk structure are a= 31.997Å b= 25.666Å c=32.018Å.

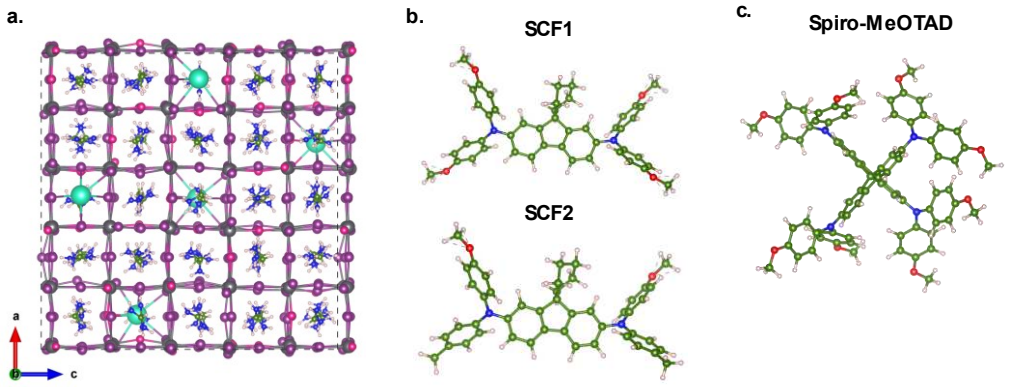

Figure 5.45. Optimized structures at PBE-TS level of theory of ***(a)*** *perovskite* $Cs_{0.05}(FA_{0.83}MA_{0.17})_{0.95}Pb(I_{0.83}Br_{0.17})_3$ *bulk,* ***(b) SCF1*** *and* ***SCF2*** *molecules* ***(c)*** *Spiro-OMeTAD. Colour code: Pb (grey), I (violet), Cs (cyan), Br (pink), C (green), N (blue), O (red) and H (white).*

Isolated HTMs **SCF1, SCF2** (Figure 5.45 b)) have been computed in a 20 Å × 15 Å × 30 Å unit cell while Spiro-OMeTAD (Figure 5.45 c)) in 30 Å × 30 Å × 30 Å unit cell. To study HTM/perovskite interfaces, we applied the surface-slab approach and build up the structural models for the perovskite surfaces by cleaving the bulk structure with optimized lattice constants along the (010) plane and then introducing 25Å of vacuum above the reoriented surface along the *c* direction.

Resulting 8-layer slabs preserve the stoichiometry of the parent bulk. For adsorption purposes, we considered both AX and PbX_2 terminations. Since the cation composition differs within each AX layer due to the random cation distribution, we considered two kinds of AX-terminations: one exposing Cs, MA and FA (CsFAMAX surface, indicated in pink in Figure 5.46 a)) and one exposing only majority MA and FA cations (FAMAX surface, indicated in pink in Figure 5.46 b)). Top views and compositions of such AX terminations are depicted in Figure 5.46 c) and 5.46 d). For the same reason, two PbX_2–terminated (010) can be distinguished based on the presence of Cs in the subsurface layer. PbX_2 – terminated perovskite surface without and with subsurface Cs are indicated with purple lines as PbX_2 and PbX_2(Cs) in Figure 5.46. a) and5.46. b), respectively. Calculations on surfaces with present or absent Cs in the surface/subsurface allow to dissect the direct/indirect role of Cs in the adsorption event for AX/PbX_2 terminations.

On these structures, we performed DFT [97] calculations with periodic boundary conditions (PBC) employing the light–tier1 basis set of numerical atom-centered orbitals (NAO) for each atom [98], as implemented in the Fritz Haber Institute ab initio molecular simulations (FHI-aims) code. [99] Within the FHI-aims framework, the electrons were described by the zero–order regular approximation (atomic ZORA). [100]As self-consistency threshold for electron density convergence, we employed a total energy criterion of 1×10^{-6} eV. We used the Perdew-Burke-Erzenhof (PBE) exchange correlation functional for all geometry optimizations including the Tkatchenko–Scheffler (TS) correction [101] [102] accounting for van der Waals dispersion forces. During geometry optimizations involving the perovskite surface, atoms of the bottommost layers have been fixed to their bulk-like positions, while the first layer and the adsorbed molecule have been allowed to relax

without symmetry constraints. Our relaxed structures present maximum forces acting on each atom below 0.05 eV/Å. Due to large dimensions of the bulk and the surfaces, the gamma point (1×1×1) k-point sampling scheme was applied for all calculations.

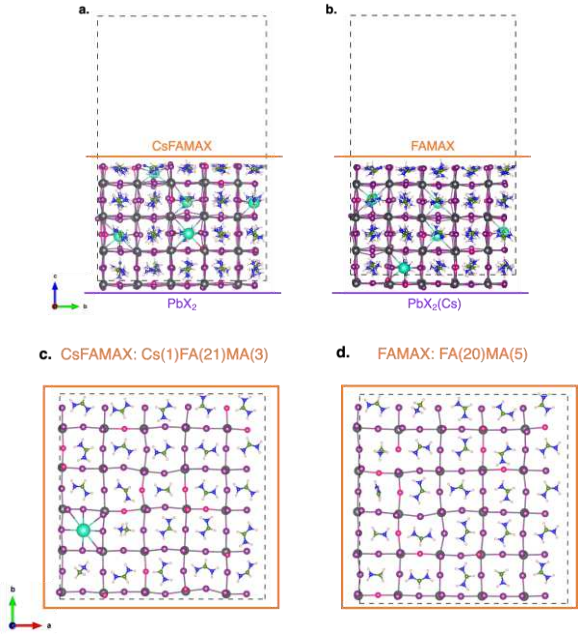

Figure 5.46. Slab models of the four surfaces considered for HTM adsorption (a) CsFAMAX, PbX_2 and (b) FAMAX, PbX_2 (Cs). (c) and (d) Top views of the CsFAMAX and FAMAX surfaces. Atoms beyond the surface layer have been omitted for clarity. Atomic colour code as in Figure 5.43.

HTM/surface binding energies (E_b) are calculated at HSE06-TS level of theory on PBE geometries as follows:

$$E_b = E_{Surf/HTM} - E_{Surf} - E_{HTM} \quad \textit{Equation 5.47}$$

where $E_{Surf/HTM}$, E_{surf} and E_{HTM} are the computed energies for each fully relaxed molecule/perovskite interface, isolated surface and isolated HTM, respectively. Binding energies have been further decomposed into three main contributions:

$$E_b = E_a + E_{dM} + E_{dS} = (E_{Surf/HTM} - E_{Surf*} - E_{HTM*}) + (E_{HTM*} - E_{HTM}) + (E_{Surf*} - E_{Surf})$$

Equation 5.48

Where E_a, E_{dM} and E_{dS} are the adhesion energy, the distortion energy of the HTM molecule and the distortion energy of the perovskite surface, respectively. E_a is calculated from the energy of the fully relaxed interface ($E_{surf/HTM}$) and the energies of the HTM and the surface already distorted at the interface geometry (E_{HTM*} and E_{Surf*}, respectively). E_a thus portrays the pure electronic interaction between the HTM and the surface. Distortion energies E_{dM} and E_{dS} are calculated as the difference between the energies of each system and the interface geometry and those at their fully relaxed state, and account for the penalty energy needed for each component to change conformation ahead of forming the interface. Defined this way, E_a is an attractive (negative) term, while E_{dM} and E_{dS} are positive quantities that partially compensate E_a to deliver the overall E_b.

X-ray photoelectron spectroscopy

X-ray photoelectron spectroscopy (XPS) measurements were performed in ultra-high vacuum employing an Al Kα X-ray source (hν = 1486.7 eV) and Argus electron spectrometer (Omicron Nanotechnology GmbH). The spectrometer binding energy scale was calibrated setting Ag $3d_{5/2}$ of metallic Ag foil to 368.0 eV. To probe the HTM–perovskite interaction low concentration of HTMs (0.25 mg ml^{-1} in chlorobenzene) was used in the spin coating instead of the concentration (10 mg ml^{-1}) optimized for solar cell performance. The thickness of HTM layer scales with the concentration and the use of low concentration allowed probing the HTM–perovskite interface by surface sensitive XPS (information depth of 5–9 nm). The chemical states of elements were determined from the XPS spectra by least-

squares fitting of synthetic line shapes after background subtraction. The analysis was made in CasaXPS software version 2.3.25PR1.0.[9]

Photoluminescence studies

A batch of glass/CsFAMA and glass/CsFAMA/HTM samples (CsFAMA is the standard triple-cation $Cs_{0.05}(FA_{0.83}MA_{0.17})_{0.95}Pb(I_{0.83}Br_{0.17})_3$ perovskite) was prepared for the photoluminescence studies with both SCF-HTMs, as well as doped Spiro-OMeTAD. The same cleaning and spin coating protocols were used as with solar cell fabrication, except the glass substrates were plasma cleaned prior to perovskite deposition. Steady-state Photoluminescence (PL) spectra were recorded with a FLS1000 spectrofluorometer (Edinburgh Instruments, UK). The time-resolved PL (TRPL) decays were obtained by using a time-correlated single photon counting (TCSPC) apparatus equipped with a Picoharp 300 controller and a PDL 800-B driver for excitation and a Hamamatsu R3809U-50 microchannel plate photomultiplier for detection in 90° configuration. To analyze the TRPL decay data for glass/CsFAMA/HTM samples, a simple rate equation was employed, which consists of the first order non-radiative recombination via trap sates, second order non-geminate free charge carrier radiative recombination, and interfacial charge transfer process (i.e. hole injection), as shown in Equation 5.49.

$$-\frac{d_n}{d_t} = k_1 n + k_2 n^2 + k_{HT} n \qquad \text{Equation 5.49}$$

where n is the photo-excited charge carrier density, k_1 is the rate constant of trap-assisted recombination, k_2 is the rate constant of charge carrier (electron-hole) recombination within the perovskite layer, k_{HT} is the injection rate constant of a hole from the valence band (VB) of perovskite to the HOMO level of HTM, and t

is the time. Note that three body Auger recombination is not considered, due to the applied weak excitation intensity of ~20 nJ cm^{-2}. [103]

By solving Equation 5.49, a fitting function is described in Equation 5.50.

$$n(t) = \frac{(k_1+k_{HT})n_0}{k_1 \exp(k_1 t+k_{HT}t)-k_2 n_0+k_2 n_0 \exp(k_1 t+k_{HT}t)+k_{HT}\exp(k_1 t+k_{HT}t)}$$

Equation 5.50

where n_0 is the initial charge carrier density at time zero (t = 0).

To analyze the perovskite excited state decay, i.e. PL decay for glass/CsFAMA, Equation 5.49. is simplified to,

$$-\frac{d_n}{d_t} = k_1 n + k_2 n^2 \qquad \text{Equation 5.51}$$

By solving Equation 5.50, a fitting function is described in Equation 5.51.

$$n(t) = \frac{k_1 n_0}{k_1 \exp(k_1 t)-k_2 n_0+k_2 n_0 \exp(k_1 t)} \qquad \text{Equation 5.52}$$

All TRPL decays were analyzed with a global fitting.

Hole trap density testing

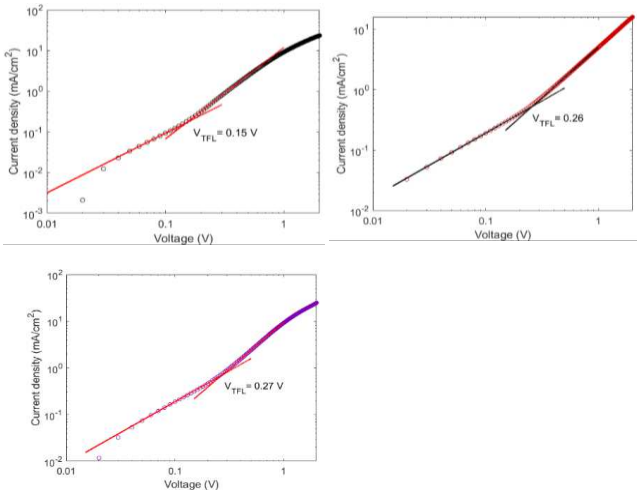

Figure 5.53. Typical dark J-V curves of hole-only devices employing a) SCF1, b) SCF2, and c) doped Spiro-OMeTAD with the structure ITO/PEDOT:PSS/CsFAMA/HTM/MoO_3/Au, with V_{TFL} kink point behaviour in perovskite films.

The applied voltage at the kink point is referred to as the trap-filled limit voltage (V_{TFL}), which can be used to calculate the trap density (N_{trap}) [104]according to the following equation:

$$N_{trap} = \frac{2\epsilon\epsilon_0 V_{TFL}}{eL^2} \qquad (Equation\ 5.54)$$

where *e* is the elementary charge, L is the thickness of perovskite layer (approximately 500 nm in our work), ϵ is the relative dielectric constant of perovskite, and ϵ_0 is the vacuum permittivity.

Solar cells fabrication

All reagents and solvents aside from the SCF-HTMs were purchased from standard commercial sources and used as received. Unless specified otherwise, processes were performed in air. The solar cells were fabricated on fluorine-doped tin oxide (FTO) glass substrates (TEC 15, Greatcell Solar) with dimensions 20×20×2.2 mm, which were wet chemically etched on one edge with 2.4 M HCl solution and zinc powder. Etched substrates were cleaned with 2 % Mucasol solution in deionized water and sonicated in DI water, acetone, and 2-propanol for 15 minutes each, followed by swiftly drying under a N_2 stream. A compact TiO_2 layer (c-TiO_2) was deposited on the substrates via spray pyrolysis at 450 °C using N_2 as the carrier gas. The precursor solution was prepared by diluting a titanium diisopropoxide bis(acetylacetonate) stock solution (75 % in 2-propanol, Sigma-Aldrich) further to 17.3 vol%. 12 layers of the precursor solution (< 8 ml) were sprayed on the substrates with 20 seconds between each cycle, followed by sintering at 450 °C in air for a minimum of 45 minutes. A mesoporous TiO_2 (m- TiO_2) scaffold layer was deposited by spin coating an ethanolic suspension of 30 NRD

TiO_2 nanoparticle paste (Greatcell Solar), with 150 mg of paste in 1 ml ethanol. 80 µl of suspension was spin coated at 4000 rpm for 10 s, followed by a few minutes of annealing at 100 °C prior to calcination at 450 °C for 30 minutes (heat ramped over ~45 minutes). The substrates were then cooled down to 150 °C and transferred to a nitrogen-filled glovebox for perovskite and HTM deposition.

The CsFAMA perovskite precursor was prepared 24–48 hours prior, comprising FAI (0.95 M, Greatcell Solar Materials), MABr (0.19 M, Greatcell Solar Materials), $PbBr_2$ (1.1 M, TCI), PbI_2 (0.20 M, TCI), and CsI (0.06 M, abcr) in a mixed solvent of DMSO:DMF (1:4 volume ratio). The solution was kept in stirring until use. 50 µl of the solution was spin coated onto the as-prepared FTO/c-TiO_2/m-TiO_2 substrates at 1000 rpm for 10 s, followed by 6000 rpm for 20 s. Antisolvent treatment was done by dropping 100 µl of chlorobenzene onto the substrate 5 seconds prior to the end of the program. The perovskite films were immediately transferred to a hot plate for annealing at 110 °C for 1 hour. After annealing and cooling down, the SCF-HTMs and reference doped Spiro-OMeTAD were dynamically spin coated on top of the perovskite film at 1800 rpm for 40 s. SCF-HTMs were tested in four concentrations (5, 10, 15, 20 mg/ml in chlorobenzene), with 10 mg/ml yielding highest performance. The doped Spiro-OMeTAD solution was prepared by dissolving Spiro-OMeTAD (Lumtec) in chlorobenzene in a 29.5 mM concentration and stirring at 60 °C for a few minutes. After cooling down dopants were added: 4-tert-butylpyridine (Sigma-Aldrich), Li-TFSI (Sigma-Aldrich, pre-dissolved in acetonitrile 520 mg/ml), and FK209 (Dyenamo, pre-dissolved in acetonitrile 300 mg/ml). Their molar equivalents to Spiro-OMeTAD were 3.2, 0.53, and 0.1, respectively. After HTM deposition, the samples were removed from the glovebox, and kept in a dry cabinet overnight. Finally, 100 nm thick gold electrodes were

evaporated on top of the HTM layer using an Edwards Auto 306 vacuum deposition unit in a vacuum of approximately 10^{-5} mbar.

Device and film characterization

The unencapsulated perovskite solar cells, with an active area of 20 mm^2 were characterized in air. The current density (J)-voltage(V) curves were recorded at a scan rate of 50 mV s^{-1} with a Keithley 2450 SMU (controlled by a measurement program written in MATLAB) and a SS150-AAA solar simulator (Sciencetech, Canada) under air mass 1.5 simulated sunlight (100 mW cm^{-2}), calibrated with a KG5 reference cell and meter (Newport, USA). The same setup was also used for recording dark J-V behaviour. The water contact angles of the HTM films were measured from the same samples as PL and TRPL by using an Attension Theta Lite optical goniometer (Biolin Scientific AB, Sweden).

Cross-sectional and top-view SEM images of fabricated PSC

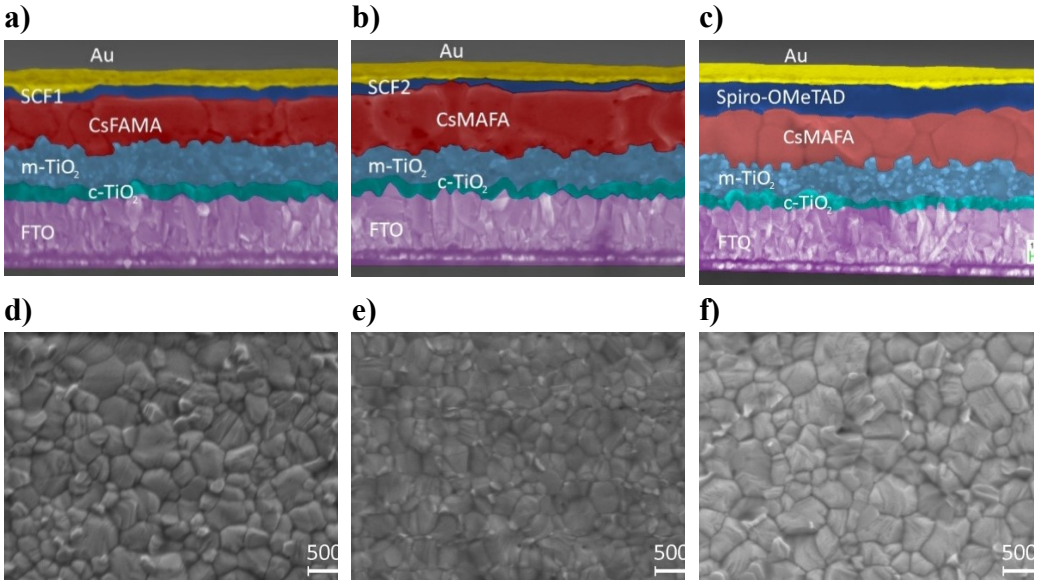

Figure 5.55. Colored cross-section SEM images obtained via scanning electron microscopy of devices utilizing a) SCF1, b) SCF2, and c) Spiro-OMeTAD as the HTM. Top-view SEM-images of 'FTO|c-TiO_2|m-TiO_2|Perovskite|HTM' samples, where HTM is d) SCF1, e) SCF2, or f) Spiro-OMeTAD.

Concentration and doping testing

Table 5.56. Photovoltaic parameters of **SCF2**-based devices with different concentrations of **SCF2** in chlorobenzene the day after fabrication. There were 6 devices each of 5, 15, and 20 mg ml^{-1}, with 3 devices of 10 mg ml^{-1} fabricated in the same batch for comparison.

Solution (mg ml^{-1})	PCE (%)	FF (%)	Jsc (mA cm^{-2})	Voc (V)
5	4.0±0.2 (4.32)[a)]	38.0±1.2 (38.29)	16.2±1.1 (16.85)	0.65±0.05 (0.67)
10	7.9±0.2 (8.18)	38.6±2.0 (41.32)	20.4±0.2 (20.20)	1.00±0.01 (0.98)
15	5.5±0.4 (6.03)	26.0±1.8 (28.33)	20.6±0.3 (20.88)	1.04±0.01 (1.02)
20	2.5±0.3 (2.97)	15.9±1.2 (17.11)	15.9±1.0 (17.03)	0.99±0.03 (1.02)

[a)] Bracketed values represent champion devices of each solution concentration.

Table 5.57 Photovoltaic parameters of 17 undoped and 3 doped **SCF1**- and **SCF2**-based devices each approximately 1 week after fabrication.

HTM	PCE (%)	FF (%)	Jsc (mA cm^{-2})	Voc (V)
SCF1	11.8±0.8 (13.9)[a)]	53.7±1.9 (57.2)	21.7±0.8 (23.3)	1.01±0.02 (1.04)
SCF2	11.4±0.9 (12.7)	52.1±1.5 (53.2)	21.6±1.2 (22.5)	1.01±0.03 (1.06)
doped SCF1	12.1±0.3 (12.4)	55.0±0.9 (56.0)	22.0±0.7 (22.2)	1.00±0.00 (1.00)
doped SCF2	11.8±1.2 (13.4)	55.8±1.1 (57.3)	20.1±1.6 (21.9)	1.05±0.01 (1.07)

[a)] Bracketed values represent champion devices of each type.

Stability of fabricated devices

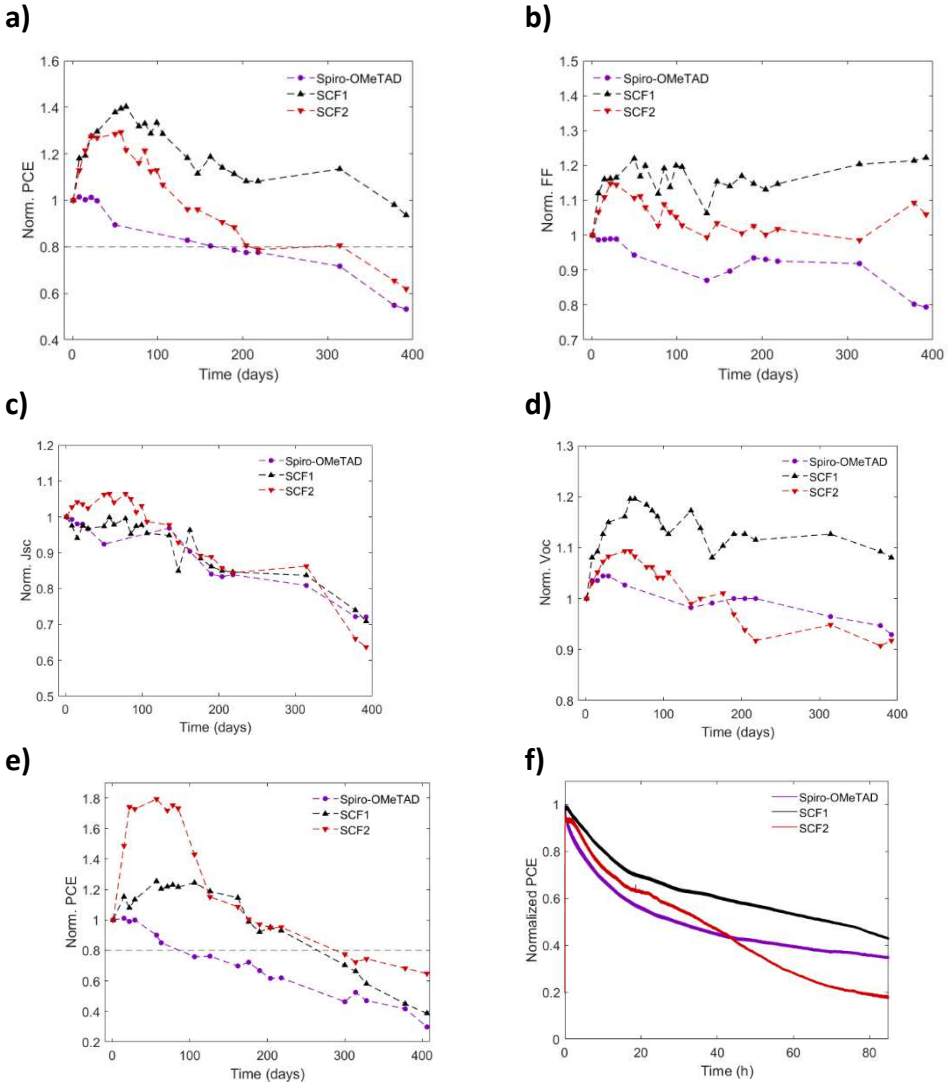

Figure 5.58. Normalized a) power conversion efficiency (PCE), b) fill factor (FF), c) short-circuit current (J_{SC}), and d) open-circuit voltage (V_{OC}) of devices employing doped Spiro-OMeTAD and pristine SCF-HTMs observed over a period of 392 days. The solar cells were stored in a drybox (T≈20 °C, RH ≤12 %) in darkness. e) Normalized power conversion efficiency of devices employing doped Spiro-OMeTAD and pristine SCF-HTMs stored in ambient air (RH≈50 %). f) Average maximum power point tracking curves of 2 unencapsulated devices each of Spiro-OMeTAD reference, **SCF1**, and **SCF2** under continuous 1 sun illumination.

Structural and electronic analysis by first-principle investigation

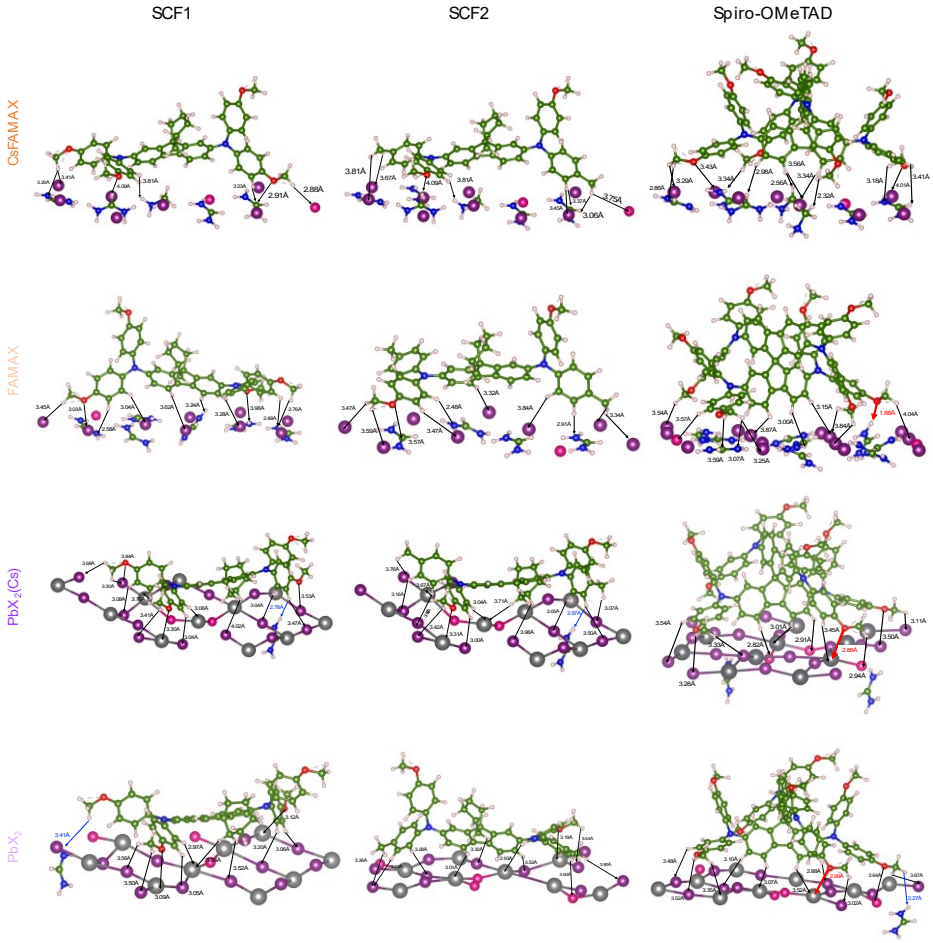

Figure 5.59. Molecule-surface specific distances of SCF1, SCF2 and Spiro-OMeTAD/$Cs_{0.05}(FA_{0.83}MA_{0.17})_{0.95}Pb(I_{0.83}Br_{0.17})_3$ interfaces (010) considering AX or PbX_2 terminations of the perovskite (010) surface with different compositions. AX terminated surfaces with/without Cs are labelled as CsFAMAX(dark orange)/FAMAX(light orange), while PbX_2 terminated surfaces with (dark purple)/without (purple) subsurface Cs are labelled as $PbX_2(Cs)/PbX_2$.

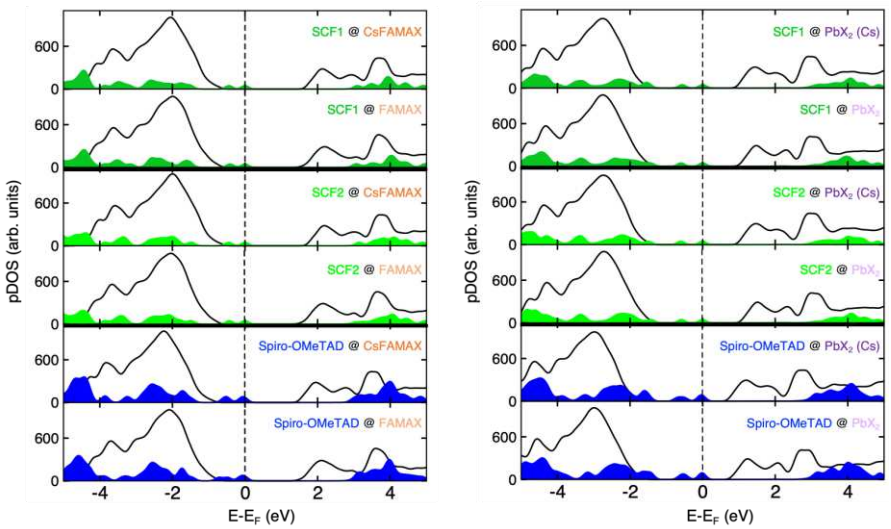

Figure 5.60. Projected density of states (pDOS) of $Cs_{0.05}(FA_{0.83}MA_{0.17})_{0.95}Pb(I_{0.83}Br_{0.17})_3$ (black line), SCF1 (solid dark green pattern), SCF2 (solid light green pattern) or Spiro-OMeTAD (solid blue pattern) for HTM adsorption on the different terminations and compositions considered. The Fermi energy (EF) is set to zero.

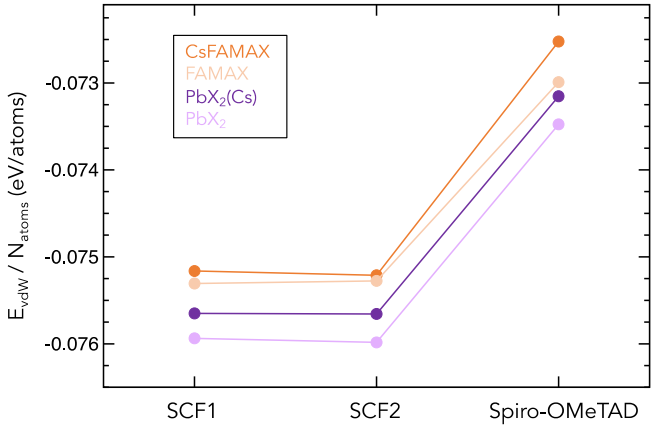

Figure 5.61. Dispersion energies per atoms (E_{vdW}/atoms) computed at HSE06 level of theory of **SCF1**, **SCF2** and Spiro-OMeTAD on $Cs_{0.05}(FA_{0.83}MA_{0.17})_{0.95}Pb(I_{0.83}Br_{0.17})_3$ (010) surface for CsFAMAX (dark orange), FAMAX (light orange), PbX_2(Cs) (dark purple), and PbX_2 (purple) terminated surfaces.

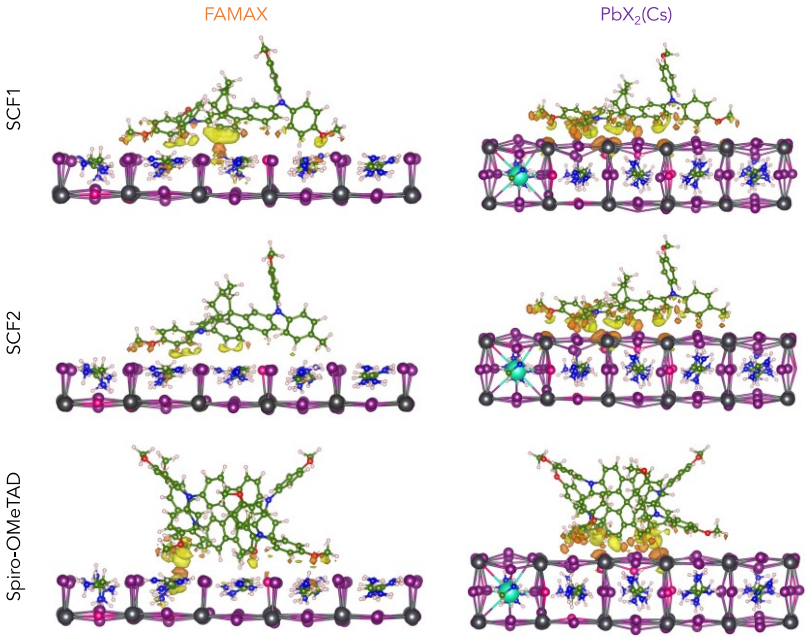

Figure 5.62. Charge difference (CD) plot ($\Delta\rho = \rho_{HTM-Surf} - \rho_{Surf} - \rho_{HTM}$) computed at HSE06 level of theory of the most favorite SCF1, SCF2 and Spiro-OMeTAD interfaces: FAMAX or PbX_2(Cs) terminations. Isodensity value: 0.005 a.u. Color code: electron gain (yellow), electron loss (orange).

X-ray photoelectron spectroscopy

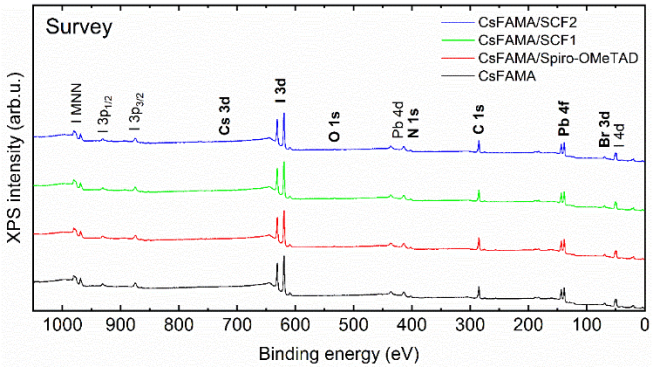

Figure 5.63. XP survey spectra for CsFAMA and CsFAMA spin coated with low concentration (0.25 mg ml^{-1} in chlorobenzene) of HTMs (Spiro-OMeTAD, SCF1 and SCF2).

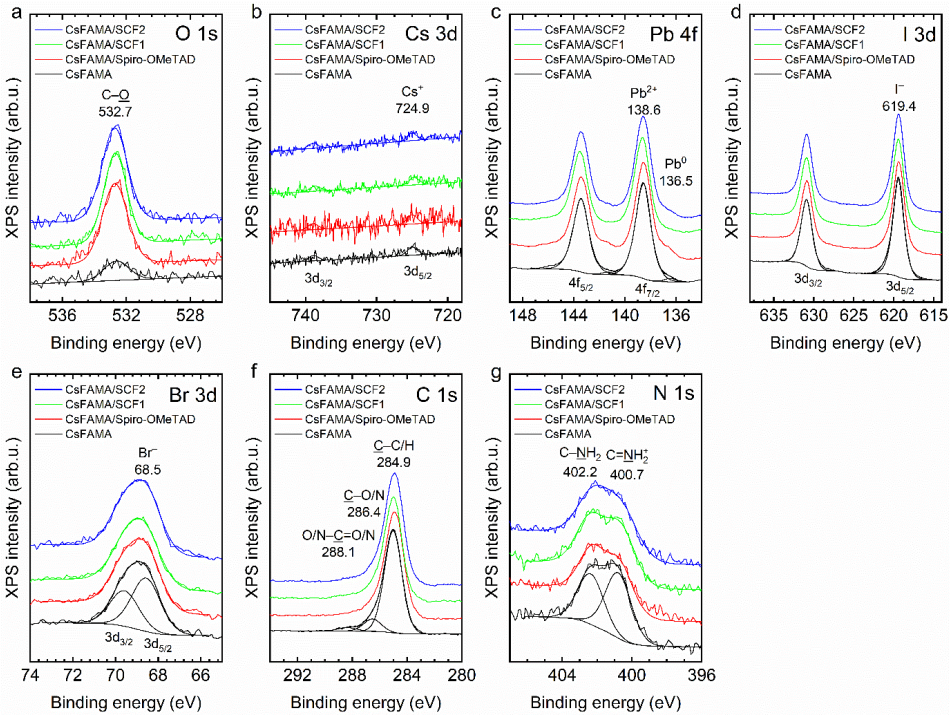

Figure 5.64. XPS spectra of (a) O 1s, (b) Cs 3d, (c) Pb 4f, (d) I 3d, (e) Br 3d, (f) C 1s, and (g) N 1s for CsFAMA and CsFAMA spin coated with low concentration (0.25 mg ml^{-1} in chlorobenzene) of HTMs (Spiro-OMeTAD, SCF1 and SCF2).

One chemical state was resolved for Cs (Cs $3d_{5/2}$ at 724.9 eV), I (I $3d_{5/2}$ at 619.4 eV) and Br (Br $3d_{5/2}$ at 68.5 eV) corresponding to the valence states of Cs^+, I^- and Br^-, respectively [105] (Figure 5.64, Table 5.65). In addition to expected Pb^{2+} (Pb $4f_{7/2}$ at 138.6 eV), a small fraction (<7%) of Pb was metallic that was observed to increase during the XPS measurement (not shown) and was therefore assigned as an X-ray induced effect. [106] Organic FA^+ (N=C–N bond) and MA^+ (H–C–N) could not be differentiated from C 1s (Figure 5.64 f) due to overlapping signals from adventitious carbon (C–C/H, C–O and O=C–O). All the samples, including the CsFAMA without any HTM, had 72–74 at.% carbon at the surface. Broad N 1s spectra were resolved with two components: one at 400.7 eV ($C=NH_2^+$) and

another one at 402.2 eV (C–$\underline{N}H_2$) corresponding to N in FA^+ and MA^+, respectively. [107] Nitrogen in the HTMs (C–N bonds) has been reported at 400.2 eV [108] [109]that overlaps with the C=$\underline{N}H_2^+$ component and was not resolved. No chlorine (Cl 2p at 200 eV) was detected at the surface.

Table 5.65. X-ray photoelectron spectroscopy (XPS) analysis of surface composition for CsFAMA and CsFAMA spin coated with low concentration (0.25 mg ml^{-1} in chlorobenzene) of HTMs (Spiro-OMeTAD, SCF1 and SCF2).

Element	O	Cs	Pb		I	Br	C			N	
Transition	O 1s	Cs $3d_{5/2}$	Pb $4f_{7/2}$		I $3d_{5/2}$	Br $3d_{5/2}$	C 1s			N 1s	
E_b (eV)	532.7	724.9	138.6	136.5	619.4	68.5	284.9	286.4	288.1	400.7	402.2
Chemical state	$\underline{O}$–C	Cs^+	Pb^{2+}	Pb^0	I^-	Br^-	$\underline{C}$-C	$\underline{C}$–O/N	O/N–$\underline{C}$=O/N	C=$\underline{N}H_2^+$	C–$\underline{N}H_2$
Concentration (at.%)											
CsFAMA	0.4	0.02	6.2	0.15	10.0	4.4	62.3	7.7	2.4	3.7	2.9
CsFAMA/Spiro-OMeTAD	1.6	0.02	6.0	0.37	8.8	4.5	62.7	8.3	2.7	2.5	2.5
CsFAMA/SCF1	1.8	0.02	5.9	0.05	9.1	4.5	62.1	7.6	2.5	3.4	3.1
CsFAMA/SCF2	1.8	0.02	5.9	0.18	8.8	4.5	62.0	8.5	2.6	2.8	2.9

Contact angle measurements

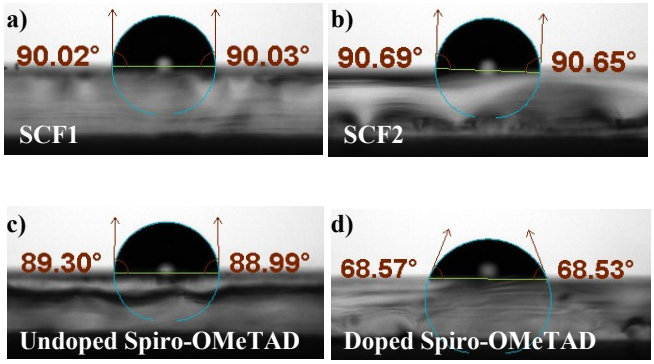

Figure 5.66. Water contact angles of a) SCF1, b) SCF2, c) undoped Spiro-OMeTAD, and d) doped Spiro-OMeTAD films coated on CsFAMA.

5.4 Synthesis of novel Bithiophene-based HTMs via Step-Economical Direct C–H Arylation Approach

5.4.1 Target

Among the many possible organic HTM structures, in this chapter my interest has been focused on arylamine derivatives, one of the most applied building blocks in OLEDs [110] , DSSCs [111] , OPVs [112] and OFETs [113] . Indeed, a number of simple donor-π-donor molecule HTMs have been synthesized by varying the central π-linker and the end capping arylamine derivatives. [114] [115] However, as mentioned above, most of the reported π-conjugated organic HTMs were synthesized exploiting the reactivity of an appropriate molecular core, employing traditional multi-step approaches that mainly relies on the connection of C–C and C–N bonds using Suzuki, Stille coupling, and Buchwald–Hartwig amination as key transformation reactions. As discussed in Chapter 1, these protocols require tedious pre-functionalization synthetic steps, such as deprotonation and lithiation, to selectively replace the halogenation of the organic compounds using n-butyl lithium and their subsequent transmetalation reactions to prepare the corresponding organotin/organoboron reagents using highly toxic trimethyl or butyl tin chloride and expensive 2-isopropoxy4,4,5,5-tetramethyl-[1,3,2]-dioxaborolane, respectively, along with the formation of toxic byproducts. Herein, with the aim to develop novel efficient and stable HTMs, it is proposed a versatile, step- and atom-economical, direct C–H arylation strategy to connect a 2,2'-bithiophene core and two different mono brominated tris(arylamines) segments through Pd-catalyzed sequential C–C bond-forming reactions. Employing this sustainable synthetic protocol increases the yield significantly and reduces the number of reaction steps as compared to the traditional methods, thereby facilitating the possible commercialization. In the targeted molecules BTC and BTF (Figure 5.67), the central 2,2'-bithiophene π-bridge unit has been introduced between two asymmetric tris(arylamines) units, namely N-(4-bromophenyl)-9-hexyl-N-(4-methoxyphenyl)-9H-carbazol-3-amine and N-(4-bromophenyl)-N-(4-methoxyphenyl)spiro[cyclohexane-1,9'-fluoren]-2'-amine, to enhance the planarity by alleviating the

torsional distortion between them and strengthen the hole transport. When BT-HTMs were employed as thin layers in n-i-p structure PSCs exhibited multifunctional features such as lowering of the HOMO closer to the VB of the perovskites and intrinsic higher hole mobility. Notably, the multifunctional features of BTC and BTF allow, when used in devices, power conversion efficiencies (PCE) (BTC 14.04% and BTF 12.80%) compared to the state-of-the-art spiro-OMeTAD (16.55%). More importantly, the BT-based devices exhibit enhanced long-term stability compared to that of spiro-OMeTAD, the cause of which will be further investigated. Therefore, this investigation provides insights into the development of low-cost and multifunctional HTMs for the realization of efficient and long-term stable PSCs in the future.

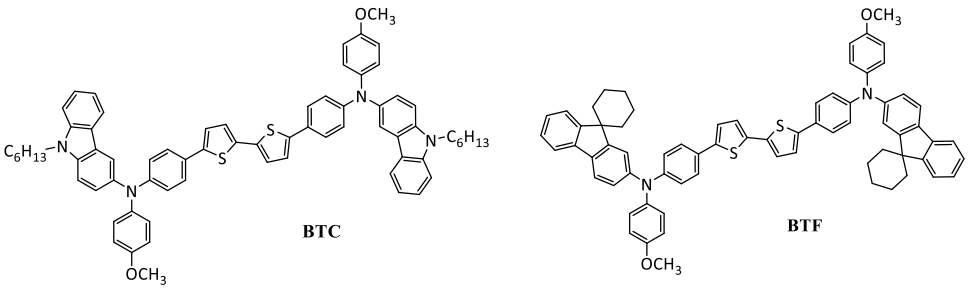

Figure 5.67. Chemical structures of the target HTMs BTC and BTF.

5.4.2 Results and discussion

Synthesis and characterization

The novel designed HTMs were synthesized according to a multistep synthetic pathway through a Pd-catalyzed direct C−H arylation approach, as depicted in Scheme 5.68. This strategy is beneficial in terms of avoiding potentially toxic pre-functionalization steps and use of toxic reagents, such as tin and boronic acid derivatives. Moreover, it required fewer synthetic steps compared to classical carbon−carbon bond coupling via traditional Stille or Suzuki reactions. 2,2'-bithiophene has been used as a C−H activation partner in this strategy. The intermediate (1) in Scheme 5.68 was synthesized by the direct and one-pot Buchwald-Hartwig coupling of 3-bromo-9-hexyl-9H-carbazole with 4-methoxyaniline and 1-bromo-4-iodobenzene with the stoichiometric ratio of 1:1 (see Experimental section 5.4.3.) in the presence of $Pd(OAc)_2$ as catalyst and dppf as ligand. The same route was pursued for the obtainment of the intermediate (2) starting from 2'-bromospiro[cyclohexane-1,9'-fluorene] as mono brominated partner. The intermediates (1) and (2) undergo direct C−H arylation with 2,2'-bithiophene in dry toluene using pivalic acid and Cs_2CO_3 in the presence of $Pd(OAc)_2$ catalyst and (o-Anisyl)$_3$P ligand combination. The BT-HTMs were obtained with the quantitative yields of 54% and 65% for BTC and BTF respectively, after column chromatography.

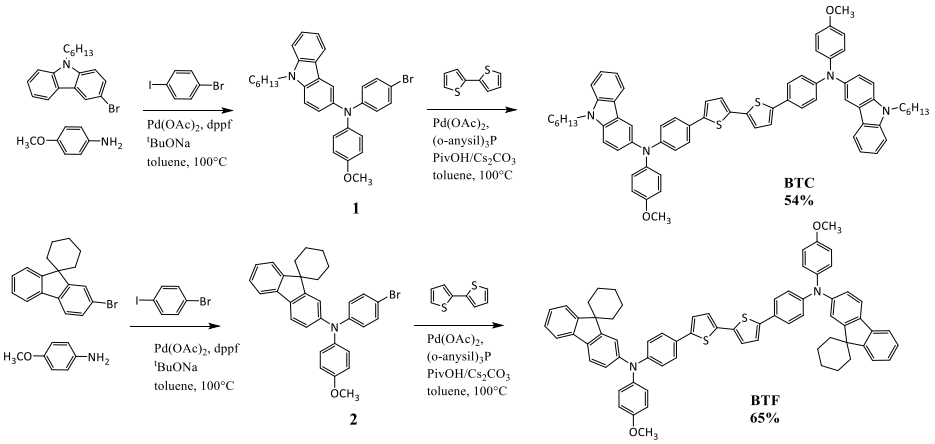

Scheme 5.68. Synthetic sequence for the obtainment of BTC and BTF and relatives yields %.

These target compounds have good solubility in common organic solvents, such as dichloromethane, chloroform, chlorobenzene, and toluene rendering these molecules suitable for application in solution-processed organic electronic devices. The molecular structures were characterized and confirmed by ^{1}H NMR spectroscopy (see Experimental section 5.3.4).

Investigation of thermal properties

The obtained compounds showed excellent thermal stability, which prevent decomposition in device operation. As shown in Figure 5.69 b), TGA carried out at a heating rate of 10 °C min^{-1} revealed very high decomposition temperatures (T_d) (5% weight loss) of 445 °C and 455 °C for BTC and BTF, respectively. DSC studies revealed (Figure 5.69 a) that both compounds exhibit high T_g, with values of 92 °C (BTC) and 136 °C (BTF). These values confirm the existence of a stabilized amorphous state particularly relevant, especially for BTF. This behavior, in both compounds, implies homogeneous films formation and avoid crystallization in device fabrication.

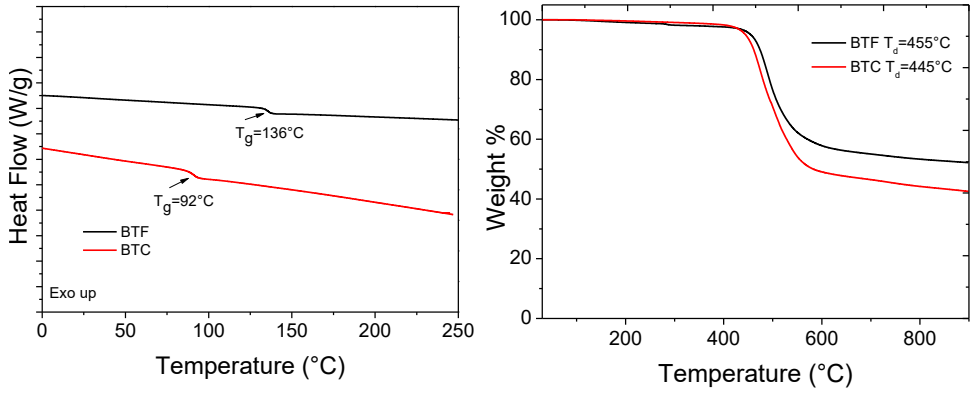

Figure 5.69. a) DSC traces of BTF (black) and BTC (red) (second heating scans) identifying the glass transitions (T_g) events. b) TGA curves of BTF (black) and BTC (red).

Optical and electrochemical properties

Optical properties of synthesized compounds were examined by UV/Vis absorption in dilute dichloromethane solutions (10^{-5} M) and reported in Figure 5.70 a); the corresponding absorption values are listed in Table 5.71. BTC shows an absorption maximum centered at 437 nm, which is due to the π-π* transition of the conjugated system while the absorption bands at the high-energy region at 300−380 nm originated from the localized aromatic π−π* transitions of the D−π−D skeleton. BTF exhibits a similar absorption maximum centered at 435 nm, while the absorption band observed at 300 nm can be ascribed to the π−π* transitions of the carbazole units. The optical band gaps of these materials could be estimated from the absorption onset. Electrochemical cyclic voltammetry (CV) has been employed to investigate the redox behavior of synthesized molecules and to determine their frontier HOMO-LUMO energy values.

Both compounds show multiple redox processes due to the triarylamine moieties which were sequential oxidized, giving two close oxidation waves.

The highest occupied molecular orbital (HOMO) energy values of these compounds were calculated from the onset of the first oxidation potential E_{ox} onset and $E_{1/2}$ of Fc^+/Fc in vacuum. These values are -5.17 eV and -5.27 eV for BTC and BTF, respectively.

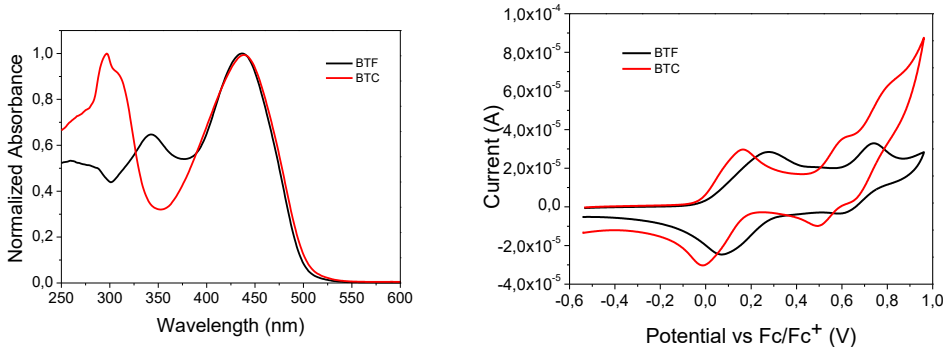

Figure 5.26 a) UV-VIS absorption spectra in dichloromethane (10^{-5} M) and b) cyclic voltammograms of BTF (black) and BTC (red).

These HOMO energy values are located above the perovskite valence band (at ca. -5.4 eV) suggesting that they could be efficient for the hole transfer processes in PSCs. The lowest unoccupied molecular orbital (LUMO) energy values were calculated from the HOMO values and optical bandgap E_g and were listed in Table 5.71. The experimental LUMO values are -2.72 (BTC) and -2.80 eV (BTF). These values are sufficiently high to avoid electron back-transfer to the perovskite layer.

Table 5.71. Thermal, Optical and Electrochemical Properties of the synthesized HTM.

HTM	T_d[a] (°C)	T_g[a] (°C)	λ_{max} [b] (nm)	E_g [c] (eV)	HOMO[d] Exp. (eV)	LUMO[e] Exp. (eV)
BTC	445	92	437	2.45	–5.17	–2.72
BTF	455	136	435	2.47	–5.27	–2.80

[a] Decomposition (T_d, 5% weight loss) and glass transition (T_g) temperatures recorded by TGA and DSC measurements, respectively (10 °C/min, N_2 atmosphere). [b] Absorption maxima measured in CH_2Cl_2 solution (10^{-5} M). [c]Optical bandgap E_g = 1240/λ_{onset} (eV). [d] Determined by cyclic voltammetry with the equation: exp. HOMO = – [E_{ox} – $E_{(Fc/Fc+)}$ + 5.10] (eV). [e]exp LUMO = exp. HOMO + E_g (eV).

Perovskite Solar Cells Employing BTC and BTF

A preliminary photovoltaic characterization of the new BT-based HTMs was pursued by the Hybrid Solar Cells team of the Chemistry and Advanced Materials group of the Tampere University, under the guidance of Prof. Paola Vivo. The hole mobility (μ_h) of SCF-HTMs, was determined by space-charge-limited current (SCLC) method. The estimated values of 1.1×10^{-4} cm^2 V^{-1} s^{-1} for BTC and 1.6×10^{-4} cm^2 V^{-1} s^{-1} for BTF were comparable with the hole mobility μ_h of the doped Spiro-OMeTAD: 3.4×10^{-3} cm^2 V^{-1} s^{-1}.

Hole extraction kinetics

Photoluminescence studies were performed with the aim to investigate the hole extraction capability of novel BT-HTMs. As depicted in Figure 5.72 a), the comparison between the steady-state photoluminescence spectra of glass|CsFAMA and glass|CsFAMA|HTMs samples, including the doped Spiro-OMeTAD as the reference, both excited at 600 nm results in a clear PL quenching for both the HTMs. The hole extraction efficiency was estimated as 98.6%, 94.9% for BTC and

BTF, respectively. The time-resolved PL (TRPL) decays for those same samples, as shown in Figure 5.29 b) demonstrate a fast hole extraction process in comparison with Spiro-OMeTAD, which is in agreement with the PL quenching data.

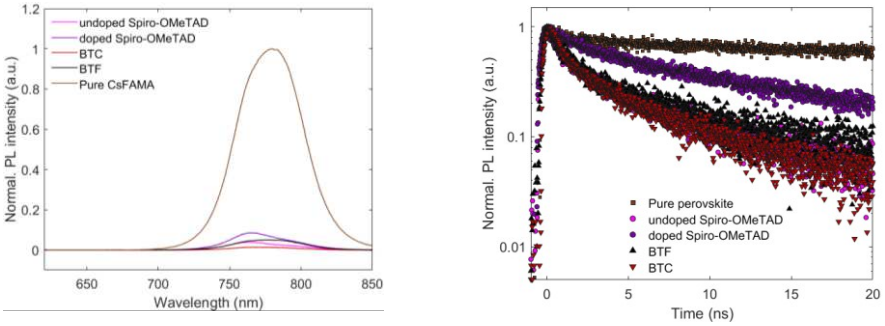

Figure 5.72. a) Normalized photoluminescence (PL) spectra (λ_{ex} = 600 nm) and b) time-resolved PL (TRPL) decays (λ_{ex} = 405 nm with a time resolution of 60 ps and monitored at λ = 755 nm) of glass/CsFAMA and glass/CsFAMA/HTM films with BT-HTMs and doped Spiro-OMeTAD as the reference. Solid lines show the fitting results with a rate law function.

Performance of SCF-HTM-based Solar Cells

Details on the fabrication and characterization of PSCs are provided in the Experimental section 5.4.3, reported above for the SCF-HTMs. To gain more information on device reproducibility, statistical data based on several batches of PSCs are shown in Figure 5.73. The optimized thickness of HTMs in PSCs were obtained by deposition from solutions of 5, 10 and 15 mg mL^{-1} concentration for BTC in chlorobenzene. The highest efficiency corresponded to reference devices, with an average PCE of 16.5%, which was closely followed by devices obtained using BTC (from 15 mg mL^{-1} and 10 mg mL^{-1}solutions) with an average in PCE of 14.0 and 13.5%, respectively. PSCs using BTF HTMs showed lower efficiencies at the same film concentrations with average PCE values ranging from 4.68% to 5.74%.

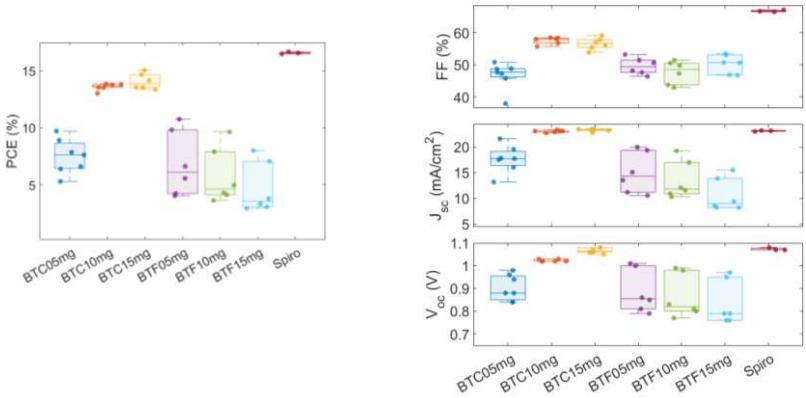

Figure 5.73. Statistical deviation of the photovoltaic parameters for PSCs using polymers BTC and doped Spiro-OMeTAD as HTMs. Whiskers show minimum and maximum values, box represents the values between 25% and 75%, circles represent mean values.

Stability study

The effect of BT-HTMs on PSC stability was evaluated in comparison with a doped Spiro-OMeTAD reference cell. The stability experiments were carried out in air (40–50% relative humidity) on unencapsulated devices, which were stored in dry air (20–25 % relative humidity) in darkness between the periodic measurements. The normalized PCEs of these samples over a period of 32 days are presented in Figures 5.74 and the photovoltaic parameters are listed in Tables 5.75 and 5.76.

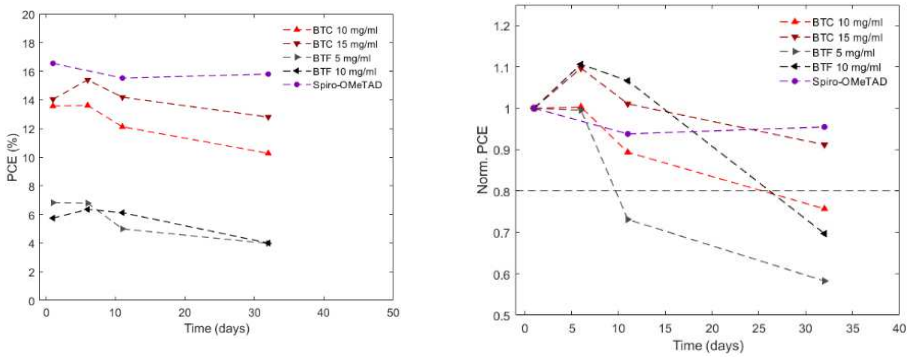

Figure 5.74. PCE (left) and Normalized power conversion efficiency (right) of devices employing doped Spiro-OMeTAD and pristine BT-HTMs stored in ambient air (RH≈50 %).

Table 5.75. Photovoltaic parameters of BT-based devices obtained from different concentrations of BTC and BTF in chlorobenzene recorded 24 h after fabrication. Data have been obtained from 6 devices for each sample of 5, 10, and 15 mg ml^{-1}, with Spiro-OMeTAD reference cell.

Day 1 averages	PCE (%)	FF (%)	Isc (mA/cm^2)	Voc (V)	H-index
BTC 5mg	7.46	46.72	17.65	0.9	1.54
BTC 10mg	13.57	57.53	23.05	1.02	1.18
BTC 15mg	14.04	56.54	23.27	1.07	1.08
BTF 5mg	6.82	49.58	14.97	0.89	1.37
BTF 10mg	5.74	47.62	13.53	0.86	1.26
BTF 15mg	4.68	50.25	10.65	0.84	1.37
Spiro	16.55	66.67	23.13	1.07	1.27

Table 5.76. Photovoltaic parameters of BT-based devices with different concentrations of BTC and BTF in chlorobenzene 32 days after fabrication. Data have been obtained from 6 devices for each sample of 5, 10, and 15 mg ml^{-1}, with Spiro-OMeTAD reference cell.

Day 32 averages	PCE (%)	FF (%)	Isc (mA/cm^2)	Voc (V)	H-index
BTC 5mg	6.13	54.30	12.90	0.88	1.03
BTC 10mg	10.27	54.74	18.34	1.03	1.03
BTC 15mg	12.80	58.46	20.72	1.06	1.03
BTF 5mg	3.98	51.61	9.14	0.84	0.93
BTF 10mg	4.00	47.83	9.77	0.85	0.93
BTF 15mg	4.25	53.60	9.22	0.86	1.08
Spiro	15.80	65.41	21.73	1.11	0.99

As shown, the performance of BT-HTM-based devices significantly improves for up to 1 week following their fabrication. This behavior was observed for devices realized by depositing the HTM from a concentration of BTF of 10 mg ml^{-1} and BTC of 15 mg ml^{-1}. Interestingly, after 32 days, the PCEs of Spiro-OMeTAD- and BTC-based PSCs became nearly identical, despite the initial discrepancy between them. These first results clearly indicate that BTC enhances the stability of perovskite-based devices exhibiting also a good efficiency, which results highly comparable to those obtained using doped-Spiro-OMeTAD. Moreover, the new HTMs were employed without any need of dopants, which can further contribute to the overall stability of devices. As a follow up of this work, the optimization of these

promising materials in PSCs will be further pursued to obtain higher PSCs performance with better devices stability.

Conclusions

The work discussed in this section aims to demonstrate a step-saving and viable synthetic approach to access novel functional small molecules for use in PSCs devices. Based on the optimized direct C–H arylation approach, we have efficiently synthesized two new molecules bearing 2,2'-bithiophene cores in good yields. The novel HTMs exhibited excellent thermal, morphological and electrochemical properties and they presented suitable HOMO levels, which were aligned with that of the perovskite material. Perovskite solar cells fabrication using BTC and BTF as hole transporting materials demonstrated power conversion efficiencies of 3.98–14.04%. Most noteworthy was that PSCs based on dopant-free BTC as the HTM afforded PCE value of 14.04% and which was comparable to that obtained employing the well-known doped Spiro-OMeTAD. In addition, the BTC-based devices showed high stability 32 days after fabrication. Certainly, further investigation is required to dig deeper into the possible advantages that these type of molecules could give. However, to date, this study clearly demonstrates that the development of new potential π-conjugated organic materials in a green chemistry compliant way enables to achieve materials for stable and efficient PSCs.

5.4.3 Experimental section

Synthesis of the hole-transporting materials and intermediates (1) and (2)

Reagents and solvents were purchased from standard commercial sources (Aldrich® and Honeywell Riedel-de-Haën™, respectively), while chemical manipulations were carried out under an inert nitrogen atmosphere using standard Schlenk techniques. The reaction courses were monitored by thin-layer chromatography (TLC) on Merck® silica gel 60 F254 aluminum sheets. ^{1}HNMR spectra were recorded on a Bruker Avance DPX 300 MHz instrument.

Synthesis of 2-bromo-9-hexyl-9H-carbazole [116]

Adapting the literature procedure, a mixture of 50% aqueous NaOH (6 mL), DMSO (20 mL) and 2-bromocarbazole (1.0 g, 4.08 mmol) was slowly added 1-bromohexane (0.68 mL, 4.90 mmol) at room temperature. The mixture was stirred overnight at 90 °C and cooled to room temperature and then added the brine. The organic phase extracted with dichloromethane was dried over Na_2SO_4. The solvent was removed and the residue was purified by silica gel column chromatography using petroleum ether as the eluent. 1.01 g of yellow liquid was obtained (75% yield). ^{1}H NMR (300 MHz, $CDCl_3$): δ 8.06 (d, 1H), 7.94 (d, 1H), 7.54 (s, 1H), 7.45 (t, 1H), 7.40 (d, 1H), 7.33 (d, 1H),7.25 (t, 1H), 4.25 (t, 2H), 1.86 (q, 2H), 1.56-1.23 (m, 6H), 0.88 (t, 3H) ppm.

Synthesis of 2'-bromospiro[cyclohexane-1,9'-fluorene] [80]

Adapting the literature procedure adopting for the synthesis of 2',7'-dibromospiro[cyclohexane-1,9'-fluorene] (see Experimental section 5.3.4), a mixture of 2-bromofluorene (2.936 g, 11.98 mmol) and tetrabutylammonium bromide (1.328 g, 4.12 mmol) in a 50% NaOH aqueous solution (26 mL) was stirred for 15 min at 60°C. To the red suspension a solution of 1,5-dibromopentane (2.755 g, 11.98 mmol) in toluene (26 mL) was added and the mixture was kept under overnight stirring. After cooling the solution, the products were extracted with petroleum ether 40-60°C and the organic layer dried over Na_2SO_4. After removing the solvent in vacuo, the crude was purified by flash chromatography (SiO_2, petroleum ether 40-60°C) to afford 1 (2.319 g, 62%) as a white solid.

Synthesis of N-(4-bromophenyl)-9-hexyl-N-(4-methoxyphenyl)-9H-carbazol-3-amine (one-pot)(1)

A mixture containing 2-bromo-9-hexyl-9H-carbazole (1.796 g, 5.44 mmol), p-anisidine (0.670 g, 5.44 mmol), palladium acetate (0.061 g, 0.27 mmol), dppf (0.301g, 0.54 mmol) and sodium tert-butoxide (1.568 g, 16.32 mmol) in toluene

(20 mL) was stirred at 100 °C for 3 hours. Then, under nitrogen flow 1-bromo-4-iodobenzene (1.539 g, 5.44 mmol) was added and the mixture was stirred overnight. After cooling down the reaction to room temperature, toluene was removed under reduced pressure and dichloromethane (50 mL) was added. The obtained mixture was washed with water (3 × 50 mL), the organic layer was collected and dried over Na_2SO_4. Upon removal of the solvent, the crude product was purified by column chromatography (SiO_2, petroleum ether 40-60 °C/CH_2Cl_2 = 3/2 vol/vol) to obtain intermediate 1 (1.916 g, yields: 58%) as an off-white solid. ^{1}H NMR (300 MHz, $CDCl_3$): δ 8.16 (d, 1H), 7.64 (d, 2H), 7.51 (m, 6H), 7.45 (m, 2H), 7.40 (d, 2H), 7.33 (d, 2H), 4.25 (t, 2H), 3.81 (s, 3H), 1.86 (q, 2H), 1.56-1.23 (m, 6H), 0.88 (t, 3H) ppm.

Synthesis of N-(4-bromophenyl)-N-(4-methoxyphenyl)spiro[cyclohexane-1,9'-fluoren]-2'-amine (one-pot)(2)

A mixture containing 2'-bromospiro[cyclohexane-1,9'-fluorene] (1.730 g, 5.44 mmol), p-anisidine (0.670 g, 5.44 mmol), palladium acetate (0.061 g, 0.27 mmol), dppf (0.301g, 0.54 mmol) and sodium tert-butoxide (1.568 g, 16.32 mmol) in toluene (20 mL) was stirred at 100 °C for 3 hours. Then, under nitrogen flow 1-bromo-4-iodobenzene (1.539 g, 5.44 mmol) was added and the mixture was stirred overnight. After cooling down the reaction to room temperature, toluene was re-moved under reduced pressure and dichloromethane (50 mL) was added. The obtained mixture was washed with water (3 × 50 mL), the organic layer was collected and dried over Na_2SO_4. Upon removal of the solvent, the crude product was purified by column chromatography (SiO_2, petroleum ether 40-60 °C/CH_2Cl_2 = 3/2 vol/vol) to obtain intermediate 1 (1.892 g, yields: 59%) as a white solid. ^{1}H NMR (300 MHz, $CDCl_3$): δ 7.96 (d, 1H), 7.74 (d, 2H), 7.38 (m, 6H), 7.15 (m, 2H), 6.98 (d, 2H), 6.79 (d, 2H), 3.81 (s, 3H), 2.06-1.90 (m, 4H), 1.56-1.23 (m, 6H) ppm.

Synthesis of N,N'-([2,2'-bithiophene]-5,5'-diylbis(4,1-phenylene))bis(9-hexyl-N-(4-methoxyphenyl)-9H-carbazol-3-amine) (C-H activation) BTC

A mixture of N-(4-bromophenyl)-9-hexyl-N-(4-methoxyphenyl)-9H-carbazol-3-amine (1) (0.607 g, 1.00 mmol), 2,2'-bithiophene (0.083 g, 0.50 mmol), palladium acetate (0.022 g, 0.10 mmol), P(*o*-Anisyl)$_3$ (0.070 g, 0.20 mol), pivalic acid (0.030 g, 0.30 mol), Cs_2CO_3 (0.978 g, 3.0 mol) and toluene (5.0 mL) was stirred at 100 °C for 24 hours. After cooling down the reaction to room temperature, toluene was removed under reduced pressure and dichloromethane (50 mL) was added. The obtained mixture was washed with water (3 × 50 mL), the organic layer was collected and dried over Na_2SO_4. Upon removal of the solvent, the crude product was purified by column chromatography (SiO_2, petroleum ether 40-60 °C/CH_2Cl_2 = 1/1 vol/vol) to obtain BTC as a white solid (0.286g, 54%). ^{1}H NMR (300 MHz, acetone-d_6) δ 8.08 (d, J = 7.7 Hz, 2H), 7.98 (d, J = 1.7 Hz, 2H), 7.61 – 7.53 (m, 4H), 7.46 (dd, J = 15.3, 8.1 Hz, 6H), 7.33 – 7.12 (m, 12H), 6.92 (dd, J = 11.6, 8.9 Hz, 8H), 4.43 (t, J = 7.1 Hz, 4H), 3.80 (s, 6H), 1.92 – 1.85 (m, 4H), 1.46 – 1.26 (m, 12H), 0.85 (t, J = 6.9 Hz, 6H) ppm.

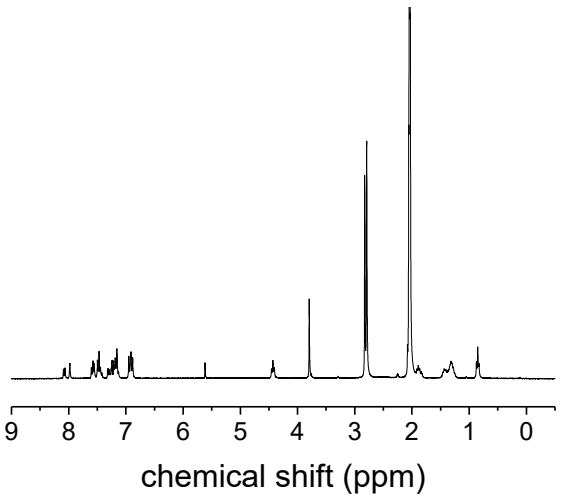

Figure 5.77. ^{1}H NMR spectrum of BTC recorded in acetone-d_6.

Synthesis of N,N'''-([2,2'-bithiophene]-5,5'-diylbis(4,1-phenylene))bis(N-(4-methoxyphenyl)spiro[cyclohexane-1,9'-fluoren]-2'-amine) (C-H activation) BTF

A mixture of N-(4-bromophenyl)-N-(4-methoxyphenyl)spiro[cyclohexane-1,9'-fluoren]-2'-amine (2) (0.510 g, 1.00 mmol), 2,2'-bithiophene (0.083 g, 0.50 mmol), palladium acetate (0.022 g, 0.10 mmol), P(*o*-Anisyl)$_3$ (0.070 g, 0.20 mol), pivalic acid (0.030 g, 0.30 mol), Cs_2CO_3 (0.978 g, 3.0 mol) and toluene (5.0 mL) was stirred at 100 °C for 24 hours. After cooling down the reaction to room temperature, toluene was removed under reduced pressure and dichloromethane (50 mL) was added. The obtained mixture was washed with water (3 × 50 mL), the organic layer was collected and dried over Na_2SO_4. Upon removal of the solvent, the crude product was purified by column chromatography (SiO_2, petroleum ether 40-60 °C/CH_2Cl_2 = 1/1 vol/vol) to obtain BTF as a white solid (0.333 g, 65%). ^{1}H NMR (300 MHz, acetone-d_6) δ 8.08 (d, J = 7.7 Hz, 2H), 7.98 (d, J = 1.7 Hz, 2H), 7.61 – 7.53 (m, 4H), 7.46 (dd, J = 15.3, 8.1 Hz, 6H), 7.33 – 7.12 (m, 12H), 6.92 (dd, J = 11.6, 8.9 Hz, 8H), 3.80 (s, 6H), 1.92 – 1.85 (m, 4H), 1.46 – 1.26 (m, 12H), 0.85 (m, 4H) ppm.

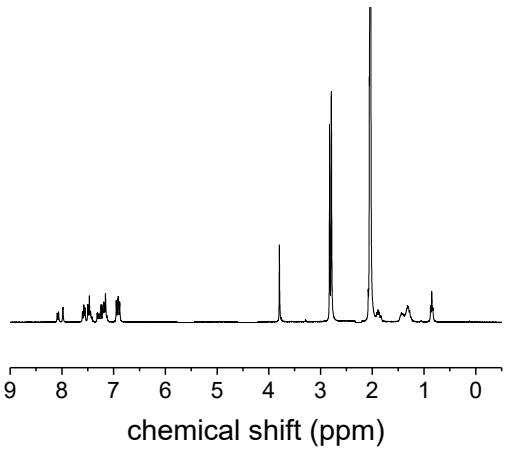

Figure 5.78. ^{1}H NMR spectrum of BTF recorded in acetone-d_6.

Spectroscopic, thermal and electrochemical characterization were performed as described in Experimental section 5.3.4. Solar cells fabrication, device and film characterization were carried out by the Hybrid Solar Cells team of the Chemistry and Advanced Materials group of the Tampere University.

5.5 References

1. IEA. Renewables 2022. [Online] 2022. https://www.iea.org/reports/renewables-2022. License: CC BY 4.0.

2. *Solar energy: a new day dawning? Silicon Valley sunrise.* O., Morton. 7107, 2006, Nature, Vol. 443, p. 19-22.

3. *A New Silicon p-n Junction Photocell for Converting Solar Radiation into Electrical Power.* D. M. Chapin, C. S. Fuller, and G. L. Pearson. 1954 , Journal of Applied Physics , Vol. 25, p. 676-677 .

4. *Brief review of cadmium telluride-based photovoltaic technologies.* Bülent M. Başol, Brian McCandless,. 1, 27 June 2014 , J. Photon. Energy , Vol. 4, p. 040996.

5. *T. Wada, Y. Hashimoto, S. Nishiwaki, T. Satoh, S. Hayashi, T. Negami and H. Miyake. 2001, Solar Energy Materials and Solar Cells, Vol. 67, p. 305-310.*

6. C. Lee, S. Lee, G.-U. Kim, W. Lee and B. J. Kim. 2019, Chemical Reviews, Vol. 119, p. 8028-8086.

7. 10. G. H. Carey, A. L. Abdelhady, Z. Ning, S. M. Thon, O. M. Bakr and E. H. Sargent,. 2015, Chemical Reviews, Vol. 115, p. 12732-12763.

8. A. Hagfeldt, G. Boschloo, L. Sun, L. Kloo and H. Pettersson,. 2010, Chemical Reviews, Vol. 110, p. 6595-6663.

9. Advanced Functional Materials, . 13. R. Wang, M. Mujahid, Y. Duan, Z.-K. Wang, J. Xue and Y. Yang,. 2019, , Vol. 29, p. 1808843.

10. Nature Energy, . T. Leijtens, K. A. Bush, R. Prasanna and M. D. McGehee,. 2018,, Vol. 3, p. 828-838.

11. Perovskite Mineral Data. [Online] http://webmineral.com/data/Perovskite.shtml#.XvhQvpMzZQI)..

12. Methodologies toward Highly Efficient Perovskite Solar Cells. Seok, S. I., Grätzel, M., Park, N.-G.,. 2018,, Small , Vol. 14, p. 1704177.

13. Challenges for commercializing perovskite solar cells. Y. Rong, Y. Hu, A. Mei, H. Tan, M. I. Saidaminov, S. I. Seok, M. D. McGehee, E. H. Sargent and H. Han,. 2018, Science, Vol. 361, p. eaat8235.

14. A new route for the shape differentiation of cesium lead bromide perovskite nanocrystals with near-unity photoluminescence quantum yield. Grisorio, Roberto and Conelli, Daniele and Giannelli, Rosa and Fanizza, Elisabetta and Striccoli, Marinella and Altamura, Davide and Giannini, Cinzia and Allegretta, Ignazio and Terzano, Roberto and Suranna, Gian Paolo. 32, 2020, Nanoscale, Vol. 12, p. 17053-17063.

15. Size-tunable and stable cesium lead-bromide perovskite nanocubes with near-unity photoluminescence quantum yield. Grisorio, Roberto and Conelli, Daniele and Fanizza, Elisabetta and Striccoli, Marinella and

Altamura, Davide and Giannini, Cinzia and Allegretta, Ignazio and Terzano, Roberto and Irimia-Vladu, Mihai and Margiotta, Nicola and Suranna, Gian Paolo. 13, 2021, Nanoscale Adv., Vol. 3, p. 3918-3928.
16. In Situ Formation of Zwitterionic Ligands: Changing the Passivation Paradigms of CsPbBr3 Nanocrystals. Roberto Grisorio, Francesca Fasulo, Ana Belén Muñoz-García, Michele Pavone, Daniele Conelli, Elisabetta Fanizza, Marinella Striccoli, Ignazio Allegretta, Roberto Terzano, Nicola Margiotta, Paola Vivo, and Gian Paolo Suranna. 11, 2022 , Nano Letters , Vol. 22, p. 4437-4444.
17. Novel Photoelectrochemical Cell with Mesoscopic Electrodes Sensitized by Lead-Halide Compounds. Kojima, A., Teshima, K., Miyasaka, T. and Yasuo, S. 2006. 210th ECS Meeting Abstract #397 .
18. Organometal Halide Perovskites as Visible-Light Sensitizers for Photovoltaic Cells. Kojima, A., Teshima, K., Shirai, Y. and Miyasaka, T. 17, 2009, Journal of the American Chemical Society , Vol. 131, p. 6050–6051.
19. 6.5% efficient perovskite quantum-dot-sensitized solar cell. Im, Jeong-Hyeok and Lee, Chang-Ryul and Lee, Jin-Wook and Park, Sang-Won and Park, Nam-Gyu. 10, 2011, Nanoscale, Vol. 3, p. 4088-4093.
20. Lead Iodide Perovskite Sensitized All-Solid-State Submicron Thin Film Mesoscopic Solar Cell with Efficiency Exceeding 9%. H.-S. Kim, C.-R. Lee, J.-H. Im, K.-B. Lee, T. Moehl, A. Marchioro, S.-J. Moon, R. Humphry-Baker, J.-H. Yum, J. E. Moser, M. Grätzel and N.-G. Park,. 591, 2012, Scientific Reports, Vol. 2.
21. M. M. Lee, J. Teuscher, T. Miyasaka, T. N. Murakami and H. J. Snaith,. 2012, Science,, Vol. 338, p. 643-647.
22. The Role of the Interfaces in Perovskite Solar Cells. . Shao, S. e Loi, M. A. 2020, Adv. Mater. Interfaces , Vol. 7, p. 1901469.
23. Halide Perovskites: Is It All about the Interfaces? Philip Schulz, David Cahen, and Antoine Kahn. 5, 2019, Chemical Reviews , Vol. 119 , p. 3349-3417.
24. Understanding Degradation Mechanisms and Improving Stability of Perovskite Photovoltaics. C. C. Boyd, R. Cheacharoen, T. Leijtens and M. D. McGehee,. 5, 2019 , Chemical Reviews , Vol. 119 , p. 3418-3451.
25. Efficiency vs. stability: dopant-free hole transporting materials towards stabilized perovskite solar cells. Rakstys, Kasparas and Igci, Cansu and Nazeeruddin, Mohammad Khaja. 28, 2019, Chem. Sci., Vol. 10, p. 6748-6769.
26. Surface passivation of perovskite film for efficient solar cells. Jiang, Q., Zhao, Y., Zhang, X. et al. 2019, Nat. Photonics , Vol. 13, p. 460–466 .
27. SOLAR CELLS. High-performance photovoltaic perovskite layers fabricated through intramolecular exchange. Yang WS, Noh JH, Jeon NJ, et al. 6240, 2015, Science, Vol. 348, p. 1234-1237.
28. Efficient, stable and scalable perovskite solar cells using poly(3-hexylthiophene) . Jung EH, Jeon NJ, Park EY, et al. 7749, 2019, Nature, Vol. 567, p. 511-515.
29. Recent Advances in Organic Hole Transporting Materials for Perovskite Solar Cells. Sheibani, E., Yang, L. and Zhang, J. 2020, Sol. RRL, Vol. 4, p. 2000461.
30. A low-cost spiro[fluorene-9{,}9′-xanthene]-based hole transport material for highly efficient solid-state dye-sensitized solar cells and perovskite solar cells. Xu, Bo and Bi, Dongqin and Hua, Yong and Liu, Peng and Cheng, Ming and Grätzel, Michael and Kloo, Lars and Hagfeldt, Anders and Sun, Licheng. 3, 2016, Energy Environ. Sci., Vol. 9, p. 873-877.
31. Facile synthesized organic hole transporting material for perovskite solar cell with efficiency of 19.8%. Hagfeldt, Dongqin Bi and Bo Xu and Peng Gao and Licheng Sun and Michael Grätzel and Anders. 2016, Nano Energy, Vol. 23, p. 138-144.
32. M. Saliba, S. Orlandi, T. Matsui, S. Aghazada, M. Cavazzini, J.-P. Correa-Baena, P. Gao, R. Scopelliti, E. Mosconi, K.-H. Dahmen, F. De Angelis, A. Abate, A. Hagfeldt, G. Pozzi, M. Graetzel and M. K. Nazeeruddin,. 2016, Nature Energy, Vol. 1, p. 15017.
33. N. J. Jeon, H. Na, E. H. Jung, T.-Y. Yang, Y. G. Lee, G. Kim, H.-W. Shin, S. Il Seok, J. Lee and J. Seo,. 2018, Nature Energy, Vol. 3, p. 682-689.
34. Efficiency vs. stability: dopant-free hole transporting materials towards stabilized perovskite solar cells. Rakstys, Kasparas and Igci, Cansu and Nazeeruddin, Mohammad Khaja. 28, 2019, Chem. Sci., Vol. 10, p. 6748-6769.

35. Hole Transport Materials in Conventional Structural (n–i–p) Perovskite Solar Cells: From Past to the Future. Kim, G.-W., Choi, H., Kim, M., Lee, J., Son, S. Y., Park, T.,. 2020, Adv. Energy Mater, Vol. 10, p. 1903403.
36. Physical Chemistry Chemical Physics. D.-Y. Chen, W.-H. Tseng, S.-P. Liang, C.-I. Wu, C.-W. Hsu, Y. Chi, W.-Y. Hung and P.-T. Chou,. 2012, Vol. 14, p. 11689-11694.
37. J. Burschka, A. Dualeh, F. Kessler, E. Baranoff, N.-L. Cevey-Ha, C. Yi, M. K. Nazeeruddin and M. Grätzel,. 2011, J. Am. Chem. Soc, Vol. 133, p. 18042-18045.
38. B. Xu, J. Huang, H. Ågren, L. Kloo, A. Hagfeldt and L. Sun,. 2014, ChemSusChem,, Vol. 7, p. 3252-3256.
39. B. Xu, E. Gabrielsson, M. Safdari, M. Cheng, Y. Hua, H. Tian, J. M. Gardner, L. Kloo and L. Sun,. 2015, Adv. Energy Mater., Vol. 5, p. 1402340.
40. S. Wang, M. Sina, P. Parikh, T. Uekert, B. Shahbazian, A. Devaraj and Y. S. Meng,. 2016,, Nano Letters, Vol. 16, p. 5594-5600.
41. E. J. Juarez-Perez, M. R. Leyden, S. Wang, L. K. Ono, Z. Hawash and Y. Qi,. 2016, Chem. Mat., Vol. 28, p. 5702-5709.
42. Grätzel, H. J. Snaith and M. 2006, Applied Physics Letters, Vol. 89, p. 262114.
43. J. Burschka, F. Kessler, M. K. Nazeeruddin and M. Grätzel. 2013,, Chem. Mat.,, Vol. 25, p. 2986-2990.
44. X.-F. Zhang, C. Liu, J. Wu and B. Xu,. 2020, Journal of Energy Chemistry, , Vol. 43, , p. 139-147.
45. A. Magomedov, E. Kasparavičius, K. Rakstys, S. Paek, N. Gasilova,K. Genevičius, G. Juška, T. Malinauskas, M. K. Nazeeruddin and V. Getautis,. 6, 2018, Journal of Materials Chemistry C, p. 8874-8878.
46. W. Zhou, Z. Wen and P. Gao,. 2018, Adv. Energy Mater, Vol. 8, p. 1702512.
47. H. D. Pham, T. C.-J. Yang, S. M. Jain, G. J. Wilson and P. Sonar,. 2020, Adv. Energy Mater., Vol. 10, p. 1903326.
48. J. Liu, Y. Wu, C. Qin, X. Yang, T. Yasuda, A. Islam, K. Zhang, W. Peng, W. Chen and L. Han,. 2014, Energy Environ. Sci.,, Vol. 7, p. 2963- 2967.
49. Semi-Locked Tetrathienylethene as a Building Block for Hole-Transporting Materials: Toward Efficient and Stable Perovskite Solar Cells. C. Shen, Y. Wu, H. Zhang, E. Li, W. Zhang, X. Xu, W. Wu, H. Tian and W.-H. Zhu,. 2019, Angewandte Chemie International Edition, Vol. 58, p. 3784-3789.
50. Protocol for Quantifying the Doping of Organic Hole-Transport Materials. R. L. Forward, K. Y. Chen, D. M. Weekes, D. J. Dvorak, Y. Cao and C. P. Berlinguette. 2019, ACS Energy Letters, Vol. 4, p. 2547-2551.
51. Journal of Materials Chemistry A. 95. H. D. Pham, S. M. Jain, M. Li, S. Manzhos, K. Feron, S. Pitchaimuthu, Z. Liu, N. Motta, H. Wang, J. R. Durrant and P. Sonar. 2019,, Vol. 7, p. 5315-5323.
52. J Am Chem Soc. C. Huang, W. Fu, C. Z. Li, Z. Zhang, W. Qiu, M. Shi, P. Heremans,A. K. Jen and H. Chen,. 2016, Vol. 138, p. 2528-2531.
53. . J. Zhou, X. Yin, Z. Dong, A. Ali, Z. Song, N. Shrestha, S. S. Bista, Q. Bao, R. J. Ellingson, Y. Yan and W. Tang,. 2019, Angewandte Chemie, , Vol. 131, p. 13855-13859.
54. Polymeric, Cost-Effective, Dopant-Free Hole Transport Materials for Efficient and Stable Perovskite Solar Cells. F. Zhang, Z. Yao, Y. Guo, Y. Li, J. Bergstrand, C. J. Brett, B. Cai, A. Hajian, Y. Guo, X. Yang, J. M. Gardner, J. Widengren, S. V. Roth, L. Kloo and L. Sun,. 2019, J. Am. Chem. Soc., Vol. 141, p. 19700-19707.
55. Efficient inorganic–organic hybrid heterojunction solar cells containing perovskite compound and polymeric hole conductors. Heo, J., Im, S., Noh, J. et al. 2013, Nature Photon , Vol. 7, p. 486–491 .
56. Efficient, stable and scalable perovskite solar cells using poly(3-hexylthiophene). E. H. Jung, N. J. Jeon, E. Y. Park, C. S. Moon, T. J. Shin, T.-Y. Yang, J. H. Noh and J. Seo,. 7749, 2019, Nature, Vol. 567, p. 511-515.
57. Dopant-Free Hole-Transporting Polymers for Efficient and Stable Perovskite Solar Cells. Silvia Valero, Silvia Collavini, Sebastian F. Völker, Michael Saliba, Wolfgang R. Tress, Shaik M. Zakeeruddin, Michael Grätzel, and Juan Luis Delgado. 6, 2019 , Macromolecules , Vol. 52, p. 2243-2254.
58. High Efficiency Planar p-i-n Perovskite Solar Cells Using Low-Cost Fluorene-Based Hole Transporting Material. Zhang, J., Sun, Q., Chen, Q., Wang, Y., Zhou, Y., Song, B., Yuan, N., Ding, J., Li, Y.,. 2019, Adv. Funct. Mater, Vol. 29, p. 1900484.
59. Dopant-free polymeric hole transport materials for highly efficient and stable perovskite solar cells. Kim, Guan-Woo and Kang, Gyeongho and Kim, Jinseck and Lee, Gang-Young and Kim, Hong Il and Pyeon, Limok and Lee, Jaechol and Park, Taiho. 7, 2016, Energy Environ. Sci., Vol. 9, p. 2326-2333.

60. Cross-Linkable Fluorene-Diphenylamine Derivatives for Electrochromic Applications. Silja Abraham, Gayathri Prabhu T. Ganesh, Sunil Varughese, Biswapriya Deb, and Joshy Joseph. 45, 2015, ACS Applied Materials & Interfaces, Vol. 7, p. 25424-25433.

61. Side-Chain Polymers as Dopant-Free Hole-Transporting Materials for Perovskite Solar Cells—The Impact of Substituents' Positions in Carbazole on Device Performance. Jianchang Wu, Chang Liu, Bo Li, Fenglong Gu, Luozheng Zhang, Manman Hu, Xiang Deng, Yuan Qiao, Yongyun Mao, Wenchang Tan, Yanqing Tian, and Baomin Xu. 30, 2019 , ACS Applied Materials & Interfaces , Vol. 11, p. 26928-26937.

62. A crosslinked polymer as dopant-free hole-transport material for efficient n-i-p type perovskite solar cells. Sun, Linqin Wang and Fuguo Zhang and Tianqi Liu and Wei Zhang and Yuanyuan Li and Bin Cai and Lanlan He and Yu Guo and Xichuan Yang and Bo Xu and James M. Gardner and Lars Kloo and Licheng. 2021, Journal of Energy Chemistry, Vol. 55, p. 211-218.

63. Facile Thiol-Ene Thermal Crosslinking Reaction Facilitated Hole-Transporting Layer for Highly Efficient and Stable Perovskite Solar Cells. . Li, Z., Zhu, Z., Chueh, Chu-Chen, Luo, J., Jen, A. K.-Y. 2016, Adv. Energy Mater., Vol. 6, p. 1601165.

64. Stacking Principles on π- and Lamellar Stacking for Organic Semiconductors Evaluated by Energy Decomposition Analysis. Yu-Ying Lai, Vi-Hsiang Huang, Hao-Ting Lee, and Hau-Ren Yang. 12, 2018, ACS Omega, Vol. 3 , p. 18656-18662.

65. Crosslinked and dopant free hole transport materials for efficient and stable planar perovskite solar cells. Zhang, Yun and Kou, Chun and Zhang, Junjie and Liu, Yahui and Li, Wenhua and Bo, Zhishan and Shao, Ming. 10, 2019, J. Mater. Chem. A, Vol. 7, p. 5522-5529.

66. Efficient solution processed CH3NH3PbI3 perovskite solar cells with polyTPD hole transport layer. Höcker J, Kiermasch D, Rieder P, Tvingstedt K, Baumann A, Dyakonov V. 1 Aug 2019 , Zeitschrift für Naturforschung A., Vol. 74, p. 665-672.

67. Sequentially Fluorinated PTAA Polymers for Enhancing VOC of High-Performance Perovskite Solar Cells. Kim, Y., Jung, E. H., Kim, G., Kim, D., Kim, B. J., Seo, J.,. 2018, Adv. Energy Mater., Vol. 8, p. 1801668.

68. A photo-crosslinkable bis-triarylamine side-chain polymer as a hole-transport material for stable perovskite solar cells. Tremblay, Marie-Hélène and Schutt, Kelly and Zhang, Yadong and Lim, Jongchul and Lin, Yen-Hung and Warby, Jonathan H. and Barlow, Stephen and Snaith, Henry J. and Marder, Seth R. 1, 2020, Sustainable Energy Fuels, Vol. 4, p. 190-198.

69. Triarylamine polymers of bridged phenylenes by (N-heterocyclic carbene)-palladium catalysed C–N coupling. Sprick, Reiner Sebastian and Hoyos, Mario and Morrison, John James and Grace, Iain Mark and Lambert, Colin and Navarro, Oscar and Turner, Michael Lewis. 20, 2013, J. Mater. Chem. C, Vol. 1, p. 3327-3336.

70. Carbazole-Based Hole-Transport Materials for High-Efficiency and Stable Perovskite Solar Cells. Liguo Gao, Tracy H. Schloemer, Fei Zhang, Xihan Chen, Chuanxiao Xiao, Kai Zhu, and Alan Sellinger. 5, 2020, ACS Applied Energy Materials, Vol. 3, p. 4492-4498.

71. Catalyst-transfer polymerization of arylamines by the Buchwald–Hartwig cross-coupling. Grisorio, Roberto and Suranna, Gian Paolo. 15, 2019, Polym. Chem., Vol. 10, p. 1947-1945.

72. Thermally Stable Perovskite Solar Cells by Systematic Molecular Design of the Hole-Transport Layer. Tracy H. Schloemer, Timothy S. Gehan, Jeffrey A. Christians, Deborah G. Mitchell, Alex Dixon, Zhen Li, Kai Zhu, Joseph J. Berry, Joseph M. Luther, and Alan Sellinger. 2, 2019 , ACS Energy Letters , Vol. 4, p. 473-482.

73. Polymer Hole Transport Materials for Perovskite Solar Cells via Buchwald–Hartwig Amination. Daniel D. Astridge, Jacob B. Hoffman, Fei Zhang, So Yeon Park, Kai Zhu, and Alan Sellinger. 11, 2021, ACS Applied Polymer Materials , Vol. 3 , p. 5578-5587.

74. Hole Transport Materials with Low Glass Transition Temperatures and High Solubility for Application in Solid-State Dye-Sensitized Solar Cells. Tomas Leijtens, I-Kang Ding, Tommaso Giovenzana, Jason T. Bloking, Michael D. McGehee, and Alan Sellinger. 2, 2012 , ACS Nano , Vol. 6, p. 1455-1462.

75. High-Efficiency Perovskite Solar Cells Using Molecularly Engineered, Thiophene-Rich, Hole-Transporting Materials: Influence of Alkyl Chain Length on Power Conversion Efficiency. Zimmermann, I., Urieta-Mora, J.,

Gratia, P., Aragó, J., Grancini, G., Molina-Ontoria, A., Ortí, E., Martín, N., Nazeeruddin, M. K.,. 2017, Adv. Energy Mater. , Vol. 7, p. 1601674.
76. The Importance of Pendant Groups on Triphenylamine-Based Hole Transport Materials for Obtaining Perovskite Solar Cells with over 20% Efficiency. Zhang, J., Xu, B., Yang, L., Ruan, C., Wang, L., Liu, P., Zhang, W., Vlachopoulos, N., Kloo, L., Boschloo, G., Sun, L., Hagfeldt, A., Johansson, E. M. J.,. 2018, Adv. Energy Mater, Vol. 8, p. 1701209.
77. Chart., NREL Efficiency. http://www.nrel.gov/ncpv/images/efficiency_chart.jpg . [Online] 2022.
78. Towards stable and commercially available perovskite solar cells. Park, NG., Grätzel, M., Miyasaka, T. et al. 2016, Nat Energy , Vol. 1, p. 16152 .
79. The Role of the Interfaces in Perovskite Solar Cells. Shao, S., Loi, M. A.,. 2020, Adv. Mater. Interfaces, Vol. 7, p. 1901469.
80. Synthesis of bifluorene-based molecular materials: effect of C-9 spirocyclohexane functionalization and end-group tailoring},. Roberto Grisorio and Claudia Piliego and Pinalysa Cosma and Paola Fini and Piero Mastrorilli and Giuseppe Gigli and Gian Paolo Suranna and Cosimo Francesco Nobile}. 37, 2008, Tetrahedron, Vol. 64, p. 8738-8745.
81. o-Methoxy Substituents in Spiro-OMeTAD for Efficient Inorganic–Organic Hybrid Perovskite Solar Cells. Nam Joong Jeon, Hag Geun Lee, Young Chan Kim, Jangwon Seo, Jun Hong Noh, Jaemin Lee, and Sang Il Seok. 22, 2014 , Journal of the American Chemical Society , Vol. 136 , p. 7837-7840.
82. Thionation Enhances the Performance of Polymeric Dopant-Free Hole-Transporting Materials for Perovskite Solar Cells. . Zhang, H., Liu, M., Yang, W., Judin, L., Hukka, T. I., Priimagi, A., Deng, Z., Vivo, P.,. 2019, Adv. Mater. Interfaces , Vol. 6, p. 1901036.
83. al.., M. J. Frisch et. Gaussian 09. s.l. : (Gaussian, Inc., Wallingford CT, 2009).
84. Lead Iodide Perovskite Sensitized All-Solid-State Submicron Thin Film Mesoscopic Solar Cell with Efficiency Exceeding 9%. . Kim, HS., Lee, CR., Im, JH. et al. 2012, Sci Rep , Vol. 2, p. 591 .
85. Photo-excitation intensity dependent electron and hole injections from lead iodide perovskite to nanocrystalline TiO2 and spiro-OMeTAD. Makuta, Satoshi and Liu, Maning and Endo, Masaru and Nishimura, Hidetaka and Wakamiya, Atsushi and Tachibana, Yasuhiro. 4, 2015, Chem. Commun., Vol. 52, p. 673-676.
86. Beyond hydrophobicity: how F4-TCNQ doping of the hole transport material improves stability of mesoporous triple-cation perovskite solar cells. Liu, M., et al. 21, 2022, J. Mater. Chem. A, Vol. 10, p. 11721-11731.
87. Moisture and Oxygen Enhance Conductivity of LiTFSI-Doped Spiro-MeOTAD Hole Transport Layer iPerovskite Solar Cells. Hawash, Z., Ono, L. K., Qi, Y. 2016, Adv. Mater. Interfaces, , Vol. 3, p. 1600117 .
88. Procedures and Practices for Evaluating Thin-Film Solar Cell Stability. . Roesch, R., Faber, T., Hauff, E. v., Brown, T. M., Lira-Cantu, M., Hoppe, H. , 2015, Adv. Energy Mater., Vol. 5, p. 1501407.
89. Recent advances in dopant-free organic hole-transporting materials for efficient{,} stable and low-cost perovskite solar cells. Yan, Pengyu and Yang, Daobin and Wang, Hongqian and Yang, Shuncheng and Ge, Ziyi. 9, 2022, Energy Environ. Sci., Vol. 15, p. 3630-3669.
90. Hill climbing hysteresis of perovskite-based solar cells: a maximum power point tracking investigation. . Pellet, N., Giordano, F., Ibrahim Dar, M., Gregori, G., Zakeeruddin, S. M., Maier, J., and Grätzel, M. 2017, Prog. Photovolt: Res. Appl., , Vol. 25, p. 942– 950.
91. Sulfonated Dopant-Free Hole-Transport Material Promotes Interfacial Charge Transfer Dynamics for Highly Stable Perovskite Solar Cells. Li, R., Liu, M., Matta, S. K., Hiltunen, A., Deng, Z., Wang, C., Dai, Z., Russo, S. P., Vivo, P., Zhang, H.,. 2021, Adv. Sustainable Syst. , Vol. 5, p. 2100244.
92. Stable perovskite solar cells with efficiency exceeding 24.8% and 0.3-V voltage loss. Jeong M, Choi IW, Go EM, et al. 6511, 2020, Science., Vol. 369, p. 1615-1620 .
93. Halogen-Bonded Hole-Transport Material Suppresses Charge Recombination and Enhances Stability of Perovskite Solar Cells. Canil, L., Salunke, J., Wang, Q., Liu, M., Köbler, H., Flatken, M., Gregori, L., Meggiolaro, D., Ricciarelli, D., De, F., Stolterfoht, M., Neher, D., Priimagi, A., Vivo, P., Abate, A.,. 2021, Adv. Energy Mater. , Vol. 11, p. 2101553.
94. J. M. Kauffman, G. Moyna,. 2003, , J. Org. Chem., , Vol. 68, p. 839–853.

95. S. Urgaonkar, J.-H. Xu, J. G. Verkade,. 2003, J. Org. Chem., Vol. 68, p. 8416–8423.
96. M. I. Saidaminov, J. Kim, A. Jain, R. Quintero-Bermudez, H. Tan, G. Long, F. Tan, A. Johnston, Y. Zhao, O. Voznyy and E. H. Sargent,. 3, 2018 , Nat. Energy , Vol. 38, p. 648–654.
97. K. Burke. 2012, , J. Chem. Phys., , Vol. 136, , p. 150901.
98. V. Blum, R. Gehrke, F. Hanke, P. Havu, V. Havu, X. Ren, K. Reuter and M. Scheffler,. 2009, Comput. Phys. Commun., , Vol. 180, , p. 2175–2196.
99. V. Havu, V. Blum, P. Havu and M. Scheffler,. 2009,, J. Comput. Phys., , Vol. 228, p. 8367–8379.
100. E. Van Lenthe, J. G. Snijders and E. J. Baerends,. 1998, , J. Chem. Phys., , Vol. 105, , p. 6505.
101. A. Tkatchenko and M. Scheffler. 2009,, Phys. Rev. Lett., , Vol. 102, , p. 073005.
102. A. Tkatchenko, R. A. Distasio, R. Car and M. Scheffler,. 2012, , Phys. Rev. Lett., , Vol. 108, , p. 236402.
103. S. Makuta, M. Liu, M. Endo, H. Nishimura, A. Wakamiya and Y. Tachibana,. Chem. Commun.
104. W. Li, X. Lai, F. Meng, G. Li, K. Wang, A. K. K. Kyaw and X. W. Sun,. 2020,, Sol. Energy Mater. Sol. Cells, Vol. 211, p. 110527.
105. N. Lamminen, G. K. Grandhi, F. Fasulo, A. Hiltunen, H. Pasanen, M. Liu, B. Al-Anesi, A. Efimov, H. Ali-Löytty, K. Lahtonen, P. Mäkinen, A. Matuhina, A. B. Muñoz-García, M. Pavone and P. Vivo,. 2022 , Adv. Energy Mater, p. 2203175.
106. J. D. McGettrick, K. Hooper, A. Pockett, J. Baker, J. Troughton, M. Carnie and T. Watson,. 2019,, Mater. Lett.,, Vol. 251, p. 98–101.
107. Q. Zhou, L. Liang, J. Hu, B. Cao, L. Yang, T. Wu, X. Li, B. Zhang and P. Gao,. 2019 , Adv. Energy Mater., Vol. 9, p. 1802595.
108. N. Cai, F. Li, Y. Chen, R. Luo, T. Hu, F. Lin, S. M. Yiu, D. Liu, D. Lei, Z. Zhu and A. K. Y. Jen,. 2021, Angew. Chemie Int. Ed., , Vol. 60, p. 20437–20442.
109. L. K. Ono, P. Schulz, J. J. Endres, G. O. Nikiforov, Y. Kato, A. Kahn and Y. Qi,. 2014, J. Phys. Chem. Lett.,, Vol. 5, p. 1374–1379.
110. Li, Z. R. Organic Light-Emitting Materials and Devices;. 2015.
111. Dye-Sensitized Solar Cells. Anders Hagfeldt, Gerrit Boschloo, Licheng Sun, Lars Kloo, and Henrik Pettersson. 11, 2010 , Chemical Reviews, Vol. 110, p. 6595-6663.
112. Kippelen, B. e Brédas, J. L. Organic Photovoltaics. 2009 . Vol. 2.
113. Organic semiconductors for solution-processable field-effect transistors (OFETs). Allard S, Forster M, Souharce B, Thiem H, Scherf U. 22, 2008, Angew Chem Int Ed Engl. , Vol. 47, p. 4070-4098 .
114. Fundamental Aspects of Property Tuning in Push–pull Molecules. . Bureš, F. ,. 2014, RSC Adv. , Vol. 4.
115. Hole-Transporting Materials for PerovskiteSensitized Solar Cells. Dhingra, P., et al. 2016,, Energy Technol. , Vol. 4, p. 891–938.
116. Synthesis and piezochromic luminescence of aggregation-enhanced emission 9,10-bis(N-alkylcarbazol-2-yl-vinyl-2)anthracenes. Yang, Lingyu Bu and Yiping Li and Jianfeng Wang and Mingxiao Sun and Meng Zheng and Wei Liu and Shanfeng Xue and Wenjun. 3, 2013, Dyes and Pigments, Vol. 99, p. 833-838.

6 CHAPTER 6

Design, synthesis and properties of TADF materials for novel metal-free and low-cost efficient OLED emitters.

6.1 INTRODUCTION

6.1.1 *Preface and motivations*

The growing search toward a more sustainable use of electricity in society requires the replacement of conventional light sources with newer and more efficient ones. Given that lighting accounts for 15% of global electricity consumption and 5% of global greenhouse gas emissions, accelerating the transition to energy-efficient lighting could be one of the most significant short-term initiatives to improve economic and climate conditions. According to the US Energy Information Administration (EIA), the energy efficiency – or "efficacy" for light sources – is expected to continue to improve through 2050, further reducing the environmental impact and lowering running costs. [1] In the meantime, it is projected that the lighting demand will be increased by 50% of the existing consumption due to an increase in the global population by 2030. [2] In this scenario, the transition to advanced lighting solutions like Solid-State Lighting (SSL) devices could essentially decrease the electricity consumption from lighting by 50% over the same period (i.e. 50% more light using 50% less electricity). [1] [2]

Presently, organic light emitting diodes (OLEDs) are promoted extensively for lighting usage. Unique features such as ultrahigh efficiency, large color gamut, thin form factors, and sufficient lifetimes of these devices are most suitable for such applications. In the recent years, OLED technology development (displayed in Fig. 6.1.) aims to reduce the energy consumption offering also a lower extent of environmental impact over the traditional incandescent and fluorescent lightings. As a result, it is argued that the introduction of innovative materials (i.e. TADF emitters) that can be manufactured cost-effectively with high performance for the conversion of electricity to light, will address the environmental

degradation concern by eliminating toxic materials/gases and elevating OLED devices as prime candidates for the next generation of lighting sources.

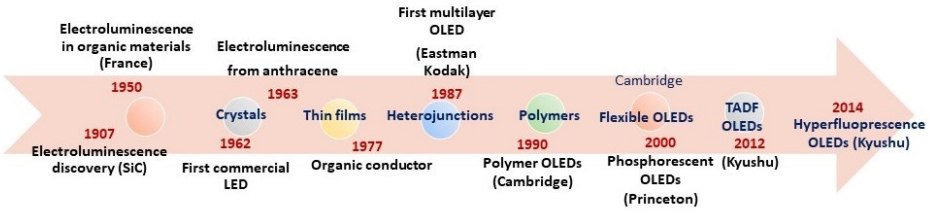

Figure 6.1. Time evolution of the OLED technology.

To date, the scientific efforts are related to the use of innovative TADF emitters which act as triplet-harvesting molecules, [3] [4] in order to exploit all excited states generated in an OLED and therefore improve significantly the quantum efficiency of these devices. The growing need to design and synthesize high performance organic π-conjugated molecules as OLED emitters – to make them more efficient and tailored for specific needs – has given a ground and became a motivation for this section of the Thesis. The aim of this chapter is to provide a comprehensive description, at the molecular level, of the fundamental photophysical processes behind TADF emitters in order to highlight the pursued results in this Thesis inherent the rational molecular design and suitable synthetic strategies paving the way to new classes of TADF materials.

6.1.2 TADF in Organic Light-Emitting Diodes

A key component of OLEDs is the light emitting layer, which usually consists of a thin film of organic material (typical thickness in the order of 100 nm). Typically, emission of an organic compound involves a transition between the ground state and the singlet excited state, S_0 and S_1. Whereas, electroluminescence (EL), which allows the operation of an OLED device, occurs after the formation of singlet excited states, resulting from the exciton recombination of the charges injected into the device. Prompt fluorescence, which occurs on a nanosecond time scale, is the classic mechanism on which an OLED is based (Figure 6.2.). However, a suitable

design of the organic emitting layer allows to reduce the energy gap existing between excited singlet states and triplet states, the latter normally non-emissives. Under these conditions, can occur the phenomenon of reverse intersystem crossing (rISC) which is the basis of thermally activated delayed fluorescence (TADF). This endothermic process increases the number of emissive states at the molecular level by lengthening the emission time on the microsecond scale and allowing to reach 100% internal quantum efficiency in the device. The $T_1 \rightarrow S_1$ conversion requires thermal energy and for this reason TADF works accordingly to a Boltzmann process, with the intensity and lifetime of the delayed fluorescence being dependent upon temperature and activation energy. As OLEDs are required to work at ca. 295 K (room temperature), there is a general trend to design emitters with negligibly small TADF activation energy as the temperature is generally kept constant. However, a main important advantage of this process relies on the possibility to obtain high efficiencies, avoiding the use of metal-based organometallic complexes (rare, expensive and toxic) and addressing the problem of device efficiency towards the search for new fully organic molecular design strategies. [5]

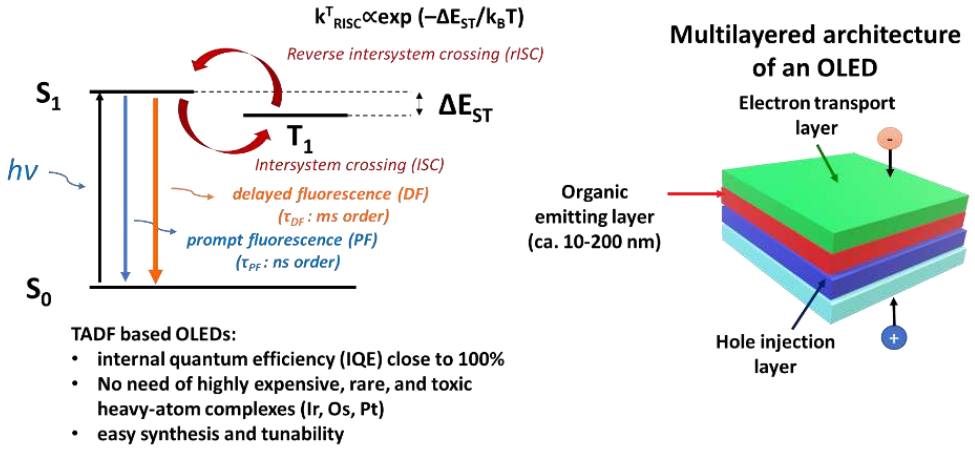

Figure 6.2. a) Schematic representation of emission, ISC, rISC, TADF and prompt fluorescence processes in a Jablonski diagram. b) Simplified physical structure of an OLED device.

6.1.3 Role of triplet harvesting in OLED

Since Tang and Van Slyke reported the first OLED device in 1987, [6] many organic luminescent materials with advanced device performances have been reported which enabled a rapid progress of OLED technology. The electroluminescence (EL) quantum efficiency is the most essential parameter for an OLED device and in particular the EQE (η_{ext}), which is defined as the ratio of the number of emitted photons outside the device to the apparent number of charges injected into the device. The guidelines for improving the efficiency of OLEDs are based precisely on the latter figure of merit, considering the main parameters of equation 6.3.

$$\eta_{ext} = \gamma \cdot \eta_r \cdot \phi_{PL} \cdot \eta_{out} \equiv \eta_{in} \cdot \eta_{out} \quad \textit{Equation 6.3.}$$

where η_{out} is the out-coupling efficiency (typically equal to 0.2-0.3), which is related to the dipole orientation of the molecules in the emissive layer, η_r is the ratio of the radiative excitons, γ represents the electron−hole balance, and Φ_{PL} (or PLQY) is the photoluminescence quantum yield.

In the excited state, statistically, the electrons of the π-conjugated organic molecules can assume four possible spin orientations with respect to each other: three triplets and one singlet state. Because the electrons the electrons and holes are injected on cathode (metal) and anode (ITO) on different molecules, their spins states are not correlated. There is an equal probability of any of these four outcomes. Therefore, 25% of all excited states that form are singlets and the remaining 75% are triplets. [7]

The first generation of OLEDs incorporated fluorescent emitters into the organic emitting layer (Figure 6.4 a). These are characterized by fast rates (ns) of radiative $S_1 \rightarrow S_0$ decay and high quantum yields. Such characteristics are shared by molecules that emit from $\pi \rightarrow \pi^*$ transitions. However, these transitions are associated with low utilization of triplet states since spin-orbit coupling is weak. Hence, in first-generation OLEDs, nearly 75% of all excited states produced were "dark," dissipating their energy as heat.[8]

The second generation of OLED technology replaced fluorescent emitters with complexes of platinum group metals like iridium, osmium and platinum. Emission from these complexes derives from metal-to-ligand or ligand-to-metal charge transfer, which, coupled with the heavy atom effect of row 5 and 6 metals, induces strong spin-orbit coupling. As such, $S_1 \rightarrow T_1$ ISC and $T_1 \rightarrow S_0$ phosphorescence are rapid processes.

Phosphorescent OLEDs were the first to make use of all electrically generated excited states through the ability to convert singlets to triplets. [9] However, limits such as the above mentioned scarcity of the platinum group metals on Earth, toxicity and high cost of these materials is triggering a strong impetus from both cost and environmental standpoints to find new ways of exploiting purely organic emitters, which in addition can offer greater flexibility to fine tune the electronic and optical properties by exploiting the synthetic organic chemistry toolbox.

In 2012, Adachi and co-workers demonstrated that the usage of nearly 100% of electrically generated excited states could be achieved with purely organic molecules by harnessing TADF. [10] They prepared the first purely organic TADF OLED with an EQE of 5.3%, which is approaching the theoretical limitation of OLEDs (5%, assuming a light out-coupling efficiency of 20%) using conventional fluorescent molecules. [11] Specifically, these materials can exploit the rISC as preferential channel to thermally repopulate the singlet state from the triplet state, leading to an increase of the luminescence intensity. This attractive feature has positioned TADF emitters as the third generation of OLED emissive materials (Figure 6.4.). Nowadays, the most accepted model of rISC is the vibronic coupling model, which is briefly presented in this section.

Figure 6.4 c shows the fundamental energy levels and the rate constants involved in the TADF mechanism. For many typical donor-acceptor (D-A) and donor-acceptor-donor (D-A-D) type TADF molecules there are two possible excitation channels. Firstly, the molecules may be excited via a strong local D (or A) π-π* transition, which forms a local excited singlet state (^{1}LE). Following this, the excitation can either undergo electron transfer (ET) to form a CT state, radiative decay to

the ground state, or intersystem crossing (ISC) to the local triplet states (^{3}LE). Secondly, they may be excited via a weak n-π* or mixed n-π*/π-π* transition directly generating the ^{1}CT state. The former is the more usual experimental situation, thus, following photoexcitation (absorption), depending on the rate of ET it is possible to detect ^{1}LE emission in the first few nanoseconds of decay. The majority of excitations, however, are transferred to the ^{1}CT manifold by very slow (on the order of 10^8 s^{-1}) ET. This ET is slow because of the decoupling between D and A units caused by near orthogonality between them even in the ground state (due to the N-C bridging bond) as discussed later in this section. Once the ^{1}CT is formed, three distinct processes follow: i.e. radiative emission yielding prompt ^{1}CT fluorescence (PF), k_{PF}; ii. non-radiative decay, $^1k_{nr}$; or iii. intersystem crossing (ISC) to the triplet states. Once the triplet states are reached, they can either recombine to the ground state by either radiative (k_{PH}) or non-radiative emissions ($^3k_{nr}$), or (spin) flip back to the singlet state (k_{rISC}). Normally it is assumed that the latter process only requires thermal energy to raise the triplet state to a vibronic sub-level that is isoenergetic with the emissive singlet states to enable reverse intersystem crossing (rISC) because a spin flip is an adiabatic process. These final emissive singlet states emit in the microsecond to millisecond regime due to the involvement of the longer-lived triplet states. This means that the thermally activated delayed fluorescence that occurs as a result of rISC is sensitive to heat and oxygen. For TADF to occur, the energy splitting between singlet and triplet states, Δ_{EST}, should be very small (less than a few hundreds of meV but ideally less than a few tens of meV for efficient rISC). Only then can most of the triplet states be up-converted back to the singlet states i.e. $k_{rISC} >> k_{PH}+3k_{nr}$.

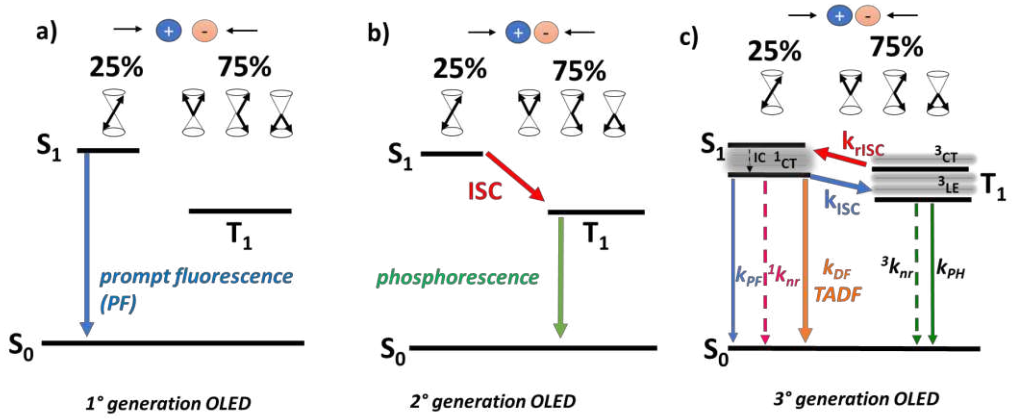

Figure 6.4. Excited state harvesting in three generations of OLED emissive materials. c) Schematic representation of the electronic energy levels involved in TADF according to the vibronic coupling model.

Is clear that an efficient TADF is achievable enabling the thermally activated rISC, which is temperature sensitive. A small ΔE_{ST} is critical because it governs the rate constant of rISC (k_{rISC}) according to the Boltzmann distribution:

$$k_{rISC} \propto exp - \frac{\Delta E_{ST}}{K_B T} \qquad \text{Equation 6.5.}$$

where $k_B = 1.38 \times 10^{-23}$ J K^{-1} is the Boltzmann constant and T is the absolute temperature. The ΔE_{ST} is the difference between the E_{S1} and E_{T1}, which can be defined as follows:

$$E_s = E_{orb} + K + J \qquad \text{Équation 6.6.}$$

$$E_T = E_{orb} + K - J \qquad \text{Équation 6.7.}$$

$$\Delta E_{ST} = E_S - E_T = 2J \qquad \text{Équation 6.8.}$$

where E_{orb} is the orbital energy, K is the electron repulsion energy and J is the exchange energy. Therefore the energy difference between singlet and triplet state (ΔE_{ST}) is 2J. [12]

J is defined by the following equation (6.9.):

$$J = \iint \varphi H(r1)\varphi L(r2)\frac{1}{|r2-r1|}\varphi H(r2)\varphi L(r1)dr1dr2 \qquad \textit{Équation 6.9.}$$

where φH and φL are the spatial distributions of the HOMO and LUMO, respectively, and r1 and r2 are position vectors.

Thus, it follows that decreasing the overlap between the HOMO and LUMO orbitals reduce both J and ΔE_{ST} values (Figure 6.10.).

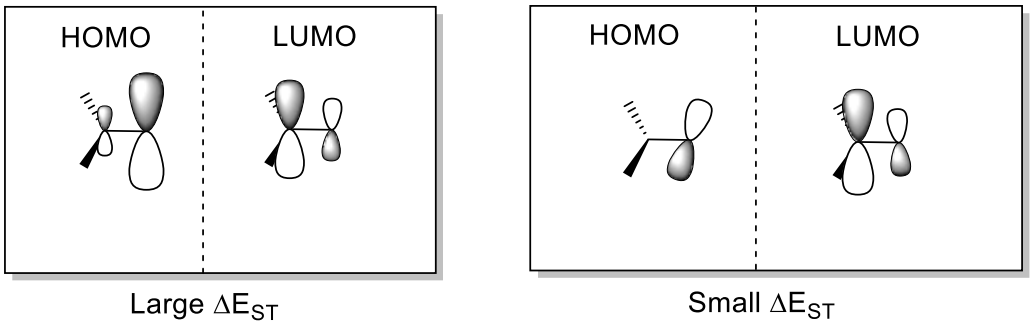

Figure 6.10. The strategy of realizing small ΔE_{ST} in organic molecules for TADF. HOMO: the highest occupied molecular orbital, LUMO: the lowest unoccupied molecular orbital, ΔE_{ST}: energy gaps between S_1 and T_1 states.

This task can be realized, in a first approximation, by spatially separating these frontier orbitals by covalently binding an electron donor (D) moiety to an electron acceptor (A). The predominant way to achieve this so far has been through donor-acceptor (D-A) charge transfer molecules with N-C bridge. In these D-A materials excited states with strong charge-transfer character (CT) are readily formed. With a N-C bridging bond between the D and A units, they tend to take a perpendicular steric conformation, minimising the interaction between the electron on the D and electron on the A in the excited state, giving near zero exchange energy and thus small Δ_{EST}.

Acceptors are typically electron-deficient heteroaromatics, and donors are electron-rich aromatic amines. If these components are orthogonal with respect to each other, then the HOMO should lie exclusively on the donor (D) unit, and the LUMO should be localized on the acceptor (A). [(11)]

6.1.4 Molecular design of TADF emitters

As mentioned above, in 2011 Adachi and co-workers have proposed the first purely organic TADF emitters developing a rational molecular design strategy, based on the introduction of electron donor and acceptor units in a way that the π-conjugation is highly distorted by steric hindrance introduced from the bulky substituents. Shortly afterwards, in 2012, the same group reported a series of groundbreaking studies on organic TADF emitters based on carbazolyl dicyanobenzene, which showed high photoluminescence (PL) efficiency and various emission wavelength ranging from sky-blue to orange (Figure 6.11.). The best OLED device using these TADF emitters provided a promising EQE of 19.3%, which surpasses by far the theoretical maximum of OLEDs employing conventional fluorescent emitters. [13]

Appl. Phys. Lett. 2011, 98, 083302

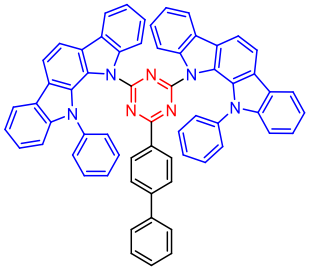

Nature 2012, 492, 234

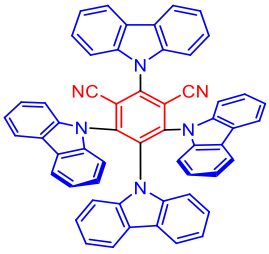

Figure 6.11. Examples of donor-acceptor type TADF molecules by the Adachi group.

To date, donor−acceptor (D−A) system exhibiting a charge-transfer (CT) transition which is enable to promote the transfer of electrons D – A in the excited state is still the most successful design strategy for TADF materials. TADF molecules are therefore generally formed by D and A units, linked through an aromatic bridge, and form excited states with a strong CT character. The singlet-triplet energy gap can be further reduced by rotating the D and A units around the D –

A axis and obtaining the relative orientation D – A close to orthogonality or, alternatively, by increasing the distance D – A, using a molecular bridge (spacer). However, another parameter to consider in the TADF molecular design is the oscillator strength f, which is an index for the light emission intensity, and is proportional to the square of the transition dipole moment Q (equation 6.12.):

$$f \propto |Q|^2 \qquad \textit{Équation 6.12.}$$

Here, the magnitude of Q also depends on the orbital overlap between the HOMO and LUMO, i.e. (6.13.):

$$Q = \iint \varphi H(r1)\varphi L(r2)|r2 - r1|\varphi H(r2)\varphi L(r1)dr1dr2 \qquad \textit{Équation 6.13.}$$

These equations indicate that a well-tuned partial orbital overlap between the HOMO and LUMO is a requisite condition for obtaining both a small ΔE_{ST} and high PLQY. The molecular design of a D-A pair combined with π-linkers providing a large dihedral angle or π-spacers can separate the HOMO and LUMO with a small orbital overlap. [14]

The donor and acceptor building blocks used to design TADF emitters play a critical role in governing the photophysical properties of TADF molecules and therefore should be carefully selected. The connectivity between units D and A also has a profound impact on the singlet-triplet energy gap and on the rate of the intersystem crossing. In general, the singlet-triplet energy difference is reduced by introducing strong donor and acceptor fractions. Electron donors such as phenoxazine, phenothiazine, dimethylacridine, carbazole and their derivatives are usually employed because of their high electron-donating abilities and easy inclusion into twisted TADF moleculear architectures. On the other hand, the choice of electron acceptors is based on more evalutations. Various electron acceptors have been successfully used for preparing efficient TADF materials, including nitrogen heterocycle-based acceptors (such as triazine, diazine, heptazine, oxadiazole and triazole), cyano-based acceptors, diphenyl sulfoxide-based

acceptors, diphenyl ketone-based acceptors, etc. [15] [16] [17] Despite significant advances in the development of TADF molecules in recent years, further studies are needed to design structures with better modulation of their emission and improved stability. The rapid progress of materials chemistry paved the way to develop, at first stage, many kinds of solution processable TADF emitters especially in the blue-green region. [18] [19] Infact, the maximum external quantum efficiency (EQE_{max}) of up to 27.13% for blue-green solution processed OLEDs has been reported. [20] Conversely, orange-red emitters are particularly limited, as the excited states are strongly affected by the non-radiative decay due to their energy levels close to the ground state, resulting in lower device efficiency. [21] [22] As an important part of the panchromatic spectrum, further molecular design is therefore required to obtain high-performance orange-red TADF materials with small ΔE_{ST} and greatly minimizing non-radiative decay. There are several potential strategies that may be employed to tune the emission energy towards longer wavelengths between 580–650 nm.

In this section of the Dissertation, the main focus relies on the rational molecular design strategies and convenient synthetic approaches toward novel compounds employing aromatic ketone electron-accepting groups.

6.1.5 Aromatic ketone-based TADF emitters

The idea of introducing a carbonyl function into a conjugated aromatic system arises from its well-known electron-withdrawing character due to the high electronegativity of sp_2 oxygen. In particular, the coplanar system involving one or more carbonyl units in an aromatic system increases the degree of conjugation and stabilizes the LUMO. These peculiarities place aromatic ketones as suitable acceptors of low energy orange-red TADF emitters. [23]Early attempts to adopt this concept began with the use of the simplest aromatic carbonyl group-derived acceptor: the benzophenone-type acceptor. [24] Nonetheless, the intramolecular rotations induced by the phenyl moieties of benzophenone have been attributed

to a non-radiative decay responsible for low reverse intersystem crossing rates (k_{rISC}). [25] The need to explore more compact and rigid benzophenone derivatives inspired part of the research activity described in this Thesis. Recently, some building blocks such as anthraquinone, [26] [27], xanthone, [28] [29] [30] [31] dibenzothiophene-benzoyl [32] [33]and phenylcarbazole-benzoyl [34] have been reported as promising acceptor groups in multiluminescent TADF emitters. Infact, interestingly, the restriction of intramolecular rotation is also the basic strategy to design TADF molecules with aggregation induced emission (AIE) properties enable to suppress the concentration quenching and enhance the solid-state luminescence, as proposed for the first time by Tang et al. In 2001. [35] In TADF-OLEDs, the introduction of AIE effect or aggregation-induced delayed fluorescence (AIDF) can help to improve the overall device performances. Molecular design plays a key role in the conformational status of the organic molecules determining their overall properties. Moreover, the possible conformers can also be interchanged by adding energy through grinding, heating, or fuming highlighting a behaviour known as mechanoluminescence (ML) behaviors. [36] The first ketone-based TADF emitters with AIE properties were reported in 2014 by Wang et al. [37] using thioxanthone as the acceptor unit in combination with the well-known hole-transporting properties of triphenylamine (TPA) and N-phenylcarbazole (N-PhCz) as electron donors (Figure 6.14.). These materials exhibit pronounced AIE activities since the PLQYs of these molecules in neat films are significantly higher than in solutions where they show very low photoluminescence quantum yields ($\Phi_{PL} < 0.05$).

Adv. Mater., 2014, 26, 5198

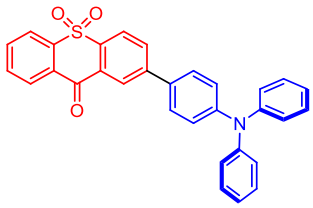

TXO-TPA

ΔE_{ST} (in 2-MeTHF)=40 meV
λ_{em} (neat film)=630 nm
ϕ_{PL} (neat film)=0.36

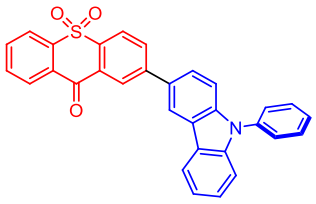

TXO-PhCz

ΔE_{ST} (in 2-MeTHF)=90 meV
λ_{em} (neat film)=491 nm
ϕ_{PL} (neat film)=0.93

Figure 6.14. Molecular structures and photophysical data of TXO-TPA and TXO-PhCz.

The π···π and C-H···π intermolecular noncovalent interactions in both emitters are crucial to restrict the free rotations and vibrations in the molecules suppressing nonirradiative thermal dissipation of the triplet excitons. Two non-doped OLEDs were constructed with these materials. TXO-TPA-based yellow electroluminescent device exhibited the maximum EQE of 18.5% while the TXO-PhCz-based green-emitting non-doped OLED achieved 21.5% of maximum EQE. Moreover, these outstanding results are also supported by excellent electroluminescence stability. Phenothiazine derivatives demonstrating the AIE-TADF properties were reported by Aizawa et al. [38] Two novel materials, PTZ-XT and PTZ-BP (Figure 6.15.), which use benzophenone and xanthone acceptors were synthesized and investigated. Both compounds exhibited emission in the yellow region with emission peaks of 545 nm for PTZ-XT and 565 nm for PTZ-BP with PLQYs of 0.53 and 0.31, respectively. Strong AIE properties of these two materials were revealed with a combination of the TADF effect provided by the low values of ΔE_{ST} in the range of 65–71 meV. Non-doped OLEDs fabricated from both compounds used as emitter layers achieved 11.1% and 7.6% of maximum EQEs for PTZ-XT and PTZ-BP, respectively. These results can be acknowledged as a valuable contribution to AIE-TADF technology utilization mostly due to very simple and low-cost synthesis of the emitters.

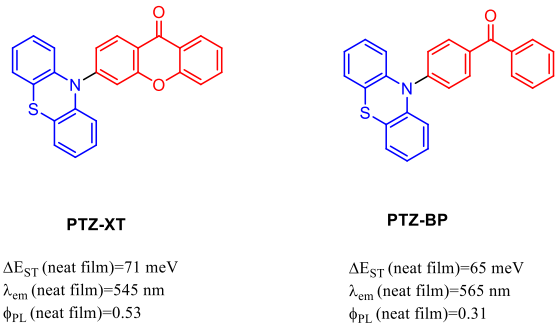

Figure 6.15. Molecular structures and photophysical data of PTZ-XT and PTZ-BP.

Red AIE-TADF emitters based on antraquinone derivatives for solution processed OLEDs were reported by Huang et al. [39] The adoption of carbazole and triphenylamine as donor moieties allowed the authors to perform simple and low-cost synthesis of donor-acceptor materials with both AIE and TADF features (Figure 6.16.a). ΔE_{ST} values were experimentally measured to be 0.11 eV and 0.05 eV for CzAQ and TPA-AQ materials and with an approved strong AIE effect of both materials, which raises the expectation of using these materials in non-doped OLEDs. The orange-emitting device with Cz-AQ as an emitter achieved 5.8% of maximum EQE while the TPA-AQ-based red-emitting device demonstrated 7.8% of maximum EQE. The performance of the OLEDs is comparable to the results achieved with red solution-processed PhOLEDs based on iridium$^{(III)}$ complexes [40] and europium$^{(III)}$ complexes. [41]More recently, Lee et al. reported a similar D–A compound, PTZ-AQ, which contained phenothiazine as a donor (Figure 6.16.b). Interestingly, this molecule showed multifunctional properties of AIDF, polymorphism, and a mechanoinduced luminescence color change. [42] Depending on the crystallization conditions, PTZ-AQ could adopt up to five different polymorphs with different emission colors from green-yellow (λ_{em} = 545, 554 nm) to red (λ_{em} = 606, 649 nm), and various Φ_{PL} values within the range 0.02–0.84. Among the different polymorphs, the R-crystal showed distinct TADF properties, with a very small ΔE_{ST} value (10 meV) and a high Φ_{PL} value (0.84). The authors suggested that

this polymorphism dependent emission was owing to a change in the degree of π–π interactions, as supported by DFT calculations.

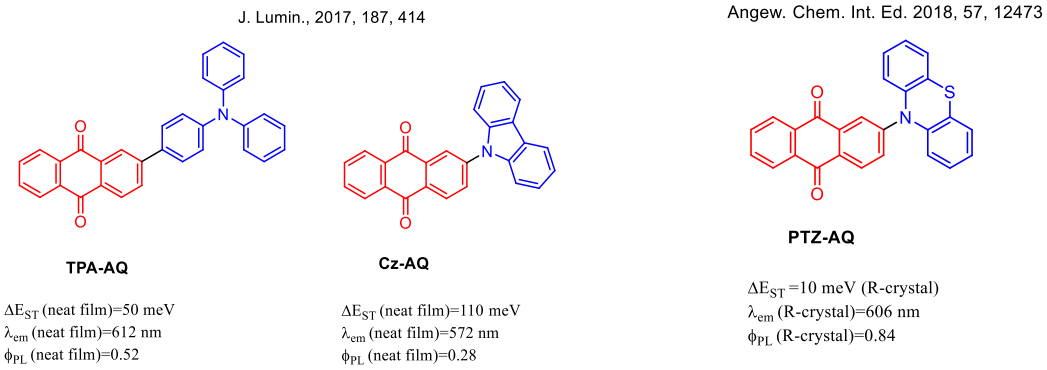

Figure 6.16. a) Molecular structures and photophysical data of TPA-AQ and Cz-AQ. b) Molecular structure and photophysical data of PTZ-AQ's R-crystal.

The main advantage of using these materials for the fabrication of OLEDs is the significant reduction of the production cost and simplification of the device manufacturing. Exploiting a combination of AIE and TADF phenomena can be established as an important breakthrough in the production of most advanced and efficient organic light-emitting devices. This approach merges all advantages of known OLED efficiency-boost techniques: high effectiveness and inexpensive production compared to PhOLEDs and simplified production compared to first TADF OLEDs.

There are still very few reports considering materials exhibiting this symbiosis of AIE and TADF phenomena. However, the main requirements for the organic materials intended for OLED application remains high thermal, chemical and electrochemical stability, suitable morphological, photophysical and energetic properties and convenient and inexpensive synthesis.

On these basis, the research activity described in this section of the Thesis aims to implement alternative design strategies based on inexpensive and simplified synthetic approaches to obtain novel ketone-based multiluminescent TADF emitters. The obtained target molecules exploit the carbonyl group effect in an

appropriate molecular system varying from unsymmetrical D-Ph-A type emitters to D-A-D triads, also introducing internal heavy atom (IHA) effect using bromine as potential singlet-triplet interconverter (Figure 6.17.). Each emitter exhibits unique luminescent properties according to the different design principles applied. The structure-properties relationships have been carefully examined to understand the nature of energy processes occurring in the molecules and the photophysical properties of the materials and their potential application in OLEDs are investigated in collaboration with the Institute of Nanotechnology CNR Nanotec of Lecce.

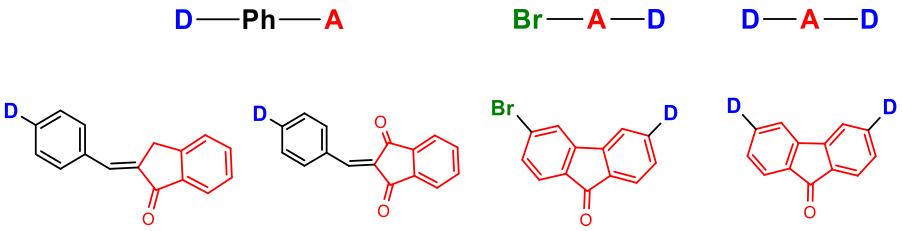

Figure 6.17. Molecular structures and design strategies adopted for the synthesized target ketone-based acceptors (red) (coupled with suitable donors (blue)) discussed in this Thesis.

6.2 Indanone/Indandione-based TADF materials with diversified emissive behaviors of AIE and MCL

6.2.1 Introduction

One of the important advantages of purely π- conjugated organic semiconductors is that the energy of levels of their peripheral orbitals and subsequent energy gaps of the organic molecules can be tuned easily by molecular design and, as a result, the photophysical and electrochemical properties can be finely adjusted. Presently, conjugated compounds with electron-donating (D) and electron-accepting (A) units receive the special attention because of their applicability in optoelectronic and electronic devices, such as organic light emitting diodes (OLEDs) [43] [44], solar cells [45]and chemical sensors. [46] Compounds which have highly twisted (or orthogonal) electron donor–acceptor (D–A) structures often exhibit narrow energy gaps resulting from intramolecular charge transfer (ICT) [47]. The nature, strength and type of the donor and acceptor fragments affect the energy levels of the frontier orbitals and thus influence light-absorbing, light-emitting, and charge-transporting properties of organic emitters. However, the HOMO–LUMO separation in a pre-twisted D–A molecular system can be deleterious, especially in terms of photoluminescence quantum yield (Φ_{PL}) of the red orange TADF materials. For this reason, the growing demand to develop novel long wavelength TADF materials (λ_{EL}>600 nm) is still challenging owing to their narrow energy gaps which often lead to an intrinsic energy loss through a nonradiative decay rate (k_{nr}) governed by the energy gap law. [48] To overcome this, the introduction of a spacer unit such as a phenyl linker, between D and A represents a recent effective strategy. The HOMO and LUMO extension to the phenyl bridge is related to a high oscillator strength, increasing the probability to reach high PLQY in the TADF emitter. At the same time, it is necessary to tune the strenght of donor and acceptor units in order to overcome the high singlet energy issue owing to the weakened CT character associated to less HOMO/LUMO separation. In this perspective, this section aims to explore the effect of the combination of

the chemical designs enable to strengthen CT character with the use of donors and acceptors modulated in terms of strenght and distortion capability of the backbone structure. [49] As anticipated in the last paragraph, the focus relies on four novel orange red TADF materials, exhibiting AIE and MCL behaviors, IN-Ph-DTC, IN-Ph-DTP, ID-Ph-DTC, ID-Ph-DTP based on an asymmetric D–Ph–A configuration (Figure 6.18.), consisting of 2,3-dihydro-1H-inden-1-one and 1H-indene-1,3(2H)-dione as A units, 3,6-di-tert-butyl-9H-carbazole and 3,7-di-tert-butyl-10H-phenothiazine as D units, and a phenylene π-bridging unit. The introduction of the tert-butyl groups in the donor moieties was pursued with the aim to effectively increase the molecular solubility and improve the AIE character. As described below, the characteristics of the molecular structures result beneficial for depicting the critical effects of π-bridge and the different strength of the donor-acceptor moieties on aggregation induced emission (AIE) characteristics and reversible mechanofluorochromism (MFC) behaviour. The investigation of the thermal, electrochemical and photophysical properties, the latter supported by theoretical analyses contributed to the further understanding of the design rules of innovative multiluminescent materials, especially those obtainable through a facile and low-cost synthesis.

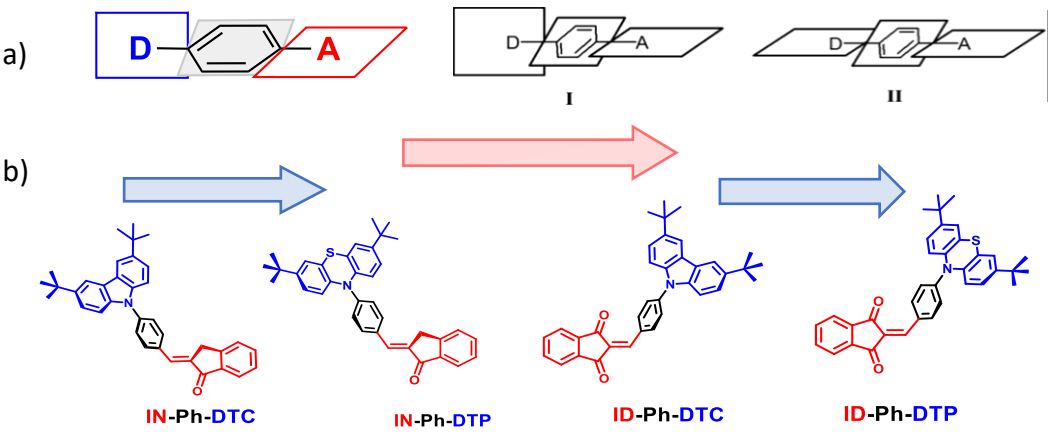

Figure 6.18. a) Model for Donor–Phenyl bridge–Acceptor molecules adopted in this section, endowed with two plausible twisting motifs (I and II). b) Chemical structures of the target molecules according to the designed donor and acceptor strengths.

6.2.2 Results and discussion

Synthesis and characterization

The four designed emitters were synthesized via catalyzed C–N Buchwald-Hartwig cross coupling reactions between the nitrogen containing donor groups 3,6-di-tert-butyl-9H-carbazole (DTC) or 3,7-di-tert-butyl-10H-phenothiazine (DTP) and the chosen Indanone/Indandione based acceptors moieties. The key intermediates IN-Ph-Br and ID-Ph-Br were respectively obtained through a simple Claisen-Schmidt condensation between 4-bromobenzaldehyde and 2,3-dihydro-1H-inden-1-one (IN) or 1H-indene-1,3(2H)-dione (ID) via a Knoevenagel condensation, performed in the same conditions. [50] The donor molecules were synthesized via Friedel-Crafts Alkylations by following two convenient literature procedures. 3,7-di-tert-butyl-10H-phenothiazine (DTP) was synthesized starting from the commercial available 10H-phenothiazine using an improved procedure enables to reduce the reaction time, without the need for chromatographic purification. [51] 3,6-di-tert-butyl-9H-carbazole (DTC) was also obtained in a similar convenient way starting from 9H-carbazole. [52] The final cross coupling reactions were performed in the presence of $Pd_2(dba)_3$ and XPhos as catalytic system, 1.5 equivalents of sodium tert-butylate as base in toluene at 100°C. After 6 hours the target molecules were obtained in satisfactory yields (from 27% to 53%) after column chromatography and recrystallization (see Experimental part 6.2.3).

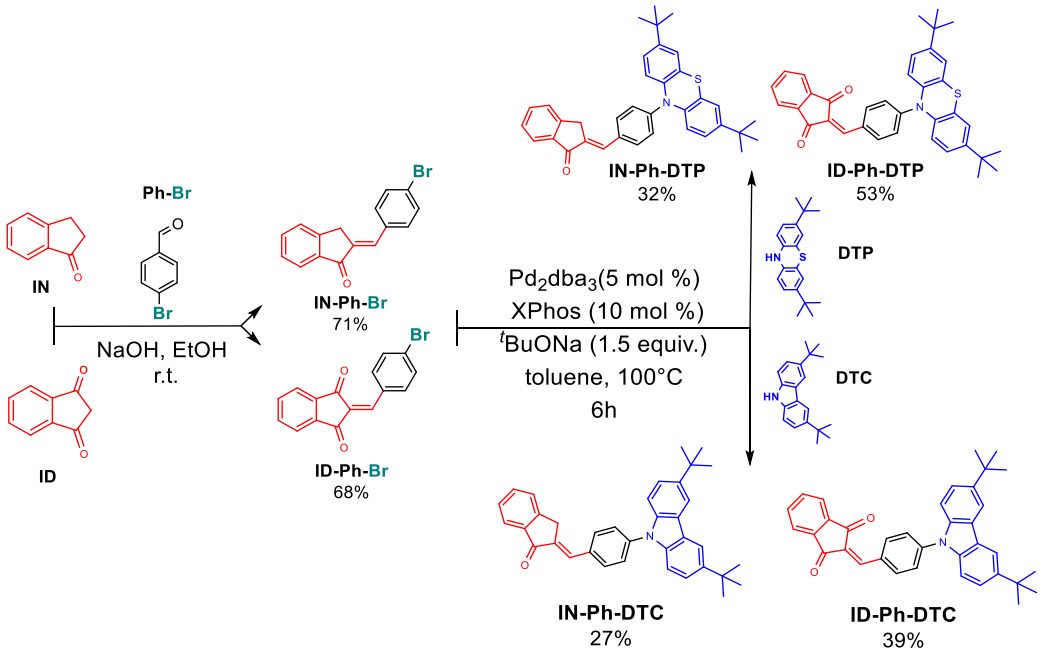

Scheme 6.19. Synthetic sequence for the obtainment of IN-Ph-DTC, IN-Ph-DTP, ID-Ph-DTC and ID-Ph-DTP and relatives yields%.

The chemical structures of the compounds were characterized by ^{1}H-NMR. The compounds were found to be well soluble in polar organic solvents, such as chloroform, acetonitrile, acetone and methylene chloride. However, solubility decreased with decreasing polarity of a solvent, e.g., the solubility in non-polar organic solvents such as n-hexane or cyclohexane was considerably lower.

Investigation of thermal properties

The morphological and thermal stability of the materials were evaluated in order to warrant the formation of stable thin films, indispensable for the operation of OLED devices. The thermal decomposition (T_d, corresponding to 5% weight loss) and glass transition temperature (T_g, according to the second heating scan) values recorded at a scanning rate of 10 °C/min under a nitrogen atmosphere are reported in Table 6.23. Notably, the DSC analysis demonstrating that, during the first heating scan, IN-Ph-DTC revealed a series of glass transitions with enthalpic relaxation at 64.0 °C, 108.0 °C and 142.0 °C respectively, followed by a cold crystallization of the amorphous material at 181.0 °C, leading to two partially overlapped endothermic events at 196.0°C and 199.0°C (Figure 6.20 a)), which can be ascribed to the melting of the different crystalline portions of the material, probably due to the conformations of the molecule. However, upon cooling, the second heating scan showed the formation of an amorphous material with a glass transition temperature at 99.6 °C suggesting that IN-Ph-DTC preferentially adopts a disordered tridimensional structure in the presence of intermolecular interactions. In the case of IN-Ph-DTP, the first heating scan revealed three similar endothermic melting events (estimated at 238.0 °C, 240.1 °C and 242.3 °C), which can be associated to the melting of three similar crystalline conformations adopted by the «butterfly shaped» 3,7-di-tert-butyl-10H-phenothiazine (DTP) donor group in the molecular system. After the thermal history erasure of the material during the cooling, only a weak glass transition temperature was revealed in the second heating scan at 117.1 °C (Figure 6.20 b)). These results indicate that the values of T_m and T_g notably increase correspondingly to the introduction of 3,7-di-tert-butyl-10H-phenothiazine (DTP) substituent in the structure. However, in both indanone based emitters the obtained data suggest a good morphological stability of the materials. As shown in Figure 6.22 a) the TGA curves of the studied compounds revealed also a high thermal stability with the temperatures of 5% weight loss corresponding to 388°C and 403°C for IN-Ph-DTC and IN-Ph-DTP respectively.

The apparent weight loss (~100 °C) observed in IN-Ph-DTC is due to the residual solvent (dichloromethane) entrapped in the crystalline structure. [54]

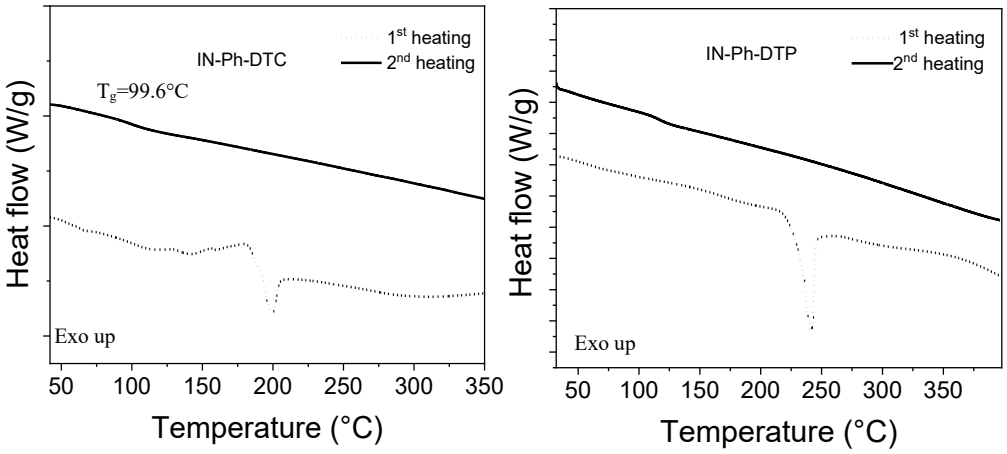

Figure 6.20. DSC traces of a) IN-Ph-DTC and b) IN-Ph-DTP (first and second heating scans) identifying the glass transitions (T_g), cold crystallization (T_c), and melting (T_m) events.

On the other hand, the thermal behaviour of ID-Ph-DTC during the first heating scan revealed two glass transitions with enthalpic relaxation at 66.1 °C and 106.3 °C, followed by two endothermic events, the first one at 162.0 °C and the second one which appears sharp and intense at 200.0 °C (Figure 6.21 a)). These events can be ascribed to the melting of the different crystalline portions of the material, probably due to conformations of the 3,6-di-tert-butyl-9H-carbazole (DTC) unit in the planar conjugated molecular system. Interestingly, also in this compound, after the thermal history erasure during the cooling, only a weak glass transition temperature was revealed in the second heating scan at the high value of 171.1°C (Figure 6.21 a)). DSC scans of ID-Ph-DTP are shown in Figure 6.21 b). A first endothermic melting peak was estimated at 205.1 °C, followed by a sharp exothermic phase transition at 209.0 °C. After these two events, three endothermic melting peaks were observed at 221.0 °C, 233.0 °C and 238.0 °C (first heating scan). This

behaviour can be ascribed to the different aggregation propensity of the molecular structures, mainly due to the axial and equatorial conformations of the 3,7-di-tert-butyl-10H-phenothiazine (DTP) unit. Upon cooling, a weak glass transition temperature was revealed in the second heating scan at 154°C.

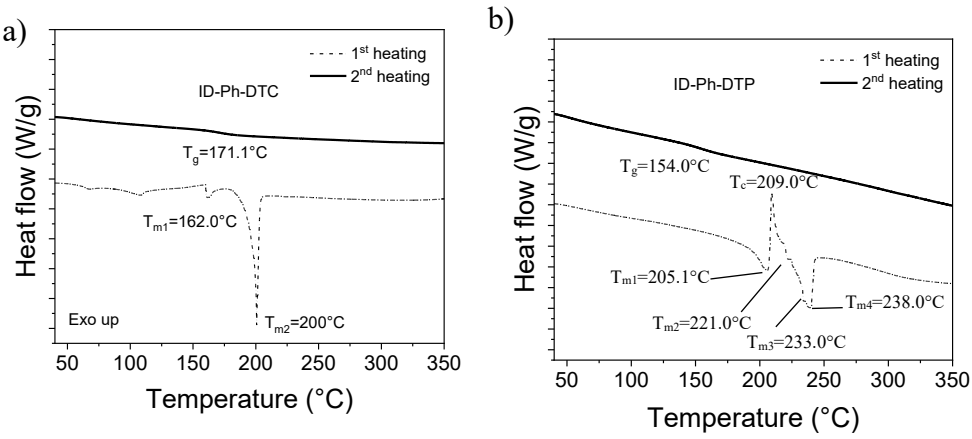

Figure 6.21. DSC traces of a) ID-Ph-DTC and b) ID-Ph-DTP (first and second heating scans) identifying the glass transitions (T_g), cold crystallization (T_c), and melting (T_m) events.

The high morphological stability of the materials was further supported by a good thermal stability. Figure 6.22 b) shows the TGA curves of the Indandione-based studied compounds. Also in this case the analysis revealed moderate thermal stability for both materials with the temperatures of 5% weight loss at 354°C and 235°C for ID-Ph-DTC and ID-Ph-DTP respectively.

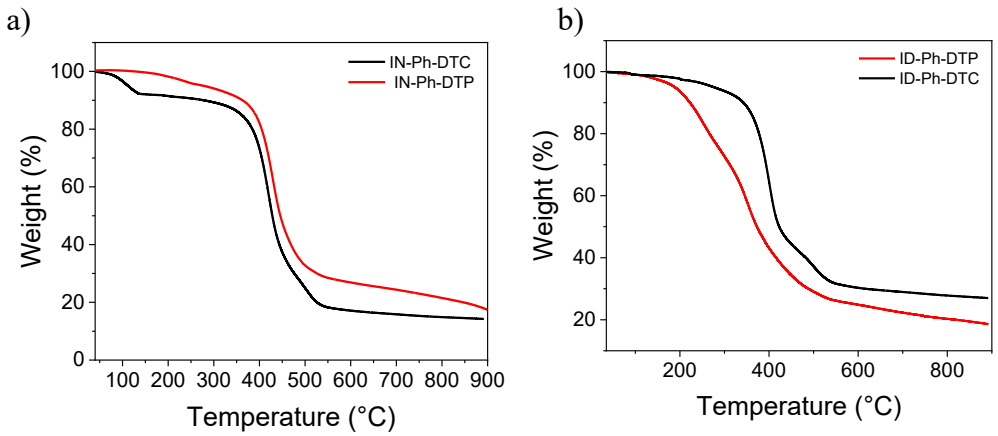

Figure 6.22. TGA curves of a) IN-Ph-DTC (black) and IN-Ph-DTP (red) and b) ID-Ph-DTC (black) and ID-Ph-DTP (red).

Electrochemical properties and theoretical calculations

To experimentally investigate the frontier orbital energy levels of the target molecules, electrochemical properties were studied by cyclic voltammetry (CV) in dichloromethane (concentration: ~10^{-4} M) containing a 0.1 M solution of tetrabutylammonium tetrafluoroborate (0.10 M) as the supporting electrolyte under N_2 atmosphere. As shown in Figure 6.24, each compound was electrochemically active and displayed a reversible oxidation and reduction wave, showing a clear electrochemical stability of the emitters. The HOMO and LUMO energy levels were calculated (DFT, see experimental part 6.2.3) with reference to the energy level of ferrocene and summarized in Table 6.23. The similar values of the LUMO levels recorded for IN-Ph-DTC and IN-Ph-DTP, can be ascribed to the formation of a radical anion which involves the ketone group of the acceptor in both the Indanone based compounds. Similar behavior was observed in the indandione based emitters ID-Ph-DTC and ID-Ph-DTP (Figure 6.24 b)). The reduction peaks of these two materials appear sharp and intense, probably owing to the effect of the additional ketone group of the Indandione acceptor. An explanation of this hypotesis lies in the shape of the LUMO orbitals and the energy diagrams reported in Figures 6.25 and 6.26 can be involved in the explanation of the reduction events. The extended π-conjugation involving the phenyl bridge

delocalizes the negative charge onto an extended portion of the molecules, as confirmed in the less prominent reoxidation events. The HOMO levels were calculated to be −5.40 and −5.24 eV for IN-Ph-DTC and IN-Ph-DTP, respectively. These low values can be attributed to the preferential localization of the HOMO energies at the donor units. The occurrence of a weak additional peak at lower potential in the oxidation wave of IN-Ph-DTP might be ascribable to the HOMO delocalization probably due to conversion between the axial and equatorial conformations of the phenothiazine unit in solution. In the case of the indandione-based molecules the HOMO levels result to be −5.48 and −5.11 eV, while the LUMO energies were -3.16 and −3.26 eV, for ID-Ph-DTC and ID-Ph-DTP, respectively. As for IN-Ph-DTP, the additional oxidation peaks at lower potential for ID-Ph-DTC and ID-Ph-DTP, can be ascribed to the further HOMO delocalization involving the donor units and the completely planarized Indandione molecular system, which can be promoted in solution for these materials. However, the trend of the experimental values of HOMO and LUMO well match those of the levels studied using density functional theory (DFT) calculations.

Table 6.23. Thermal, electrochemical properties and DFT calculation data of the synthesized emitters.

Emitter	T_g (°C)[a]	T_d (°C)[b]	E_g (eV)[c]	E_g (eV)[d]	DFT HOMO (eV)[e]	DFT LUMO (eV)[e]	exp. HOMO (eV)[f]	exp. LUMO (eV)[f]
IN-Ph-DTC	99.6	388	2.75	2.15	-5.56	-2.46	–5.40	–3. 25
IN-Ph-DTP	117.0	403	2.94	1.97	-5.31	-2.51	–5.24	–3.27
ID-Ph-DTC	171.0	354	2.25	2.32	-5.64	-2.89	–5.48	–3.16
ID-Ph-DTP	153.7	235	2.35	1.85	-5.33	-2.97	–5.11	–3.26

[a]Glass transition temperature (2nd heating scan) obtained by DSC under N_2. [b]Decomposition temperature (5% weight loss) obtained by TGA under N_2. [c]$E_g = 1240/\lambda_{onset}$ (eV). [d]Determined by cyclic voltammetry: $E_g=E_{HOMO}-E_{LUMO}$ [e]Calculated at the B3LYP/6-31G(d,p) level of theory. [f]Determined by cyclic voltammetry: exp. HOMO = $-[E_{ox} - E_{(Fc/Fc^+)} + 5.10]$ (eV); exp. LUMO= $-[E_{red} - E_{(Fc/Fc^+)} + 5.10]$

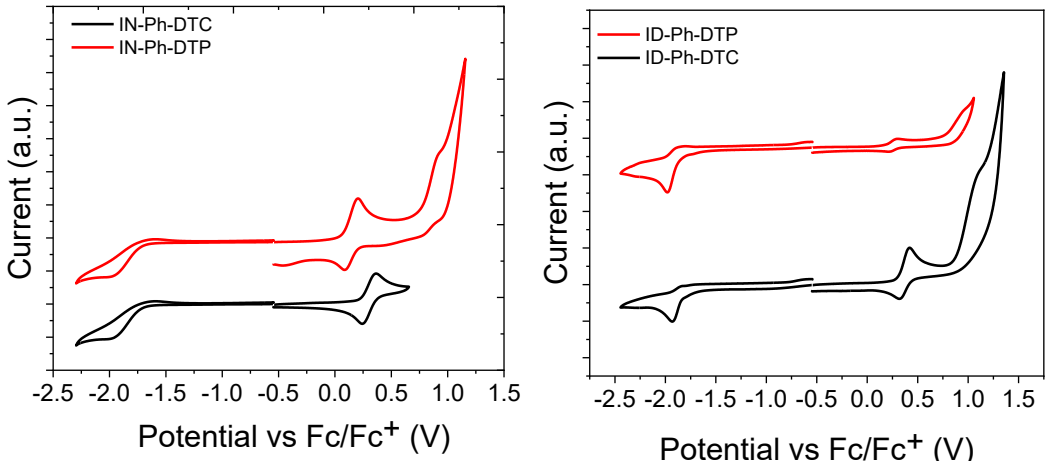

Figure 6.24. a) Cyclic voltammograms of IN-Ph-DTC and IN-Ph-DTP (left) and b) ID-Ph-DTC and ID-Ph-DTP (right) measured in dichloromethane (1.0×10^{-4} M) using Bu_4NBF_4 (0.1 M) as the supporting electrolyte.

Density functional theory (DFT) calculations resulted fundamental also to understand the structure-property relationship of the compounds at the molecular level. The analyses of the ground-state geometries were studied using the Gaussian 09 software package. The geometrical and electronic properties of IN-Ph-DTC and IN-Ph-DTP (Figure 6.25) highlight the spatial distributions of the frontier molecular orbitals. Notably, the HOMO and LUMO distributions of the emitters containing the stronger donor DTP are clearly separated, owing to the large dihedral angles between the donor and the phenyl bridge linked to the acceptor planes.
In the IN-Ph-DTC molecule, the smaller dihedral angle between the 3,6-di-tert-butyl-9H-carbazole (DTC) unit and the acceptor moiety is responsible of the insufficient twist, as a consequence, both the HOMO and LUMO of IN-Ph-DTC are extended to the central benzene bridge which exhibits electrophilic character.
However, the presence of two tert-butyl groups in the positions 3 and 6 of the carbazole unit represents an effective strategy to ensure that the chromophore moiety can be efficiently surrounded by the bulky groups to avoid exciton

quenching induced by intermolecular electron exchange. [53]The small overlap between the HOMO and LUMO in this case generates high photoluminescence quantum yield (PLQY, Φ_{PL}) in polar solvents, as discussed below, thus ensuring a small ΔE_{ST} simultaneously. In the case of the molecule IN-Ph-DTP, the electron density of the HOMO orbital of IN-Ph-DTP is localised on the peripheral "butterfly shaped" DTP moiety excluding also the phenyl spacer, while the LUMO is delocalized on the acceptor involving, also in this case, the central phenyl bridge. This distribution of the frontier orbitals confirms the extremely small HOMO−LUMO overlaps mainly due to the strong donor unit. All the possible conformers associated to the 3,7-di-tert-butyl-10H-phenothiazine (DTP) unit in the D-Ph-A molecular system would result in effective ICT and thereby multiple emissive excited states correlated with those conformers can exist. [54]As shown in the energy diagram of the molecular orbitals depicted in Figure 6.25, the theoretically calculated HOMO/LUMO energy levels of IN-Ph-DTC and IN-Ph-DTP are -5.56 eV/-2.46 eV and -5.31 eV/-2.51 eV. Clearly, the HOMO energy level of IN-Ph-DTP is 0.25 eV higher than IN-Ph-DTC, while the LUMO energy is slightly shifted down (0.05 eV). Therefore, the electron donating ability of DTP in the designed molecular system is stronger than DTC. Simultaneously, the spatial separation between HOMO and LUMO, which would lead to an effective reversed intersystem crossing (rISC) process, can anticipate the trend of the small ΔE_{ST} values for both emitters being consistent with the principle that the ΔE_{ST} value of a molecule decreases as the overlap of the HOMO and LUMO wavefunction diminishes.

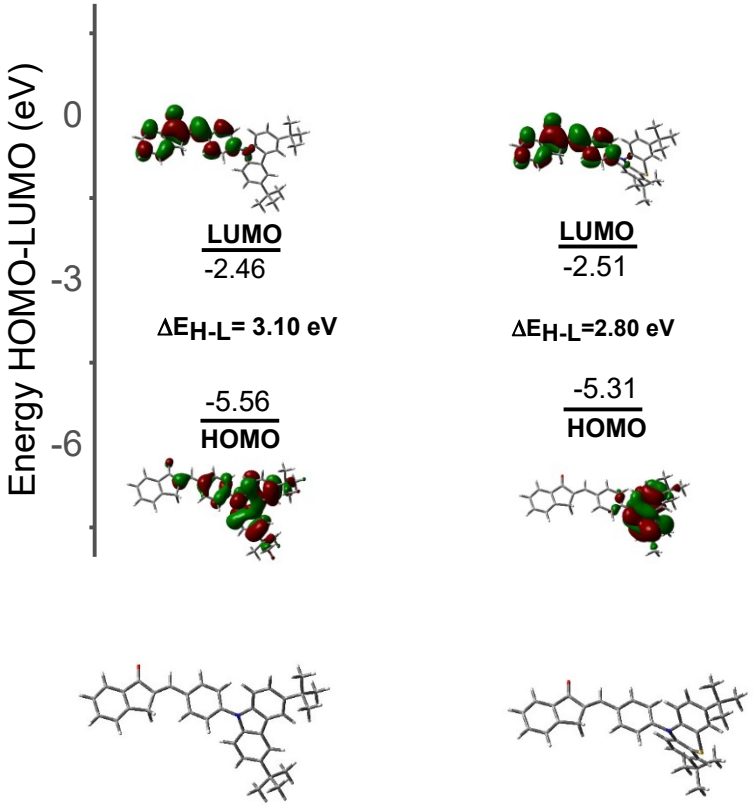

Figure 6.25. Energy diagram and molecular orbitals of IN-Ph-DTC (left) and IN-Ph-DTP (right) calculated by the DFT method at the B3LYP/6-31+G(d,p) level of theory and relatives conformations

The presence of an additional ketone function in the Indandione based compounds is reflected in the geometrical and electronic properties of ID-Ph-DTC and ID-Ph-DTP (Figure 6.24). A comparison of the electronic structures revealed that the electron density distribution in the HOMO results correlated to the donor moiety adopted in each designed emitter, thus is rather similar for all molecules and tended to localize on the electron-donating DTP moiety in ID-Ph-DTP (similarly to IN-Ph-DTP), while is partially extended to the acceptor unit in the

molecules which contain DTC as donor group ID-Ph-DTC and IN-Ph-DTC, following the same trend discussed above.

The main differences in the electronic structure can be observed in the LUMO distribution. For the 1H-indene-1,3(2H)-dione-substituted compounds (ID-Ph-DTC and ID-Ph-DTP), the LUMO distribution involves also the second carbonyl group localized in position 3 of the acceptor. This effect results fundamental for imparting deeper levels of LUMO in both emitters by conferring potential TADF emissions toward longer wavelength in the red region spectrum. All these considerations have been crucial during the research activity described in this dissertation, directing the synthetic effort towards innovative molecules with promising multi-luminescent properties allowing to realize an efficient HOMO-LUMO transition having a pronounced ICT character.

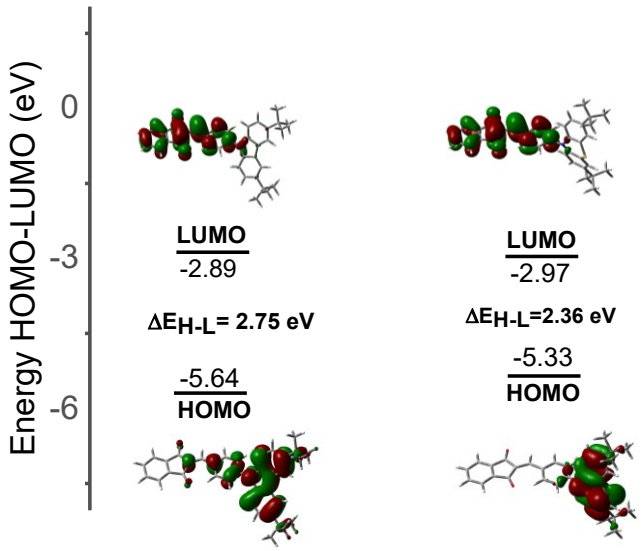

Figure 6.26. Energy diagram and molecular orbitals of ID-Ph-DTC (left) and ID-Ph-DTP (right) calculated by the DFT method at the B3LYP/6-31+G(d,p) level of theory.

Photophysical properties

The photophysical properties of the novel D-Ph-A indanone/indandione derivatives IN-Ph-DTC, IN-Ph-DTP and ID-Ph-DTC, ID-Ph-DTP were studied in cooperation with the Institute of Nanotechnology CNR Nanotec of Lecce.

The optical properties were initially studied in diluted solution (10^{-6} M/10^{-5} M) in three solvents of different polarity: cyclohexane (CH), toluene (TOL), and dichloromethane (DCM). Absorption spectra of IN-Ph-DTC (Figure 6.26.a) showed a broad, moderately intense absorption band between 350 and 450 nm attributable to intramolecular charge transfer (ICT) between donor and acceptor. This band appears to be resolved in CH, red shifted and with larger FWHM as the solvent polarity (DCM) increases. This observation highlights the effect of the dipolar interaction of the solvent which promote the formation of numerous CT states similar in energy. In the case of IN-Ph-DTP the lower energy band is much less intense with an evident double absorption (Figure 6.26. b), which can be attributed to the CT and n-π* transitions, the lower intensity is probably due to the fact that the strong donor effect of 3,7-di-tert-butyl-10H-phenothiazine (DTP) generates a large dihedral angle in the molecule decreasing the electron density communication between HOMO-LUMO.

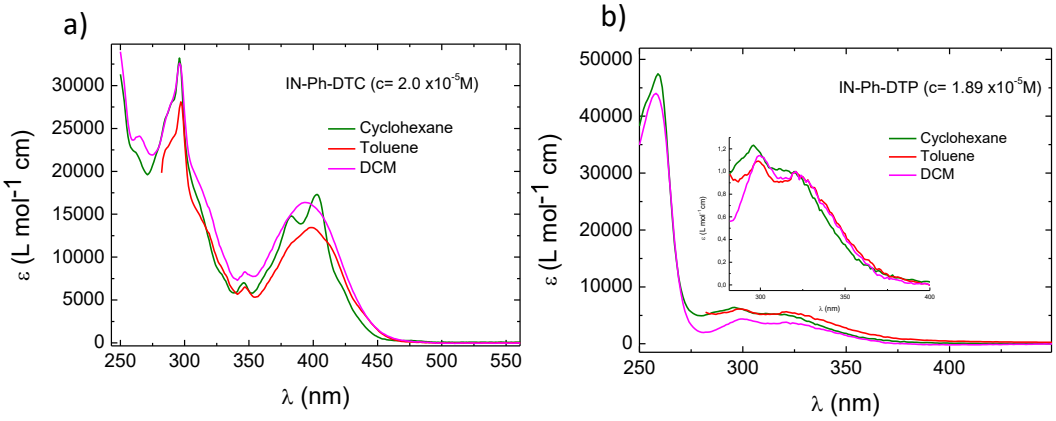

Figure 6.26. UV-VIS absorption spectra of a) IN-Ph-DTC and b) IN-Ph-DTP (with an inset focused on the range 280-400 nm) in cyclohexane (10^{-5} M, green), in toluene (10^{-5} M, red) and dichloromethane (10^{-5} M, magenta).

In ID-Ph-DTC, the acceptor is replaced with 1H-indene-1,3(2H)-dione which, being a stronger acceptor, shifts the CT state to lower energies and increases the intensity of the absorption (Figure 6.27.a). In ID-Ph-DTP, 3,7-di-tert-butyl-10H-phenothiazine (DTP) has a much stronger donor potency than 3,6-di-tert-butyl-9H-carbazole (DTC) in ID-Ph-DTC. This results in a more intense and less resolved CT band as it does not need the polarity stabilizing effect of the solvent (Figure 6.27.b). The highest energy peaks in all molecules are associated with transitions located on the donor or acceptor.

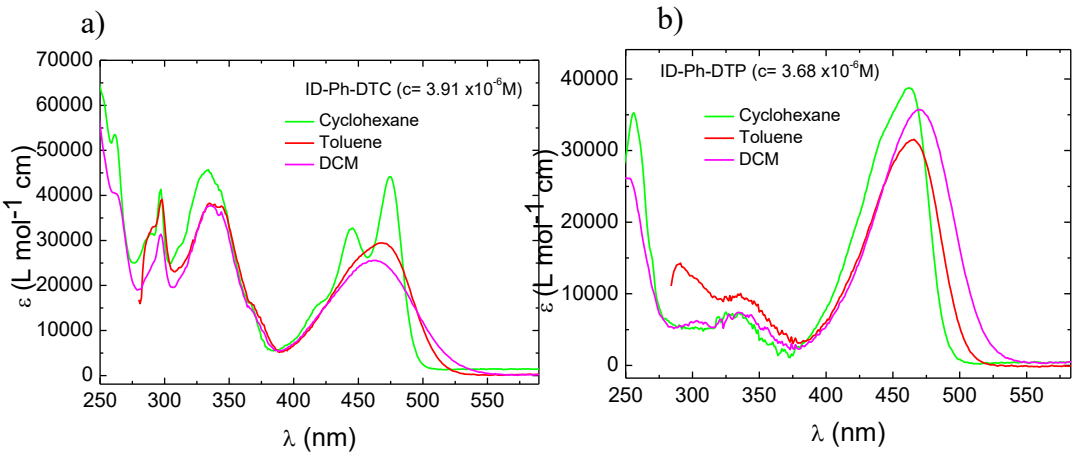

Figure 6.27. UV-VIS absorption spectra of a) ID-Ph-DTC and b) ID-Ph-DTP in cyclohexane (10^{-5} M, green), in toluene (10^{-5} M, red) and dichloromethane (10^{-5} M, magenta).

The photoluminescence spectra of IN-Ph-DTC and ID-Ph-DTC bearing 3,6-di-tert-butyl-9H-carbazole (DTC) as donor, appear well resolved in CH becoming gradually red-shifted as the polarity of the solvent increases, this behaviour confirms the CT nature of the emissive states which are sensitive to the polarity of the solvent (stabilizing effect as the polarity increases) (Figure 6.28 a,c). As reported in Table 6.29 the PLQY value of IN-Ph-DTC increases with the polarity of the solvent (up to 34% in DCM), while the PLQY value of ID-Ph-DTC reaches the maximum value in TOL (2.4%) and then drastically decreases in DCM (0.4%), indicating an over stabilizing effect. This effect is more pronounced in ID-Ph-DTC where the

stronger electron acceptor effect of the 1,3-indandione moiety allows a fast over stabilization which is reached earlier than in IN-Ph-DTC (which is observed only in ACN). In IN-Ph-DTP and ID-Ph-DTP the electron donor group is very strong (3,7-di-tert-butyl-10H-phenothiazine (DTP)) and the PL emission in CH shows a Gaussian form indicating that the CT state is already strong even in a non-polar solvent. As the polarity of the solvent increases, a bathochromic shift in the emission occurs. In IN-Ph-DTP there is no further shift in DCM with respect to the TOL and the PLQY value is much lower than in IN-Ph-DTC, reaching 1.8% only in deoxygenated CH solution.

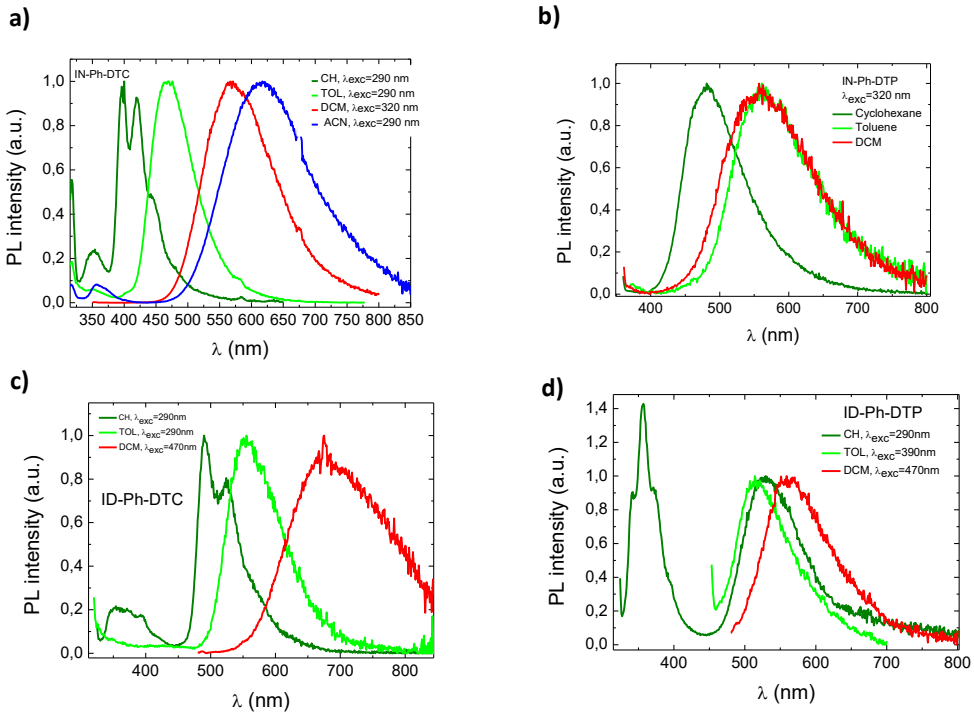

Figure 6.27. Normalized PL spectra of a) IN-Ph-DTC, b) IN-Ph-DTP, c) ID-Ph-DTC, d) ID-Ph-DTP in cyclohexane (10^{-5} M, olive), in toluene (10^{-5} M, green) and dichloromethane (10^{-5} M, red).

The higher PLQY in CH is due to the fact that strong donor effect enables the formation of a strong state of CT without the aid of the polarity of the solvent, which would rather tend to over stabilize the whole molecular system. It can also

be observed that in this case the PLQY value increases by about 100% when the oxygen is removed from the system, thus hinting the possibility of a delayed fluorescence. The PL emission of ID-Ph-DTP in CH shows a very intense and resolved high energy peak attributed to the LE emission of 3,7-di-tert-butyl-10H-phenothiazine (DTP), and a low energy Gaussian emission of CT nature, red shifted only in DCM. The very small amount of the shift depends on the fact that the CT state is probably already strong in CH. Furthermore, the low PLQY values, obtained by exciting at 440-470 nm in the three solvents, indicate that in solution the non-radiative decay channels are more efficient than the emission from the CT state. However, in the case of ID-Ph-DTP, in CH a PLQY of 18% is achieved when the emission of LE status is also considered.

Table 6.29.
Optical and photophysical properties recorded in diluted solutions of the synthesized emitters.

Emitter	λ_{PL} (nm)[a]	λ_{abs}(nm)[a]	$\phi_{PL}^{air}/\phi_{PL}^{deg}$ (%) Cyclohexane λ_{exc}=440nm	$\phi_{PL}^{air}/\phi_{PL}^{deg}$ (%) Toluene λ_{exc}=440nm	$\phi_{PL}^{air}/\phi_{PL}^{deg}$ (%) Dichloromethane λ_{exc}=470nm
IN-Ph-DTC	568	298/398	0.3/0.3	2.2/2.2	34.0/34.1
IN-Ph-DTP	560	259/299	1.0/1.8	0.4/0.6	0.1/0.2
ID-Ph-DTC	679	336/462	1.0/1.1	2.0/2.4	0.4/0.4
ID-Ph-DTP	565	333/469	18.0[b]/18.2[b]	0/0.1	0.0/0.1

[a] λ_{PL}= emission maxima, λ_{abs}= absorptions maxima measured in CH_2Cl_2 solution (10^{-5} M) at room temperature.

[b] λ_{exc}=290nm. PLQY values were recorded in air-equilibrated and degassed solutions.

Dynamic photophysical measurements revealed interesting properties of the molecules, especially in the solid state. Notably, for this type of investigation, the photophysical study in solid state was carried out on the molecules dispersed in PMMA films (0.1 %wt), in order to study the isolated molecules emission in a rigid

matrix, in zeonex® (0.1 wt%) and in neat films (100%) prepared by drop-casting of DCM solutions on a quartz slide.

As shown in Figure 6.30 a) IN-Ph-DTC, dispersed in zeonex®, exhibits two emission regions, a well resolved high energy one which can be assigned to the localized emission (LE π-π* transition) of 3,6-di-tert-butyl-9H-carbazole (DTC), and a lower energy one (which appears structured) which is assigned to a CT emission with a partial localized character. Two emissions are also visible in the PMMA film, but the higher energy emission appears much less intense than in the CT, which has a Gaussian shape and follows the profile of the emission obtained in zeonex®. This difference depends on the higher polarity of the PMMA which tends to better stabilize the CT state differently from the zeonex®, which is a nonpolar matrix, less polar than toluene or DCM. Interestingly, the PL emissions of both indanone based emitters IN-Ph-DTC and IN-Ph-DTP in neat film are strongly red-shifted (about 70-100 nm) compared with the isolated molecules in the polymer matrices, and this effect is attributed to the formation of aggregate states which also exhibit PL decay profiles with longer lifetimes and a bi-exponential trend. As depicted in Table 6.32. the PLQY values recorded in neat films result higher compared to the values of the isolated molecules dispersed in the polymer, confirming that the molecules do not suffer from aggregation induced quenching (ACQ).

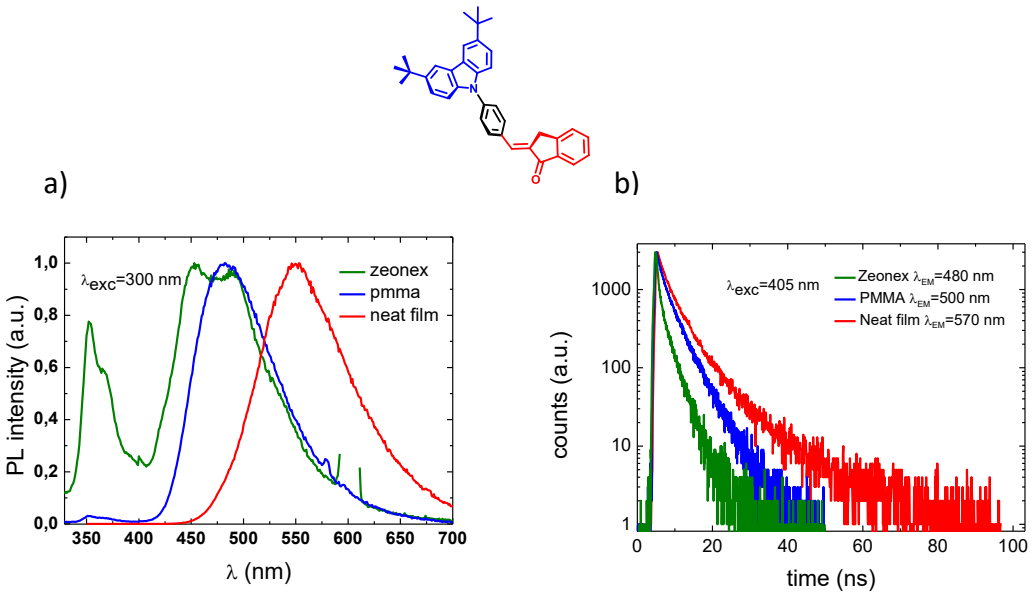

Figure 6.30. a) Normalized PL spectra and b) Transient PL decay curves of IN-Ph-DTC in zeonex® (0.1 % wt, green), in PMMA (0.1 %wt, blue) and neat film (red).

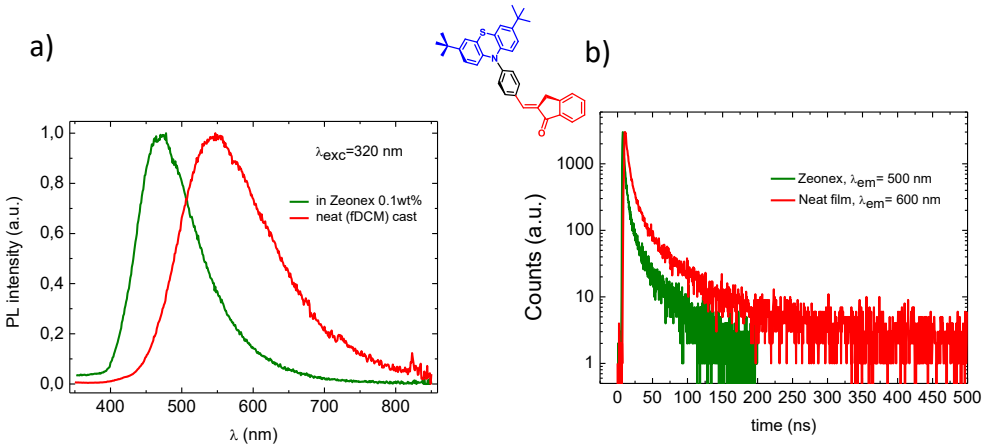

Figure 6.31. a) Normalized PL spectra and b) Transient PL decay curves of IN-Ph-DTP in zeonex (0.1 % wt, green) and neat film (red).

Table 6.32.
Photophysical properties recorded in zeonex (0.1 % wt), PMMA (0.1 %wt) and neat film

Emitter	$\%\phi_{PL}$ Zeonex	τ_1/τ_2 (ns) Zeonex	$\%\phi_{PL}$ PMMA	τ_1/τ_2 (ns) PMMA	τ_1/τ_2 (μs) PMMA	$\%\phi_{PL}$ NEAT FILM	τ_1/τ_2 (ns) NEAT FILM
IN-Ph-DTC	0.8	0.8/3.0	13.4	n.d.	1.5/4.4	15	2.8/8.2
IN-Ph-DTP	2.2	14.2/38.0	n.d.	2.6/8.1	n.d.	1.8	11.3/50.4
ID-Ph-DTC	1.2	1.1/3.1	34.3	2.1/5.3	10.7/82.4	21.5[a]	2.8/6.2
ID-Ph-DTP	1.8	0.6/1.8	6.5	2.1/5.3	3.5/17.5	7.6[a]	6.1/10.7

n.d.= not defined.
τ_1= prompt fluorescence lifetime determined from PL decay.
τ_2= delayed fluorescence lifetime determined from PL decay.
[a]measured on the crystalline powders.

As depicted in Figure 6.33, the PL emissions of the Indandione based emitters ID-Ph-DTC and ID-Ph-DTP resulted structured with outlined vibronic replicas in zeonex®, while in PMMA the emissions showed red-shifted Gaussian shapes owing to the higher polarity of the PMMA which stabilizes the CT state.
Very interesting properties were observed in the behaviour of the crystalline powder. In both emitters there is a red shift of the emission attributed to the formation of an aggregated state. It is interesting to note how the PLQY values increase drastically (more than an order of magnitude) compared to the solutions clearly hinting an effect of aggregation induced emission (AIE) or aggregation induced emission enhancement (AIEE). The time resolved PL decays of the excited states in the nanosecond scale showed a biexponential trend. In the polymer the short time is attributed to the LE state while the long time is related to the CT. In the crystal powders the short lifetime decays are attributable to the CT decay of the monomer while the longer lifetime decays arise from the aggregated states of the molecules, thus confirming their AIE properties. Furthermore, the study of emission lifetimes on the scale of hundreds of microseconds revealed that both molecules ID-Ph-DTC and ID-Ph-DTP dispersed in PMMA exhibit very long emission lifetimes attributable to TADF.

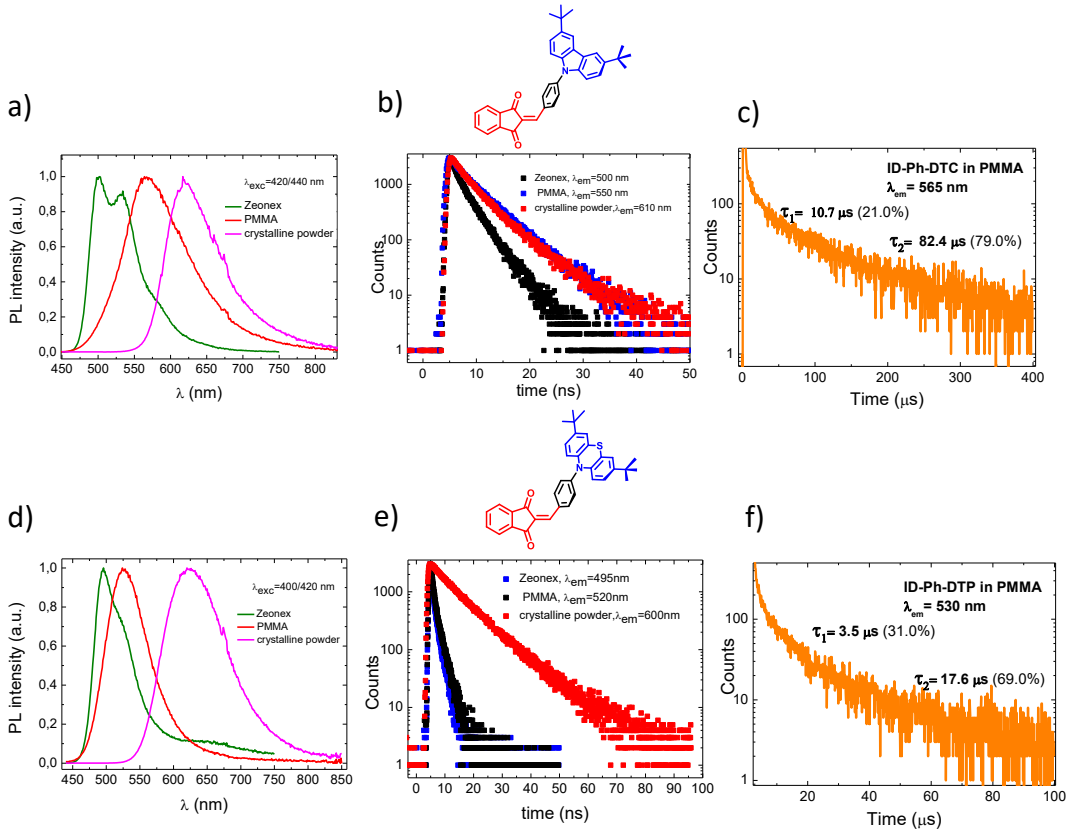

Figure 6.33. a),d) Normalized PL spectra, b),e) Transient PL decay curves (ns scale) in zeonex® (0.1 % wt), PMMA (0.1 % wt) and in crystalline powder and c),f) Transient PL decay curves (μs scale) in PMMA (0.1 % wt) of ID-Ph-DTC and ID-Ph-DTP.

Multicolor-Mechanocromic Luminescence (MCL) properties

The promising solvatochromic properties of the studied materials emerged from a prominent emission phenomenon which was already observed during the synthesis. When irradiated at 365 nm with a UV lamp, the solutions of IN-Ph-DTC exhibit an intensely bright emission with an evident change in colour according to the solvent used. Infact, as discussed above, the polarity of the solvent results crucial promoting a bright yellow emission in dichloromethane (λ_{em}=557 nm) and a strong blue shift in a less polar solvent as toluene (λ_{em}=471 nm), as depicted in Figure 6.34. However, the most interesting properties were observed after the

crystallization of the material starting from these solutions, in fact IN-Ph-DTC exhibits different bright emissions in the solid state according to the starting solvent, thus indicating a morphology-dependent luminescence. To gain a better understanding of the structure–property relationships of these materials, the pristine solids obtained were further studied, highlighting intriguing mechanochromic phenomena. Upon mechanical grinding, the colour of the pristine powder of IN-Ph-DTC (obtained from DCM) changed very little to the naked eye, but the sample became brighter and clearly turned from orange (λ_{em} = 582 nm) to yellowish green (λ_{em} = 568 nm) under UV illumination. The pristine powder crystallized from toluene retains a blue shifted emission (λ_{em} = 573 nm) compared to the sample obtained from dichloromethane, probably due to the effect of the interaction with the residual solvent molecules. Notwithstanding, also in this case, the subsequent grinding leads to a slight blue-shift aligning the emission of the two samples, thus indicating the generation of an amorphous state. Thereafter, the ground samples were exposed to ethanol vapor for 5 minutes. The effect of the ethanol exposure was detected on the photoluminescence spectrum generating a clear emission blue-shift. After the air-drying, the respective emissions revert back to 582 nm and 573 nm, which are consistent with their emissions in pristine state, probably due to two different crystalline forms, as confirmed from the DSC analysis in Figure 6.20 a). Plausibly, after the solvent vapor exposure, the air-drying facilitates the rearrangement of molecules from random to ordered. The choice of ethanol arises from the observation that, for all the investigated emitters, methanol and ethanol are very poor solvents which can facilitate the observed reversible fluorescence changing. Also the introduction of the tert-butyl groups in the donor units plays a key role, promoting the self-assembly activity of the molecules. To further verify the activity of the molecular arrangement, the effect of the temperature was studied, confirming the AIE property of the material in a neat film.

The aggregated state in these types of molecules, in fact, can be controlled through thermal annealing (Figure 6.34 b) and c)).

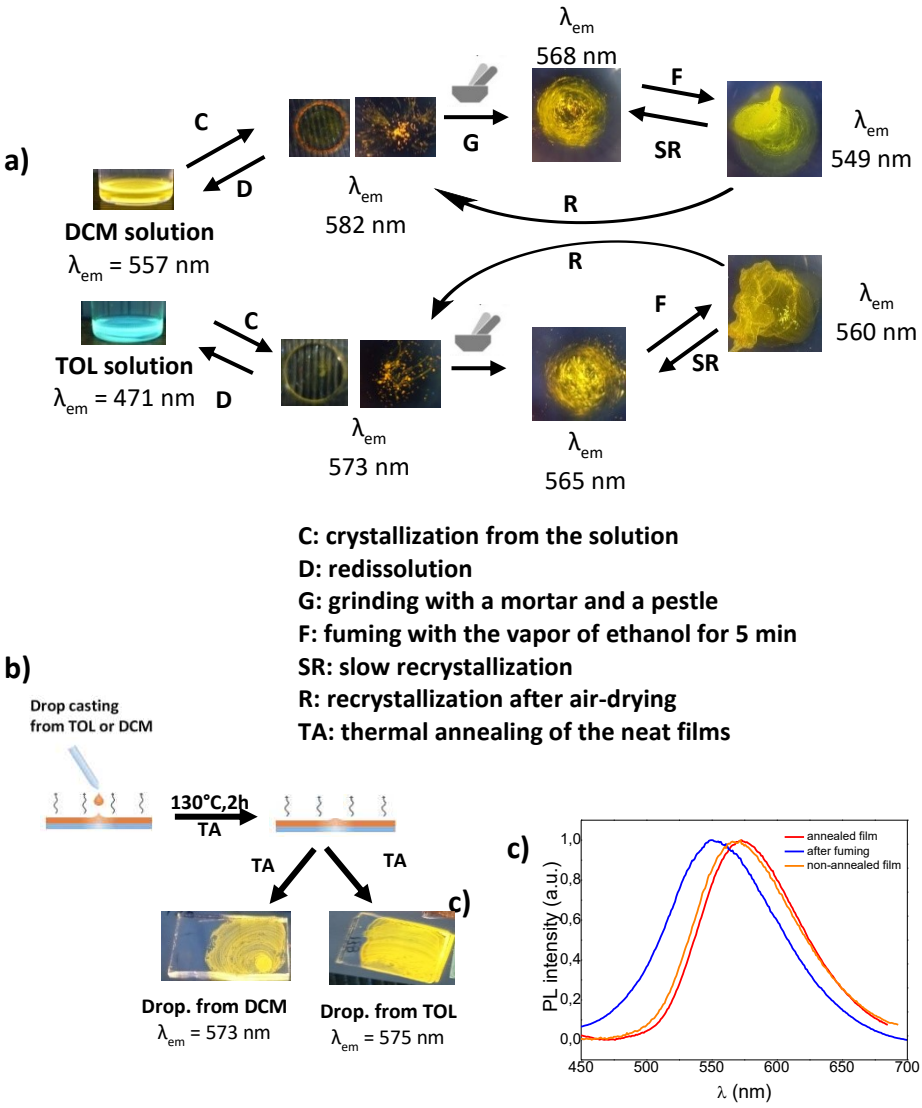

Figure 6.34. a) Schematic diagrams of the multicolor-changing MCL behavior of IN-Ph-DTC (photographs were taken under irradiation with UV light (365 nm)). b) Thermal annealing process of IN-Ph-DTC on quartz slides drop-casted by solutions. c) Overlaid PL emission spectra of the neat film of IN-Ph-DTC, on quartz slide drop-casted by DCM, before annealing (orange), annealed (red) and after fuming with ethanol vapor for 5 min.

Annealing of neat films obtained through drop casting from DCM and TOL were performed at temperature of 130 °C (which is much lower than melting points of 196 °C and 199 °C of IN-Ph-DTP) for 2 hours. PL spectra of annealed neat films were slightly red-shifted (573 nm and 575 nm respectively) compared to the non-annealed one (568 nm) (Figure 6.34 c)), which is consistent with the possibility to change the dihedral angle between donor and acceptor fragment in peculiar conditions. A very peculiar mechanically induced luminescence shift was observed in IN-Ph-DTP. As shown in Fig. 6.35 a), in the pristine form obtained after the crystallization from dichloromethane, IN-Ph-DTP showed a yellowish-green emission under UV illumination (λ_{em}=560 nm). Upon grinding, the color of the solid material drastically changed to orange (λ_{em}=600 nm) and when the ground powder was exposed to ethanol vapor the fluorescence emission were partially restored after 3 minutes and completely recovered at its original state after 30 minutes.

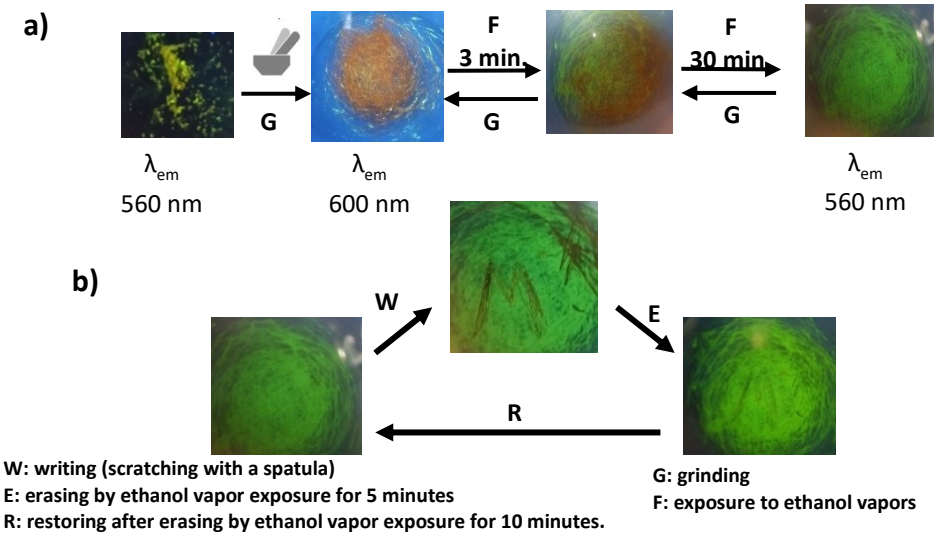

Figure 6.35. a) Repeated switching of the solid-state fluorescence of solid IN-Ph-DTP by grinding and fuming cycles using ethanol vapor b) Repeated luminescence writing/erasing process performed on the ground solid IN-Ph-DTP loaded on the mortar and restored by ethanol fuming. Photographs were taken under irradiation with UV light (365 nm).

The MCL property observed indicates that grinding the emitter causes conformational changes in the molecules in such a way to be more twisted and thus enhancing the ICT delocalization, leading to emission at a longer wavelength. The feasibility of using such a smart material for practical applications is also explored in these studies.

As reported in Figure 6.35 b), the ground powder can be utilized in a writing–erasing process. When a conventional sign (the letter 'M') is impressed on the mortar bottom using a spatula, pressing the emitting material, the letter emits TADF orange light, which is clearly distinguished from the yellowish-green background. The letter can be easily erased by ethanol vapor fuming for 10 minutes. IN-Ph-DTP thus may be used for example as a promising security ink or applied in smart textiles. [55]Quite interestingly, these processes are all reversible and the samples can be subjected to multiple analogous writing-erasure cycles.

To gain a better understanding the molecular interactions in these peculiar systems, the mechanochromic properties of the Indandione based emitters ID-Ph-DTC and ID-Ph-DTP were also explored. The as synthesized pristine powders of both compounds appear red-orange to the naked eye, but the samples exhibit a bright orange (λ_{em} = 598 nm) and red (λ_{em} = 623 nm) fluorescence emission for ID-Ph-DTC and ID-Ph-DTP respectively, under UV illumination. As shown in Figure 6.36, the MCL properties observed indicates that grinding the emitters could causes conformational changes probably related to the phase transitions from crystalline to relatively amorphous states in the molecules, as will be confirmed by further investigations.

Notably, the more extended planarized regions of the molecules containing the stronger indandione acceptor unit can be involved to explain the observed MCL color changes in response to external forces. Upon grinding, the emission color of ID-Ph-DTC is changed from orange (λ_{em} = 598 nm) to red (λ_{em} = 613 nm). This evident red-shifted emission can be ascribed to the variations of intramolecular D-Ph-A twisting due to the DTC rotation. Probably, a more disordered amorphous state can be generated under mechanical stimuli allowing to the DTC unit to

assume a more twisted conformation stabilizing the ICT delocalization and leading to emission at a longer wavelength. Also in this case the emission revert back to 598 nm after exposure to ethanol vapor, which promote the rearrangement of molecules to an ordered state (Figure 6.36 a)). A particular mechano-chromic behavior was observed for ID-Ph-DTP. As shown in Figure 6.36 b), upon grinding, the pristine powder color drastically quenchs the fluorescent emission under UV light exposure. Interestingly, when the ground powder was exposed to ethanol vapor, the fluorescence emission was completely restored at the original state after 30 minutes. This reversible phenomenon might be correlated to the tendency for DTP to form distinct conformers upon contact with ethanol vapors, which promote crystallization. The red wavelength emission of the pristine powder probably originates from the highly twisted equatorial-equatorial conformer of the DTP unit which can be formed in an ordered state of the molecules, as also observed by Minakata et al. [54] The reversible turn off of the emission properties under external stimuli will be further explored in this molecular system, especially for the interesting future application of the material in the optoelectronic field.

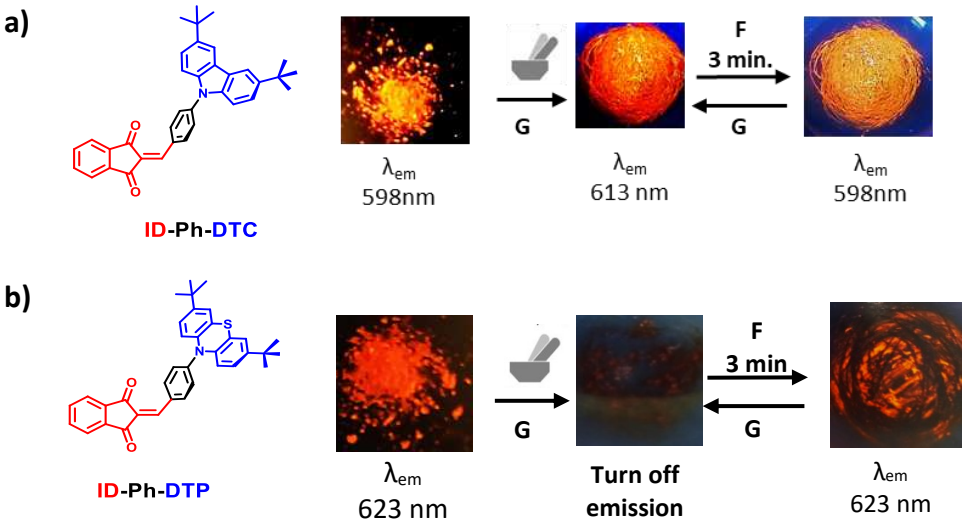

G: grinding
F: exposure to vapors of ethanol for 3 minutes

Figure 6.36. Chemical structures and schematic diagrams of the multicolor-changing MCL behaviors of a) ID-Ph-DTC and b) ID-Ph-DTP. Photographs were taken under irradiation with UV light (365 nm).

Conclusions and outlook

In summary, the section 6.2 of this chapter describes an intriguing design strategy adopted for the development of four new ketone-based multifunctional organic luminescent materials with AIE, TADF and mechano-chromic luminescence (MCL) properties in the solid state. The asymmetric D–Ph–A configuration of the target molecules were pursued through a straightforward synthetic approach based on a palladium-catalyzed Buchwald–Hartwig amination reaction. The introduction of tert-butyl groups in the donor fractions aims to introduce an innovative and effective strategy to rigidified donor around C-N bond and modulate the multiluminescent properties of the target molecules, also imparting stability and processability. The materials demonstrated moderate to excellent thermal stability and a glass-forming ability with glass transition temperatures in the range of 99.6°C–171°C. All compounds also exhibited excellent electrochemical stability with the trend of experimental HOMO and LUMO values matching those studied using density functional theory (DFT) calculations. The adoption of one

(indanone) or two (indandione) ketone groups in the acceptor moieties and the combination with electron donors endowed with different strength allowed us to investigate the structure-property relationship which determined the TADF characteristic. All compounds appear as deeply coloured and their photoluminescence covers the visible range between 550 and 650 nm. Both the steady-state and time-resolved measurements show that these molecules are characterized by formation of different electronic excited states of localized (LE) and charge transfer (CT) nature responsible of the TADF. The synthesized emitters exhibited reversible Multicolor-Mechano-chromic Luminescence (MCL), demonstrating how molecular assembly and external stimuli, are parameters that play an important role in the control of the CT state energy, which influences both the colour emission and the TADF behaviour.

At this stage, further experiments are underway, e.g. especially XRD analysis on the crystalline powders. This will allow to provide a deeper insight into the structure-property relationships governing the modification of the photophysical properties of these materials.

I think that based on the results obtained in this study, it would be worthwhile to further explore the supramolecular properties of innovative donors (D) attached to a ketone-based acceptor (A) moieties systems, in order to better understand the key factors that allow improving the solid-state photophysical properties in term of TADF, MCL and AIE. In perspective, this work opens up a new approach for further research on the multifunctional long-wavelength (orange-red) organic emitters that will eventually be applied, among others, to devices such as solution-processed OLED.

6.2.3 Experimental section

General remarks

Reagents and solvents were purchased from standard commercial sources (Aldrich® and Honeywell Riedel-de-Haën, respectively). All syntheses and chemical manipulations were carried out under inert nitrogen atmosphere using standard Schlenk techniques. The reaction courses were monitored by thin-layer chromatography (TLC) on Merck® silica gel 60 F254 aluminum sheets. Column chromatography purifications were carried out on a Biotage Isolera One instrument. ^{1}H-NMR spectra were recorded on a Bruker Avance DPX 300 MHz instrument. Thermogravimetric analysis (TGA) was carried out on a Perkin-Elmer Pyris 6 TGA instrument under a nitrogen flow (40 mL/min) at a heating rate of 10 °C/min. Differential scanning calorimetry (DSC) was recorded on a Q2000 TA instrument under a nitrogen flow (50 mL/min) at a temperature scan of 10 °C/min.

The cyclic voltammetry experiments were carried out on a Metrohm Autolab PGSTAT 302-N potentiostat in dichloromethane (emitter concentration: ~10^{-4} M) containing tetrabutylammonium tetrafluoroborate (0.10 M) as the supporting electrolyte at a 100 mV/s scan rate. The potentials were measured with respect to Ag/Ag^{+} quasi-reference electrode, that was calibrated against ferrocene/ferrocenium^{+} (Fc/Fc^{+}) after each experiment. The HOMO and LUMO energy levels were calculated according to the following equations:

$$E_{HOMO} = -\left[E_{OX} - E_{(Fc/Fc+)} + 5.10\right](eV) \quad \textit{Equation 6.37}$$

$$E_{LUMO} = -\left[E_{RED} - E_{(Fc/Fc+)} + 5.10\right](eV) \quad \textit{Equation 6.38}$$

where $E_{(Fc/Fc+)}$ represents the half-wave potential of the Fc/Fc^{+} couple, E_{OX} and E_{RED} represent respectively the half-wave oxidation and reduction potential of the emitter. E_g corresponds to the optical band gap calculated by $E_g = 1240/\lambda_{onset}$ (eV) (where λ_{onset} represents the onset of the emitter absorption curve recorded in DCM solution) and was compared to the E_g calculated by the experimental difference E_{HOMO}-E_{LUMO}. The analyses of the ground-state geometries were carried out

by density functional theory (DFT) calculations using the B3LYP function in conjunction with the 6-31G(d,p) basis set on isolated molecules. Calculated energies of the relevant molecules along with their optimized geometries were carried out with the 6-311G(d,p) basis set including solvent effects (conductor-like polarizable continuum model method, CH_2Cl_2). These theoretical calculations have been carried out using the Gaussian09 program package. Steady-state photoluminescence (PL) spectra from pristine, ground, annealed and fumed samples were acquired on a Varian Cary Eclipse instrument. A 1 mm^2 quartz cell was used for the solid measurement. Each sample was held in the cell holder in a diagonal position, and the fluorescence was measured at selected excitation wavelengths of the emitter in DCM solution.

Synthesis of the intermediate (E)-2-(4-bromobenzylidene)-2,3-dihydro-1H-inden-1-one (IN-Ph-Br) [50]

According to a literature procedure, 2,3-dihydro-1H-inden-1-one (IN) (679.30 mg, 5.14 mmol) and 4-bromobenzaldehyde (1.00 g, 5.40 mol) were dissolved in ethanol (10 mL), and then sodium hydroxide (256.06 mg, 6.40 mmol) was slowly added thereto at 0°C. After, the mixture was stirred at room temperature for 3 hours; during this reaction time the colour of the mixture turned from white to pink after 0.5 hours. The prepared solid was separated by filtering under reduced pressure and sequentially washed with methanol, distilled water, and methanol. The resultant material was dried, thereby obtaining (E)-2-(4-bromobenzylidene)-2,3-dihydro-1H-inden-1-one (1.101 g, 71.8%) as a yellow solid.

^1H NMR (300 MHz, $CDCl_3$) δ 7.92 (d, J = 7.2 Hz, 1H), 7.58 (7H, m), 7.44 (t, J = 6.9 Hz, 1H), 4.05 (s, 2H) ppm.

Synthesis of the intermediate 2-(4-bromobenzylidene)-1H-indene-1,3(2H)-dione (ID-Ph-Br) [50]

Adapting the literature procedure used for the synthesis of IN-Ph-Br, 1H-indene-1,3(2H)-dione (ID) (445.76 mg, 3.05 mmol) and 4-bromobenzaldehyde (592.06 mg, 3.2 mmol) were dissolved in ethanol (6.40 mL), and then sodium hydroxide

(152.00 mg, 3.80 mmol) was slowly added thereto at 0°C. After, the mixture was stirred at room temperature for 3 hours, the prepared solid was separated by filtering under reduced pressure and sequentially washed with methanol, distilled water, and methanol. The resultant material was dried, thereby obtaining 2-(4-bromobenzylidene)-1H-indene-1,3(2H)-dione (668.62 mg, 70.0%) as a white solid.

^{1}H NMR (300 MHz, DMSO-d_6) δ 8.42 (d, J = 7.2 Hz, 1H), 7.97 (2H, m), 7.88-7.72 (6H, m) ppm.

Synthesis of the donor 3,7-di-tert-butyl-10H-phenothiazine (DTP) (51)

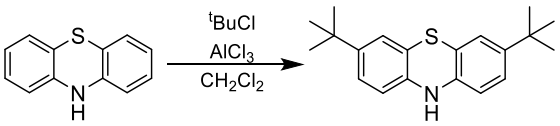

DTP

Scheme 6.37. Synthetic procedure for the obtainment of 3,7-di-tert-butyl-10H-phenothiazine (DTP).

To a vigorously stirred suspension of phenothiazine (5.00 g, 25.10 mmol) and anhydrous $AlCl_3$ (7.03 g, 52.70 mmol) in CH_2Cl_2 (50 mL) was added tert-butyl chloride (10.93 mL, 100.40 mmol) dropwise under N_2 at 0° C. After addition of tert-butyl chloride the mixture was stirred at the same temperature for 5 min, then it was poured into water (300 ml), and NaOAc (5.00 g, 60.95 mmol) was added. The phases were shaken well, separated, and the aqueous phase was extracted with CH_2Cl_2 (3×50 mL). The combined organic phase was dried over Na_2SO_4, filtered, and the solvent was removed. The crude product was triturated with hexane and then was dried to give 3,7-di-tert-butyl-10H-phenothiazine (DTP) as an off-white solid (6.41 g, 82%).^{1}H NMR (300 MHz, DMSO-d_6) δ 1.23 (s, 18H, t-Bu), 6.62 (d, J=8 Hz, 2H, ArH), 6.89 (s, 2H, ArH), 6.98 (d, J=8 Hz, 2H, ArH), 8.38 (s, 1H, NH) ppm.

Synthesis of the donor 3,6-di-tert-butyl-9H-carbazole (DTC) [52]

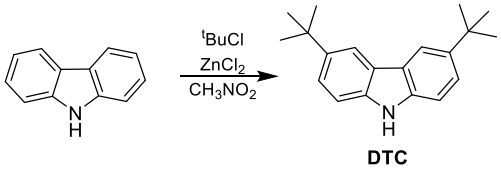

DTC

Scheme 6.37. Synthetic procedure for the obtainment of 3,6-di-tert-butyl-9H-carbazole (DTC).

9-H-carbazole (3.30 g, 20.00 mmol), 100 mL of nitromethane, and $ZnCl_2$ (8.10 g, 60.00 mmol) were added to a three-neck flask under a N_2 atmosphere. Then tert-butyl chloride (6.5 ml, 60 mmol) was added dropwise under stirring. The mixture was stirred at room temperature for 5 h and then hydrolyzed with 100 mL of water. The product was extracted with CH_2Cl_2 (3 x 50 mL). The organic layer was washed with H_2O (2 x 100 mL), dried with Na_2SO_4, and evaporated under vacuum to yield 4.5 g (81%) of off-white solid. ^{1}H NMR (300 MHz, $CDCl_3$) δ 1.45 (s, 18H, t-Bu), 7.33 (dd, J = 5.56, 0.49 Hz, 2H, ArH), 7.49 (dd, J = 8.46, 1.93 Hz, 2H, ArH), 7.83 (s b, 1H, NH), 8.08 (d, J = 1.92 Hz, 2H, ArH) ppm.

Synthesis of (E)-2-(4-(3,6-di-tert-butyl-9H-carbazol-9-yl)benzylidene)-2,3-dihydro-1H-inden-1-one (IN-Ph-DTC)

A mixture of IN-Ph-Br (298.36 mg, 1.00 mmol), DTC (306.90 mg, 1.10 mmol), Pd_2dba_3 (22.89 mg, 0.025 mmol), XPhos (23.84 mg, 0.050 mmol) and sodium tert-butoxide (158.58 mg, 1.65 mmol) in toluene (5 mL) was stirred at 110 °C for 6 h. After cooling down the reaction to room temperature, the reaction mixture was diluted with dichloromethane (20 mL) and the obtained organic layer was washed with water (3 × 30 mL). The organic phase was separated, dried over Na_2SO_4, and filtered. Upon solvent removal, the crude product was purified by column chromatography (SiO_2, petroleum ether 40-60°C/CH_2Cl_2 = 2/3 vol/vol) to obtain IN-Ph-DTC (134.38 mg, 27 %) as a bright yellow solid. ^{1}H NMR (300 MHz, acetone-d_6) δ 8.33 (d, *J* = 1.1 Hz, 2H, ArH), 8.12 (d, *J* = 8.4 Hz, 2H, ArH), 7.83 (m, *J* = 8.8 Hz, 3H, ArH), 7.77 – 7.67 (m, 3H, 2ArH + 1CH vin.), 7.52 (dt, *J* = 20.8, 5.2 Hz, 5H, ArH), 4.27 (s, 2H, CH_2), 1.45 (s, 18H, t-Bu) ppm.

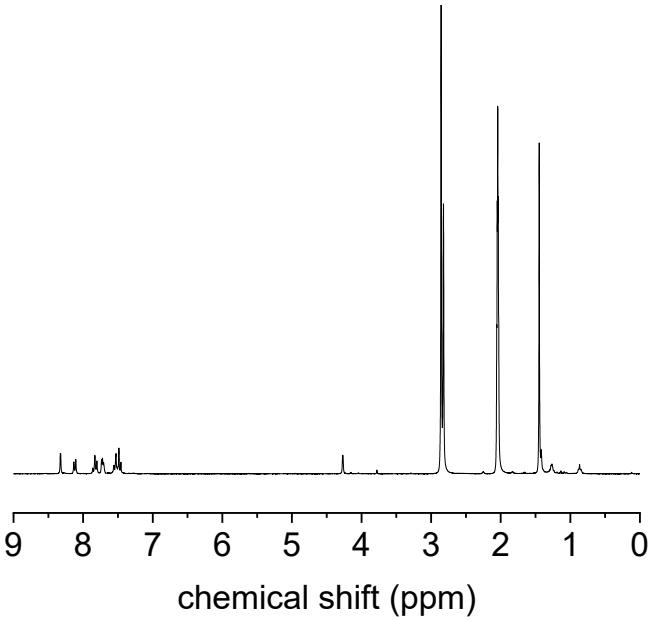

Figure 6.38. ^{1}H NMR spectrum of IN-Ph-DTC recorded in acetone-d_6.

Synthesis of (E)-2-(4-(3,7-di-tert-butyl-10H-phenothiazin-10-yl)benzylidene)-2,3-dihydro-1H-inden-1-one (IN-Ph-DTP)

A mixture of IN-Ph-Br (298.36 mg, 1.00 mmol), DTP (345.77 mg, 1.11 mmol), $Pd_2(dba)_3$ (22.89 mg, 0.025 mmol), XPhos (23.84 mg, 0.050 mmol) and sodium tert-butoxide (158.58 mg, 1.65 mmol) in toluene (5 mL) was stirred at 110 °C for 6 h. After cooling down the reaction to room temperature, the reaction mixture was diluted with dichloromethane (20 mL) and the obtained organic layer was washed with water (3 × 30 mL). The organic phase was separated, dried over Na_2SO_4, and filtered. Upon removing the solvent, the crude product was purified by column chromatography (SiO_2, petroleum ether 40-60°C/CH_2Cl_2 = 2/3 vol/vol) to obtain IN-Ph-DTC (169.52 mg, 32 %) as a yellowish green solid. ^{1}H NMR (300 MHz, acetone-d_6) δ 7.89 (d, *J* = 8.6 Hz, 2H, ArH), 7.81 (d, *J* = 7.5 Hz, 1H, ArH), 7.68 (s, 2H, ArH), 7.60 (s, 1H, CH vin.), 7.47 (dd, *J* = 10.8, 5.5 Hz, 2H, ArH), 7.33 (dd, *J* =

7.4, 5.4 Hz, 3H, ArH), 7.22 (dd, *J* = 8.5, 2.2 Hz, 2H, ArH), 6.82 (d, *J* = 8.5 Hz, 2H, ArH), 4.16 (s, 2H, CH_2), 1.30 (s, 18H, t-Bu).

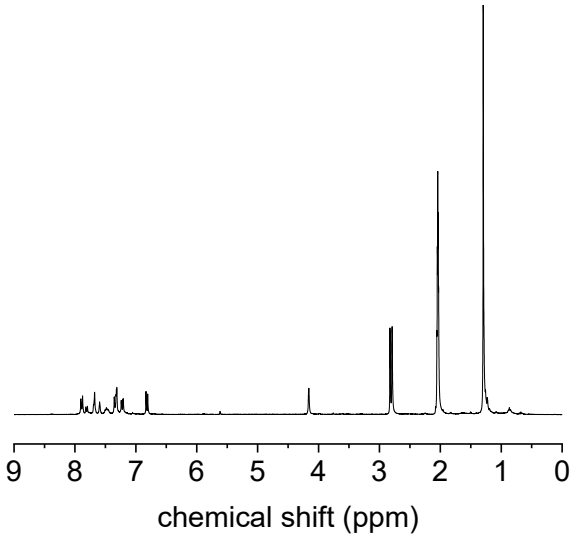

Figure 6.39. ^{1}H NMR spectrum of IN-Ph-DTP recorded in acetone-d_6.

Synthesis of 2-(4-(3,6-di-tert-butyl-9H-carbazol-9-yl)benzylidene)-1H-indene-1,3(2H)-dione (ID-Ph-DTC)

A mixture of ID-Ph-Br (313.17 mg, 1.00 mmol), DTC (306.90 mg, 1.10 mmol), $Pd_2(dba)_3$ (22.89 mg, 0.025 mmol), XPhos (23.84 mg, 0.050 mmol) and sodium tert-butoxide (158.58 mg, 1.65 mmol) in toluene (5 mL) was stirred at 110 °C for 6 h. After cooling down the reaction to room temperature, the reaction mixture was diluted with dichloromethane (20 mL) and the obtained organic layer was washed with water (3 × 30 mL). The organic phase was separated, dried over Na_2SO_4, and filtered. Upon removing the solvent, the crude product was purified by column chromatography (SiO_2, petroleum ether 40-60°C/CH_2Cl_2 = 2/3 vol/vol) to obtain IN-Ph-DTC (199.50 mg, 39 %) as a bright orange solid. ^{1}H NMR (300 MHz, acetone-d_6) δ 8.92 (d, *J* = 8.6 Hz, 2H, ArH), 8.34 (s, 2H, ArH), 8.16 – 7.95 (m, 5H, 4ArH + 1CH vin.), 7.91 (d, *J* = 8.5 Hz, 2H, ArH), 7.61 – 7.53 (m, 4H, ArH), 1.45 (s, 18H, tBu) ppm.

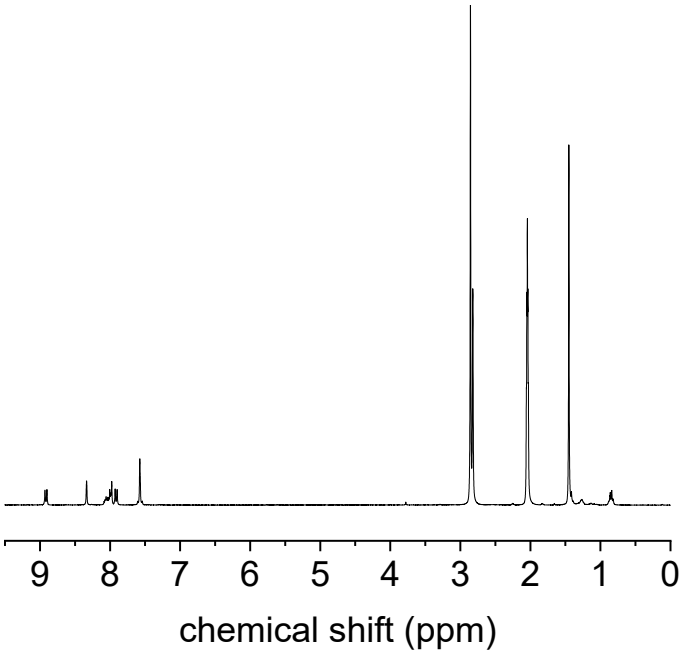

Figure 6.40. ^{1}H NMR spectrum of ID-Ph-DTC recorded in acetone-d_6.

Synthesis of 2-(4-(3,7-di-tert-butyl-10H-phenothiazin-10-yl)benzylidene)-1H-indene-1,3(2H)-dione (ID-Ph-DTP)

A mixture of ID-Ph-Br (313.17 mg, 1.00 mmol), DTP (345.70 mg, 1.11 mmol), $Pd_2(dba)_3$ (22.89 mg, 0.025 mmol), XPhos (23.84 mg, 0.050 mmol) and sodium tert-butoxide (158.58 mg, 1.65 mmol) in toluene (5 mL) was stirred at 110 °C for 6 h. After cooling down the reaction to room temperature, the reaction mixture was diluted with dichloromethane (20 mL) and the obtained organic layer was washed with water (3 × 30 mL). The organic phase was separated, dried over Na_2SO_4, and filtered. Upon removing the solvent, the crude product was purified by column chromatography (SiO_2, petroleum ether 40-60°C/CH_2Cl_2 = 2/3 vol/vol) to obtain IN-Ph-DTC (199.50 mg, 39 %) as a bright red solid. ^{1}H NMR (300 MHz, acetone-d_6) δ 8.56 (d, *J* = 9.0 Hz, 3H, ArH), 7.92 (d, *J* = 3.5 Hz, 2H, ArH), 7.74 (s,

1H, CH vin.), 7.59 (s, 3H, ArH), 7.53 (s, 4H, ArH), 7.17 (d, *J* = 8.9 Hz, 2H, ArH), 1.36 (s, 18H, t-Bu) ppm.

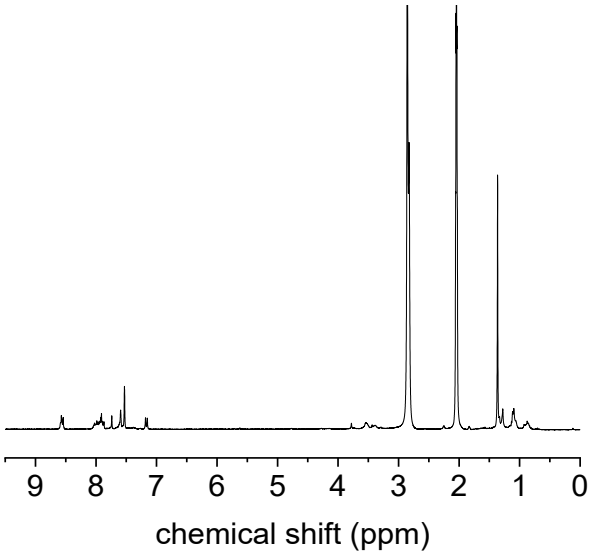

Figure 6.41. ^{1}H NMR spectrum of ID-Ph-DTP recorded in acetone-d_6.

6.3 Activation of red thermally activated delayed emission via aggregate formation in fluorenone-based molecules

6.3.1 Introduction

As already highlighted in this chapter, the employment of novel design strategies and synthetic approaches for the development of new luminescent materials for organic optoelectronics is very important to achieve highly performance OLED devices. Suitable donor-acceptor molecules for TADF OLEDs application must fit a lot of requirements: low ΔE_{ST} values, high PLQY thermal and electrochemical stability, moreover decent morphological properties are desirable for a potential application in an effective OLED. The presence of AIEE effect can be an additional advantage to use materials as neat films inside OLED devices without the need to disperse them in a matrix in order to avoid self-quenching. Novelty in design also can be implemented through an alternative way of ICT in donor-acceptor materials, for example tuning the effective HOMO/LUMO separation in the almost perpendicularly twisted D–A systems and D–A–D triads. [54] In the selection of donors and acceptors, the organic chemistry have offered various options, but it should be noted that the design and synthesis of highly efficient TADF materials exhibiting strong AIE properties remains a way forward, which should also be achieved through low-cost and sustainable synthetic methods. In this perspective, the aim of this thesis relies on the selection of a suitable and appropriate donor to the corresponding selected acceptor as well as achieving efficient red emission from their cooperation. Among the reported ketone-based acceptors discussed in this chapter, it is found that the mono-ketone derivatives covered emission range from blue to green while the diketone derivatives extended the emission to orange-red range. [55] However, unfrequently mono-ketone based moieties have been exploited as TADF acceptors in constructing orange red emitters. [56] Keeping this in mind, herein the focus is on the molecular design, step-economy based synthesis, and characterization of two novel organic emitters, 3-bromo-6-(3,7-di-tert-butyl-10H-phenothiazin-10-yl)-9H-fluoren-9-one (Br-FL-DTP) and 3,6-bis(3,7-di-tert-butyl-10H-phenothiazin-10-yl)-9H-fluoren-9-one (DTP-FL-DTP),

based on a fluorenone electron-accepting unit . A U-shaped donor–acceptor-donor (D-A-D) architecture was adopted using a central fluorenonic core activated to be substituted on positions 3 and 6 which, as reported in the literature, [57] favors the possibility of modulating its photoemissive properties by suitably selecting the donors (Figure 6.42).

In this section of the Dissertation most promising results were obtained using a substituent with a strong electron donor character based on a phenothiazine functionalized, in turn, in the positions 3 and 7 with two tertbutyl groups in order to warrant a larger steric hindrance and solubility to the corresponding molecules, modulating also the molecular distortion towards potential longer wavelength emissions of the emitters. One of the target molecules was designed with the aim to explore the results of the combination of the planar structure of the fluorenone unit with the residual bromine atom (a potential halogen bonding extremity). This variant promotes the formation of strong intermolecular interactions, introducing also a potential heavy atom effect of the halogen, which could be an effective approach to facilitate spin conversion and boost triplet exciton utilization for the TADF emission. [58] A suitable synthetic strategy was devised in order to obtain both emitters in a single step. The obtained compounds were characterized by investigated spectroscopic, thermal and electrochemical properties, supported by DFT calculations. Also due to the large dihedral angle between donor and acceptor units, these new materials exhibit TADF and AIE behavior reaching long-wavelength emissions > 600 nm in peculiar conditions. The promising results reported in this discussion indicate that, through a suitable molecular design strategy, the obtainment of efficient multifunctional luminescent organic materials for TADF can be pursued through an economically viable synthetic approach.

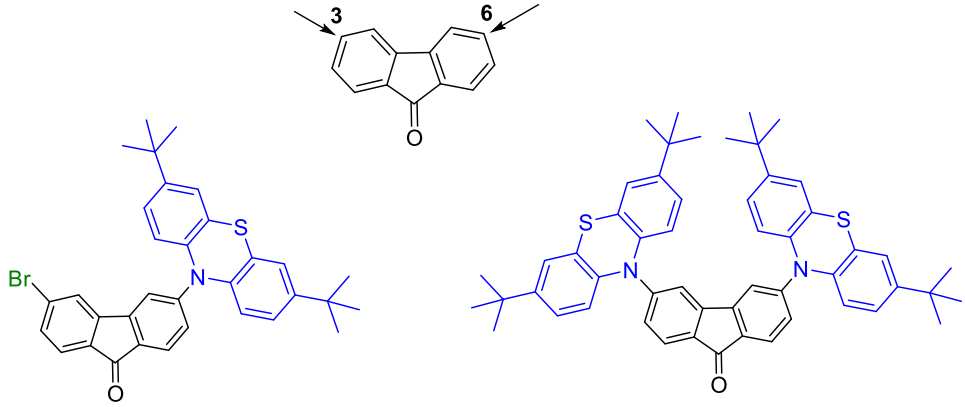

Figure 6.42 Chemical structures of the target fluorenone-based emitters outstanding the 3 and 6 activated positions on the fluorenone core.

6.3.2 Results and discussion

Synthesis and characterization

The acceptor core 3,6-dibromo-9H-fluoren-9-one was synthesized by following a literature procedure which allows to obtain the product through a clean synthetic approach, not requiring chromatographic separation. As reported in the experimental part 6.3.3., this approach starts from 3,6-dibromophenanthrene-9,10-dione, thus avoiding also the bromination step. [60]The synthetic strategy adopted for the obtainement of the target molecules was pursued via a suitable one-step $Pd^{(0)}$ catalyzed C–N Buchwald-Hartwig cross coupling reaction between the nitrogen-containing donor group 3,7-di-tert-butyl-10H-phenothiazine (DTP) and 3,6-dibromo-9H-fluoren-9-one (Scheme 6.43.). In order to obtain a regiocontrol of the reaction we selected an appropriate catalytic system consisting of palladium acetate $Pd(OAc)_2$ and a bidentate phosphine such as diphenylphosphine ferrocene (dppf). In these conditions the palladium ligation state plays a key role in hampering the chain-walking mechanism, commonly observed also in the catalytic chain growth polymerizations, thus controlling the rate of the oxidative addition of the nascent monoarylated product and the dissociation of the catalyst from product at the end of a catalytic cycle. [61] Using 1.0 equivalents of 3,7-di-

tert-butyl-10H-phenothiazine the reaction was carried out obtaining an equimolar mixture of the two target molecules in a single step, with satisfactory yields. Chromatographic purification allowed the purification of the individual molecules.

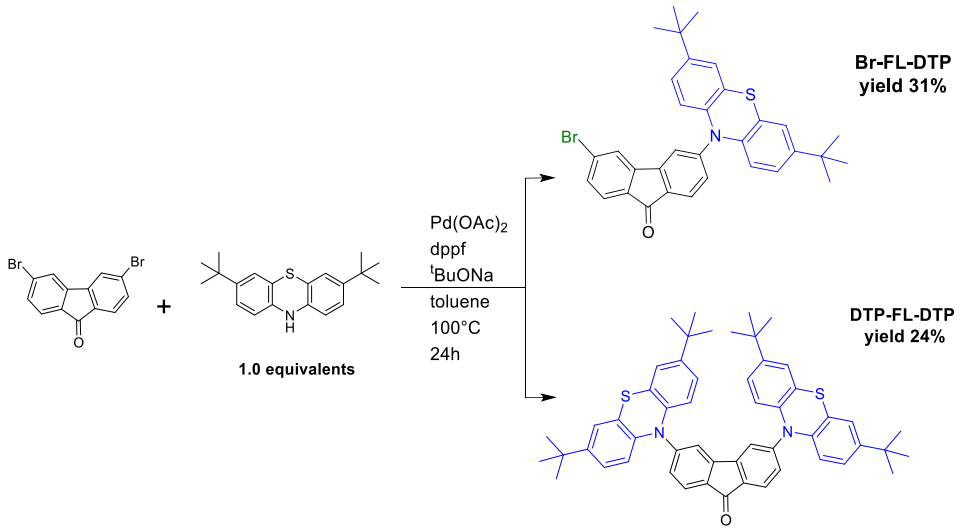

Scheme 6.43. Synthetic sequence for the obtainment of Br-FL-DTP and DTP-FL-DTP and relatives yields %.

The molecular structures of the materials were confirmed by a detailed ^{1}H-NMR spectroscopic characterization (see Experimental section 6.3.3.) in order to attribute the mono- and di-substitution pattern of the fluorenonic core and confirm a purity > 95% of the two target molecules (Figure 6.44.). The target compounds, isolated as solids after recrystallization from n-hexane/dichloromethane in 2:1 ratio, appeared intensely colored. Both Br-FL-DTP yellow solid powder and DTP-FL-DTP red powder were found to be well soluble in polar organic solvents, such as chloroform, acetonitrile, acetone and methylene chloride. However, solubility is greatly decreased in non-polar organic solvents such as n-hexane or cyclohexane.

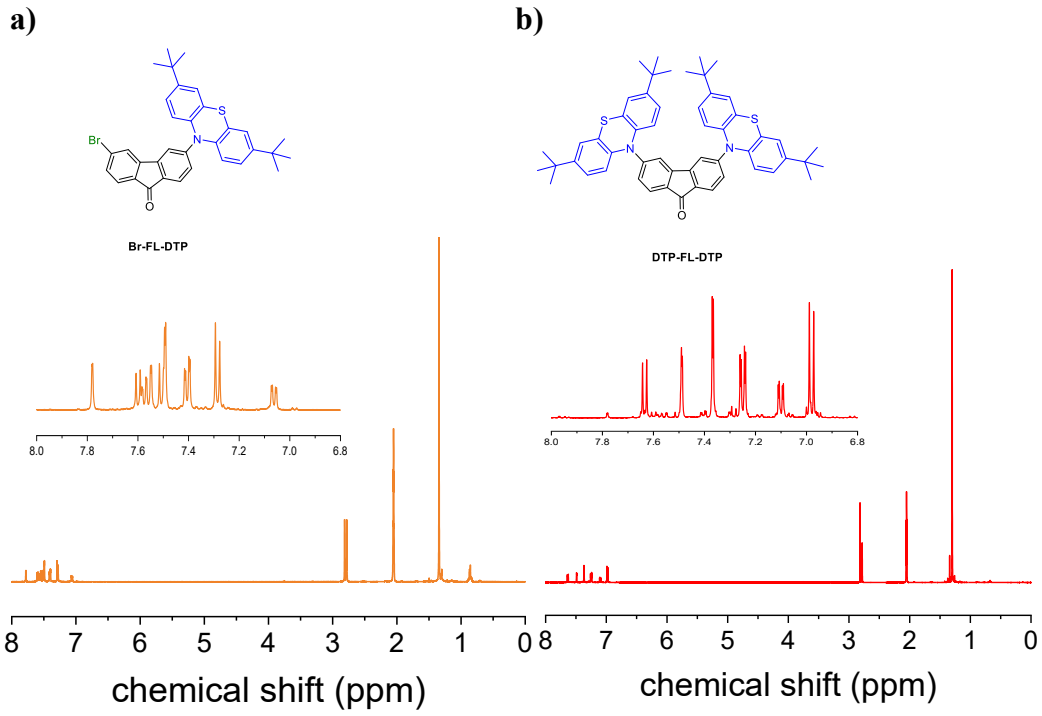

Scheme 6.44. ^{1}H NMR spectra of a) Br-FL-DTP and b) DTP-FL-DTP recorded in acetone-d_6. Insets highlight the aromatic mono- and di- substitution pattern of the fluorenone core.

Investigation of thermal properties

To gain insight about the impact of the design strategy adopted, the morphological and thermal behavior of the two materials were investigated. The thermal decomposition (T_d, corresponding to 5% weight loss) and glass transition temperature (T_g, according to the second heating scan) values recorded at a scanning rate of 10 °C/min under a nitrogen atmosphere are depicted in Figure 6.45 and Table 6.47. Notably, the DSC analysis demonstrating that, during the first heating scan, Br-FL-DTP revealed the presence of two endothermic events (Figure 6.45 a)), which can be ascribed to the melting of the different crystalline portions of the material, probably due to axial and equatorial conformations of the phenothiazine unit. The satellite event at 191 °C of the main melting (212 °C) can be attributed to the dissociation of the halogen bonding. [62] However, upon cooling,

the second heating scan showed the formation of an amorphous material with a glass transition temperature at 112 °C. This result suggests that Br-FL-DTP preferentially adopts a disordered tridimensional structure in the presence of intermolecular interactions. In the symmetric molecule DTP-FL-DTP, the effect of the steric hindrance related to the introduction of the second donor moiety, within the increased twisted conformation, impacts on the morphological state of the solid material. As observed in Figure 6.45 b) the first and the second heating scans revealed the amorphous nature of the solid with a reproducible glass transition temperature at 162 °C. This behavior hints that the "butterfly shaped" designed molecular structure cannot assume a co-facial intermolecular π···π stacking in the solid state. As shown in Figure 6.22 a) the TGA curves of the studied compounds revealed also an excellent thermal stability with the temperatures of 5% weight loss corresponding to 402°C and 405°C for Br-FL-DTP and DTP-Ph-DTP respectively. The apparent weight loss (~200 °C) observed in Br-FL-DTP is due to the residual solvent (probably n-hexane) entrapped in the crystalline structure. In this latter compound, on the basis of the DSC and TGA analyses it is possible to argue that the molecules can interact via weak π ···π and C–H···π bonds forming lamellar layer structures and definite cavities in the solid which allow the inclusion of the solvent molecules. [54] These results indicate that the morphological properties of the D-A-D emitters can be optimized through the suitable choice of the donor units with the possibility to increase the glass transition of the material correspondingly to the symmetric introduction of 3,7-di-tert-butyl-10H-

phenothiazine (DTP) substituents in the structure. However, further experiments based on DFT calculations and XRD analysis are still ongoing and will allow to support these observations.

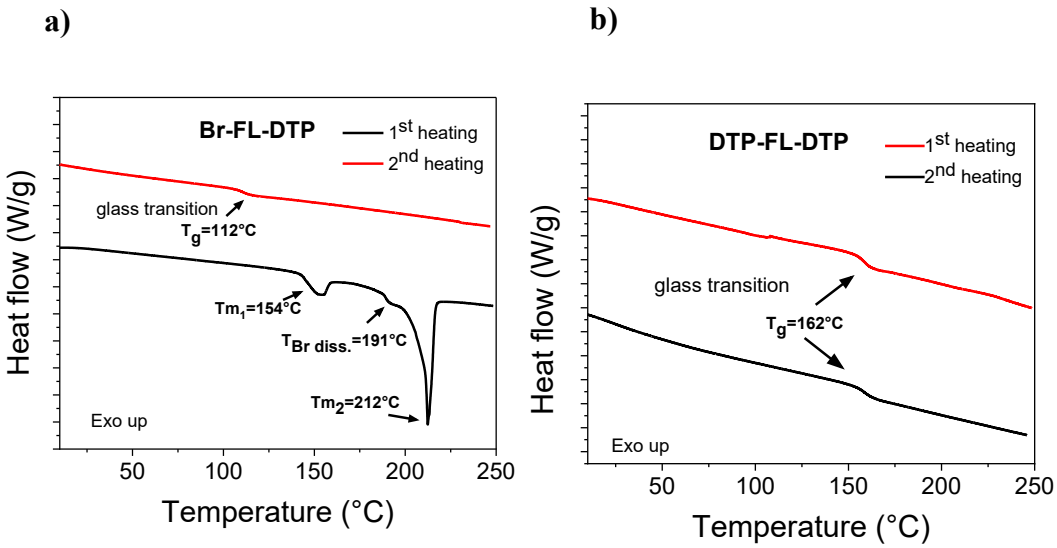

Figura 6.45. DSC traces of a) Br-FL-DTP and b) DTP-FL-DTP (first and second heating scans) identifying the glass transitions (T_g) and melting (T_m) events.

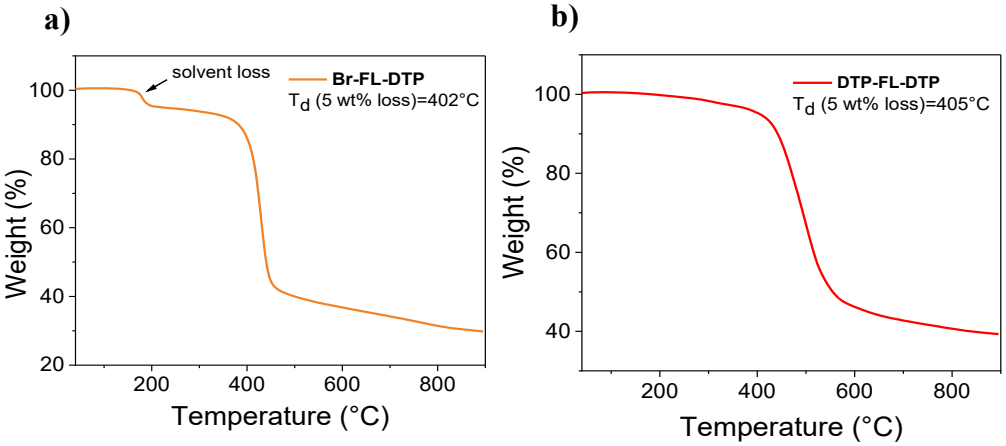

Figure 6.46. TGA curves of a) Br-FL-DTP (orange) and b) DTP-FL-DTP (red).

Electrochemical properties and theoretical calculations

The electrochemical behavior and the energy levels of the synthesized molecules were experimentally investestigated by cyclic voltammetry (CV) in dichloromethane (emitter concentration: ~10^{-4} M) containing a 0.1 M solution of tetrabutylammonium tetrafluoroborate (0.10 M) as the supporting electrolyte under N_2 atmosphere. As shown in Figure 6.48., both compounds are electrochemically active and exhibit a reversible oxidation and reduction wave in the CV traces, outstanding an high electrochemical stability. The HOMO and LUMO energy levels were determined with reference to the energy level of ferrocene and summarized in Table 6.47. The HOMO levels were calculated to be −5.40 and −5.47 eV for Br-FL-DTP and DTP-FL-DTP, respectively. These low values can be attributed to the oxidation of the DTP unit and the lower HOMO determined for the DTP-FL-DTP molecule results consistent with the increased electron withdrawal effect of the second DTP subtituent. The similar values of the LUMO levels of -3.48 eV and -3.52 eV determined for Br-FL-DTP and DTP-FL-DTP respectively, can be ascribed to the formation of a radical anion which involves the ketone group of the fluorenone core in both compounds. The shape of HOMO and LUMO frontier orbitals and the energy diagram shown in Figure 6.49 support the rationalization of these experimental data. As reported in Table 6.47, the trend of the experimental values of HOMO and LUMO well match those of the levels studied using density functional theory (DFT) calculations.

Table 6.47.
Thermal, electrochemical properties and DFT calculation data of the synthesized emitters.

Emitter	T_g (°C)[a]	T_d (°C)[b]	E_g (eV)[c]	E_g (eV)[d]	DFT HOMO (eV)[e]	DFT LUMO (eV)[e]	exp. HOMO (eV)[f]	exp. LUMO (eV)[f]
Br-FL-DTP	112.0	402	2.46	1.92	-5.32	-2.83	–5.40	–3. 48
DTP-FL-DTP	162.0	405	2.44	1.95	-5.35	-2.84	–5.47	–3.52

[a] Glass transition temperature (2nd heating scan) obtained by DSC under N_2. [b] Decomposition temperature (5% weight loss) obtained by TGA under N_2.

[c] $E_g = 1240/\lambda_{onset}$ (eV).

[d] Determined by cyclic voltammetry: $E_g = E_{HOMO} - E_{LUMO}$

[e] Calculated at the B3LYP/6-31G(d,p) level of theory.

[f] Determined by cyclic voltammetry: exp. HOMO = $-[E_{ox} - E_{(Fc/Fc^+)} + 5.10]$ (eV); exp. LUMO= $-[E_{red} - E_{(Fc/Fc^+)} + 5.10]$

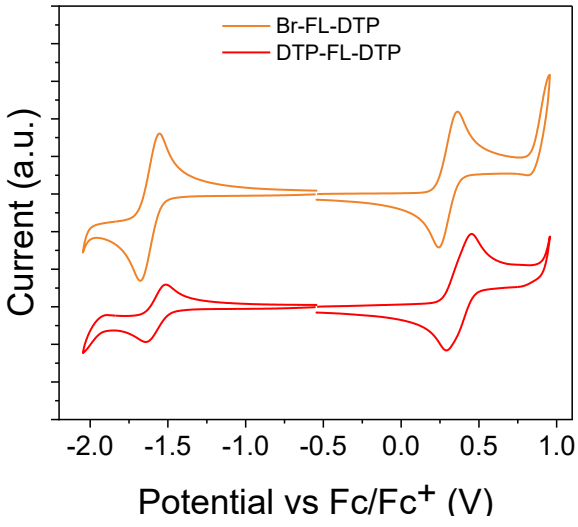

Figure 6.48. Cyclic voltammograms of Br-FL-DTP (orange) and DTP-FL-DTP (red) measured in dichloromethane (1.0×10^{-4} M) using Bu_4NBF_4 (0.1 M) as the supporting electrolyte.

The HOMO energy of DTP-FL-DTP is the lowest, and the orbital calculated electron density is mainly located on the two strong donor fragments (Figure 6.49). The possible conformers of the DTP units in the D-A-D molecular system reach

highly twisted arrangement with dihedral angles at the C-N bond > 81.1°. In this way the π-conjugation between the donor units and the central acceptor core decreases as result of the cooperation of the DTP fragment in the "U shaped" system. Evidently, the bromine atom in Br-FL-DTP cannot exert the same bulking effect as the DTP fragment, although the dihedral angle around the C-N bond, with the only DTP donor moiety included in the molecule, can reach values higher than 80.3°. The similar LUMO energy of the two emitters are in agreement with the exclusively fluorenone localized LUMOs and the experimental reduction potentials, which suggested the formation of a fluorenone radical anion. The discrete HOMOs and LUMOs distribution in the asymmetric Br−FL–DTP and symmetric DTP-FL-DTP materials aid to predict the realization of small ΔE_{ST}.

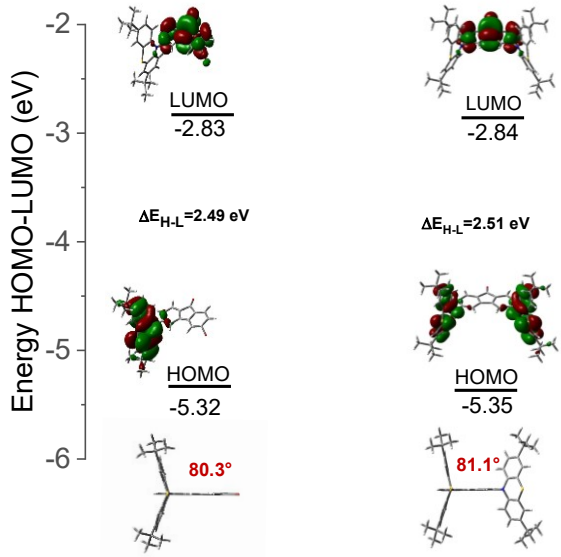

Figure 6.49. Energy diagram and molecular orbitals of Br-FL-DTP (left) and DTP-FL-DTP (right) calculated by the DFT method at the B3LYP/6-31+G(d,p) level of theory and relatives conformations and dihedral angles.

Photophysical properties

The preliminary photophysical properties of the two novel fluorenone based emitters were collaboratively studied with the Institute of Nanotechnology CNR Nanotec of Lecce. In order to determine the solvatochromic behaviour typically exhibited by highly twisted D-A and D-A-D molecular architectures, the optical properties were initially studied in diluted solution (10^{-6}M/10^{-5}M) in three solvents of different polarity: cyclohexane (CH), toluene (TOL), and dichloromethane (DCM). Absorption spectra of Br-FL-DTP (Figure 6.50 a)) and DTP-FL-DTP (Figure 6.51 a)) showed similar trends with two main bands that can be assigned to locally excited (LE) or CT excitations. The low-energy CT bands exhibited evident bathochromic shift with increased solvent polarity.

As shown in Figures 6.50 b) and 6.51 b) the steady-state emission spectra recorded in the same solutions confirm the typical trend of the CT state which resulted sensitive to the solvent polarity (a stabilizing effect occurs as the solvent polarity increases).

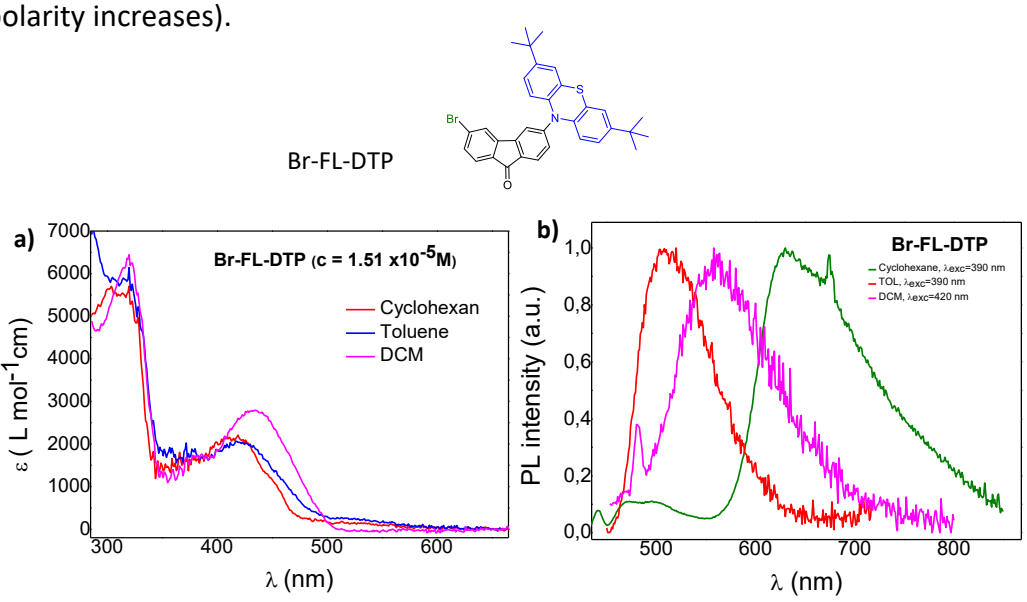

Figure 6.50. a) UV-VIS absorption spectra and b) Normalized PL spectra of Br-FL-DTP in cyclohexane (10^{-5} M, green), in toluene (10^{-5} M, red) and dichloromethane (10^{-5} M, magenta).

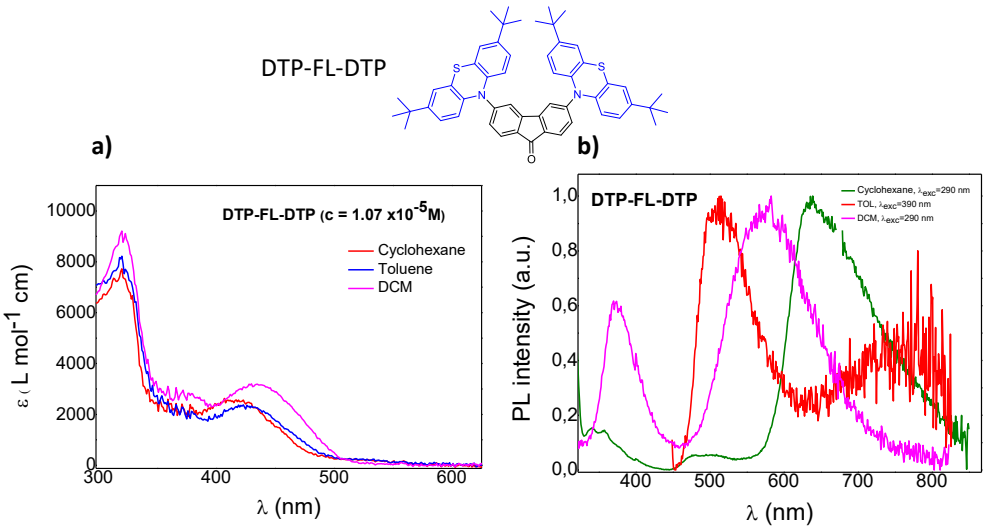

Figure 6.51. a) UV-VIS absorption spectra and b) Normalized PL spectra of DTP-FL-DTP in cyclohexane (10^{-5} M, green), in toluene (10^{-5} M, red) and dichloromethane (10^{-5} M, magenta).

However, a peculiar emission was observed in CH, 10^{-5} M. Both emitters, in fact, clearly show two different emissions, the first, less intense, at higher energy which within a vibronic resolution (470 and 496 nm), and another at lower energy (λ_{max}>600 nm) which is much more intense, strongly red shifted and with larger FWHM. The emissions at higher energy (470, 496 nm) can be ascribed to the S_1-S_0 radiative deactivation of isolated molecules, while the emissions at lower energy resulted at 618 nm for Br-FL-DTP and 623 nm for DTP-FL-DTP and are assigned to the S_1-S_0 radiative deactivation process of aggregated states, that can plausibly be ascribed to the generation of excimers. In fact, the well-resolved and structured emission of the isolated molecules (monomers) in CH indicates that the S_1 state has a weak CT character in non-polar solvents. This is due to the very small dipole moment of CH that do not stabilize efficiently the CT state, and hence, the fluorescence comes from mixed LE and CT state. As observed, despite the dilution of $1x10^{-5}$ M is optimal to study the isolated molecules PL properties, the low solubility of these materials in CH leads to the formation of aggregates also at such dilution.

Table 6.51.
Optical and photophysical properties recorded in diluted solutions of the synthesized emitters.

Emitter	λ_{PL}(nm)[a]	λ_{abs}(nm)[a]	$\phi_{PL}^{air}/\phi_{PL}^{deg}$ (%) Cyclohexane λ_{exc}=400nm	$\phi_{PL}^{air}/\phi_{PL}^{deg}$ (%) Toluene λ_{exc}=400nm	$\phi_{PL}^{air}/\phi_{PL}^{deg}$ (%) Dichloromethane λ_{exc}=400nm
Br-FL-DTP	618	320/435	2.2/3.5	0.1/0.1	<0.1/<0.1
DTP-FL-DTP	623	323/436	2.1/4.2	0.1/0.2	<0.1/<0.1

[a] λ_{PL}= emission maxima of the aggregates in cyclohexane solution (10^{-5} M) at room temperature.

[b] λ_{abs}= absorptions maxima measured in CH_2Cl_2 solution (10^{-5} M) at room temperature.

ϕ_{PL}^{air}= PLQY measured in aerated conditions. ϕ_{PL}^{deg}= PLQY measured in deoxygenated conditions

In Table 6.51. are also reported the photoluminescence quantum yields (Φ_{PL}) of the emitter solutions in the three solvents in aerated and deoxygenated conditions. The Φ_{PL} in TOL and DCM is very low (~0.1%), while the Φ_{PL} in CH increases more than 20 times for both materials. However, since most of the emission in CH arises from the aggregated states (Figures 6.50 b) and 6.51 b)), an aggregation induced emission (AIE) effect is evident. Moreover, the Φ_{PL} in TOL and DCM is not affected by oxygen quenching (contrarily to CH case where Φ_{PL} increases from 2.2 to 3.5% for Br-FL-DTP and from 2.1 to 4.2% for DTP-FL-DTP, Table 6.51.). Since only the emission bands of the aggregate increases upon deoxygenated conditions it can be argued that the single molecules (monomers) present prompt fluorescence (PF) only, while in the aggregated state beyond the AIE properties is also activated the delayed fluorescence (DF). The transient decays collected on the excimer emission at λ_{em}=618 nm (Figure 6.52 a)) for Br-FL-DTP and at λ_{em}=623 nm for DTP-FL-DTP showed two components; the first can be assigned to the prompt emission derived from the direct S_1->S_0 transitions of the excimer states, which have lifetimes (τ_1 in Table 6.53) in the range 7-11 ns. The second components are much longer lived (in the μs range; τ_2 in Table 6.53) and are related to the delayed fluorescence resulting from the successive ISC and rISC up-conversion of the excitons from the T_1 states to the S_1 states of the excimers.

As depicted in the Figure 6.52., the long-lived PL components are still present in oxygenated conditions, suggesting that aggregated molecules have tight packings, which do not completely allow oxygen to permeate and diffuse through the materials and thus partially preventing the quenching of long-lived excited states.

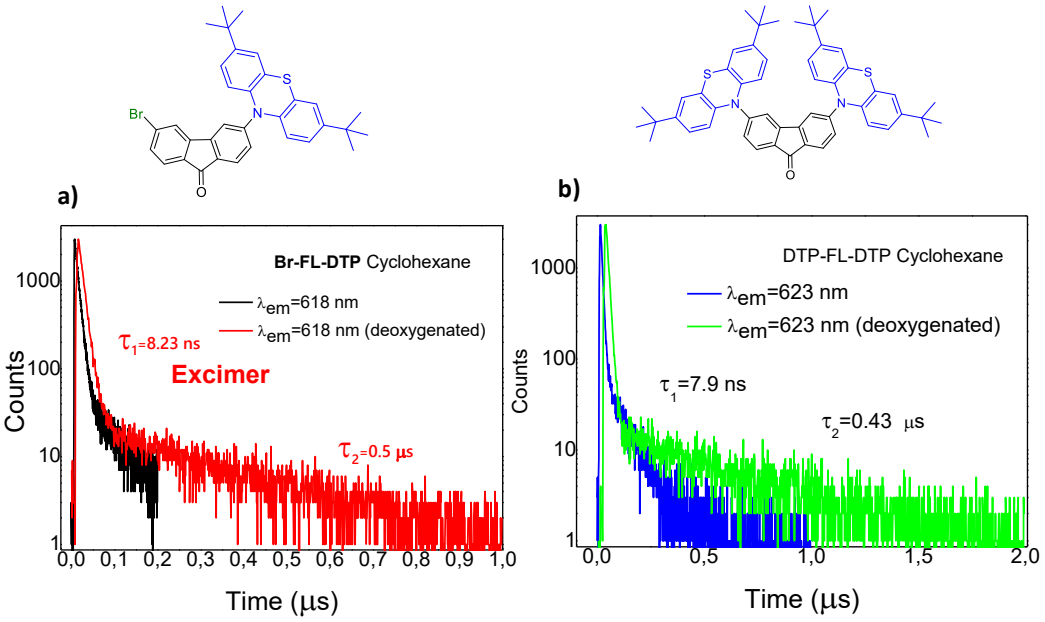

Figure 6.52. Transient PL decay curves of a) Br-FL-DTP and b) DTP-FL-DTP recorded on the PL emission maxima of the aggregates in aerated (black and blue) and deoxygenated (red and green) cyclohexane solutions (10^{-5} M) at room temperature.

Table 6.53.
Photophysical properties recorded in cyclohexane solutions (10^{-5} M)

Emitter	τ_1 air	τ_2 air	X^2 air	τ_1 deox	τ_2 deox	X^2 deox
Br-FL-DTP	8.2 ns	91.2 ns	1.12	10.6 ns	0.50 μs	1.04
DTP-FL-DTP	7.9 ns	84.09 ns	1.02	11.0 ns	0.43 μs	1.13

τ_1= prompt fluorescence lifetime determined from PL decay.
τ_2= delayed fluorescence lifetime determined from PL decay.
X^2= chi square value of the biexponential decay fitting.

In summary, the preliminary photophysical investigation revealed that these novel materials show a strong enhancement of emission when the molecules are blocked in a rigid configuration enable to promote the aggregation; it can be argued that the appropriated design of twisted D-A and D-A-D systems allows to modulate the aggregated packing of the resultant materials imparting AIE properties with a strong red shifts of the emission in the deep red region. More interestingly, it could be demonstrated that as aggregated materials a TADF emission is activated.

Conclusions and outlook

In summary, the last section of this chapter describes an improved design strategy based on the D-A and D-A-D molecular systems enable to exploit the tunability of the luminescent properties of a mono-ketone based core. A “U shaped” functionalization of the selected fluorenone acceptor allowed us to study a suitable synthetic strategy and obtain two different emitters in a single step. The obtained compounds were characterized by investigated spectroscopic, thermal, electrochemical and photophysical properties, supported by DFT calculations. Also due to the large dihedral angle between donor and acceptor units, the obtained molecules, namely DTP-FL-DTP and Br-FL-DTP, exhibited TADF and AIE behavior reaching long-wavelength emissions at 623 nm and 618 nm respectively, in peculiar conditions. In fact, the aggregated states of these materials activate TADF emission that appears strongly red shifted. The preliminary photophysical studies hint that the origin of the activation of TADF properties in these molecules is the formation of new intermolecular CT states typical of the excimers. However, further experiments are in progress and result necessary to provide insight into the solid state properties of these materials.

The internal heavy atom effect exerted by the Bromine in the D-A molecule will further be investigated in order to evaluate the impact on the rISC process and render the delayed fluorescence more distinct.

Considering these promising results, I think that this study represents a new powerful strategy for developing TADF materials with deep reed or infrared emission, thus contributing to a further advancement in the field of red TADF which remains still rare. Moreover, once optimized in terms of efficiency the AIE properties of these materials along with the red emission properties might find application in many fields such as optoelectronic devices, [63] sensors, [64] anticounterfeiting, [65] bioimaging, memory chips. [66]

6.3.3 Experimental section

General remarks

See Experimental section reported in paragraph 6.2.3.

Synthesis of 3,6-dibromo-9H-fluoren-9-one [60]

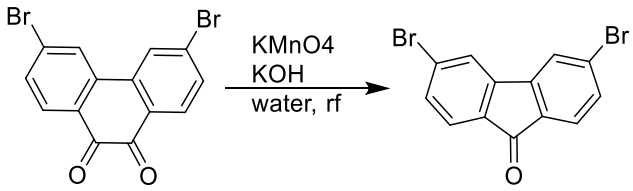

Scheme 6.54. Synthetic procedure for the obtainment of 3,6-dibromo-9H-fluoren-9-one.

According to a literature procedure, a mixture of 10.88 g (68.80 mmol) $KMnO_4$ and 80.00 g KOH in 210 ml water was heated to reflux. Then, 1.80 g (5.00 mmol) 3,6-dibromophenanthrenequinone was added at once. Heating was continued for 4 hours. The mixture was allowed to cool to room temperature and dichloromethane was added. The organic layer was separated, dried (Na_2SO_4), filtered and concentrated. After column separation (SiO_2, dichloromethane) 0.625 g (37 %) of product was obtained as a yellow powder.

^1H NMR ($CDCl_3$): δ 7.71 (d, J=1.5 Hz, 2H), 7.58 (d, J=8 Hz, 2H), 7.52 (dd, J=1.5 Hz, J=8 Hz, 2H).

Synthesis of the donor 3,7-di-tert-butyl-10H-phenothiazine (DTP) [51]
3,7-di-tert-butyl-10H-phenothiazine (DTP) was synthesized as described in the Experimental Part 6.2.3.

Synthesis of 3-bromo-6-(3,7-di-tert-butyl-10H-phenothiazin-10-yl)-9H-fluoren-9-one (Br-FL-DTP) and 3,6-bis(3,7-di-tert-butyl-10H-phenothiazin-10-yl)-9H-fluoren-9-one (DTP-FL-DTP)
A mixture of 3,6-dibromo-9H-fluoren-9-one (572.90 mg, 1.68 mmol), DTP (523.32 mg, 1.68 mmol), $Pd(OAc)_2$ (18.86 mg, 0.084 mmol), DPPF (93.14 mg, 0.168 mmol) and sodium tert-butoxide (242.20 mg, 2.52 mmol) in toluene (10 mL) was stirred at 110 °C for 16 h. After cooling down the reaction to room temperature, the reaction mixture was diluted with dichloromethane (20 mL) and the obtained organic layer was washed with water (3 × 30 mL). The organic phase was separated, dried over Na_2SO_4, and filtered. Upon removing the solvent, the crude product was purified by column chromatography (SiO_2, petroleum ether 40-60°C/CH_2Cl_2 = 2/3 vol/vol) to obtain as first fraction Br-FL-DTP (148.59 mg, 31 %) as a bright yellow solid and DTP-FL-DTP as second fraction (161.52 mg, 24%).

Br-FL-DTP:
^{1}H NMR (500 MHz, acetone-d_6) δ 7.78 (d, J = 1.2 Hz, 1H, FLH), 7.61 – 7.56 (m, 2H, FLH), 7.56 – 7.50 (m, 2H, FLH), 7.49 (d, J = 2.1 Hz, 2H, 1FLH+1DTPH), 7.41 (dd, J = 8.4, 2.1 Hz, 2H, DTPH), 7.29 (d, J = 8.4 Hz, 2H, DTPH), 7.06 (dd, J = 8.3, 2.0 Hz, 1H, DTPH), 1.34 (s, 18H, t-Bu) ppm.

DTP-FL-DTP:
^{1}H NMR (500 MHz, acetone-d_6) δ 7.63 (d, J = 8.1 Hz, 2H, FLH), 7.49 (d, J = 1.7 Hz, 2H, FLH), 7.37 (d, J = 2.2 Hz, 4H, 2FLH+ 2DTPH), 7.25 (dd, J = 8.5, 2.2 Hz, 4H, DTPH), 7.10 (dd, J = 8.1, 2.0 Hz, 2H, DTPH), 6.98 (d, J = 8.5 Hz, 4H, DTPH), 1.30 (s, 36H, t-Bu) ppm.

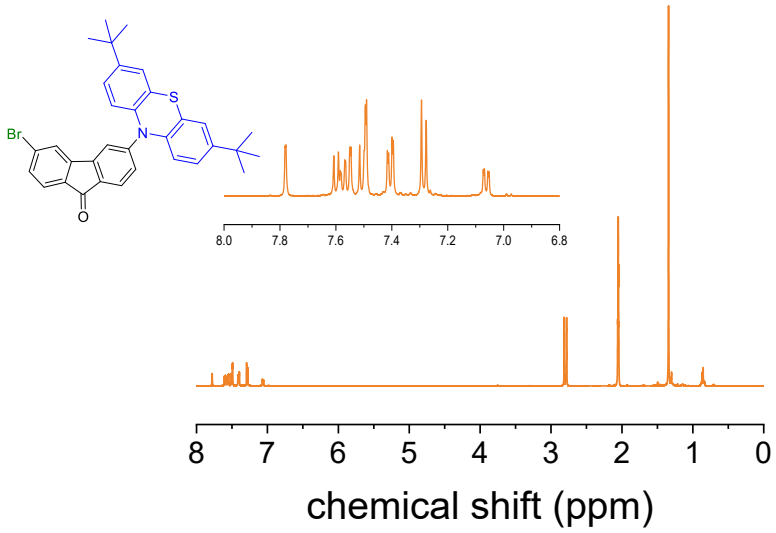

Figure 6.55. ^{1}H NMR spectrum of Br-FL-DTP recorded in acetone-d_6.

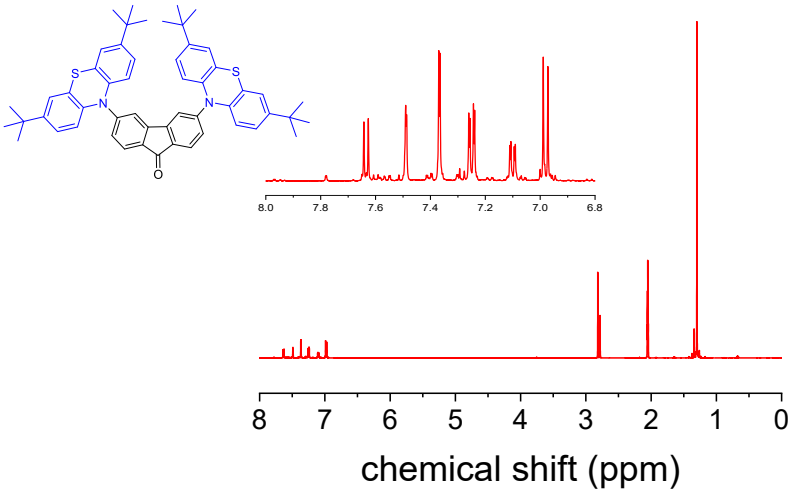

Figure 6.56. ^{1}H NMR spectrum of DTP-FL-DTP recorded in acetone-d_6.

6.4 References

1. IEA. *Targeting 100% LED lighting sales by 2025.* Paris : IEA, 2022. License: CC BY 4.0.

2. Energy, Ministerial Clean. *Global lighting challenge campaign (GLC).* Clean Energy Ministerial. 2022. GLC fact sheet.

3. *Highly efficient organic light-emitting diodes from delayed fluorescence.* Uoyama H, Goushi K, Shizu K, Nomura H, Adachi C. 7428, 2012, Nature, Vol. 492, p. 234-238.

4. *Nearly 100% internal phosphorescence efficiency in an organic light-emitting device.* Chihaya Adachi, Marc A. Baldo, Mark E. Thompson, and Stephen R. Forrest ,. 2001, Journal of Applied Physics, Vol. 90.

5. *An Optical Thermometer Based on the Delayed Fluorescence of C70.* Baleizão, C., Nagl, S., Borisov, S., Schäferling, M., Wolfbeis, O. and Berberan-Santos, M. 2007, Chemistry – A European Journal, Vol. 13, p. 3643-3651.

6. *Organic Electroluminescent Diodes.* Tang, C. W. e VanSlyke, S. A. 12, 1987, Appl. Phys. Lett. , Vol. 51 , p. 913–915.

7. *Excitonic singlet-triplet ratio in a semiconducting organic thin film.* Baldo, M. A. and O'Brien, D. F. and Thompson, M. E. and Forrest, S. R. 20, 1999, Phys. Rev. B, Vol. 60, p. 14422-14428.

8. *Recent advances on organic blue thermally activated delayed fluorescence (TADF) emitters for organic light-emitting.* Bui T.T., Goubard F., Ibrahim-Ouali M., Gigmes D., Dumur F. 2018, Beilstein J. Org. Chem. , Vol. 14, p. 282–308.

9. *Highly efficient phosphorescent emission from organic electroluminescent devices.* Baldo, M., O'Brien, D., You, Y. et al. 1998, Nature , Vol. 395, p. 151–154 .

10. *Highly efficient organic light-emitting diodes from delayed fluorescence.* Uoyama H, Goushi K, Shizu K, Nomura H, Adachi C. 7428, 2012, Nature, Vol. 492, p. 234-238.

11. *Efficient up-conversion of triplet excitons into a singlet state and its application for organic light emitting diodes.* Ayataka Endo, Keigo Sato, Kazuaki Yoshimura, Takahiro Kai, Atsushi Kawada, Hiroshi Miyazaki, and Chihaya Adachi. 083302, 2011 , Appl. Phys. Lett. , Vol. 98.

12. *Photophysical Characterisation of Thermally Activated Delayed Fluorescence (TADF) Materials.* Pander P., Dias F.B. 2017, Disp. Imaging, Vol. 2, p. 249-63.

13. *Highly efficient organic light-emitting diodes from delayed fluorescence. .* Uoyama H, Goushi K, Shizu K, Nomura H, Adachi C. 7428, 2012, Nature., Vol. 492, p. 234-238.

14. *Molecular Design Based on Donor-Weak Donor Scaffold for Blue Thermally-Activated Delayed Fluorescence Designed by Combinatorial DFT Calculations.* Tsuchiya Y, Tsuji K, Inada K, Bencheikh F, Geng Y, Kwak HS, Mustard TJL, Halls MD, Nakanotani H, Adachi C. 8, May 2020 , Front Chem. , Vol. 6, p. 403.

15. *Thermally activated delayed fluorescence materials towards the breakthrough of organoelectronics.* Tao Y, Yuan K, Chen T, et al. 47, 2014, Adv Mater., Vol. 26, p. 7931-7958. .

16. *Photophysics of thermally activated delayed fluorescence molecules.* Dias FB, Penfold TJ, Monkman AP. 1, 2017, Methods Appl Fluoresc., Vol. 5, p. 012001.

17. *Purely Organic Thermally Activated Delayed Fluorescence Materials for Organic Light-Emitting Diodes.* Wong, M. Y., Zysman-Colman, E.,. 2017, Adv. Mater., Vol. 29, p. 1605444.

18. *High efficiency blue organic light-emitting diodes with below-bandgap electroluminescence .* Vasilopoulou, M., Mohd Yusoff, A.R.b., Daboczi, M. et al. 2021 https://doi.org/10.1038/s41467-021-25135-z, Nat. Commun. , Vol. 12, p. 4868 .

19. *Dual-channel charge transfer-based thermally activated delayed fluorescence emitter facilitating efficient and low roll-off non-doped devices.* Hao-Ze Li, Feng-Ming Xie, Kai Zhang, Yang Shen, Wei Zhou, Yan-Qing Li, Wen-Jun Wang, Jian-Xin Tang,. 135234, 2022, Chemical Engineering Journal, Vol. 436.

20. *High-Efficiency Solution-Processable OLEDs by Employing Thermally Activated Delayed Fluorescence Emitters with Multiple Conversion Channels of Triplet Excitons.* Liu, Y., Hua, L., Zhao, Z., Ying, S., Ren, Z., Yan, S.,. 2021, Adv. Sci., Vol. 8, p. 2101326.

21. *Red to orange thermally activated delayed fluorescence polymers based on 2-(4-(diphenylamino)-phenyl)-9H-thioxanthen-9-one-10,10-dioxide for efficient solution-processed OLEDs.* Khammultri, Praetip

and Chasing, Pongsakorn and Chitpakdee, Chirawat and Namuangruk, Supawadee and Sudyoadsuk, Taweesak and Promarak, Vinich. 40, 2021, RSC Adv., Vol. 11, p. 24794-24806.
22. *Molecular design strategy for orange red thermally activated delayed fluorescence emitters in organic light-emitting diodes (OLEDs) .* K. Rayappa Naveen, K. Prabhu CP, R. Braveenth, J. Hyuk Kwon,. 2022, Chem. Eur. J., Vol. 28, p. e202103532.
23. *Aromatic-Imide-Based Thermally Activated Delayed Fluorescence Materials for Highly Efficient Organic Light-Emitting Diodes.* Li M, Liu Y, Duan R, et al. 30, 2017, Angew Chem Int Ed Engl. , Vol. 56, p. 8818-8822.
24. *Luminous Butterflies: Efficient Exciton Harvesting by Benzophenone Derivatives for Full-Color Delayed Fluorescence OLEDs. .* Lee, S.Y., Yasuda, T., Yang, Y.S., Zhang, Q. and Adachi, C. 2014, Angew. Chem. Int. Ed., , Vol. 53, p. 6402-6406.
25. *Suppression of benzophenone-induced triplet quenching for enhanced TADF performance.* Kreiza, Gediminas and Banevičius, Dovydas and Jovaišaitė, Justina and Maleckaitė, Karolina and Gudeika, Dalius and Volyniuk, Dmytro and Gražulevičius, Juozas V. and Juršėnas, Saulius and Kazlauskas, Karolis. 7, 2019, J. Mater. Chem. C, p. 11522-11531.
26. *Anthraquinone-Based Intramolecular Charge-Transfer Compounds: Computational Molecular Design, Thermally Activated Delayed Fluorescence, and Highly Efficient Red Electroluminescence.* Qisheng Zhang, Hirokazu Kuwabara, William J. Potscavage Jr., Shuping Huang, Yasuhiro Hatae, Takumi Shibata, and Chihaya Adachi. 52, 2014 , Journal of the American Chemical Society, Vol. 136, p. 18070-18081.
27. *Simple aggregation–induced delayed fluorescence materials based on anthraquinone derivatives for highly efficient solution–processed red OLEDs.* Sun, Bin Huang and Yigang Ji and Zijing Li and Na Zhou and Wei Jiang and Yan Feng and Baoping Lin and Yueming. 2017, Journal of Luminescence, Vol. 187, p. 414-420.
28. *Yuewei Zhang, Huili Ma, Shipan Wang, Zhiqiang Li, Kaiqi Ye, Jingying Zhang, Yu Liu, Qian Peng, and Yue Wang. 35, 2016 , The Journal of Physical Chemistry C , Vol. 120 , p. 19759-19767.*
29. Versatile Molecular Functionalization for Inhibiting Concentration Quenching of Thermally Activated Delayed Fluorescence. Lee, J., Aizawa, N., Numata, M., Adachi, C., Yasuda, T.,. 2017, Adv. Mater., Vol. 29, p. 1604856.
30. Aggregation-induced delayed fluorescence from phenothiazine-containing donor–acceptor molecules for high-efficiency non-doped organic light-emitting diodes. . Aizawa, N., Tsou, CJ., Park, I. et al. 2017 , Polym J , Vol. 49, p. 197–202.
31. High-efficiency organic light-emitting diodes with fluorescent emitters. . Nakanotani, H., Higuchi, T., Furukawa, T. et al. 2014 , Nat. Commun., Vol. 5, p. 4016 .
32. Achieving High-Performance Nondoped OLEDs with Extremely Small Efficiency Roll-Off by Combining Aggregation-Induced Emission and Thermally Activated Delayed Fluorescence. Guo, J., Li, X.-L., Nie, H., Luo, W., Gan, S., Hu, S., Hu, R., Qin, A., Zhao, Z., Su, S.-J., Tang, B. Z.,. 2017, Adv. Funct. Mater. , Vol. 27, p. 1606458.
33. Robust Luminescent Materials with Prominent Aggregation-Induced Emission and Thermally Activated Delayed Fluorescence for High-Performance Organic Light-Emitting Diodes. Jingjing Guo, Xiang-Long Li, Han Nie, Wenwen Luo, Rongrong Hu, Anjun Qin, Zujin Zhao, Shi-Jian Su, and Ben Zhong Tang. 8, 2017 , Chemistry of Materials , Vol. 29 , p. 3623-3631.
34. Highly Efficient Nondoped OLEDs with Negligible Efficiency Roll-Off Fabricated from Aggregation-Induced Delayed Fluorescence Luminogens. Huang J, Nie H, Zeng J, et al. 42, 2017, Angew Chem Int Ed Engl. , Vol. 56, p. 12971-12976.
35. J. Luo, Z. Xie, J. W. Y. Lam,L. Cheng,B. Z. Tang,H.Chen,C.Qiu, H. S.Kwok, X. Zhan,Y. Liu, D. Zhu,. 2001, Chem.Commun., p. 1740–1741.
36. E. Ubba, Y. Tao, Z. Yang, J. Zhao, L. Wang, Z. Chi,. 3106, 2018, Chem. Asian J. , Vol. 13 .
37. Novel Thermally Activated Delayed Fluorescence Materials–Thioxanthone Derivatives and Their Applications for Highly Efficient OLEDs. Wang, H., Xie, L., Peng, Q., Meng, L., Wang, Y., Yi, Y. and Wang, P. 26, 2014, Adv. Mater., p. 5198-5204.
38. Aggregation-induced delayed fluorescence from phenothiazine-containing donor–acceptor molecules for high-efficiency non-doped organic light-emitting diodes. . Aizawa, N., Tsou, CJ., Park, I. et al. 2017, Polym J , Vol. 49, p. 197–202 .

39. Simple aggregation–induced delayed fluorescence materials based on anthraquinone derivatives for highly efficient solution–processed red OLEDs. Bin Huang, Yigang Ji, Zijing Li, Na Zhou, Wei Jiang, Yan Feng, Baoping Lin, Yueming Sun,. 2017, Journal of Luminescence, Vol. 187, p. 414-420.
40. Synthesis, characterization of the phenylquinoline-based on iridium(III) complexes for solution processable phosphorescent organic light-emitting diodes. Juhyeon Park, Jin Su Park, Young Geun Park, Jin Yong Lee, Jae Wook Kang, Jun Liu, Liming Dai, Sung-Ho Jin,. 9, 2013, Organic Electronics, Vol. 14, p. 2114-2123.
41. Highly photo- and electroluminescent 1,3-diketonate Eu(iii) complexes with spiro-fluorene-xantphos dioxide ligands: synthesis and properties. Pietraszkiewicz, Marek and Maciejczyk, Michal and Samuel, Ifor D. W. and Zhang, Shuyu. 48, 2013, J. Mater. Chem. C, Vol. 1, p. 8028-8032.
42. Manipulation of Molecular Aggregation States to Realize Polymorphism, AIE, MCL, and TADF in a Single Molecule. B. Huang, W.-C. Chen, Z. Li, J. Zhang, W. Zhao, Y. Feng, B. Z. Tang, C.-S. Lee,. 2018, Angew. Chem. Int. Ed., Vol. 57, p. 12473.
43. Electroluminescent materials for white organic light emitting diodes. Farinola, Gianluca M. and Ragni, Roberta. 7, Chem. Soc. Rev., Vol. 40, p. 3467-3482.
44. Strategies to Design Bipolar Small Molecules for OLEDs: Donor-Acceptor Structure and Non-Donor-Acceptor Structure. Duan, L., Qiao, J., Sun, Y. and Qiu, Y. (2011),. 2011, Adv. Mater., Vol. 23, p. 1137-1144 .
45. New starburst sensitizer with carbazole antennas for efficient and stable dye-sensitized solar cells. Tang, Jin and Hua, Jianli and Wu, Wenjun and Li, Jing and Jin, Zeguo and Long, Yitao and Tian, He. 11, 2010, Energy Environ. Sci., Vol. 3, p. 1736-1745.
46. Conjugated carbazole dimer as fluorescence carrier for preparation of iodine-sensitive chemical sensor. Yu, Chen-Xu Jiao and Qi Shen and Shuang-Yan Huan and Guo-Li Shen and Ru-Qin. 2, 2005, Analytica Chimica Acta, Vol. 528, p. 229-234.
47. Organic luminescent molecule with energetically equivalent singlet and triplet excited states for organic light-emitting diodes. Sato K, Shizu K, Yoshimura K, Kawada A, Miyazaki H, Adachi C. 24, 2013, Phys Rev Lett. , Vol. 110, p. 247401 .
48. Molecular Design Strategy for Orange Red Thermally Activated Delayed Fluorescence Emitters in Organic Light-Emitting Diodes (OLEDs). K. Rayappa Naveen, K. Prabhu CP, R. Braveenth, J. Hyuk Kwon,. 2022, Chem. Eur. J. , Vol. 28 , p. e202103532.
49. Molecular Design Strategy of Organic Thermally Activated Delayed Fluorescence Emitters. Yirang Im, Mounggon Kim, Yong Joo Cho, Jeong-A Seo, Kyoung Soo Yook, and Jun Yeob Lee. 5, 2017 , Chemistry of Materials , Vol. 29 , p. 1946-1963.
50. NAM, Hyun Goog, et al. NEW ELECTRON TRANSPORT MATERIAL AND ORGANIC ELECTROLUMINESCENT DEVICE USING THE SAME. WO2013/180376 5 12 2013.
51. Synthesis and anion recognition studies of novel 5,5-dioxidophenothiazine-1,9-diamides. Huszthy, Attila Kormos and Ildikó Móczár and Attila Sveiczer and Péter Baranyai and László Párkányi and Klára Tóth and Péter. 35, 2012, Tetrahedron, Vol. 68, p. 7063-7069.
52. Largely blue-shifted emission through minor structural modifications: molecular design, synthesis, aggregation-induced emission and deep-blue OLED application. Huang, Jing and Sun, Ning and Chen, Pengyu and Tang, Runli and Li, Qianqian and Ma, Dongge and Li, Zhen",. 17, 2014, Chem. Commun., Vol. 50, p. 2136-2138.
53. Achieving Efficient Blue Delayed Electrofluorescence by Shielding Acceptors with Carbazole Units. Zong Cheng, Zhiqiang Li, Yincai Xu, Jixiong Liang, Chunhui Lin, Jinbei Wei, and Yue Wang. 31, 2019 , ACS Applied Materials & Interfaces , Vol. 11, p. 28096-28105.
54. Thermally activated delayed fluorescent phenothiazine–dibenzo[a{,}j]phenazine–phenothiazine triads exhibiting tricolor-changing mechanochromic luminescence. Okazaki, Masato and Takeda, Youhei and Data, Przemyslaw and Pander, Piotr and Higginbotham, Heather and Monkman, Andrew P. and Minakata, Satoshi. 4, 2017, Chem. Sci., Vol. 8, p. 2677-2686.
55. An aggregation-induced emission luminophore with multi-stimuli single- and two-photon fluorescence switching and large two-photon absorption cross section. Xu, Bingjia and Xie, Mingyuan and He, Jiajun and

Xu, Bin and Chi, Zhenguo and Tian, Wenjing and Jiang, Long and Zhao, Fuli and Liu, Siwei and Zhang, Yi and Xu, Zhizhan and Xu, Jiarui. 3, 2013, Chem. Commun, Vol. 49, p. 273-275.

56. Anthraquinone-Based Intramolecular Charge-Transfer Compounds: Computational Molecular Design, Thermally Activated Delayed Fluorescence, and Highly Efficient Red Electroluminescence. Qisheng Zhang, Hirokazu Kuwabara, William J. Potscavage Jr., Shuping Huang, Yasuhiro Hatae, Takumi Shibata, and Chihaya Adachi. 52, 2014 , Journal of the American Chemical Society , Vol. 136, p. 18070-18081.

57. Recent Progress of Highly Efficient Red and Near-Infrared Thermally Activated Delayed Fluorescent Emitters. Kim, J. H., Yun, J. H., Lee, J. Y.,. 1800255, 2018, Advanced Optical Materials, Vol. 6 .

58. Revisiting fluorenone photophysics via dipolar fluorenone derivatives. Estrada LA, Yarnell JE, Neckers DC. 24, 23 Jun 2011 , The Journal of Physical Chemistry A. , Vol. 115, p. 6366-6375.

59. Heavy Atom Effect of Bromine Significantly Enhances Exciton Utilization of Delayed Fluorescence Luminogens. Shifeng Gan, Shimin Hu, Xiang-Long Li, Jiajie Zeng, Dongdong Zhang, Tianyu Huang, Wenwen Luo, Zujin Zhao, Lian Duan, Shi-Jian Su, and Ben Zhong Tang. 20, 2018 , ACS Applied Materials & Interfaces , Vol. 10, p. 17327-17334.

60. Journal of the American Chemical Society . Klemens Brunner, Addy van Dijken, Herbert Börner, Jolanda J. A. M. Bastiaansen, Nicole M. M. Kiggen, and Bea M. W. Langeveld. 19, 2004 , Vol. 126 , p. 6035-6042.

61. The Road Less Traveled: Unconventional Site Selectivity in Palladium-Catalyzed Cross-Couplings of Dihalogenated N-Heteroarenes. Neufeldt, Jacob P. Norman and Sharon R. 19, 2022 , ACS Catalysis , Vol. 12 , p. 12014-12026.

62. Synergistical Dipole–Dipole Interaction Induced Self-Assembly of Phenoxazine-Based Hole-Transporting Materials for Efficient and Stable Inverted Perovskite Solar Cells. N. Cai, F. Li, Y. Chen, R. Luo, T. Hu, F. Lin, S.-M. Yiu, D. Liu, D. Lei, Z. Zhu, A. K.-Y. Jen,. 2021, Angew. Chem. Int. Ed., Vol. 60, p. 20437.

63. All-organic thermally activated delayed fluorescence materials for organic light-emitting diodes. Liu, Y., Li, C., Ren, Z. et al., 2018, Nat Rev Mater, Vol. 3, p. 18020. https://doi.org/10.1038/natrevmats.2018.20

64. Polyesters with Built-in Threshold Temperature and Deformation Sensors. Maki Kinami, Brent R. Crenshaw, and Christoph Weder, 2006, Chemistry of Materials, Vol. 18, p. 946. DOI: 10.1021/cm052186c

65. Multiple Anti-Counterfeiting Guarantees from a Simple Tetraphenylethylene Derivative–High-Contrasted and Multi-State Mechanochromism and Photochromism. Guangxi Huang, Qing Xia, Wenbin Huang, Jianwu Tian, Zikai He, Bing Shi Li, Ben Zhong Tang., 2019, Angew. Chem. Int. Ed., Vol. 58, p. 17814.

66. Recent Developments on Multi-Functional Metal-Free Mechanochromic Luminescence and Thermally Activated Delayed Fluorescence Organic Materials. Barman D, Gogoi R, Narang K, Iyer PK. 2020, Front Chem., Vol. 8, p.483., doi:10.3389/fchem.2020.00483.

7 Concluding remarks and future perspectives

The work outlined in this Thesis highlights how materials design and synthesis can be used to tailor optoelectronic properties and reducing the environmental impact concerning the development of new conjugated organic materials. In this framework, the C−H bond activation reactions have been investigated as a central topic of the experimental studies described in the first 4 chapters in order to obtain a sustainable synthesis of specific polyconjugated organic materials. In particular, in the course of these three years I studied the effects of the « green » solvents (i.e., CPME, anisole and propylene carbonate) in consolidated polycondensations, such as the tandem Suzuki–Heck and the direct arylation polymerizations (DArP). With the intention of making environmental considerations from the beginning the first aim was the search for optimal reaction conditions also regarding the catalytic system and the base quantity, which both potentially jeopardize the DarP sustainability in a green, ethereal solvent (CPME) for the preparation of P3HT. To sum up, one of the important result of the systematic study, discussed in **Chapter 2**, is based on the possibility of reducing, with respect to the common DArP protocols, the amount of the expensive base (i.e. Cs_2CO_3) in the adopted reaction conditions without influencing the quality of the resulting polymer. Furthermore, the satisfactory results in terms of molecular weights, obtained after the extension of the optimized reaction conditions to the copolymerization of other differently structured monomer units consolidate the sustainable DArP protocols as an appealing alternative to the commonly employed polymerization methods.

In a further investigation presented in **Chapter 3**, I studied the effects of the best "green" solvents (i.e., anisole and propylene carbonate) in tandem Suzuki–Heck and the direct arylation polymerizations (DArP). In the synthesis of poly(9,9-dioctylfluorenylene-vinylene), the selected green solvents yielded better results with respect to conventional media. Additionally, the modulation of the medium polarity using mixtures of these green solvents and changing the reaction temperature affords a suitable compromise between high molecular weights and

regioregularity of the resulting polymers. Concerning the DArP of 2-bromo-3-hexylthiophene yielding poly(3-hexylthiophene) (P3HT), the catalyst performances in anisole strictly depend on the palladium source used. The best conditions are obtained using $PdCl_2(PPh_3)_2$ as the precatalyst, affording a highly regioregular (93%) P3HT in quantitative yields (98%) and high molecular weights (26.7 kg/mol).

Although, as discussed above, the implementation of sustainable solvents from the point of view of safety, health and the environment has been proposed, their compatibility with aerobic reaction conditions has remained thus far poorly explored. In this perspective, in **Chapter 4** was reported a further investigation concerning the viability of applying anisole in the preparation of poly(9,9-dioctylfluorene-2,2'-bithiophene) (PF8TT) under undried and aerobic conditions by employing the catalytic system consisting of $(PPh_3)_2PdCl_2$/P(o-Anisyl)$_3$/Cs_2CO_3 in the presence of pivalic acid as the proton transfer agent. As emerged from the polymerization kinetics, the catalyst rapid deactivation is the main reason of the low molecular weights obtained for the resulting polymers. At the same time, it was ascertained that the adopted aerobic reaction conditions preclude an uncontrolled polymer growth via radicalic pathways and the incorporation of structural defects. Therefore, the optimization of the work-up protocol enables the obtainment of PF8TT endowed with high molecular weights (M_n = 15900 Da) under completely "green" conditions, thus consolidating this C–H activation route as a sustainable protocol for the construction of conjugated polymers.

In summary, the studies discussed in the first four chapters further consolidate sustainable C-H activation protocols as an attractive alternative to commonly employed polymerization methods and suggests that in the future, by combining different green design elements, the discussed innovative reaction protocols will offer promising starting points for applied research which will finally enable the industrial of C−H activation.

One of the research highlights of the second part of this Thesis is the development of a rational approach of molecular design, synthesis and characterization of novel and structurally simplified organic molecules in each chapters.

Chapter 5 described the development of novel Hole-Transporting-Materials, low cost and dopant-free for Perovskite Solar Cells (PSCs).

Firstly, two novel polymer HTMs were synthesized utilizing a Buchwald−Hartwig-type polycondensation of aniline derivatives and a poly-alkylated dibromofluorene-based monomer in high yielding, low-cost, and simple workup reactions. The novel HTMs exhibited excellent thermal and optoelectronic properties and they presented suitable HOMO levels, which were perfectly aligned with that of the perovskite material. Co-polymerizations of groups that perform well will also be investigated in order to customize favorable polymer properties. Further investigations are needed to explore the possible advantages that these polymers could give, since devices were not optimized and also investigations regarding stability are required.

Thanks to a collaborative and interdisciplinary investigation regarding the development of new small molecular HTMs, as simplified and cost-competitive alternatives to the traditional Spiro-OMeTAD HTM, I had the opportunity to synthesize two fluorene-based hole transport materials (SCF1 and SCF2). The rationale behind these molecules was to reduce the molecular distortion required for the surface interaction between the HTM and the perovskite. Both SCF-HTMs were synthesized through a convergent and high-yield synthetic procedure, featuring significantly lower material and manufacturing costs.

The enhanced perovskite|SCF1 interface is reflected in excellent hole extraction, low hole trap density and an impressive shelf-lifetime (T_{80} = 431 days) of the corresponding unencapsulated devices, which is one of the longest lifetimes ever reported for PSCs.

Along this trend, the research activity, which is actually in progress, aims to demonstrate a step-saving and viable synthetic approach to access novel functional small molecules for use in PSCs devices. Based on the optimized direct C–H

arylation approach, I have efficiently synthesized two new molecules bearing 2,2'-bithiophene cores in good yields (BTC and BTF). The novel HTMs exhibited excellent thermal, morphological and electrochemical properties and they presented suitable HOMO levels, which were aligned with that of the perovskite material. Further investigations are needed to explore the possible advantages that this type of molecule could give. However, to date, this study clearly demonstrates that the development of new potential π-conjugated organic materials in a green chemistry compliant manner leads to stable and efficient PSC materials.
Lastly, the potentialities of π-conjugated organic materials were exploited in this Thesis with the aim to contribute at the introduction of innovative materials (i.e. TADF emitters) exhibiting high performance for the conversion of electricity to light for applications in OLED devices. In this regard, **Chapter 6** describes an intriguing design strategy adopted for the development of new ketone-based multifunctional organic luminescent materials with AIE, TADF and mechanochromic properties in the solid state. The asymmetric D–Ph–A configuration of the target molecules discussed in **section 6.2.** were pursued through a straightforward synthetic approach based on a palladium-catalyzed Buchwald–Hartwig amination reaction. The adoption of one (indanone) or two (indandione) ketone groups in the acceptor moieties and the combination with electron donors endowed with different strength allowed us to investigate the structure-property relationship which determined the TADF characteristic, especially at the aggregated state. The synthesized emitters exhibited reversible Multicolor-Mechanochromic Luminescence (MCL), demonstrating how molecular assembly and external stimuli, are parameters that play an important role in the control of the CT state energy, which influences both the colour emission and the TADF behaviour. At this stage, further experiments are underway, e.g. especially XRD analysis on the crystalline powders. This will allow to provide a deeper insight into the structure-property relationships governing the modification of the photophysical properties of these materials. I think that based on the results obtained in this study, it would be worthwhile to further explore the supramolecular properties of

innovative donors (D) attached to a ketone-based acceptor (A) moieties systems, in order to better understand the key factors that allow improving the solid-state photophysical properties in term of TADF, MCL and AIE. In perspective, this work opens up a new approach for further research on the multifunctional long-wavelength (orange-red) organic emitters that will eventually be applied, among others, to devices such as solution-processed OLED. In the same context, the last section of this chapter describes an improved design strategy based on the D-A and D-A-D molecular systems enable to exploit the tunability of the luminescent properties of a mono-ketone based core. A "U shaped" functionalization of the selected fluorenone acceptor allowed us to study a suitable synthetic strategy and obtain two different emitters in a single step. The aggregated states of these materials activate TADF emission that appears strongly red shifted. The preliminary photophysical studies hint that the origin of the activation of TADF properties in these molecules is the formation of new intermolecular CT states typical of the excimers. However, further experiments are in progress and result necessary to provide insight into the solid state properties of these materials. The internal heavy atom effect exerted by the Bromine in the D-A molecule will further be investigated in order to evaluate the impact on the rISC process and render the delayed fluorescence more distinct. Considering these promising results, I think that this study represents a new powerful strategy for developing TADF materials with deep red or infrared emission, thus contributing to a further advancement in the field of red TADF. In conclusion, this Ph.D Thesis has shown that the research field in organic electronics is maturing and it will be increasingly important to consider as many factors as possible in order to map the full impact of a structural modification done on a conjugated molecular system. Thus, the rational design of new π-conjugated organic materials will be key for solving important challenges related to the generation and storage of clean energy, the environmentally-friendly production of chemicals, and the manufacturing of new electronic components and sensors.

8 Acknowledgements

Firstly, I would like to express my sincere gratitude to my supervisor Prof. Gian Paolo Suranna, for the continuous support during this Ph.D., for his motivation, insightful comments and encouragement.

I wish to express my gratitude to Dr. Roberto Grisorio, for his contributions, remarks and advices on all steps of this work, as well as for his enthusiasm and confidence in my research which motivated me a lot.

My special thanks go to the people that were directly involved with my work and helped with all aspects of the work presented in this Thesis: the Hybrid Solar Cells team of the Chemistry and Advanced Materials group at Tampere University directed by the Professor Paola Vivo for the fabrication and measurement of Perovskite Solar Cells, Prof. Michele Pavone and Prof. Ana Belén Muñoz-García (Federico II University of Naples) for the computational studies inherent the perovskite/HTM interactions and Prof. Nicola Margiotta of the Department of Chemistry, University of Bari for NMR measurement. Furthermore, I want to thank Dr. Vincenzo Maiorano and Dr. Antonio Maggiore of the Institute of Nanotechnology CNR Nanotec of Lecce for the photophysical measurement described in Chapter 6.

I would like to extend my sincere thanks to the members of the PPSM laboratory of the École Normale Supérieure Paris-Saclay, especially Prof. Pierre Audebert, Prof. Fabien Miomandre and Dr. Laurent Galmiche for their kind welcome and support during my French period that allowed me to increase my experience in scientific research.

Last but not least, I would like to express my gratitude to the people closest to me for the support in these three years.

List of abbreviations

A	Electron accepting unit/molecule
ACQ	Aggregation-caused quenching
AIEE	Aggregation induced enhancement emission
AIE	Aggregation induced emission
AM 1.5 G	Annual average solar irradiance at mid-latitudes
a.u.	Arbitrary unite
BT-HTMs	Bithiophene-based HTMs
CB	Conduction Band
CE	Counter Electrode
CIGS	Copper Indium Gallium Selenide
CMD	Concerted Metalation-Deprotonation
CPME	Cyclopentyl methyl ether
CT	Charge Transfer
CV	Cyclic Voltammetry
D	Electron donor unit/molecule
D-A/D-A-D	Donor-acceptor/donor-acceptor-donor
DCM	Dichloromethane
DF	Delayed fluorescence
DFT	Density Functional Theory
DMA	N,N-Dimethylacetamide
DPA	Diphenylamine
dppf	1,1'-Bis(diphenylphosphino)ferrocene
DSC	Differential Scanning Calorimetry
DSSCs	Dye Sensitized Solar Cells
e^-	electron
EJ	Exajoule
E_{ox}	oxidation potential
EQE	External quantum efficiency
E_S	Energy of singlet state
E_T	Energy of triplet state
E_g	Energy gap

ETM	Electron-Transport Material
FF	Fill Factor
FTO	Fluorine doped Tin Oxide
F8BT	Poly(9,9-dioctylfluorene-alt-benzothiadiazole)
GDP	Gross Domestic Product
GPC	Gel Permeation Chromatography
h^+	hole
HOMO	Highest Occupied Molecular Orbital
HTMs	Hole-Transporting Materials
IC	Internal conversion
ICT	Internal charge transfer
IEA	International Energy Agency
IHA	Internal-heavy-atom effect
IPCE	Incident photon-to-electron conversion efficiency
IQE	Internal quantum efficiency
ISC	Inter system crossing
J-V	current-voltage
J_{SC}	short-circuit current
LE	Locally Excited
LiTFSI	bis(trifluoromethane)sulfonamide lithium salt
LUMO	Lowest Unoccupied Molecular Orbital
MCL	Multi-Color mechanochromic Luminescence
MFC	Mechanofluorochromic materials
Me	Methyl
MEH-PPV	Poly[2-methoxy-5-(2'-ethylhexyloxy)-1,4-phenylene vinylene]
MeOH	Methanol
MeTHF	2-methyltetrahydrofuran
MS	Mass spectrometry
NMP	N-Methyl-2-pyrrolidone
NMR	Nuclear Magnetic Resonance

OFET	Organic Field-Effect Transistor
OLED	Organic Light Emitting Device
OMe	Methoxy
OPV	Organic Photovoltaic Cell
OSCs	Organic Solar Cells
P3HT	Poly(3-hexylthiophene)
PA	Polyacetylene
PAVs	Poly(arylene-vinylene)s
PC	Propylene Carbonate
PCE	Power Conversion Efficiency
PEDOT:PSS	poly(3,4-ethylenedioxythiophene):poly(styrenesulfonate)
PFO	Poly-dioctylfluorene
PFV	Poly(fluorene-vinylene)
Ph	Phenyl
PhOLED	Phosphorescent OLED
PivOH	Pivalic acid (t-BuC(O)OH)
PL	Photoluminescence
PLQY	Photoluminescence quantum yield
PSCs	Perovskite Solar Cells
PTAA	poly[bis(4-phenyl)(2,4,6-trimethylphenyl)amine]
PV	Photovoltaic
rISC	Reversed intersystem crossing
SPC	Suzuki polycondensation
Spiro-OMeTAD	2,2',7,7'-tetrakis(N,N'-di-p-methoxyphenylamine)-9,9'-spirobifluorene
TADF	Thermally activated delayed fluorescence
t-BP	4-tert-butylpyridine
T_c	Temperature of crystallization
T_d	Temperature of degradation (5% weight loss)
TFSI	bis(trifluoromethane)sulfonamide
T_g	Glass-transition temperature

TGA	Thermogravimetric analysis
TiO_2	Titanium dioxide
T_m	Melting temperature
TOL	Toluene
TPA	Triphenylamine
TRPL	Time resolved photoluminescence
UV/Vis	Ultraviolet–visible spectroscopy
VB	Valence Band
V_{OC}	open-circuit voltage
λ	Wavelength
$\lambda_{abs}/\lambda_{em}$	Wavelength of maximum absorption/emission
τ	Excited-state lifetime
χ	Estimated error
ΔE_{S-T}	Singlet-triplet energy gap
μ_H	hole mobility
Φ_{PL}	Photoluminescence quantum yield

Short Curriculum Vitae

Daniele Conelli

Contact

Email:
daniele.conelli@poliba.it
ORCID:
https://orcid.org/0000-0001-6969-2496
Google scholar Profile:
https://scholar.google.com/citations?user=l4aHIn8AAAAJ&hl=en

Skills
Languages
Italian: mother tongue
English: very good

Team working
Leadership: good
Problem solving: good Communication: very good
Public Speaking: very good

Data analysis
ChemSketch, ChemDraw, Origin Pro 8, Origin 21, Mestre C: very good
Microsoft Office: very good

EDUCATION

Polytechnic University of Bari
Department of Civil, Environmental, Land, Building Engineering and Chemistry (DICATECh)
2019 – 2023 PhD in Risk and Environmental, Territorial and Building Development XXXV cycle

Department of Pharmacy-Drug Science. University of Bari Aldo Moro
2018 Advanced degree in Pharmaceutical Chemistry and Technology
Dissertation about "Delivery of Proapoptotic Agents in Glioma Cell Lines by TSPO Ligand–Dextran Nanogels"

PROFESSIONAL EXPERIENCES

Visiting Ph.D student - 01/2022 to 04/2022
Laboratoire de Photophysique et Photochimie Supramoléculaires- et Macromoléculaires (PPSM) UMR CNRS 8531. École Normale Supérieure Paris-Saclay (Gif/Yvette, France). Research activity under the supervision of Pr P. Audebert. Research project: "synthesis of new photoluminescent organic materials based on heptazines".

Research fellow – 04/2019 to 04/2020
Polytechnic University of Bari. Department of Civil, Environmental, Land, Building Engineering and Chemistry (DICATECh). "Study of solvents and innovative methodologies in the synthesis of nanomaterials". DEMETRA project, funded by the Apulia Region within the INNOLABS tender (C.U.P. B33D17002570007 - COD. ID. Y8V9H90).

MAIN SCIENTIFIC PUBLICATIONS

Conelli, D., Margiotta, N., Grisorio, R., Suranna, G. P., Implementation of Sustainable Solvents in Green Polymerization Approaches. Macromol. Chem. Phys. 2021, 222, 2000382. https://doi.org/10.1002/macp.202000382

R. Grisorio, D. Conelli, E. Fanizza, M. Striccoli, D. Altamura, C. Giannini, I. Allegretta, R. Terzano, M. Irimia-Vladu, N. Margiotta, G. P. Suranna, Size-tunable and stable cesium lead-bromide perovskite nanocubes with near-unity photoluminescence quantum yield, Nanoscale Adv., 2021, 3, 3918-3928. DOI: 10.1039/D1NA00142F

Conelli, D., Grisorio, R., Suranna, G. P., Optimization of the Reaction Conditions for Direct Arylation Polymerizations in a Sustainable Solvent. Macromol. Chem. Phys. 2020, 221, 2000041. DOI https://doi.org/10.1002/macp.202000041.

R. Grisorio, D. Conelli, R. Giannelli, E. Fanizza, M. Striccoli, D. Altamura, C. Giannini, I. Allegretta, R. Terzano and G. P. Suranna, A new route for the shape differentiation of cesium lead bromide perovskite nanocrystals with near-unity photoluminescence quantum yield, Nanoscale, 2020, 12, 17053–17063. DOI https://doi.org/10.1039/D0NR04246C.

R. Grisorio, F. Fasulo, A. B. Muñoz-García, M. Pavone, D. Conelli, E. Fanizza, M. Striccoli, I. Allegretta, R. Terzano, N. Margiotta, P. Vivo, and G. P. Suranna. In Situ Formation of Zwitterionic Ligands: Changing the Passivation Paradigms of $CsPbBr_3$ Nanocrystals. Nano Letters, 2022, 22 (11), 4437-4444. DOI: 10.1021/acs.nanolett.2c00937.

C. Carlucci, D. Conelli, O Hassan Omar, N. Margiotta, R. Grisorio and G.P. Suranna,
Toward eco-friendly protocols: insights into direct arylation polymerizations under aerobic conditions in anisole, Polym. Chem., 2023, 14 (3), 343-351. DOI: 10.1039/D2PY01214F.

P. Mäkinen, F. Fasulo, M. Liu, G. K. Grandhi, D. Conelli, B. Al-Anesi, H. Ali-Löytty, K. Lahtonen, S. Toikkonen, G. P. Suranna, A. B. Muñoz-García, M. Pavone, R. Grisorio, and P. Vivo. Less Is More: Simplified Fluorene-Based Dopant-Free Hole Transport Materials Promote the Long-Term Ambient Stability of Perovskite Solar Cells. Chemistry of Materials 2023 35 (7), 2975-2987. DOI: 10.1021/acs.chemmater.3c00145